

**Dissertation
Submitted to the
Combined Faculties for the Natural Sciences and for Mathematics
of the Ruperto-Carola University of Heidelberg, Germany
for the degree of
Doctor of Natural Sciences**

Presented by

Vamsi Krishna Kodali
M.Sc Biomedical Engg
Born in Guraza, India

New Materials and Methods for Studying Macrophages at Interfaces

Referees: Prof. Dr. Thomas Holstein

Prof. Dr. Joachim P. Spatz

Acknowledgments

Pursuing a PhD is both an enjoyable and painful process. A good support system is important for surviving and staying sane in grad school. I have been fortunate to interact with many people who have helped and greatly influenced me. One of the pleasures of finally finishing is this opportunity to thank them.

First and foremost I wish to express my sincere thanks and profound gratitude to Prof. Jennifer Curtis and Prof. Joachim Spatz for giving me this wonderful opportunity. My sincere gratitude goes to Prof. Joachim Spatz for granting me the opportunity to explore the world of nanopatterning. Prof. Jennifer Curtis's perpetual energy, enthusiasm and motivation in research helped me immensely. She was always accessible and willing to help. Jennifer was supportive and gave me the freedom to pursue my ideas. Apart from the myriads of things I learnt during my PhD journey, Prof. Curtis taught me the three P's Perfection, patience and persistence. I hope to retain these characters throughout my life.

A special thanks goes to my thesis co-advisor Prof. Thomas Holstein and my thesis committee members Prof. G. Elisabeth Pollerberg and Dr. Frauke Gräter for spending their valuable time and helping me through the thesis.

When I first joined the Spatz group I was totally disoriented by the myriad of techniques and the infinite number of projects. The awesome colleagues in the Spatz group who quickly turned to be good friends helped me feel the Spatz group a second home. I especially treasured the group lunches and the stimulating discussions. A more encouraging and diverse work place environment is hard to imagine. I thank Frau Bozeck who went beyond her duty as secretary and helped me settle in Heidelberg. I especially thank Heike, Christian, Daniel, Simon, Kai and Theo for guiding and helping me. Christian, Kai and Daniel were always available to discuss and share ideas. Jens and Tamash helped me learn and perfect the art of microscopy. I really appreciate Ada and Julia's help with cell culture and molecular biology techniques. I thank Heike for always cheerfully helping me with my 11th hour requests. I am grateful to Daniel for help with Zusammenfassung. A special thanks goes to Vera, Nadine, Nicole, Ilia, Jacques, Theresa, Marco, Marcus, Philippe, Patrick, Babak, Johannes, Patricia, Tobias, Aaron and Mercedes. Without all your help my work and life in Heidelberg would not have been the same. I thank everyone in Spatz group for being what they are i.e. being awesome!!!!

I have been extraordinarily lucky to work with Prof. Jennifer Curtis at Georgia tech during my thesis. I appreciate the support and assistance of my colleagues Louis, Mauricio, Jan, Keith, Anthony and Daniel.

I had my share of good fortune in having excellent collaborators. I thank Stephan Schmidt and Prof. Fery from University of Bayreuth for their help with polyelectrolyte capsules. I thank Debin Wang, William Underwood, Jonas Jarvholm, Prof. Marder, Prof. King and Prof. Riedo from Georgia Tech for their help with TCNL. Without the help and support of these excellent collaborators I can't imagine completing this work.

Jan and Louis carefully read and provided valuable insights during the manuscript preparation. I sincerely appreciate and thank you guys for helping me through the countless versions of corrections.

I wish to thank my parents and sister's family for their encouragement when it was most required. The smiles from my little nieces cheered me up during times of gloom. Last,

but not the least, I thank my wife Suma for her never ending patience and for enduring me during the PhD journey. Without her love, sacrifice and emotional support this work would not have been possible.

“Thank you.....thank you everyone”

Summary

Macrophages are a key cellular component of the immune system. In the body they act as front line immune defense and are vital chemical factories that respond to their environment by secreting various chemical mediators. A complete understanding of the molecular details of phagocytotic process and macrophages ability to modulate the signaling activity is still lacking. In the present thesis we designed and used novel nano-materials to understand and modulate macrophage behavior.

In order to decipher the cell mechanics and signaling occurring during phagocytotic uptake, we used hollow polyelectrolyte capsules as force sensors. In order to enumerate the forces from the deformations, the capsules were calibrated and a stiffness of 0.11 ± 0.02 nN/nm was found. Using a swept field confocal microscope, we could follow the deformations occurring on the capsule during the phagocytotic uptake. This allowed us for the first time to decipher the mechanics of phagocytosis uptake in its natural state without applying any external mechanical forces or perturbing the cells. It was observed that macrophages during the retraction phase of the uptake, buckled or irreversibly deformed the capsules. From the mechanical characterization, we know that it takes 150 nN to buckle the capsules, this upper limit of the “PhagoSensor” approach is thirty fold higher than the values previously measured by other techniques. To systematically decipher the mechanistic roles of individual molecules in phagocytotic cup formation, we inhibited key signaling molecules PI3-Kinase and SYK, the eccentricity of the deformed capsules was found to be 0.87 ± 0.05 and 0.75 ± 0.05 respectively. This showed that the activation occurs in a sequence.

In the second part of the thesis, new implant surfaces were designed for people having a propensity for chronic inflammation. These engineered surfaces can modulate and make macrophages secrete anti-inflammation cytokines. The surfaces comprised of nanopatterned substrates with regular hexagonal spacing of 36, 63, 80 and 125 nm, decorated with Fc fragments. There was a modulation in cell area and cytokine production on the nanopatterns. It was found that the Fc nanopatterns were superior in eliciting anti-inflammation response (TGF- β & IL-10) than random presentation of Fc fragments. We found that the anti-inflammation effect starts after 24 hrs and at 48 hrs we could see reduced pro-inflammation. Comparing the pro- and anti-inflammatory cytokine production, it was concluded that 36 nm spaced patterns are ideal for eliciting cytokine mediated anti-inflammation signaling.

To include both the beneficial effects of polymer surfaces and nanopatterning, a new protein nanopatterning approach for thermochemical nanolithography (TCNL) was developed. This technique can generate high-resolution, multi-protein patterns in arbitrary shapes on polymer substrates. TCNL uses a resistively heated AFM tip to unmask amine groups. We modified the micro and nano patterns generated to include different chemical functionalities and thereby allowing us to bind multiple proteins on the same substrate in different shapes. Several approaches have been developed to immobilize proteins and other biomolecules like DNA onto these templates. These templates are stable and can be stored for later bio-functionalization for at least 4-6 weeks. A strategy to prevent protein adsorption on the surfaces was developed. It was demonstrated that these passivated surfaces reduced the non-specific binding of proteins by approximately 20 times. Finally, the bioactivity of the patterned proteins was demonstrated using an *in-vitro* protein assay and *in-vivo* cell assay.

Zusammenfassung

Makrophagen sind eine der Schlüsselkomponenten des Immunsystems. Diese Zellen bilden die vorderste Linie der Immunabwehr gegen eindringende Pathogene und dienen als lebenswichtige chemische Fabriken, die auf ihre Umgebung mit der Segregation verschiedener Zytokine und chemischer Mediatoren reagieren. Ein umfassendes Verständnis der molekularen Details des phagozygotischen Prozesses und der Fähigkeit der Makrophagen die Signalaktivität zu modulieren fehlt bis heute.

Nanometerstarke, hohle, 4,5 μm große Polyelektrolytkapseln wurden als Kraftsensoren benutzt, um die Mechanik während der Phagozytose zu untersuchen. Um diese Kräfte aus den beobachteten Deformationen zu bestimmen, wurden die Kapseln zuerst kalibriert und mechanisch charakterisiert. Die Steifigkeit der Kapseln war $0,11 \pm 0,02$ nN/nm. Die Dynamik der Kapseln während der Phagozytose wurde mit Hilfe eines swept-field Konfokalmikroskops verfolgt. Dies erlaubte es uns, erstmalig die Mechanik der phagozytotischen Aufnahme in ihrem natürlichen Zustand ohne das Anwenden externer Kräfte oder anderweitiger Störung der Zellen zu messen. Es konnte beobachtet werden, dass Makrophagen während der Rückzugphase des Aufnahmeprozesses die Kapseln eindellten oder irreversibel zerstören. Aus der mechanischen Charakterisierung ist bekannt, dass ca. 150 nN benötigt werden, um die Kapseln einzudellen. Diese mit dem „Phagosensor“ gemessene Wert ist 30 fach höher als alle zuvor mit anderen Techniken gemessene Werte. Um die mechanistische Rolle individueller Moleküle bei der Bildung des phagozytotischen Cups zu entschlüsseln, wurden die Schlüsselsignalmoleküle PI3-Kinase und SYK inhibiert. Wie erwartet war die Exzentrizität der deformierten Kapseln für SYK inaktivierte Zellen $0,87 \pm 0,05$ und für PI3-Kinase inaktivierte Zellen $0,75 \pm 0,05$. So konnte gezeigt werden, dass die Aktivierung sequenziell verläuft.

Im zweiten Teil dieser Arbeit wurden neue Implantatoberflächen entwickelt für Patienten mit einer Neigung zu chronischen Entzündungen. Diese Oberflächen können Makrophagen modulieren und dazu bringen, anti-inflammatorische Zytokine zu segregieren. Die Oberfläche dieser Substrate war mit nanostrukturierten Fc-Fragmenten in hexagonalen Abständen von 36, 63, 80 und 125 nm dekoriert. Es konnte eine Modulierung der Zellfläche und der Zytokinproduktion auf den Nanostrukturen gezeigt werden. Desweiteren konnte nachgewiesen werden, dass nanostrukturierte Fc-Fragmente eine stärkere anti-inflammatorische Antwort (TGF- β & IL-10) auslösen als zufällig verteilte. Die anti-inflammatorische Antwort begann nach 24 h und bis zu 48 h konnte eine reduzierte Entzündungsantwort beobachtet werden. Wenn man die pro- und anti-inflammatorische Zytokinproduktion betrachtet, kann gefolgert werden, dass Nanostrukturen mit 36 nm optimal für das Auslösen einer anti-inflammatorischen Antwort sind.

Um die Vorteile von Polymeroberflächen und Nanostrukturierung zu verbinden, wurde eine neue Strukturierungsmethode, die sogenannte thermochemische Nanolithographie (TCNL), entwickelt. Diese Technik kann hochaufgelöste multi-Proteinstrukturen in beliebigen Formen auf Polymeroberflächen generieren. TCNL verwendet eine widerstandserhitzte AFM-Spitze, um Aminofunktionen zu entschützen. TCNL ist 10^6 Mal schneller als Standard-Dip-Pen-Nanolithographie. Die hergestellten Mikro- und Nanostrukturen wurden so verändert, dass verschiedene chemische Funktionalitäten resultierten. Es wurden verschiedene Verfahren entwickelt, um Proteine oder andere Biomoleküle auf diesen Mustern zu immobilisieren. Die Flexibilität dieses Ansatzes wurde durch die Strukturierung mehrerer verschiedener Proteine auf einer Oberfläche in

verschiedenen Formen demonstriert. Die mit TCNL hergestellten Oberflächen sind stabil und können für eine spätere Biofunktionalisierung mindestens 4 bis 6 Wochen aufbewahrt werden. Es wurde weiterhin eine Polyethylenglykol-Passivierung entwickelt, für die gezeigt werden konnte, dass unspezifische Proteinadsorption um einen Faktor von 20 reduziert war. Schließlich konnte die Bioaktivität der Proteinstrukturen in *in-vitro* Experimenten, wie auch in *in-vivo* Zellexperimenten gezeigt werden.

Table of Contents

| | |
|---|-----------|
| DECIPHERING PHAGOCYTOTIC UPTAKE USING POLYELECTROLYTE CAPSULES AS FORCE SENSORS | 2 |
| 1. Introduction | 4 |
| 2. Background | 8 |
| I. Phagocytotic Uptake..... | 8 |
| 3. Novel Experimental Approaches to Study Phagocytosis..... | 11 |
| I. Pillar Substrate Array for Force Sensing | 11 |
| II. Polyelectrolyte Capsules as Force Transducers | 12 |
| 4. Materials and Methods..... | 14 |
| I. PDMS Array Fabrication..... | 14 |
| i. Protein Adsorption to Pillar Interfaces..... | 15 |
| II. Polyelectrolyte Capsule Fabrication..... | 15 |
| i. Fluorescent Protein Labeling and Adsorption of the Capsules | 16 |
| III. Temperature Treatment of Capsules | 17 |
| IV. Cell Culture | 18 |
| i. Fixing Cells..... | 18 |
| V. SEM and Critical Point Drying | 19 |
| i. Scanning Electron Microscopy..... | 19 |
| ii. Critical Point Drying | 19 |
| 5. Results and Discussion | 20 |
| I. PDMS Arrays as Force Sensors in Frustrated Phagocytosis | 20 |
| II. Mechanical Characterization and Calibration of PSS/PAH Capsules | 22 |
| III. Buckling Force and Force of Phagocytosis..... | 25 |
| IV. Buckling and the Role of pH..... | 26 |
| V. Understanding the Role of PI3-Kinase and SYK Kinase Activity in Phagocytotic Uptake | 28 |
| i. Role of PI3-Kinase Activity in Phagocytotic Uptake..... | 29 |
| ii. Role of SYK in Phagocytotic Uptake | 30 |
| VI. Temporal Understanding of Phagocytotic Uptake | 31 |
| 6. Conclusions and Outlook | 34 |
| ENGINEERING AN ANTI-INFLAMMATORY MACROPHAGE RESPONSE USING BIOACTIVE NANOPATTERNED SUBSTRATES..... | 36 |
| 1. Statement of Problem | 38 |
| I. Background | 38 |
| II. Problem..... | 39 |
| III. Hypothesis..... | 39 |
| IV. Rationale | 40 |

| | |
|--|-----------|
| V. Objective | 40 |
| VI. Significance..... | 40 |
| 2. Literature Review | 41 |
| I. Macrophage Phenotypes M1 and M2, the Killer and Healer Cells..... | 41 |
| 3. Materials and Methods..... | 42 |
| I. APTES Treatment..... | 42 |
| II. Fc Fragment Modification and Chemical Characterization..... | 42 |
| III. Cell Culture..... | 43 |
| i. Cell Culture..... | 43 |
| ii. Fixing Cells..... | 43 |
| iii. Cell Membrane Labeling and Quantification..... | 44 |
| IV. Enzyme-linked Immunosorbent Assay (ELISA) | 44 |
| V. Optical and Atomic Force Microscopy | 45 |
| VI. Quartz Crystal Microbalance (QCM) | 45 |
| VII. Ellipsometry..... | 46 |
| VIII. Block Copolymer Lithography | 47 |
| IX. PEG Passivation | 49 |
| X. Fc Fragment Nanopatterning Strategy..... | 49 |
| 4. Results and Discussion | 50 |
| I. Characterization of the Nanopatterned Bio-Interfaces for Macrophage Studies..... | 50 |
| i. QCM Study of SH Modified Fc Binding to Gold and Its Bioactivity..... | 50 |
| ii. Ellipsometry Confirmation of the Fc Bound to Gold..... | 51 |
| iii. Fourier Transform Infrared Spectroscopy (FTIR) to Verify PEG Passivation..... | 52 |
| iv. Contact Angle Goniometry to Verify PEG Passivation on Nanopatterns..... | 52 |
| v. AFM Conformation of Fc Fragment Binding to the Patterned Gold Dots | 53 |
| vi. Fc Concentration of the Incubated Liquid versus Amount Bound On Glass Substrate..... | 54 |
| II. Quantifying Cell Spreading of M2 Activated Macrophages | 55 |
| i. Change in Cell Area on Glass Slides with High Fc fragment Concentration..... | 56 |
| ii. Modulation of Cell Spreading On Nanopatterned Substrates | 57 |
| iii. Time Dependent Modulation in Cell Area on Fc Coated Glass Slides and Control Glass Slides with No Fc | 60 |
| III. Cytokine Modulation | 60 |
| i. TNF- α Production on PEG Passivated Nanopatterned Substrates without Fc | 62 |
| ii. Anti-Inflammation Cytokine Production at 24 and 48 Hours..... | 63 |
| a. IL-10 and TGF- β Production with Changing Fc Concentration on Glass Substrate..... | 63 |
| b. IL-10 and TGF- β Production on Fc Coated, PEG Passivated Nanopatterned Substrates..... | 66 |
| iii. Pro-Inflammation Cytokine Production at 24 and 48 Hours..... | 68 |
| a. Pro-Inflammation Cytokine Production with Changing Fc Concentration on Glass Substrate..... | 68 |
| b. Pro-Inflammation Cytokine Production on Fc Coated, PEG Passivated Nanopatterned Substrates..... | 69 |
| 5. Conclusions and Outlook | 72 |

| | |
|--|-----------|
| THERMOCHEMICAL NANOLITHOGRAPHY | 74 |
| 1. Introduction | 76 |
| 2. Materials and Methods..... | 79 |
| I. Materials, Synthesis and Characterization | 79 |
| i. Synthesis of tetrahydropyran-2-ol | 79 |
| ii. Synthesis of tetrahydropyran-2-yl N-(2-methacryloxyethyl)carbamate | 79 |
| iii. Synthesis of methyl 4-(3-methacryloxypropoxy)cinnamate | 80 |
| iv. Synthesis of poly((tetrahydropyran-2-yl N-(2-methacryloxyethyl)carbamate)-co-(methyl 4-(3-methacryloxypropoxy)cinnamate))..... | 80 |
| v. Synthesis of 4-allyloxybenzophenone..... | 81 |
| vi. Synthesis of 4-(3-(chlorodimethylsilyl)propoxy)benzophenone | 81 |
| vii. Binding of 4-(3-(chlorodimethylsilyl)propoxy)benzophenone to glass substrates | 81 |
| II. Transmittance Fourier Transformed Infrared Spectroscopy (FTIR) Spectra of the Polymer upon Bulk Heating | 82 |
| III. Atomic Force Microscopy with Thermal Cantilevers | 83 |
| IV. Fluorescence Microscopy | 83 |
| V. Thermogravimetric Analysis | 84 |
| VI. Cell Culture and Immunostaining..... | 85 |
| VII. Proteins and Reagents | 85 |
| VIII. Polymer Film Preparation | 86 |
| IX. Polymer Film Deposition on the QCM Crystal and Glass Slides | 86 |
| 3. Results and Discussion | 87 |
| I. Protein Patterning with Thermochemical Nanolithography (TCNL)..... | 87 |
| II. TCNL Micropatterns of One Protein Species | 89 |
| i. Protein Micropatterning with Glutaraldehyde Crosslinking | 90 |
| ii. Biotin-Streptavidin Based Protein Labeling..... | 91 |
| iii. Protein Labeling and SH Creation | 91 |
| III. Multi-Protein Micro Patterns (Orthogonal Functionality) | 92 |
| i. Chemical Dual Functionality | 92 |
| ii. Two Protein Patterning..... | 93 |
| IV. Protein Nano Arrays | 94 |
| V. Oriented Immobilization..... | 96 |
| VI. DNA Arrays | 96 |
| VII. Summary of the Functionalization Strategies..... | 97 |
| VIII. Viability and Bioactivity of TCNL Patterned Proteins | 99 |
| IX. Storage of TCNL Patterns and Aging | 100 |
| X. PEG Passivation | 101 |
| i. PEG Passivation of Polymer Coated Slides and QCM Crystals | 101 |
| ii. Effect of Salt | 102 |
| iii. Fluorescent PEG Passivation: Fluorescent Testing of PEG Binding on Surface..... | 103 |
| iv. Passivating TCNL Patterned Polymer Slides | 104 |
| v. Contact Angle Measurement..... | 105 |
| XI. QCM Analysis of Non-Specific Adsorption..... | 106 |
| i. Comparison of Non-Specific Adsorption of BSA on Different Polymer Coated QCM Crystals | 107 |
| ii. Non-Specific Adsorption of BSA on TCNL Polymer without Crosslinking | 108 |

| | |
|---|------------|
| iii. Non-Specific Adsorption of BSA On 4-(3'-Chlorodimethylsilyl) Propoxy Benzophenone Crosslinked Carbamate Polymer Coated Sensors..... | 110 |
| iv. Non-Specific Adsorption of BSA on Pegylated Polymer Coated Sensors | 112 |
| 4. Conclusions and Outlook | 115 |
| Abbreviations | 117 |
| Table of Figures | 119 |
| Bibliography | 123 |

Deciphering Phagocytic Uptake Using Polyelectrolyte Capsules as Force Sensors

1. Introduction

Phagocytosis is a highly conserved, complex process that has evolved to counter the constant threat posed by pathogens, dead cells and debris¹. Classically defined as a mechanism for internalizing and destroying particles greater than 0.5 μ m in size², it is a receptor mediated actin-driven process³. The most well studied phagocytic system is that of Fc receptor mediated phagocytosis^{2,4}. In Fc receptor mediated phagocytosis the Fc receptor, a transmembrane receptor present on the cell surface of the immune cells binds to the Fc portion of the Immunoglobulin G (IgG) present on the surface of the invading pathogen or foreign body. Binding of Fc receptors to the Fc portion of IgG leads to pseudopodial extension of the plasma membrane around the foreign body. This process continues until the entire particle becomes enveloped and the membrane closes, producing a bilayer lipid membrane coated particle that is brought into the interior of the cell. The resultant intracellular vesicle is referred to as a phagosome⁵. Phagocytic uptake involves a complicated rearrangement of the actin cytoskeleton³ that facilitates the membrane deformation and engulfment of the particle, a process that is believed to include actin polymerization, actin bundling by proteins, myosin based contraction⁶ and de-polymerization of actin filaments⁷. Due to the mechanical and stepwise nature of the occurrence of these processes, we hypothesize that distinctive signature forces are exerted on the phagosome throughout uptake the process.

The molecular details of many aspects of the phagocytotic process are not well understood. It is not clear how Fc-receptor binding to IgG triggers the phagocytotic machinery and the mechanism by which the actin cytoskeleton is regulated to achieve the pseudopodia extension and closure of the cell around the engulfed particle. Several competing theories exist to explain the uptake process; it is remarkable that decade-old interpretations of the mechanics of phagocytosis such as the zipper model of Griffin *et. al.*⁸, the trigger mechanism of Silverstein *et. al.*⁹ or the cortical cytoskeleton expansion model of Southwick and Stossel *et. al.*¹⁰ have barely been readdressed since their inception. Since there is a signature force associated with each step during the uptake process⁵, to understand and readdress such a dynamic system like uptake process; we can monitor the change in force applied during uptake process with a high temporal and spatial resolution. Understanding the forces can help us understand the underlying biochemical signals thereby helping us understand the mechanism.

It is known that cells in general are modulated by mechanical force¹¹⁻¹³ and from Bason *et. al.*'s¹⁴⁻¹⁵ work, It is known that extracellular pressure can modulate macrophage's phagocytotic ability by inhibiting a pathway involving focal adhesion kinase (FAK) and extracellular signal-regulated kinases (ERK). Thus, to measure the true force of phagocytotic uptake, the measuring techniques should not interfere or apply external force during the uptake process. Moreover, the force on the phagocytic target during phagocytotic uptake as shown in Figure 1B is contractile in nature. This is analogues to a sphere being squeezed but the force measured with traditional techniques like magnetic tweezers¹⁶⁻¹⁷, optical tweezers¹⁸ or through micropipette aspiration¹⁹ is like tug of war between the cell and measuring probe. These measurements are tensile in nature instead of contractile as depicted in Figure 1C. Keeping these facts in consideration, In order to measure the true contractile forces and prevent the noise arising from signaling events occurring due to the measuring technique, the experimental approach has to be designed in a way so that we

can measure the contractile force occurring during uptake while not applying any external mechanical force or perturbing the cells.

As shown in the Figure 1A, the uptake process occurs in a series of stages rather than just one gulp⁴. There are several intermediate stages of constriction process that occur and this whole process is dynamic in nature and is tightly controlled temporally²⁰. Due to the limitation of the existing force measuring techniques that are typically used to interrogate phagocytosis such as optical tweezers¹⁸, magnetic tweezers¹⁶⁻¹⁷ or micropipette aspiration¹⁹, only a limited view of the different stages and their corresponding forces have been accessible. In particular, the constriction of the actin around the particle as the pseudopodia advance, as well as the closure of the pseudopodia at the top of the particle and the possible resultant squeezing has not been quantitatively measured. A measuring technique that can continually monitor the force dynamics occurring during the uptake process can help us give a picture of the events that have not been monitored previously.

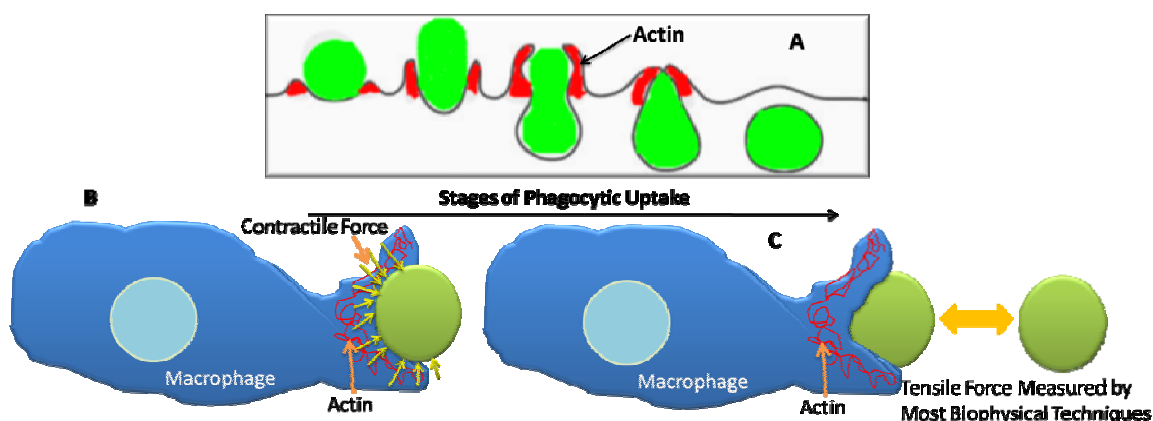


Figure 1 (A) Depicts stages involved in phagocytotic uptake. The uptake process occurs in a series of stages rather than just one gulp. (B) Contractile force applied on the target during phagocytotic uptake. (C) Tensile force measured during phagocytotic uptake by most biophysical techniques.

The other constraint in measuring the force of phagocytotic uptake is the scope or span of the force that can be measured with traditional biophysical assays. As seen from Table 1 the force of phagocytotic uptake that has been measured till has been confined to >5 nN¹⁶⁻¹⁸. Since there are different stages involved in phagocytotic uptake, there can be different force regimes which can be really low during the initial receptor activation and gradually increase as the particle undergoes phagocytotic uptake. To measure such a dynamic system we need a technique that can measure forces over a wide range, between pN to nN.

In order to gain an accurate picture of the force during phagocytotic uptake we need to measure the contractile forces being exerted by the cell on the phagosome target. By following the deformations occurring on a soft spherical probe undergoing phagocytosis we can follow the contractile forces being exerted during phagocytotic uptake. Moreover, by changing the mechanical properties of the soft capsules the force regimes can be modified to achieve force regimes much higher than that previously measurable or can be adjusted to have high sensitivity to small force regimes. Using phagosensor we can assemble a

chronology of molecular events during phagosome formation and examine the contributions of phosphoinositide 3-kinase (PI3-kinase) and spleen tyrosine kinase (SYK) to these dynamics.

| <i>Cell Type and Experimental Technique</i> | <i>Force</i> | <i>Reference</i> |
|---|---|------------------|
| J774, Magnetic Tweezers | >5nN | 16-17 |
| J774 and RAW Optical Tweezers | >15pN | 18 |
| Human Granulocytes Micropipette | $\sim 10^3$ N/m ² (Average contractile Stress) | 19 |
| Neutrophil Traction Analysis | 28 ± 10nN (Chemokinesis) 67 ± 10nN (Chemotaxis) | 21 |

Table 1 Forces involved in phagocytotic uptake and their corresponding measuring techniques.

2. Background

I. Phagocytotic Uptake

Phagocytosis is a process in which certain cells called phagocytes engulf and destroy foreign objects. The process of engulfing foreign particles is of fundamental importance to a wide diversity of organisms. From simple unicellular organisms that use phagocytosis to obtain their next meal, to complex multi-cellular organisms in which phagocytic cells represent an essential branch of the immune system. Regardless of the organism or specific molecules concerned, all phagocytic processes are driven by a finely controlled rearrangement of the actin cytoskeleton³. As shown in the schematic in Figure 2, a multitude of signaling activity converges to locally reorganize the actin cytoskeleton to form a membrane bound organelle called phagosome. Several receptors exist to trigger phagocytosis². These receptors can be broadly defined as those that recognize epitopes on the surface of unmodified bacteria and fungi (nonopsonic phagocytosis)²². Examples of the later include receptors for the Fc portion of IgG (FcγRs)²³ and receptors that recognize various components of the compliment (like CR3)²⁴. The best-studied phagocytic system is that of the receptors that bind to the Fc portion of immunoglobulin^{2,23}. One of the reason for Fc receptor system being a model system is that, like in Fc receptor mediated phagocytosis for most of the other receptor mediated phagocytosis ITAM's start occurring after receptor activation site²⁵ strongly suggesting a generalization in signaling after receptor activation.

As shown in the Figure 2, initial Fcγ receptor activation takes place upon ligand binding to the extracellular domain. Binding of immunoglobulins (IgG) to foreign particles leads to the prompt clearance of those particles from the organism. IgG acts as an opsonin, a molecule that renders the particle they coat more susceptible to engulfment by phagocytic cells. The conserved Fc domain of the IgG is recognized by Fc receptors present on professional phagocytes, such as neutrophils and macrophages, and the opsonized particle is rapidly internalized. This internalization is characterized by the dramatic, actin-dependent extension of the plasma membrane around the particle³. Fcγ receptors traditionally signal through an immunoreceptor tyrosine based activation motif (ITAM)²⁶ or through inhibitory residues found in an immunoreceptor tyrosine based inhibitory motif (ITIM)²⁷. The classic ITAM motif consists of two YxxL sequences separated by 7 amino acids²⁸.

Following its phosphorylation, the ITAM motif acts as a docking site for SYK²⁹. Docking of SYK leads to its phosphorylation³⁰ and activation, although note that SYK is also capable of auto-activation³¹. SYK is clearly a critical component for Fc Receptor signaling (but not complement-receptor-mediated phagocytic uptake)³², since macrophages lacking SYK cannot internalize IgG-opsonized particles³²⁻³⁴. The point at which SYK acts remains controversial. Some authors report it to be required for formation of the actin filament 'cup' that assembles beneath the bound particle during Fc Receptor^{30,35-36} phagocytosis, whereas others describe normal actin rearrangement but a subsequent failure to internalize particles in cells lacking SYK³³. Interestingly, macrophages lacking SYK show reduced phosphorylation of the Fc Receptor tail (or associated γ subunit) in response to ligand binding³²; this suggests that SYK cooperates with the Src kinases to phosphorylate the receptor and thus initiate signaling.

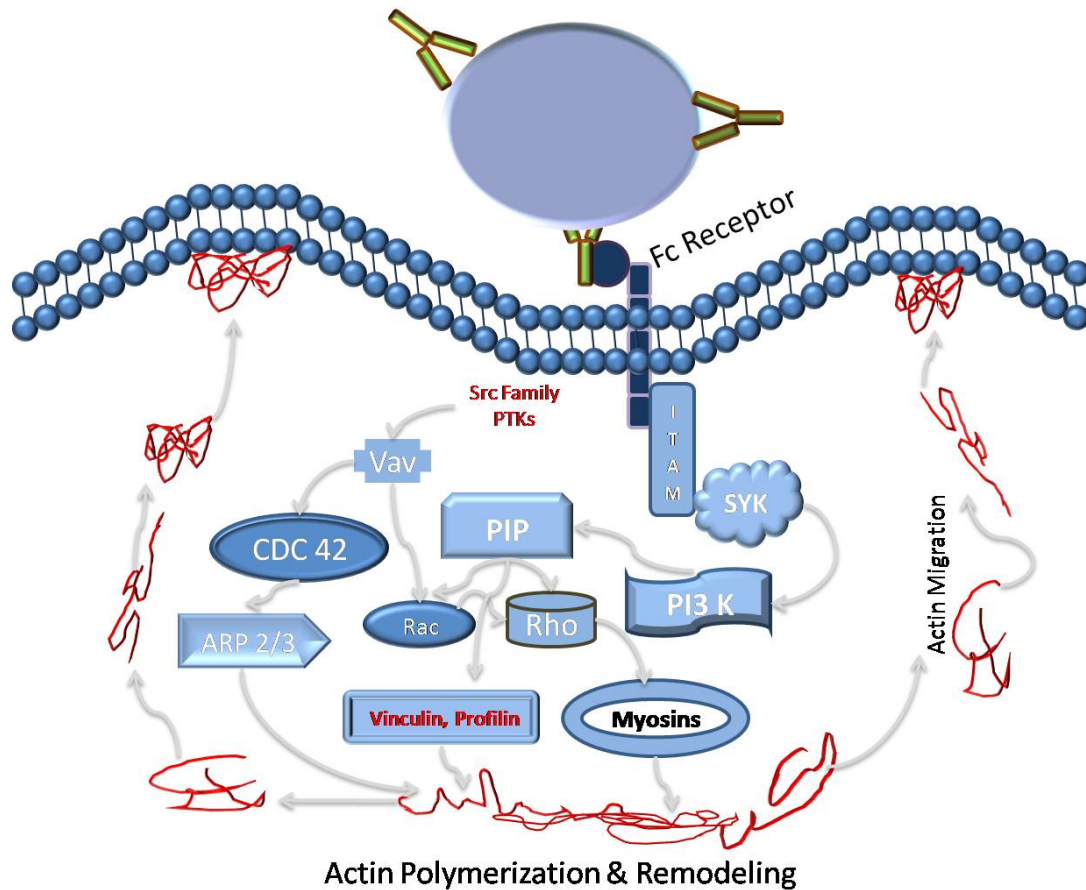


Figure 2 Depiction of pathway for FcγR mediated phagocytic uptake.

The other important signaling proteins are the phosphoinositol lipids which are major regulators of actin remodeling during several cellular phenomena³⁷. To date, the major phosphoinositide kinase implicated in phagocytosis is phosphoinositide 3-kinase (PI3-K). Unlike most signaling proteins implicated in phagocytosis, PI3-K does not seem to accumulate at nascent phagosomes³⁸, perhaps because it is displaced from its binding partners (such as FcγRIIA³⁹) by binding to phosphatidylinositol 3,4,5-trisphosphate (PtdIns(3,4,5)P₃), one of its products⁴⁰⁻⁴¹. PI3-K is, however, activated by Fc receptors⁴², associates with FcγRIIA in platelets³⁹ and is required for Fc receptor-mediated phagocytic uptake by macrophages⁴²⁻⁴⁴. In addition, Cox *et al.*⁴⁴ have shown PI3-K to be required for CR3 mediated phagocytotic uptake although, PI3-K is not required for phagocytosis in Dictyostelium⁴⁵. PI3-K appears not to regulate the initial actin polymerization during phagocytosis, which proceeds normally when PI3-K is inhibited, but rather to control closure of the phagosome⁴³⁻⁴⁴. The dependence on PI3-K is reduced for smaller particles⁴⁴ PI3-K might therefore have a role in the regulation of membrane availability. Intriguingly, although not required for actin polymerization, PI3-K is nevertheless able to induce local actin reorganization and subsequent particle uptake if it is artificially activated beneath bound beads⁴⁶. Fusion of the membrane leading to particle internalization requires actin remodeling and possibly vesicle trafficking steps, which are driven by the PI3-K product PtdIns (3, 4, 5) P₃. It appears that at least three phosphoinositide products regulate phagocytosis. (1) PtdIns (4, 5) P₂ is synthesized early during engulfment and may control actin assembly at the

phagosome. (2) The activity of PLC then degrades $\text{PtdIns}(4,5)\text{P}_2$, producing DAG, and either the loss of $\text{PtdIns}(4,5)\text{P}_2$ or the increase in DAG controls further cytoskeletal changes⁴⁷. (3) Simultaneously, PI3-K converts $\text{PtdIns}(4,5)\text{P}_2$ to $\text{PtdIns}(3,4,5)\text{P}_3$, triggering phagosome closure.

After initiation of a phagocytotic signal, the cell needs to prepare to internalize the bound particle into the cell and enclose it in a phagosome. A crucial step is the ability of a phagocytic signal to proceed from tyrosine phosphorylation to actin rearrangement for pseudopod formation. The ability to stimulate actin polymerization occurs by an as yet incompletely understood pathway. It has been proposed that the signal sequence leading to actin polymerization includes the activation of Rho GTPases such as Rac, CDC42, PI3-K, ERK, PKC and others^{4,48}. The rearrangement of actin to form a phagocytic cup has been experimentally shown to be dependent on Rac and CDC42⁴⁹⁻⁵¹. This Rho family of GTPases is a crucial effector of phagocytosis as inhibition of either of these GTPases enzymes results in significantly reduced phagocytosis⁵². Activation of GTPases such as Rac and CDC42 involve guanine nucleotide exchange factors (GEF), Subsequently CDC42 accumulates at the phagocytic cup where it associates with Wiskott-Aldrich syndrome protein (WASP)⁵³. WASP can then associate with the Arp 2/3 complex, which seems to mediate the actual actin nucleation to form the phagocytic cup. Studies have shown that omission of any of these proteins in knockout experiments or in human disease results in significantly decreased phagocytosis⁵³⁻⁵⁵.

Understanding phagocytotic uptake will provide a window into the coordinate functioning of the cytoskeleton elements and can serve as a model system for analyzing diverse biological phenomena including synaptic transmission, mitogenesis, and morphogenesis.

3. Novel Experimental Approaches to Study Phagocytosis

Several approaches facilitate the exploration of biological processes mediated by mechanical signals. These techniques have a force resolution from 0.1 to 10^4 piconewton. Table 2 below shows a brief snapshot of the force regimes that can be measured with different force assays.

| | <i>Force Range (pN)</i> | <i>References</i> |
|-------------------------------|--|-------------------|
| Optical Tweezers | 0.1–100 | 56-57 |
| Magnetic Tweezers | 10^{-3} – 10^2 (0.01 – 10^2) | 17,58-59 |
| AFM | 10 – 10^4 | 60-61 |
| Pillar Substrate Array | 10 – 10^4 | 62-63 |

Table 2 Force range for different biological force measuring techniques

Although all these techniques are excellent, each with their own advantages they also have some shortcomings. For a fundamental or predictive understanding of phagocytotic uptake and a better understanding of the events during signaling we need a force measuring technique that

- Is able to measure forces temporally in high resolution so that we can capture the different stages of phagocytotic uptake and have a clear picture of the force dynamics.
- Is able to measure the contractile or squeeze like forces exerted during phagocytotic uptake rather than the tensile forces measured using traditional techniques.
- Is able to measure different force regimes during phagocytosis, which can be really low during the initial receptor activation stage and gradually increase as the particle undergoes phagocytotic uptake.
- Is able to capture the forces in natural state. The experimental approaches have to be designed in a way we can measure the forces without applying any external mechanical forces or perturbing the cells.

In order to understand and characterize this intriguing phenomenon, we initially used pillar substrate array to capture the dynamics of frustrated phagocytosis. Pillar substrate arrays although have been previously used to capture forces during adhesion and migration, they have never been used to measure the dynamics of frustrated phagocytosis. During the course of the experiments, it was found that although macrophages deformed the pillars during frustrated phagocytosis, they seem to envelop individual pillars. In order to overcome this we have developed “PhagoSensor” a new force sensing approach using polyelectrolyte capsules as force sensors.

I. Pillar Substrate Array for Force Sensing

When macrophages encounter a foreign object that is larger than itself, such as an implant, the macrophages experience “frustrated phagocytosis”⁶⁴⁻⁶⁷. This process is

important in the context of medical devices such as implants⁶⁸, where macrophages attempt to phagocytosis foreign materials, and instead achieve a state of frustrated phagocytosis. During frustrated phagocytosis, macrophages spread on the surface and destroy the foreign object⁶⁷. Phagocytosis, especially the first stage, crucially depends on the transmission of mechanical forces generated by actin and myosin³. Here we describe and test an experimental approach to measure the forces generated by macrophages during frustrated phagocytosis.

Quantitative force measurements during adhesion and migration have been explained previously using micro-fabricated polydimethylsiloxane (PDMS) pillar structures which are arrays of vertical pillars on flat substrate^{63,69}. These substrates can be used as force transducers as each pillar has a defined elasticity. We have extended the use of these substrates to measure traction forces resulting from frustrated phagocytosis. As shown in Figure 3, we use these closely spaced array of flexible micro-pillars coated on their tops with IgG to map forces exerted by cells on their substrate. Arrays of closely spaced micro-pillars, made with the elastomeric material (PDMS) were fabricated (for details refer to PDMS fabrication in materials and methods). It is known that when phagocytes spread on surfaces coated with ligands such as IgG, they form a tight seal with the substrate⁷⁰. We hypothesize that cells seeded on the top of these IgG coated pillars experience frustrated phagocytosis similar to what they experience on IgG coated glass slides⁷⁰⁻⁷². Once these cells start forming a tight seal with the underlying pillar substrate they deflect the pillars. The pillars can be modeled as simple springs and thus their deflection is proportional to the force applied by the cell in the linear elastic regime⁷³. In this case, the micro-pillars act as passive force sensors. The pillar approach described here uses vertically standing pillars resulting in force measurement in two dimensions.

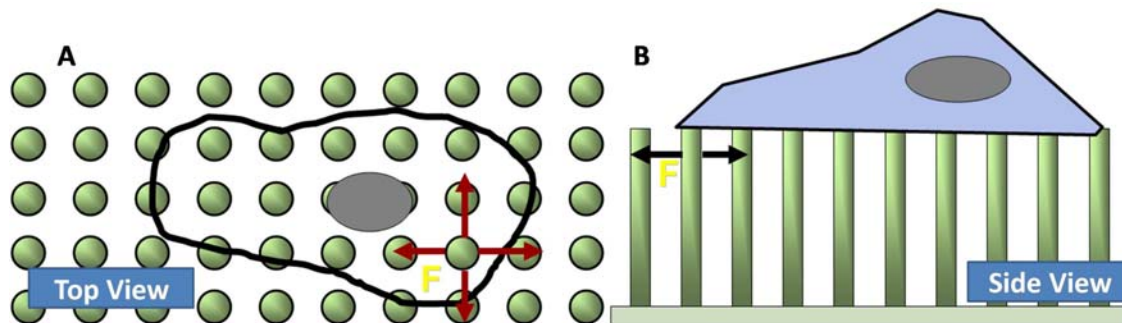


Figure 3 Schematic images of pillar arrays used in this study to analyze frustrated phagocytic traction forces. (A) Top view of cell lying on a pillar substrate. Pillar bending is related to the forces a cell exerts on their environment. By measuring the displacement of the pillar heads in a top view approach, the exerted forces can be obtained. (B) Side view of a cell lying on a pillar array.

II. Polyelectrolyte Capsules as Force Transducers

Polyelectrolyte's are polymers whose repeating units bear an electrolyte group⁷⁴. Step-wise adsorption of polyelectrolyte's can be used to fabricate hollow micro and nano capsules with determined size, capsule wall composition and thickness⁷⁵ (for making of the capsules refer to materials and methods). Hollow polyelectrolyte capsules created by layer-by-layer technique have been found to be a promising candidate for drug delivery⁷⁶. However their adjustable properties make them an interesting engineering tool that can be

applied to multitude of fields. In this work we exploit their well characterized mechanical properties for force sensing applications. Previous studies have shown that the deformation for PSS/PAH capsules depends on applied force, and that for small deformation regimes the force versus deformation is well defined⁷⁷. This particularly interesting mechanical property of the capsules allows their use as force transducers to study contractile forces applied in 3D during phagocytotic uptake.

As shown in the schematic in Figure 4, the force applied by macrophage during phagocytotic uptake was measured indirectly by measuring the deformation of mechanically well characterized 4.5 μm diameter, 18 nm thick polyelectrolyte multilayer capsules in an aqueous environment. Using this method we can measure not only the forces exerted by macrophage during key phagocytic events, but can also monitor the subtle changes spatially and temporally to determine the forces during the intermittent stages of phagocytotic uptake.

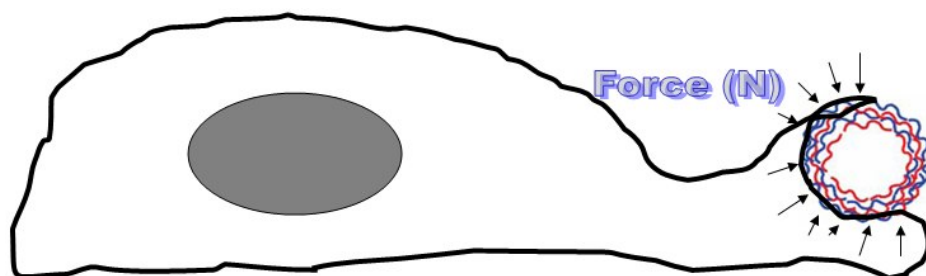


Figure 4 Schematic of a polyelectrolyte capsule being engulfed by a macrophage during phagocytotic uptake.

4. Materials and Methods

I. PDMS Array Fabrication

The PDMS array, which is also called micropillar arrays are composed of a transparent silicone rubber called polydimethylsiloxane (PDMS)⁶³. PDMS can be modified with different surface treatments to allow protein deposition (IgG) onto the top of the posts⁷⁸. The devices are fabricated with techniques developed by the semiconductor industry for integrated circuits and microelectrical mechanical systems (MEMS).

The first step involves photolithography of a hard master made from photoresist SU-8. Next, the master is molded in PDMS to create soft replicas of the micropost arrays.

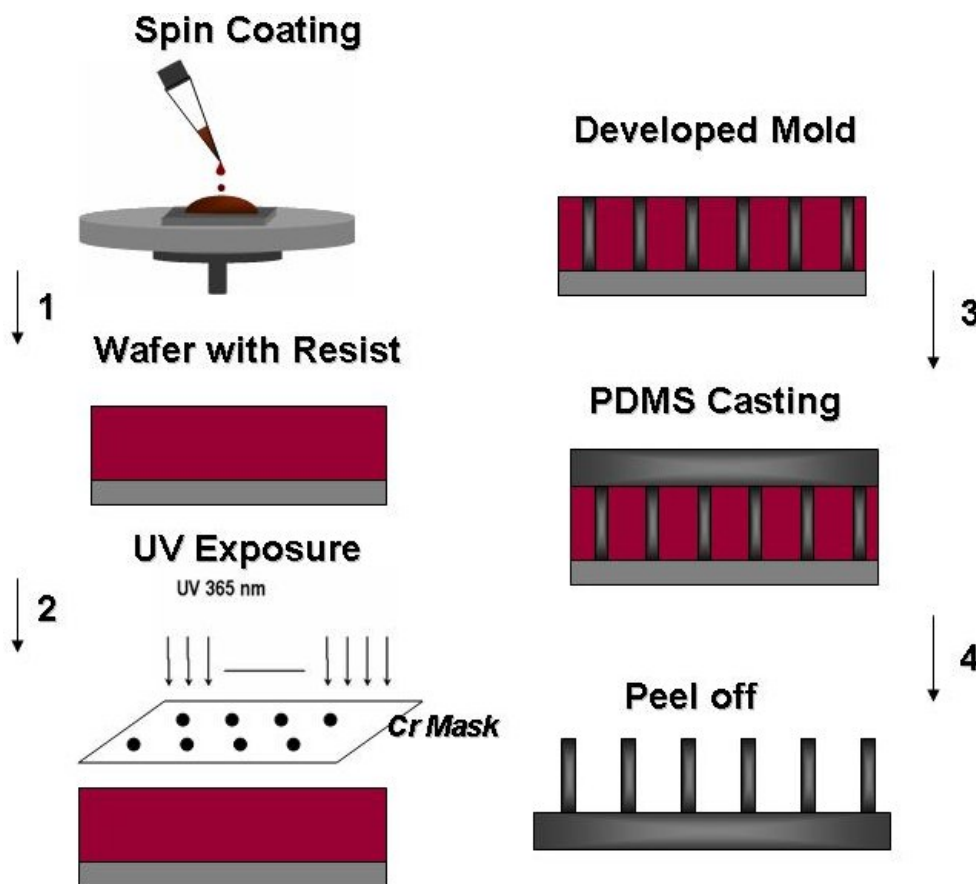


Figure 5 Schematic of pillar array preparation. The pillar array is prepared by spincoating a silicon or glass slide with a layer of negative photo resist. After developing the SU-8 with holes in it, PDMS is poured into this mold. Curing is performed at 65 °C and subsequently the PDMS pillar array can be peeled off.

As shown in the Figure 5 conventional photolithography is used to pattern silicon wafers with an array of cylindrical pits. The desired pattern is designed and drawn using a master-mask writer (DWL 66, Heidelberg Instruments, Germany). Then it is written with a laser into a photo resist layer (AZ-1505, Microchemicals, Germany) which is previously spin coated on a glass plate. After developing, a non-transparent (i.e. thicker than 100 nm) layer of chromium is sputtered on top and a lift off is performed. The master-mask can be used

many times to make cylindrical holes in a thick SU-8 photo resist layer, using a master-mask patterned with disks. The cylindrical holes in the SU-8 photo resist can be used as a replica for PDMS pillars. The polydimethyl-siloxane (PDMS (Sylgard 184, Dow-Corning)) used for casting is mixed with a thermo-crosslinker (curing agent) at a weight-ratio 10:1. The PDMS is then cured in an oven, resulting in a flexible PDMS layer which can then be peeled off the substrate. The steps taken before developing were performed in a clean room. The PDMS mixing and curing can easily be performed in a normal chemical laboratory. It is important that after cleaning, the wafers are silanized with tridecafluoro-trichlorosilane in vapor phase to facilitate the release of the elastomer from the wafers. The PDMS pillars fabricated for our experiments were 3 μm in diameter and 10 μm in length.

i. Protein Adsorption to Pillar Interfaces

Prior to experiments, the pillar substrates were treated with hydrogen plasma (10 sec, 150 W in plasma etcher (Tepla)) and subsequently immersed in 20 $\mu\text{g}/\text{ml}$ IgG (Rockland Immunochemicals, Inc) for 30 minutes. The surface tension and hydrophobicity prevents the protein from flowing down the pillars⁷⁹⁻⁸¹ leading to protein functionalization limited to the very top of the pillars.

II. Polyelectrolyte Capsule Fabrication

Polyelectrolyte's are polymers whose repeating units bear an electrolyte group⁸² it can be defines as a macromolecule in which a substantial portion of the constituent units have ionizable or ionic groups. As a working definition and a matter of convenience, people started calling polymers with high ion content as polyelectrolytes. Polyelectrolyte's are also called polysalts⁸³ as they have properties of both electrolytic salts and polymers⁸⁴. These solutions are electrically conductive like salt solutions and are viscous like polymer solutions. Polyelectrolyte's can be used to grow thin films by using layer-by-layer (LbL) deposition⁸⁵⁻⁸⁷. During LbL deposition, a suitable substrate is dipped back and forth between dilute baths of positively and negatively charged polyelectrolyte solutions. During each dip a small amount of polyelectrolyte is adsorbed and the surface charge is reversed. This allows the gradual and controlled build-up of electronically stitched films of polycation-polyanion layers. LbL can also be carried out by rapid procedures like spincoating⁸⁸ or spray deposition⁸⁹⁻⁹⁰ and can be extended to any shape, including micron sized colloidal particles. Based on this LBL approach, hollow microcapsules can also be produced⁹¹⁻⁹². The process predominantly makes use of electrostatic interactions⁹³, but the importance of hydrophobic interactions⁹⁴⁻⁹⁵ and hydrogen bonding⁹⁶ has also been demonstrated. These LBL layers have been further modified to incorporate nano particles⁹⁷, DNA⁹⁸, proteins⁹⁹⁻¹⁰⁰, viruses¹⁰¹ and lipids¹⁰² as building blocks to make engineered substrates with specific applications.

We used LBL assembly approach to create hollow polyelectrolyte capsules¹⁰³. Our system of Polystyrene sulfonate/Polyallylamine hydrochloride (PSS/PAH) capsules are 4.5 μm in diameter and 9 layers in thickness accounting to approximately 19 nm in thickness. As shown in Figure 6 the fabrication of the capsules starts with a colloidal particle on which oppositely charged electrolytes poly(allylamine hydrochloride) and polystyrene sulfonate are deposited until the required thickness is reached. The colloidal core is then dissolved using tetrahydrofuran (THF), yielding hollow capsules with 4.5 μm in diameter and 19 nm in

thickness. As described by Khopade *et. al.*⁹³ the high charge on the capsules was used to electrostatically bind IgG on the surface of the capsules.

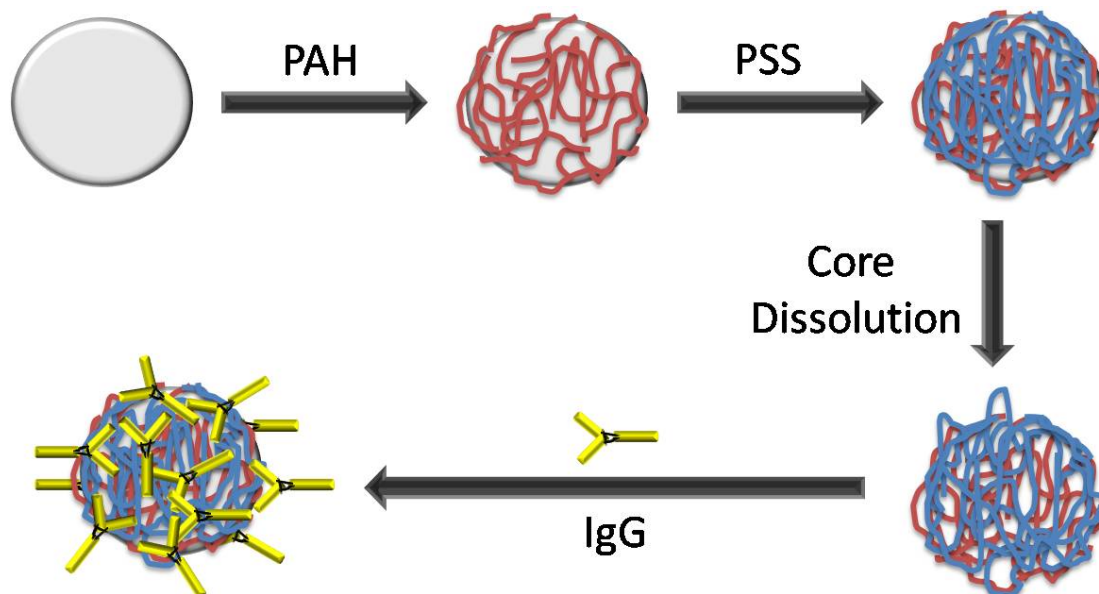


Figure 6 Schematic of preparation and IgG coating of the hollow capsules. Consecutive adsorption of PAH (Red) and PSS (Blue) is performed on a core particle. After achieving the required dimensions, the core is dissolved leading to formation of hollow capsules. Finally the protein (IgG) is bound on the surface by electrostatic forces.

i. Fluorescent Protein Labeling and Adsorption of the Capsules

We use optical microscopy to measure the mechanical deformation of capsules during phagocytosis. It is important to acquire good 3d images of the capsules for understanding these deformations. In order to image these minute deformations, we use fluorescence confocal microscopy. Many common fluorescent labels, e.g. Fluorescein isothiocyanate (FITC), show rather low photostability¹⁰⁴⁻¹⁰⁶. This is a serious draw-back in microscopy and other techniques based on the confocal principle¹⁰⁷⁻¹⁰⁹. Since we need to image the capsules over extended period of time with high intensity we utilized Atto dye label which are designed to be much more stable under prolonged irradiation, providing better photostability¹⁰⁴.

Mouse IgG whole molecule (Rockland Immunochemicals Inc, USA; catalogue # 010-0102) was fluorescently labeled with atto 488-NHS ester (Sigma-Aldrich Inc) following the manufacturers protocol¹¹⁰. In detail, 2 mg/ml of mouse IgG in phosphate buffer solution (10 mM, pH 8) was added to atto 488 NHS-ester (1 mg/ml in DMSO) and gently stirred overnight at 4°C. A threefold molar excess of reactive dye to the protein solution was used to obtain the manufacturers recommended degree of labeling of 2 (dye-to-protein ratio, Molar Ratio). Part of the applied dye NHS ester will hydrolyze during the labeling reaction and must be removed from the labeled protein. To purify the labeled protein we used dialysis filter with 7000 molecular weight membrane (Thermo Scientific).

The degree of labeling (DOL, dye-to-protein ratio) was obtained using Lambert-Beer law

Absorbance (A) = extinction coefficient (ϵ) \times molar concentration \times path length (d) Equation 1

The UV-VIS absorption spectra of the conjugate solution was obtained after dialysis filtration and measured in a quartz (UV-transparent) cell. The absorbance (A_{\max}) at the absorption maximum (λ_{abs}) of the dye and the absorbance (A_{280}) at 280 nm (absorption maximum of proteins) were determined. The concentration of bound dye is given by: $c(\text{dye}) = A_{\max} / \epsilon_{\max} \times d$, where ϵ_{\max} is the extinction coefficient of the dye at the absorption maximum. The protein concentration is obtained in the same way from its absorbance at 280 nm. As all dyes show some absorption at 280 nm, the measured absorbance A_{280} must be corrected for the contribution of the dye. This is given by $A_{\text{prot}} \times CF_{280}$. According to manufacturer¹¹⁰ Atto 488 had a $\lambda_{\text{abs}} = 501$, $\epsilon_{\max} = 9 \times 10^4$, $CF_{260} = 0.25$, $CF_{280} = 0.10$. We know from Jhonston *et. al*¹¹¹ that for IgG at 280 the extinction coefficient is 13.5

$$\text{Concentration of protein is: } c(\text{protein}) = A_{\text{prot}} / \epsilon_{\text{prot}} \times d,$$

$$\text{Concentration of bound dye: } c(\text{dye}) = A_{\max} / \epsilon_{\max} \times d$$

ϵ_{prot} is the extinction coefficient of the protein at 280 nm

ϵ_{\max} is the extinction coefficient of the dye at the absorption maximum

$$A_{\text{prot}} = A_{280} - A_{\max} \times CF_{280}$$

The degree of labeling (DOL) is $= c(\text{dye}) / c(\text{protein})$

$$\text{DOL} = \frac{A_{\max} / \epsilon_{\max}}{A_{\text{prot}} / \epsilon_{\text{prot}}} = \frac{A_{\max} \cdot \epsilon_{\text{prot}}}{(A_{280} - A_{\max} \cdot CF_{280}) \cdot \epsilon_{\max}} \quad \text{Equation 2}$$

From the absorption we found $A_{280} = 2.8 \times 10^{-4}$, $A_{\max} = 3.8068$

$$\text{DOL} = (3.8068 \times 13.5) / (2.8 \times 10^{-4} - 3.8068 \times 0.10) \times 9 \times 10^4$$

$$\text{DOL} = 1.8$$

The analysis revealed that the ratio of dye to protein obtained after labeling was 1.8. The degree of labeling obtained here is good.

One of the key advantages of the polyelectrolyte capsules is the high charge present on the capsules. For the capsules used here, the final surface charge is negative, while the Atto-IgG is slightly positive. As described by Khopade *et. al*⁹³ in order to label the capsules, electrostatic interactions can be used to facilitate non-specific adsorption of oppositely charged molecules onto the polyelectrolyte capsules, such as the fluorescently labeled IgG. To produce the protein labeled fluorescent capsules, 50 $\mu\text{g}/\text{ml}$ of fluorescently labeled IgG was added to the capsules while gently stirring them for 3 hours. To purify the labeled capsules from the unbound protein solution the capsules were centrifuged at 300 RPM for 3 minutes. The capsules were re-suspended in PBS and then spun down four times, to obtain the fluorescent protein labeled polyelectrolyte capsules.

III. Temperature Treatment of Capsules

A heating-induced morphological change of polyelectrolyte capsules has been previously studied by Kohler *et. al*¹¹², Gao *et. al*¹¹³, Ibarz *et. al*¹¹⁴ and Leporatti *et. al*¹¹⁵. As shown in Figure 7, it is expected that heating induces an increase in the wall thickness

proportional to a decrease in capsule diameter¹¹². As our experiments take place at 37°C (optimal temperature for cell survival) it is important that there is no temperature dependent softening of the capsules. To overcome this temperature induced response, the capsules were annealed before the experiments. The capsules were annealed at 40°C in a water bath for 30 minutes and then slowly cooled to room temperature. Annealing of the capsules was performed before the protein was bound to the surface of the capsules. The capsules were maintained in deionized water with 18.2 MΩ-cm resistivity at all times.

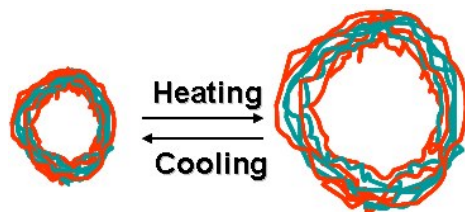


Figure 7 Schematic of capsule swelling and shrinking as a result of temperature changes. Heating causes the capsule to soften and increase in size, while cooling of the annealed capsule induces shrinking.

IV. Cell Culture

Murine macrophage cell line, J774A.1, Mouse BALB/c (TIB-67, American Type Culture Collection, Rockville, MD) was routinely maintained in Dulbeccos modified Eagles medium (Mediatech Inc, USA) supplemented with 10% fetal bovine serum (Mediatech Inc, USA) and a 2 mM L-Glutamine. The cells were always maintained at 37 °C in a humidified atmosphere of 5% CO₂ in air. Cells were passaged by scrapping, centrifuging and resuspending in fresh medium. All experiments were performed with cells between passage numbers 1-10.

To determine the cell number and the number of vital cells used in the experiments, a cell suspension in DMEM was diluted 1:10 in a 0.05% trypan blue (VWR) solution in deionized water. This colored substance enters and stains only dead cells. The cell suspension in trypan blue was transferred into two hemocytometer chambers (Neubauer counting chamber). Using a 10x objective and light microscopy, the cells were counted in 8 fields (each field having an area of 1mm²) and the average number of cells per volume (ml) was calculated (excluding cells stained in blue which are dead).

i. Fixing Cells

Petridishes containing cells were washed with cell culture media and then filled with 3% glutaraldehyde (Electron Microscopy Science Inc Catalogue #16310) solution in distilled water. Treating cells with glutaraldehyde leads to establishment of chemical cross-links between free amino groups. When the cross-links join different molecules, a latticework of interactions occurs that holds the overall architecture of the cell together. The petridish was left in glutaraldehyde solution and was then transferred to confocal microscope for imaging.

V. SEM and Critical Point Drying

i. Scanning Electron Microscopy

The scanning electron microscope (SEM) is a type of electron microscope that images the sample surface by scanning it with a high-energy beam of electrons in a raster scan pattern¹¹⁶. Samples were prepared for scanning electron microscopy by critical point drying and sputtering with a thin layer of carbon or gold. Images were made taken on a Leo 1530 field emission scanning electron microscope (Carl Zeiss Gmbh) using an accelerating voltage of either 3 or 10 kV.

ii. Critical Point Drying

Critical point drying is based on the process of “the continuity of state”, where there is no apparent difference between the liquid and gas state of a medium; therefore, the surface tension between these interfaces is reduced to zero¹¹⁷⁻¹¹⁸. This occurs at a specific temperature and pressure with resulting density, and is known as the Critical Point. The condition of zero surface tension can be used to dry biological specimens, avoiding the damaging effects of surface tension. In fact, if cells are air-dried the evaporation of water molecules can disrupt the cell membrane because of the surface tension of water. Therefore, when biological specimens are prepared for the SEM, the water in the cell is first replaced by ethanol. Then, in the critical point dryer, the ethanol is replaced by liquid CO₂. The critical temperature and pressure for CO₂ (31°C, 75 Bar)¹¹⁷ is obtained so that the liquid CO₂ changes to a gas; this conversion does not affect cell membrane and cell structures. The first step, after removal of the culture media, is fixation of samples in 2% glutaraldehyde in PBS for 15 min; then the dehydration is achieved by incubating the samples in graded Ethanol (25%, 50%, 75%, 95% and 100%, each 10 min). The samples are transferred in a shallow glass dish containing 100% dry ethanol and brought into the chamber of the critical point dryer (CPD 030 Critical point dryer, Bal-Tec). The chamber is one third filled with 100% ethanol and then the cap is closed airtight. When the temperature is 10°C and the pressure 50 Bar, the chamber is filled with CO₂ and the chamber is filled and emptied with liquid for 6-8 times without uncovering the sample. Then, the chamber is completely filled with fluid and heated at 40°C at a pressure of 90 Bar. Samples were finally sputter-coated with a carbon layer to be imaged by SEM.

5. Results and Discussion

I. PDMS Arrays as Force Sensors in Frustrated Phagocytosis

When macrophages are challenged with IgG coated surfaces, they engage that surface as if to engulf it. This process of trying to engulf objects larger than the cell itself has been termed “frustrated phagocytosis”^{64,119-122}. During frustrated phagocytosis, macrophage tend to bind to the surface tightly with the aim to destroy the underlying substrate⁷⁰. In the present work we used PDMS pillar arrays to measure the force exerted by macrophages during frustrated phagocytosis.

In situ force measurements of frustrated phagocytosis was conducted on IgG topped force sensor arrays with calibrated pillars 3 μm in diameter, 10 μm in height and 10μm inter pillar distance from center to center (refer to materials and methods section for making of PDMS pillars). These arrays had individual pillars with a nominal stiffness of 0.17 (N/m)¹²³. The macrophage monocyte cell line J774A.1 from mouse BALB/c was used to calculate the force during frustrated phagocytosis. The surface tension and hydrophobicity prevented the IgG from flowing down the pillars leading to functionalization only on the top of the pillars. As discussed in Ulmer *et. al*¹²³ the IgG was plated only briefly on the pillars and washed with PBS before plating the cells. Cells attached and spread across multiple posts causing deflection of the underlying posts as shown in Figure 8D. When adhered strictly to the top surface of pillar arrays, cells locally exert forces on the tips of each post. Because each post is deflected independently, localizing the origin of the forces exerted by the cell is straightforward process.

Forces applied laterally to the pillar tops can bend the pillar. By recording the pillar top displacement the exerted force can be determined when the pillar stiffness is known. The pillar bending stiffness can be calculated from equation

$$F = \left(\frac{3EI}{L^3} \right) 2r \quad \text{Equation 3}$$

Where F, E, I, L, and 2r are the bending force, Youngs modulus, moment of inertia, length, and resulting deflection of the post, respectively as described in Crandall *et. al*¹²⁴. A schematic of the pillar can be seen in Figure 8D.

As shown in Figure 8A, the angle and dimensions of the pillars were obtained from electron micrographs. The forces these cells exert are relatively large and it was seen that the contracting cells can easily bend the PDMS pillars on which they were plated. The force exerted by the cells can be calculated precisely by making an image of the pillars at 45° and using the calibrated scale bar on the scanning electron micrograph to measure the diameter and length of the pillar. Hereby the angle under which the image is taken needs to be taken into account. As shown in the image there was an angle of 59.7° giving a 2r or deflection of the post to be 5.15 μm. Since we know from Ulmer *et. al*¹²³ that the pillars had a stiffness of 0.17 (N/m). We calculated that the cells exerted a force of 8.75nN on the pillar.

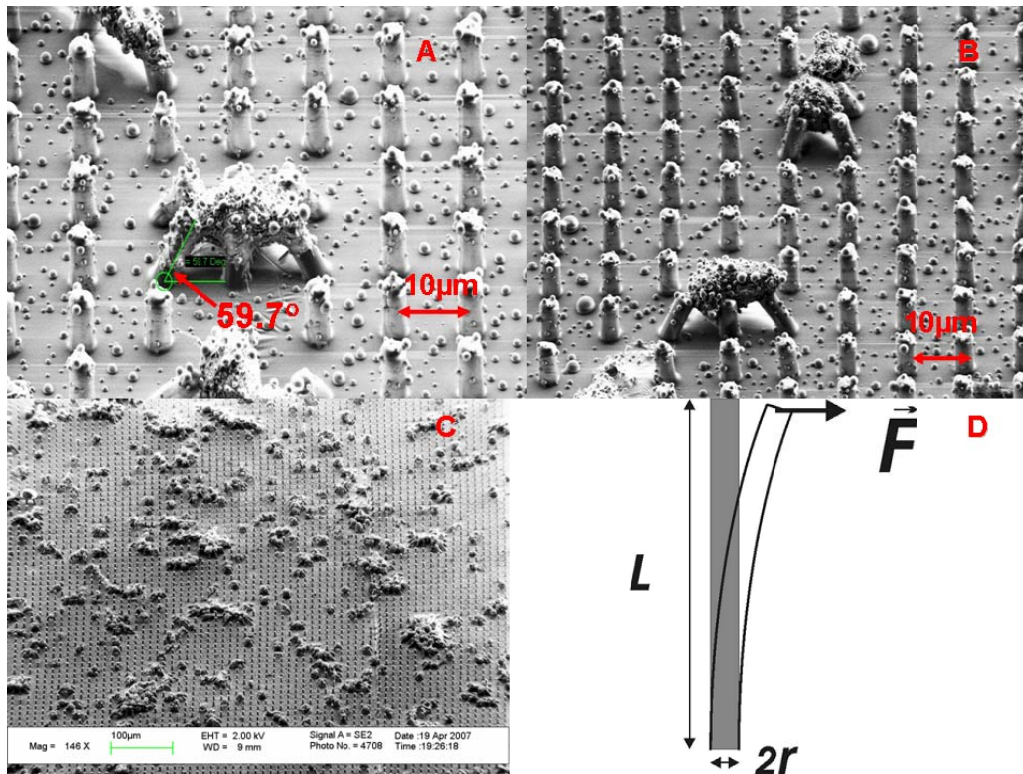


Figure 8 SEM image of PDMS arrays acting as force sensors in frustrated phagocytosis. (A) Image of a macrophage on an array taken at 45° showing that the cell deflecting a pillar by 59.7° . (B) and (C) Array images at different magnifications. (D) Schematic of an individual pillar in the pillar array. The force F exerted by the cell can be calculated by measuring the displacement $2r$.

As seen in Figure 9D, the cells seem to be hindered by the pillar substrate and envelop individual pillars leading to phagocytosis of the individual pillars. The cells also distribute the force unevenly on the pillar array due to sinking of cells into the pillars. Membrane spreading on the edge of the pillars can be seen in Figure 9B. A schematic of this is presented in Figure 9C.

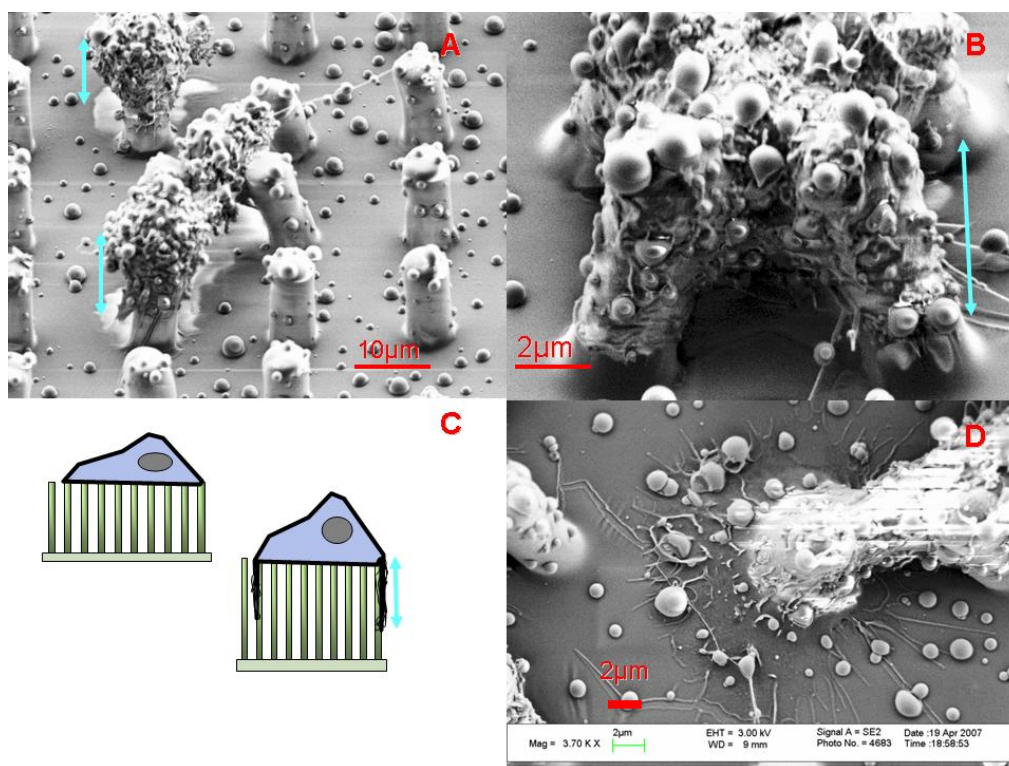


Figure 9 SEM image of PDMS arrays acting as force sensors in frustrated phagocytosis. (A) and (B) Images of a macrophage on an array taken at 45° showing cells deflecting pillars. The blue arrow shows the problem of the macrophages trying to eat the pillar instead of spreading during frustrated phagocytosis. (C) Schematic of expected frustrated phagocytosis and macrophage spreading for accurate calculation of force and a schematic showing the problem in measuring the forces as the cells start spreading on the edges. (D) Macrophage engulfing a pillar.

Due to this inherent limitation, we went ahead and devised a new approach to decipher phagocytotic uptake using novel PSS/PAH polyelectrolyte capsules.

II. Mechanical Characterization and Calibration of PSS/PAH Capsules

As shown in Figure 10A, in order to calibrate the mechanical properties of the capsules and identify the elastic modulus and failure behavior of the capsules, force versus deformation characterization of the capsules was performed in collaboration with our collaborators. A defined force was applied on the capsule and the resulting deformation of the capsule was captured. When low forces were applied the capsules as shown in

Figure 10B, the capsules act as simple springs. To investigate the deformability of the capsules an atomic-force microscope mounted on an inverted optical microscope equipped with an RICM (Reflection Interference Contrast Microscopy) imaging capability was employed. A Zeiss Axiovert 200 (Zeiss, Germany) was used in Reflection Interference Contrast Microscopy (RICM) mode¹²⁵. For applying forces a Molecular-Force Probe (MFP) 1D AFM (Asylum, Santa Barbara, USA) was used. A nanopositioning sensor (LVDT sensor) allowed independent measurement of the piezo extension and allowed correction due to hysteresis. The force was applied using a glass bead bound¹²⁶ to tipless contact cantilever

(Micromash, Estonia) with a low spring constant (average 0.08 N/m). The spring constant of the cantilevers was determined by their thermal resonance frequency spectra¹²⁷⁻¹²⁸.

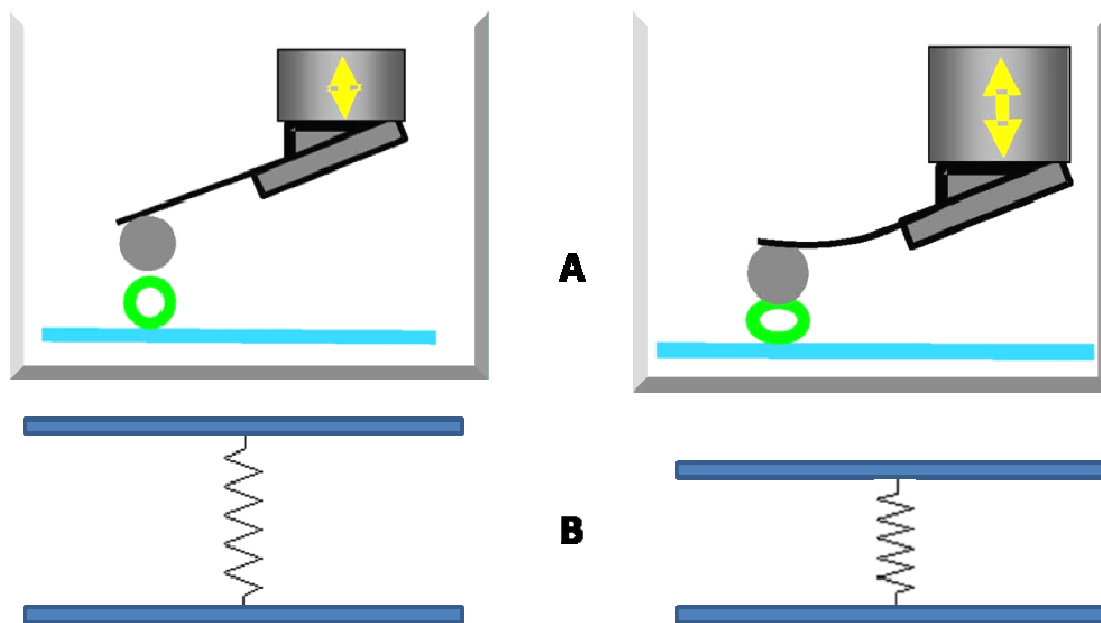


Figure 10 (A) Schematic illustration of a capsule being deformed by the AFM. By applying defined force and measuring the resulting deformation we can understand and calibrate the mechanical properties of the polyelectrolyte capsules. (B) A simple mechanical equivalent circuitry representation of the force being applied to capsules.

Before the force was applied on the capsules, a reference curve on the glass coverslip (that can be considered as a nondeformable surface) was performed. The force is deduced from the spring constant and the deflection of the cantilever. Figure 12 shows a force versus deformation curve for a 4.5 μm PSS/PAH shell. One can distinguish three different regions in the force-deformation behavior. For weak deformations (linear regime), the force response is proportional to the deformation. This regime extended from 1-100 nN. The corresponding RICM pictures showed that only very small changes occur in the contact area or shape of the capsule in this regime. Thus, the deformation of the capsule mainly occurs in the contact zone between the capsule and the glass bead and remains local. In the intermediate part of the curve, there was an increase in the contact area, the deformation occurs on top and at the bottom of the capsules. When the force is further increased the capsules deform irreversibly and this phenomenon is called buckling. Buckling of the capsule occurs around 150 nN.

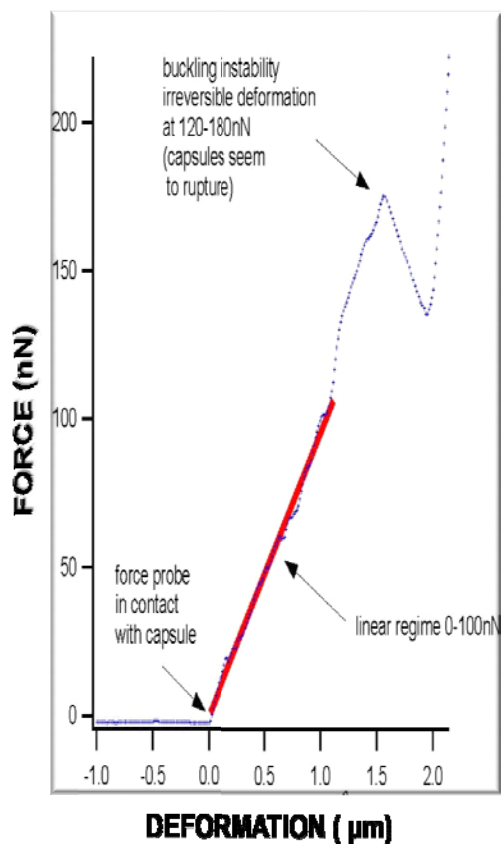


Figure 11 Graph showing force versus deformation of the 9 layers 4.5 μm diameter PSS/ PAH polyelectrolyte capsules. The red line indicates the linear regime of the capsule. In this regime the capsules are perfectly elastic and go back to their original state when the applying force is relaxed. The buckling regime or irreversible deformation of the capsule occurs around 150 nN.

By extracting the slope of the linear part of the force versus deformation curve for various capsules of the same defined thickness and radius to get statistical results we obtained the Young's Modulus of the capsules (E). These measurements were repeated for 45 capsules to get a more accurate measurement. As expected, there was heterogeneity in the mechanical properties of the capsules and is shown in the graph below. This heterogeneity is evident from the histograms shown below in Figure 12 and 14. The majority of the capsules buckled between 120 nN -180 nN. The average buckling force was 150 nN. The capsule stiffness varied between 0.08 to 0.14 nN/nM. The average stiffness was 0.11 nN/nM.

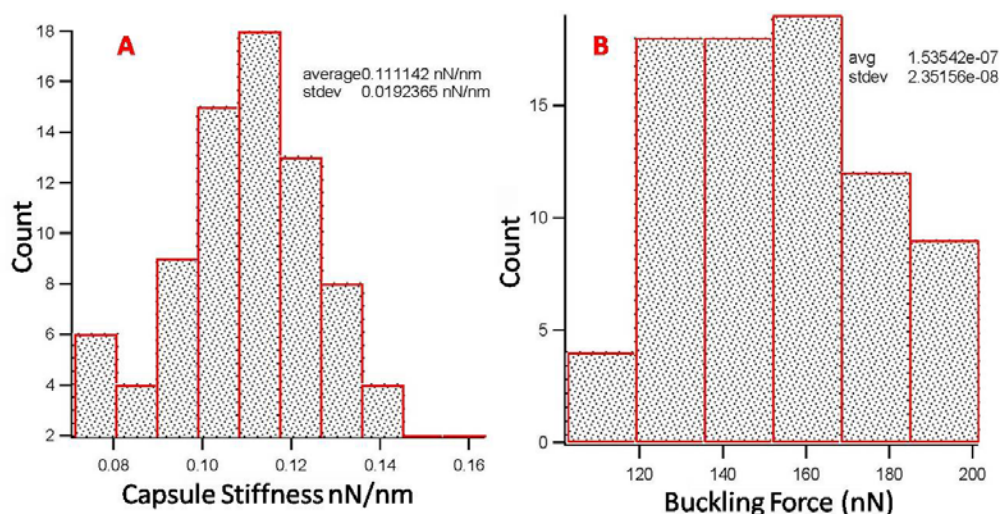


Figure 12 (A) Histogram of capsule stiffness in the linear regime. The average stiffness of the capsules was 0.12 nN/nM. (B) Histogram of the force required to buckle or irreversibly deform the capsules. The average buckling force of the capsules was 150 nN.

III. Buckling Force and Force of Phagocytosis

In order to calculate the forces being exerted on the engulfed particle, we pulse J774A.1 macrophages, nanometer thick hollow PSS/PAH capsules which are 4.5 μm in diameter. Once the cell starts taking up these capsules the force of phagocytosis visibly deforms the capsules. These deformations are captured using fluorescence microscopy. In order to enumerate the forces from the deformations observed, the capsules were initially calibrated and characterized mechanically to find the elastic modulus and failure behavior. In essence we are trying to use the mechanical cues to understand chemical signaling.

As described earlier when we did the mechanical calibration of the capsules we found the capsules to have stiffness of the capsule to be 0.11 ± 0.019 nN/nm. The force versus deformation curve shows that there is a linear regime up to 100 nN. During the linear regime the capsules spring back to their original position after the force applied is removed. The buckling or irreversible breaking of the capsule occurred between 120-180 nN with an average of 150 ± 24 nN. The huge buckling force can help us understand the maximum force regime that can occur during phagocytosis.

The first observation when we added the capsules was that the cells were able to buckle or irreversibly deform the capsules during the phagocytotic process (see Figure 13(A-G)). This was surprising as we know from the calibration data of the capsules that the force required to buckle is $>150 \pm 24$ nN. This force is several magnitudes higher than what was observed by Vonna *et. al*¹⁶ during phagocytotic uptake which they determined to be >5 nN using magnetic tweezers or >15 pN measured using optical tweezers by Kress *et. al*¹⁸. This clearly shows that cells can exert huge forces, although clearly the reason for observing this is the inherent advantage of the present technique to observe much higher forces than the traditional techniques employed before. The other reason we think we observe these huge forces is the other advantage of the technique where we follow the entire process of phagocytotic uptake rather than the first stage of initial uptake or the initial protrusion phase of the uptake process measured by the other techniques.

In the Figure 13, image G shows cells with capsules at different stages of phagocytosis. Capsules that were not engulfed were still spherical. The capsules that just got engulfed were elliptical and can be found on the edge of the cells. A whole set of capsules that went through phagocytotic uptake and were buckled can also be found in the center of the cell.

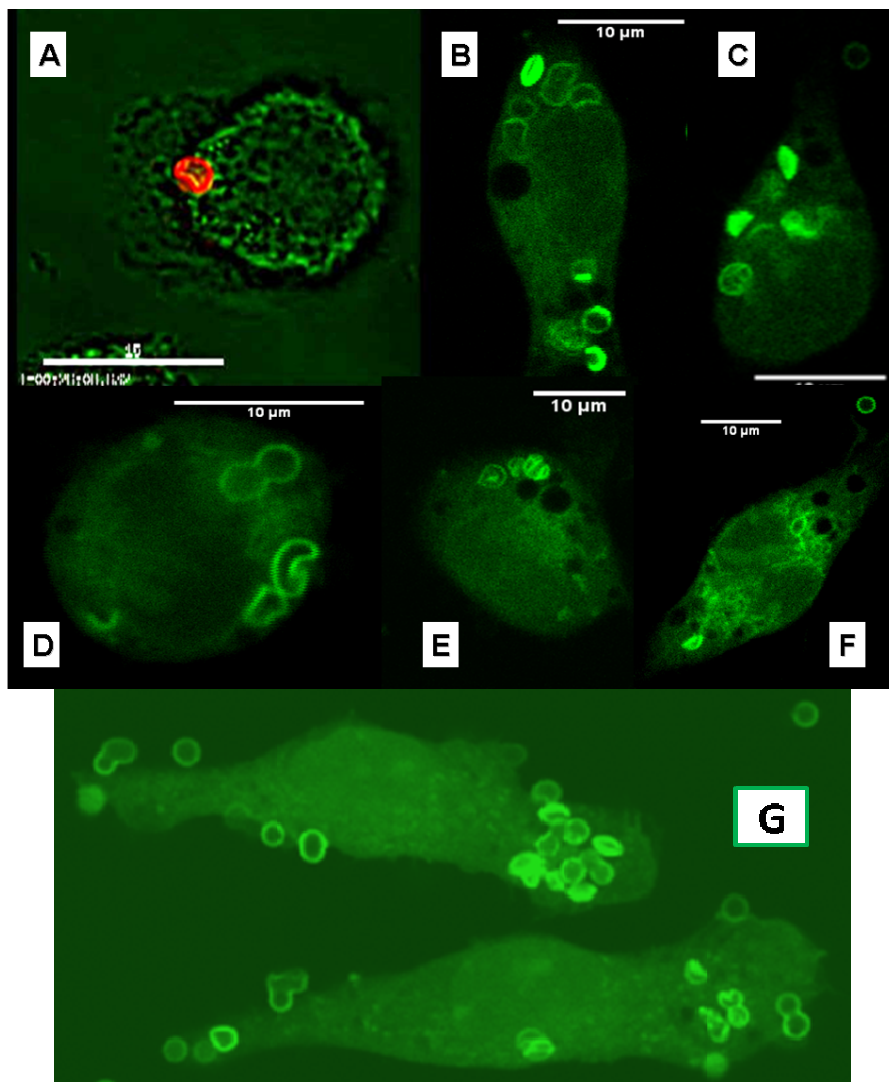


Figure 13 (A, B, C, D, E, F, G) show macrophages J774a.1 with 4.5 μm diameter PSS/PAH capsules engulfed by cells after 90 minutes. It can be observed that most of the capsules were buckled. Round unbuckled capsules can be seen outside the cell area in the right hand corner of images (C) and (F).

IV. Buckling and the Role of pH

Here we want to test if the pH change that occurs inside the cell can cause buckling or irreversibly deformation of the capsules. The PSS/PAH capsules used as force sensors are made by physisorption of oppositely charged polyelectrolyte's on a charged spherical solid surface. We use layers of alternating polystyrene sulfonate (PSS) and polyallylamine hydrochloride (PAH). This polyelectrolyte pair is composed of a strong polyanion (PSS) and

weak polycation (PAH). It has been reported before¹²⁹ that at low pH the PSS/PAH multilayer is permeable for dextran (neutral polymer) molecules. The high amount of ionic pairs present in the multilayers¹³⁰⁻¹³¹ might serve as the cross-linking units between the multilayer's. If at least one polyelectrolyte in the multilayer is weak, the pH can be used to control the ionic cross-link density and conformations and, therefore, should affect the stiffness of the capsules and Young's modulus of multilayer films. Depending on physicochemical conditions there can be capsule softening, this softening is due to either an increase in the permeability of the capsules (low pH) or a decrease in Young's modulus of the multilayer (high pH, salt)¹³².

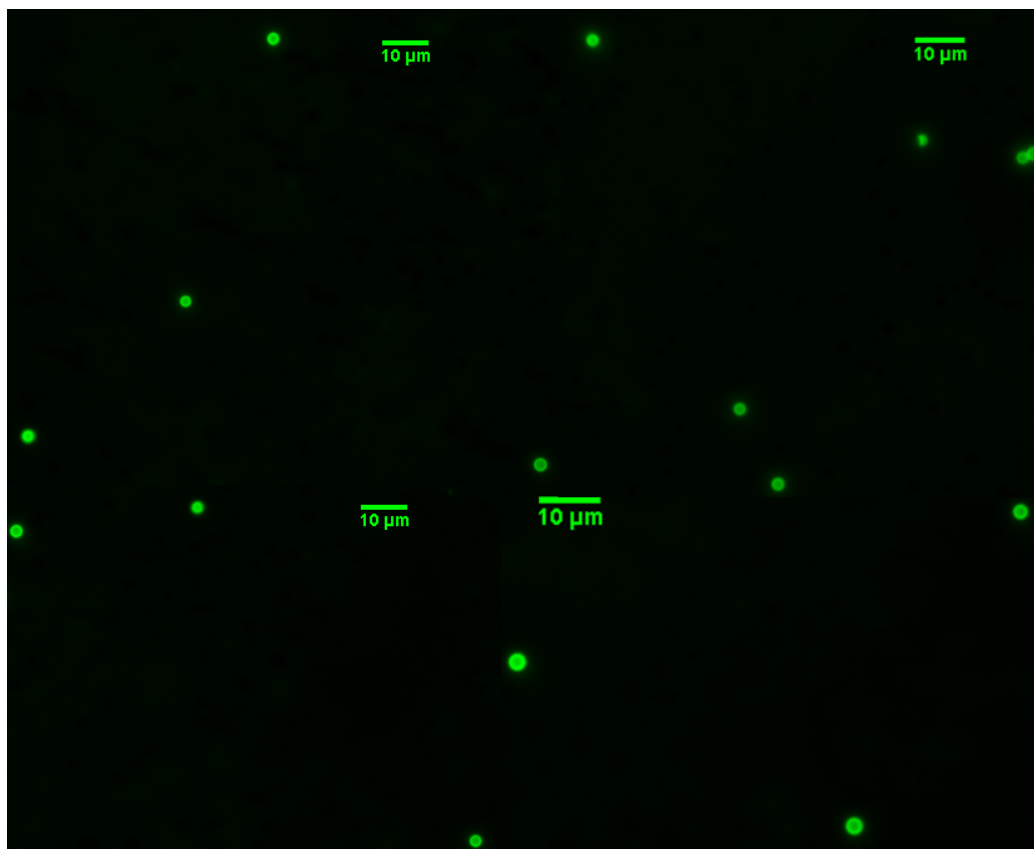


Figure 14 Four images with capsules in pH 4 buffer after 24 hours. It can be seen that most of the capsules are perfectly spherical.

Once the capsules are engulfed, they go through retrograde motion where they interact with different organelles like lysosomes and peroxisomes. Lysosomes are organelles containing digestive enzymes (acid hydrolases). The pH inside the lysosomes is between 4.5 - 4.8. Since we know from earlier studies by Lulevich *et. al*¹³² that at low pH (pH 3) the capsules become softer and there is an increase in permeability. To check if this would adversely affect the properties of the capsules during retrograde motion, we added the capsules to standard pH 4 buffer (Potassium Acid Phthalate) from JTBaker Inc. We found that the capsules were perfectly spherical in pH 4 buffer even after 24 hours. This clearly shows that just pH change that occurs inside the cell is not enough to buckle or irreversibly deform the capsules.

V. Understanding the Role of PI3-Kinase and SYK Kinase Activity in Phagocytotic Uptake

The mechanism by which Fc γ stimulate the polymerization of actin and induce the formation of phagosomes is not known² although PI3-kinase^{42,133} the rho family of GTPases⁵¹, protein kinase C (PKC)¹³⁴⁻¹³⁵, and motor proteins¹³⁶⁻¹³⁷ appear to participate. To further validate our experimental setup we inhibited SYK and PI3-Kinase known to be involved in phagocytosis at different stages^{33,138} using well established pharmaceutical inhibitors 50 μ M piceatannol^{36,139} and 50 μ M LY294002¹⁴⁰. If our experimental setup works as proposed, we should observe varying contractile activity of the capsules when we inhibit the cells with the above mentioned inhibitors. This would also help us systematically decipher the mechanistic roles of these individual molecules in phagocytotic cup formation and uptake process.

During Fc receptor based phagocytosis it is known that the FcR which are members of the immunoreceptor class of receptor tyrosine kinases contain the receptors in their cytoplasmic tails or in associated subunits the immunoreceptor tyrosine-based activation motif (ITAM). Clustering of the FcR by IgG-opsonized particles induces phosphorylation of tyrosines within the ITAM motifs and initiates assembly of a complex of proteins around the FcR on the cytoplasmic side of the membrane¹⁴¹. Lyn and Hck, members of the Src family of tyrosine kinases, phosphorylate the ITAM motifs following clustering¹⁴². The phosphorylated ITAMs then recruit Syk kinase. Syk signaling is required for efficient phosphorylation of the p85 regulatory subunit of phosphatidylinositol 3-kinase (PI3-K)³³, which activates the PI3-K catalytic subunit p110 β ¹⁴³, generating PI-3,4,5-trisphosphate [PI(3,4,5)P₃] from PI-4,5-bisphosphate [PI(4,5)P₂] in the membrane near the receptor complex. In essence we have SYK followed by PI3-Kinase activity during the uptake process. As shown in Figure 15, phagocytosis mediated by SYK and PI3-Kinase provides a simple model system to study signal transduction and the associated cytoskeletal alterations induced by clustered ligands. Here phagocytosis is just a model system and the role of SYK and PI3-Kinase if deciphered can help us extend our knowledge in other actin dependent cell process like cell motility¹⁴⁴ that require SYK¹⁴⁵ and PI3-Kinase^{133,146} activity.

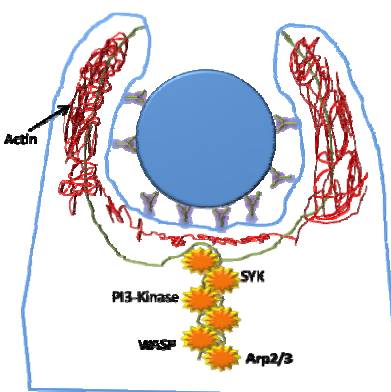


Figure 15 A mechanistic model of the phagocytic cup formation showing how the signaling events are interlinked like gears in a device. The phagocytotic signaling starts with the receptor recognition followed by different signaling events including SYK activation leads to PI3-Kinase and the signaling event continues until the phagocytotic cup closure occurs.

i. Role of PI3-Kinase Activity in Phagocytotic Uptake

FcγR is coupled functionally, via a tyrosine kinase, to PI3-kinase, which may regulate the phagocytotic activity of the cells. PI3-K is necessary for phagocytosis of IgG-opsonized particles larger than 2 μm diameter¹³⁸. Phosphatidylinositol 3-kinase (PI3-kinase) has also been implicated previously in signaling by all three classes of Fcγ receptor¹⁴⁷⁻¹⁴⁸. Activation of PI3-Kinase results in the appearance of the lipid products of this enzyme, phosphatidylinositol 3,4-bisphosphate and phosphatidylinositol 3,4,5-trisphosphate¹⁴⁹⁻¹⁵⁰. The PI3-Kinase is composed of a catalytic subunit p110 and an associated regulatory subunit p85¹⁵¹⁻¹⁵². Phosphorylated phosphoinositides generated in the phagosome by the action of PI3-Kinase may position the contractile apparatus, either directly by binding a myosin, or indirectly by activating Rho¹⁵³⁻¹⁵⁴, or by organizing a complex of integral membrane proteins that can assemble a contractile apparatus.

Previous studies¹³⁸ have shown that Fcγ receptor (FcR)-mediated phagocytosis and macropinocytosis in macrophages consist of two dissociable activities: a phosphoinositide 3-kinase (PI3-K) independent extension of phagocytic cups and a PI3-K dependent contractile mechanism that closes phagosomes and ruffles into intracellular organelles. Inhibitors of phosphoinositide 3-kinase (PI3-kinase) allow pseudopodia to extend onto an opsonized particle, but prevent them from closing into phagosomes, indicating that PI3-Kinase regulates phagosome closure⁴³.

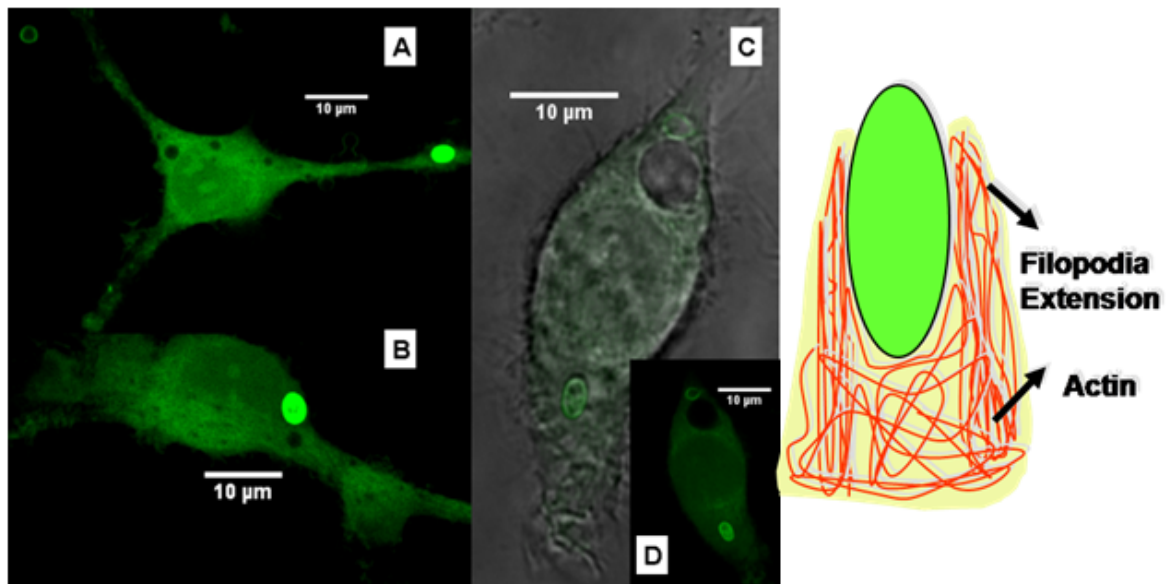


Figure 16 (A, B, C, D) Shows macrophages J774a.1 with 4.5 μm diameter PSS/PAH capsules engulfed by cells after 90 minutes. The PI3-Kinase is inhibited by adding 50 μM LY294002. It can be observed that most of the capsules were oval but not buckled after 90 minutes. Round spherical capsule can also be seen outside the cell area in the top left hand corner of image (A).

To inhibit PI3-Kinase, 50 μM LY294002 was added to cell petridish for 2 hours. After the cells were inhibited, capsules were pulsed for 90 minutes. Finally the cells were fixed in 3% glutaraldehyde in PBS. As previously reported the inhibition of PI3-kinase⁴³ allowed regulation of actin polymerization that led to cup formation but prevented closure. We found constriction of the capsules that were stuck to the outer membrane of the cells but the

capsules were not really uptaken. It was found that there was enough force to turn perfectly spherical capsules slightly oval but not enough to buckle them. When the eccentricity of the capsules (major axis/minor axis) was calculated with PI3-Kinase inhibited in the cells the eccentricity was 0.75 ± 0.05 . The data was collected from 8 different petri dishes. It was observed that the capsules were elliptical but not buckled showing that the step during the uptake process that exerts the maximum force needs PI3-Kinase activity.

ii. Role of SYK in Phagocytotic Uptake

It is known that the phosphorylation of SYK precedes the activation of PI3-kinase. In order to understand the role of SYK kinase in phagocytotic uptake process and calculate the mechanistic role of SYK in cup formation, we inhibited SYK by pretreating them with 50 μM piceatannol³⁶, a SYK-selective inhibitor for 2 hours before pulsing with capsules for 90 minutes. When SYK was inhibited it allowed regulation of actin polymerization that led to cup formation but prevented phagosome cup closure. None of the capsules entered the cells, showing that it prevented phagocytotic uptake. We found constriction of the capsules that were stuck to the outer membrane of the cells but the capsules were not really uptaken. The amount of constriction varied but the capsules were mostly slightly oval to spherical. It was found that there was enough force to turn perfectly spherical capsules slightly oval but not enough to buckle them. The eccentricity of the capsules for SYK inhibited cells was 0.87 ± 0.05 .

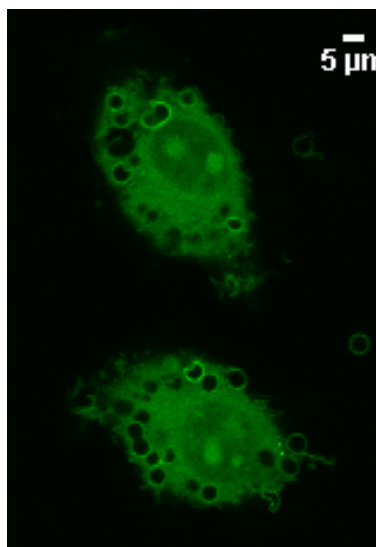


Figure 17 Macrophages J774a.1 with 4.5 μm diameter PSS/PAH capsules engulfed by cells after 90 minutes. The SYK kinase activity was inhibited by adding piceatannol. It can be observed that most of the capsules were slightly oval but not buckled after 90 minutes. Round spherical capsule can also be seen outside the cell area in middle portion of the image.

Together, these inhibition experiments indicated that for the cells to exhibit maximum contractile force after the initial cup formation stage and to exert maximum contractile forces it needs both SYK and PI3-Kinase activity. This increase in constriction with SYK and PI3-Kinase inhibition suggests that, phagocytic cup formation occurs in a step wise fashion. The

zipper mechanism, the longest standing model, when evaluated in the context of our data indicates zipper mechanism as a plausible mechanism for uptake.

After its first description 120 years back, much work remains to be done in understanding the signaling pathways elicited by different phagocytic receptors. Phagocytosis is known to involve several steps. One purpose of the present work was to test if we can use the “phagosensor” the capsule based methodology to measure forces temporally so as to elucidate the key signaling regulatory features that control phagocytic response, shining light into many of the current ‘black boxes’ in our knowledge. Like the inhibition assays of SYK and PI3-Kinase in this work, we can further silencing key unknown components in phagocytotic process and compare it with controls thereby understanding the complex signaling networks that regulate this fundamental mechanism of the immune response.

VI. Temporal Understanding of Phagocytotic Uptake

In order to gather complex data in a highly dynamic and spatially complex system like phagocytotic uptake, we use 4D live cell imaging. Imaging in 4D will help in getting a more complete representation and 4D imaging is done by recording the data in three spatial dimensions over time (four-dimensional (4D) imaging). In our experiments we used a Nikon LiveScan Swept Field Confocal Microscope built on a Nikon TE-2000U microscope platform. The imaging was performed on a 60X Nikon Plan Apo VC water-immersion objective (NA 1.2). The objective was mounted on a high precision motor (piezo-stepper); the piezo-stepper allowed us to image the specimen in Z. Image acquisition was performed with a Photometrics cooled-CCD camera. When imaging in 4D¹⁵⁵, it is crucial to have a suitable compromise between sufficient, but not toxic, illumination, spatial resolution in the x, y and z axes, temporal resolution and the signal-to-noise ratio, so that the maximum number of acceptable images can be acquired before the specimen is completely photobleached or the cells are killed.

One of the serious drawbacks in 4D imaging is the resolution along the z axis, which, in light microscopes, is about threefold lower than resolution along the x and y axes; this causes anisotropy in the recorded 3D image¹⁵⁶. In order to optimize z resolution, deconvolution microscopy¹⁵⁷ is used to Image stacks of images in z and then they are processed using iterative algorithms that assign out-of focus light back to the fluorescent object that comes from the correct focal plane. Deconvolution can yield high-resolution 3D information from widefield images¹⁵⁸⁻¹⁵⁹. By contrast, confocal laser-scanning microscopes excite the fluorophore by moving a focused laser beam line-by-line over the specimen and record each image pixel sequentially on a point detector. A confocal aperture in front of the detector rejects out-of-focus light before it reaches the detector and confocal stacks therefore immediately yield 3D images with good axial resolution¹⁶⁰. Deconvolution and confocal microscopy both have their specific advantages and disadvantages, which depend on the specific biological application¹⁶¹⁻¹⁶³.

To get quantitative information alternatively, 4D data can be projected in the x–y plane, neglecting the z dimension¹⁶⁴⁻¹⁶⁷. Although this allows a more intuitive access to the data by viewing it as a simple 2D movie, it sacrifices spatial information. In order to include spatial information several algorithms have been developed like maximum intensity projection¹⁶⁸ and mean-intensity projection¹⁶⁹. Maximum intensity projection¹⁶⁸ produces images that have a particularly high contrast for small structures. In maximum intensity

projection, 3D data is projected into the visualization plane by projecting the voxels (volumetric pixels) with maximum intensity that fall in the way of parallel rays traced from the viewpoint to the plane of projection. However, it does not quantitatively represent fluorescence concentrations and cannot be used for analysis where intensity concentration is needed. Instead, mean-intensity projection¹⁶⁹ should be used for quantification for such applications, although it does not produce such crisp images. Mean intensity projections can be useful to measure relative fluorophore concentrations and their dynamic changes over time. This can be used as an approximation of the real concentration of fluorescently labeled molecules, which can only be derived from 3D analysis¹⁷⁰. For analyzing morphology changes, both methods can be used¹⁷⁰.

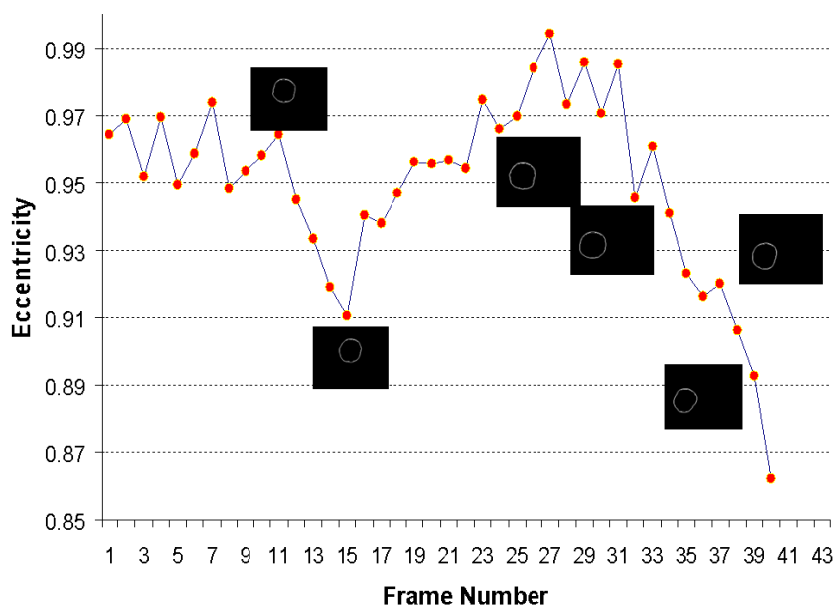


Figure 18 Eccentricity of a capsule after phagocytosis is initiated. The capsules outline for some of the data points can be seen in the inserts.

For a temporal quantitative characterization of the uptake process, capsules were pulsed with J774A.1 macrophages and the deformation on the capsules was observed in 4D using a high speed confocal microscope. To quantify the images in Z, each time-point in the movie was made into a maximum intensity projection of the volume for that time point. More information regarding 4d quantitative studies using maximum intensity projection can be obtained from Gerlish *et. al*¹⁷⁰. Images in the column of Figure 19Aa are maximum intensity projected images of a time point in z. As shown in Figure 19Ab, a home built algorithm was used to find the edges of these capsules. Using the capsules edges, the capsules eccentricity was determined using the principle in Figure 19C. The decrease in eccentricity with time can be seen in the eccentricity versus time graph shown in Figure 19B. Once the pseudopodium starts surrounding the capsule and binding to the capsule, this process of phagocytosis starts and this was quantified by measuring the eccentricity corresponding to contraction occurring on the capsule. It can be observed from Figure 18 that the capsules exhibited abrupt kinetics. It has been seen that, initially the cell endeavors to ingest the capsule but misses and finally achieves it. The slope during initial uptake process was similar to what was observed during the last few stages when the capsule was finally

ingested. We choose in our experiments a 4.5 μm diameter capsule as we know from previous work of Cox et. al¹⁷¹ and Chavrier et. al¹⁷² that, with increase in size and around 4.5 μm the uptake process turns slower and multi-step. This increase in uptake process may be due to involvement of PI3-Kinase which is known to regulates actin polymerization¹⁷³ causing delayed phagocytosis⁴⁴.

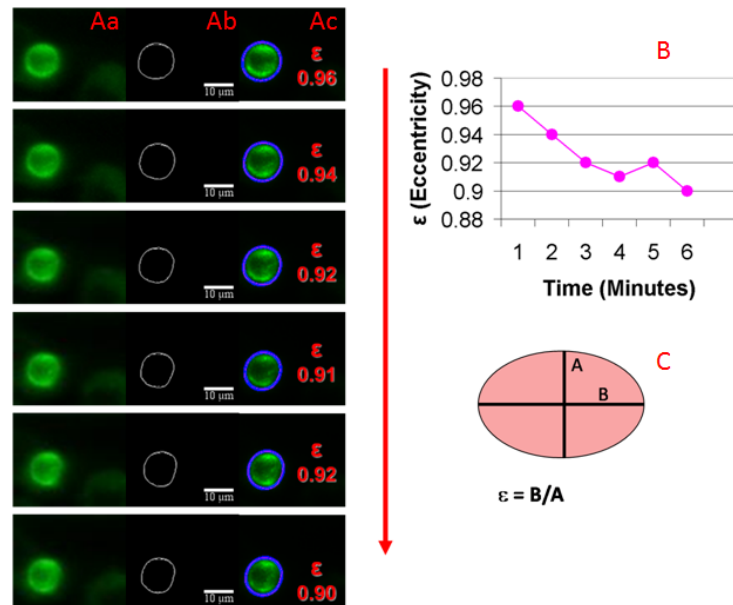


Figure 19 Methodology of eccentricity determination of the capsules. In order to determine the eccentricity as shown in images Figure 19 (Aa) column, we initially did a maximum intensity projection of the 4d movie. As shown in (Ab) we then found the edges of the capsules. As shown in the Figure 19 (C) we found the dimensions of maximum axis/ minimum axis of the ellipse to determine the eccentricity. The top right portion (B) of the Figure 19 shows the eccentricity changes with time during phagocytotic uptake of the capsules.

Closer inspection of the initial intake process shows two distinct phases. We hypothesize that the first phase, a random motion of the capsule around cell is caused due to pseudopodia trying to grab the capsule. The second phase occurs with a rapid retraction of the capsule towards the cell. In the second phase the brisk motion caused the capsules to buckle, showing that there is a force $>150 \pm 24$ nN (buckle force) occurring during this stage.

6. Conclusions and Outlook

Although much work has been performed in understanding Fc based phagocytosis, still work remains to be done in understanding the signaling pathways elicited by different phagocytic receptors and their corresponding signaling activity. One purpose of the present work was to test if we can use the “PhagoSensor”, the capsule based methodology to measure forces temporally so as to elucidate the key signaling regulatory features that control phagocytic responses. This will help shine light into many of the current ‘black boxes’ in our knowledge. In order to enumerate the forces from the deformations observed, the capsules were initially calibrated and characterized mechanically to find the elastic modulus and failure behavior. For the 4.5 μM PSS/PAH, 9 layer, 18 ± 2 nm thick capsules that were used for our experiments we found the stiffness of the capsule to be 0.11 ± 0.019 nN/nm. The force versus deformation curve shows that there is a linear regime till 100 nN. During the linear regime the capsules spring back to their original position after the force applied is removed. Our time lapse measurements in 3d clearly show that we can obtain quantitative information temporally. The buckling or irreversible breaking of the capsule occurred between 120-180 nN with a peak around 150 nN. Imaging of molecular dynamics in living cells indicated that formation of phagocytic cups involves discrete mechanical steps occurring due to distinct patterns of signaling at various stages of their formation, because of discrete cytoskeleton activation steps. To prove that we can annotate and systematically decipher the mechanistic roles of these individual molecules in phagocytotic cup formation and uptake, we inhibited key signaling molecules PI3-Kinase and SYK. To give a quantitative face to the observed deformation, we calculated the eccentricity (Major/Minor axis of the ellipse) of the capsules. It is known that SYK and PI3-Kinase activation occurs in succession during uptake. As expected the capsule deformations observed for SYK inhibited cells was 0.87 ± 0.05 and for PI3-Kinase inhibited cells was 0.75 ± 0.05 , showing that activation occurs in sequence. This sequential activation of signaling molecules shows zipper mechanism as a plausible mechanism for J774A.1 phagocytic cup formation in Fc receptor phagocytosis.

Due to the inherent advantage of the present technique we can tune the mechanical properties of our sensor target i.e. the polyelectrolyte capsules, allowing us to observe much higher forces than the traditional techniques. Since we follow the entire process of phagocytotic uptake rather than the first stage of initial uptake or the initial protrusion phase of the uptake process measured by the other techniques, we were able to observe huge forces exerted by cells during phagocytosis. Unlike the other measuring procedures like magnetic tweezers (>5 nN)¹⁶ or >15 pN using optical tweezers¹⁸ our capsule based methodology pushed the measuring techniques upper limit upto 150 nN, a thirty fold increase to the previous measurements.

The key advantage of the present technique compared to the existing techniques is the non-invasive nature of the measuring procedure. Using “PhagoSensor” approach we can measure forces in the natural state during phagocytotic uptake process without applying any external mechanical forces or by perturbing the cells. Since activation and differentiation signals appear to enhance, or modify the signaling enzymes that regulate phagocytosis, we expect this technique to measure the events more efficiently and depict the process more accurately.

The analogies between cell adhesion, motility and phagocytosis are strong. These “PhagoSensor” studies provide an imaginative approach to gathering details about the acto-

myosin machinery that regulates phagocytosis as well as multiple other mechanical processes including cell adhesion, cell motility and cytokinesis. We expect that the details learned in these specific studies will have direct translational value to other acto-myosin systems and other studies focused on mechano-chemical coupling and mechanosensitivity. These studies will directly contribute to our understanding of mechano-chemical coupling and mechano-sensitivity, two broad themes of great interest in molecular and cell biology.

For an effective sensor assay to be built using these capsules, work has to be done to make capsules with much more uniform mechanical properties. A clear challenge is to design polyelectrolyte capsules that would allow us to measure much more sensitive capsules that can sense small changes but also push the upper limit of the force they can bear before they buckle. The capsules should also be fabricated to have lesser response to osmotic stress and have a lower elastic modulus distribution within a batch.

A much more precise mechanism like a micropipette to deliver the capsules should be designed so that we can study the uptake process more accurately and spatio-temporally. The mechanisms by which physical features of particles feed back to signal transduction pathways remain to be determined. It would be interesting to study mechano-transduction of phagocytosis using capsules with different elastic modulus.

The future work is concentrated in de-convolving the forces from the deformations observed in terms of eccentricity. Like the inhibition assays of SYK and PI3-Kinase in this work we can further silencing key unknown components in phagocytotic process. Comparing these with controls could help us understand the complex signaling networks that regulate this fundamental mechanism of the immune response.

Engineering an Anti-Inflammatory Macrophage Response Using Bioactive Nanopatterned Substrates

1. Statement of Problem

I. Background

Macrophages are specialized immune cells that have a unique role in innate immunity (non-specific) as well as in initiating specific defense response (adaptive immunity). These cells are the primary defense against foreign invasion, infection² and implant material¹⁷⁴⁻¹⁷⁶. Macrophages are also responsible for clearing dead host cells and foreign material². When a material is implanted in the human body, host response to the material is initiated. Host response starts with blood-material interaction which deposits plasma proteins on the implant surface¹⁷⁷⁻¹⁷⁹. The plasma-derived proteins primarily consist of two major opsonins, Immunoglobulin G (IgG) and the complement-activated fragment¹⁸⁰. Meanwhile, as cells in the surrounding tissue encounter the implant, a cell/tissue is triggered¹⁸⁰. This cell response consists of three stages. The first stage is inflammation¹⁸¹ - the focus of this work - followed by tissue repair and remodeling¹⁸²⁻¹⁸³. The duration and severity of the inflammatory response varies with the type and functionality of the implanted materials¹⁸⁴. A prolonged inflammatory response may eventually lead to failure of the implant^{176,185-186}. Inflammation is caused by activated macrophages at the implant site¹⁸⁰, which are considered a key regulator of the intensity and duration of inflammatory responses¹⁸⁷. *Controlling or suppressing the inflammation stage has been a central area of interest in research towards designing smart implant materials*¹⁸⁸⁻¹⁹³. Inflammation serves to contain, neutralize, dilute, or wall off the injurious agent or process. It sets into motion a series of events that may heal and reconstitute the implant site through replacement of the injured tissue.

Macrophages play a pivotal role in modulating the repair process and produce a myriad of cytokines to control wound healing and cell recruitment as well as proliferation^{187,194-195}. Macrophages exist in at least two functionally distinct phenotypes, M1 and M2 that are triggered in response to different stimuli. M1 macrophages are referred to as classically-activated macrophages and M2 as alternatively activated macrophages¹⁹⁶⁻¹⁹⁸. Classically-activated M1 macrophages are induced by interferon-gamma (IFN- γ) either alone or in concert with microbial stimuli such as lipopolysaccharide (LPS). IFN- γ in concert with cytokines such as tumor necrosis factor-alpha (TNF- α) and granulocyte macrophage colony-stimulating factor (GM-CSF)¹⁹⁹ can also lead to M1 macrophage activation. M2 is a generic label for the various forms of macrophage activation that are not the classic M1¹⁹⁹. M1 activated macrophages are efficient producers of effector molecules (reactive oxygen and nitrogen intermediates) and pro-inflammatory cytokines (IL-1 β , TNF- α , IL-6)²⁰⁰. M1 activated macrophages induce pro-inflammation which results in tissue destruction and tumor resistance. On the other hand, M2 activated macrophages induce an anti-inflammation response, secreting anti-inflammatory cytokines IL-10 and TGF- β , which leads to tissue remodeling and growth of new blood vessels (angiogenesis)²⁰¹⁻²⁰². It has been shown that macrophages stimulated by Fc receptors leads to a M2 response. Further, it was observed that in this alternatively (Fc) activated state, macrophages secrete high concentrations of anti-inflammatory IL-10, producing a robust anti-inflammatory response causing reversal of a pro-inflammatory response²⁰³.

II. Problem

There is a growing demand for artificial implants like orthopedic prosthesis, bone substitutes²⁰⁴, stents²⁰⁵, pacemakers²⁰⁶, cochlear implants²⁰⁷⁻²⁰⁸ and dental implants²⁰⁹⁻²¹¹. Approximately two million fracture-fixation devices (nails, external-fixation pins, plates, and screws) and about 600,000 joint prosthesis are inserted annually in the United States²¹².

In a healthy body, depending on the surface of the implant^{180,213}, the host reaction starts with pro-inflammation cytokines secretion which is eventually superseded by the timely secretion of anti-inflammation cytokines. These events usually create an environment for the proper integration of the implant into the tissue. During several immuno-compromised conditions like infections, diabetes, arthritis and several other non-resolving inflammatory diseases²¹⁴ where, chronic inflammation occurs when an implant is placed in individuals. The prolonged inflammatory response typical of chronic inflammation eventually leads to failure of the implant^{176,185-186}. There have been several disease models that have been shown to cause chronic inflammation and implant failure like, in diabetic patients there is more persistent inflammation with prolonged pro-inflammation cytokine secretion like TNF- α ²¹⁵⁻²¹⁶. This has multiple effects, including a tendency toward greater matrix degradation, destruction of the tissue around implants and delayed wound healing²¹⁷⁻²¹⁸. This tendency causes the implant integration in diabetic patients to fail²¹⁹ or be delayed. Likewise, in stent implants, it is known that restenosis^{205,220} or re-narrowing of blood vessels, which is responsible for restricting the blood flow and failure of the stent, is caused primarily due to the inflammation response of macrophages²²¹⁻²²². Due to these undesirable chronic inflammation responses, implants are generally built using biocompatible material like TiO₂, stainless steel or some plastic material that minimizes chronic inflammation. However, such materials have been found by trial and error and not by systematic approach that allows the control of inflammation in a predictable way¹⁹³.

The other inherent problem associated with the immune system's response to an implant is the implant's propensity to be coated by plasma proteins from the host shortly after implantation¹⁷⁸. These proteins can elicit non-specific activation of macrophages causing either M2 signaling via interactions between IgG and Fc receptors, fibrinogen with complement receptors²²³ or pro-inflammation signaling via interactions with lipoproteins like LDL²²⁴. Specific response is only possible if we can prevent these other interactions.

The success or failure of an implanted biomedical device depends on the cascade of events organized by the cytokines that are released. Several conditions exist where chronic or persistent inflammation leads to the failure of implants. Therefore, it is desirable to create a surface on the implant that would stimulate an anti-inflammatory response in order to negate or completely suppress the pro-inflammation occurring around the implant.

III. Hypothesis

We hypothesize that macrophages can be programmed to secrete high amounts of anti-inflammatory cytokines, specifically IL-10, when Fc-receptor phagocytosis is activated by macrophage interaction with surfaces coated with Fc fragments.

Further, it is hypothesized that macrophage cytokine production can be modulated by changing the concentration of the Fc coating on an implant surface.

IV. Rationale

Macrophages play a central role in modulating the wound repair process, mediating phagocytosis, by producing a myriad of cytokines which control wound healing and cell recruitment as well as proliferation^{176,187,194-195} around implanted biomedical devices^{184,190,211,225}. It was previously demonstrated that stimulation of macrophage's Fc receptors generates IL-10, leading to a reversal of macrophage pro-inflammatory response²⁰³. IL-10 plays an auto-regulatory role inhibiting (pro-inflammatory) cytokine synthesis²²⁶ and promotes healing²²⁷. IL-10 a potent anti-inflammatory cytokine²²⁸ is known to switch-off of an already activated M1 macrophage²²⁹⁻²³¹ and remove the consequent pro-inflammatory sequel including tissue destructive reactive oxygen species and nitric oxide^{202,232}.

By coating surfaces with Fc fragments, we can expect to stimulate macrophages to activate into M2 phenotype. These cells can then act as immunomodulatory and pro-healing by producing anti-inflammatory cytokines.

V. Objective

The main objective of this work is to engineer a method that elicits a site-specific anti-inflammatory response from macrophages via Fc-receptor activation. To achieve this goal, we have developed an approach to nanopattern large arrays of Fc fragments with well-defined concentration based on micellar nanolithography²³³⁻²³⁵. Inflammatory response and macrophage activation will be monitored using a combination of ELISA to monitor cytokine production and cell spreading area, which is related to the activated macrophage state^{200,236}. With these approaches, there are three aims that will help accomplish the main objective:

- To demonstrate that Fc-fragment covered surface can induce an anti-inflammatory response in macrophages.
- To optimize the anti-inflammatory response of macrophages by varying surface coverage presented by both nanopatterns and standard surfaces.
- To correlate cell spreading area of M2 macrophages with the degree of macrophage activation determined by ELISA.

VI. Significance

This work would help us achieve bioactive surfaces that can induce macrophages to secrete anti-inflammation agents. Smart bioactive surfaces like these can help people with a propensity for chronic inflammation, minimizing the need for external immunosuppressive agents²³⁷ or steroids²³⁸⁻²³⁹.

2. Literature Review

I. Macrophage Phenotypes M1 and M2, the Killer and Healer Cells

Macrophages respond to stimuli and exist in at least two distinct phenotypes, classically activated (M1) macrophages and alternatively activated (M2) macrophages. Classically activated, M1 or “killer” macrophages produce pro-inflammatory cytokines and act as effectors of cell killing. Alternatively activated M2 or “healer” macrophages on the other hand are responsible for tissue remodeling, repair and act to dampen pro-inflammatory response.

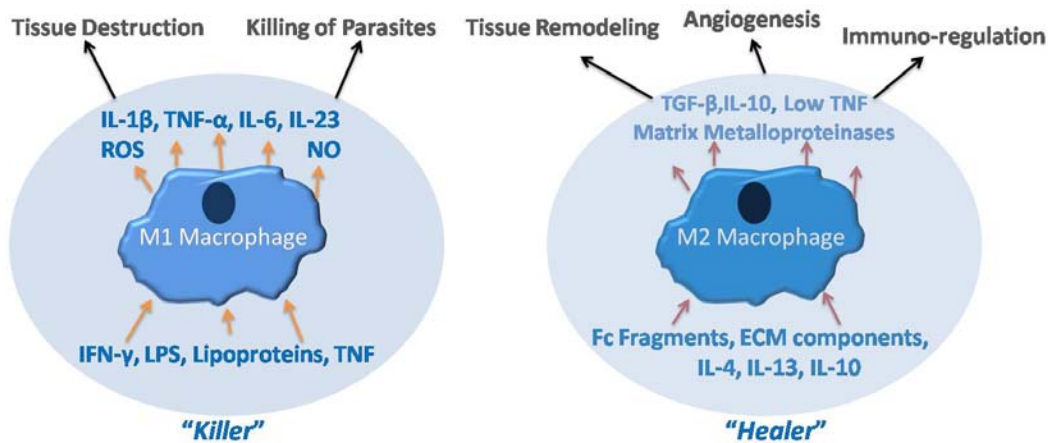


Figure 20 Schematic showing key properties and functions of the two different macrophage phenotypes M1 and M2. Macrophages acquire different functional properties in response to environment-derived stimuli and express different cytokines.

As shown in Figure 20, classically activated M1 macrophages are induced by interferon-gamma (IFN- γ) either alone or in concert with microbial stimuli such as lipopolysaccharide (LPS). IFN- γ in concert with cytokines such as tumor necrosis factor-alpha (TNF- α) and granulocyte macrophage colony-stimulating factor (GM-CSF)¹⁹⁹ can also lead to M1 macrophage activation. M1 activated macrophages are efficient producers of effector molecules (reactive oxygen and nitrogen intermediates) and pro-inflammatory cytokines (IL-1 β , TNF- α , IL-6)²⁰⁰, these cells induce inflammation which results in tissue destruction and tumor resistance. Thus, once macrophages are M1 activated by either IFN- γ or LPS, they become fully equipped to attack and destroy.

M2 is a generic label for the various forms of macrophage activation that are not the classic M1¹⁹⁹. M2 activated macrophages induce an anti-inflammation response, secreting anti-inflammatory cytokines IL-10 and TGF- β , which leads to tissue remodeling and growth of new blood vessels (angiogenesis)²⁰¹⁻²⁰². It was observed by Sutterwala *et. al.*²⁰³ that in this alternatively (Fc) activated state, macrophages secrete high concentrations of anti-inflammatory IL-10. Although the precise mechanism by which Fc ligation induces IL-10 and anti-inflammation is not clear, it is known that IL-10 induces the expression of the protein, suppressor of cytokine signaling 3 (SOCS-3)²⁴⁰⁻²⁴¹, a potent inhibitor of pro-inflammation^{226,231,241}.

3. Materials and Methods

I. APTES Treatment

3-aminopropyltriethoxysilane (APTES) was used to derivatize amino groups on glass slides. APTES has an NH_2 group on one end that is coupled to glass through the silane group present on the other end. Prior to APTES treatment, glass slides were cleaned in piranha solution (mixture of sulfuric acid (H_2SO_4) and hydrogen peroxide (H_2O_2) in ratio of 3:1. Piranha treatment of glass slides leads to removal of organic matter present on the slides and will create an extremely hydrophilic surface with a high density of hydroxylate groups (OH). Piranha cleaned glass slides were then silanized by treatment with APTES (Sigma-Aldrich) see schematic in Figure 21. Slides were rinsed twice with acetone to remove any moisture or residual water and immersed in a solution of 2 vol% APTES ($\text{C}_9\text{H}_{23}\text{NO}_3\text{Si}$) in acetone for 30 min at room temperature. Slides were then rinsed twice with acetone to remove unreacted silane and twice with deionized water. The slides were finally dried and baked at 120°C for 30 min to anneal the silane coating on the glass slides.

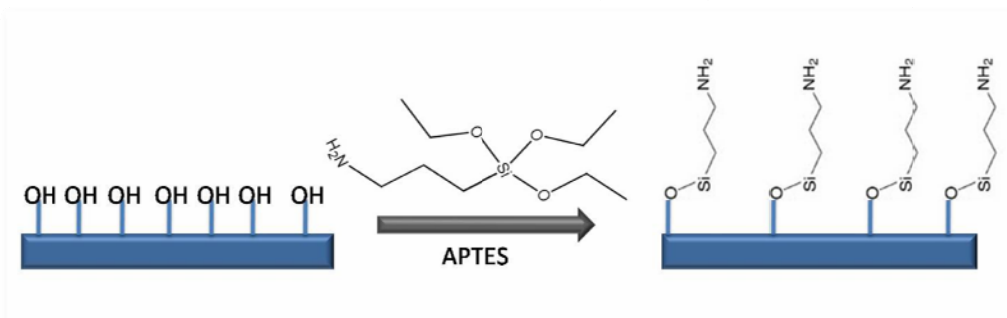


Figure 21 Schematic of amine derivatization on glass using APTES treatment.

II. Fc Fragment Modification and Chemical Characterization

Fc fragments of IgG (mouse) obtained by pepsin digestion were purchased from Rockland Inc, USA. As shown in the schematic in Figure 22, in order to modify and add sulfhydryl group (SH) to the Fc fragment, we used *N*-Succinimidyl 3-(2-pyridyldithio)-propionate (SPDP). SPDP is a bi-functional; amine- and sulfhydryl-reactive crosslinking agent that reacts with the amine present on the Fc and leaves a protected SH group (pyridyl disulfide). The reaction was performed in pH 8, 0.1 M phosphate buffer with 0.01 M ethylenediaminetetraacetic acid (EDTA) for 12 hours. Dialysis was performed to purify the Fc fragment from the excess SPDP. The dialysis buffer constituted 0.1 M phosphate buffer with 0.01 M EDTA at pH 7. To remove excess oxygen that can hydrolyze the SH, the buffers were degassed before the experiments were performed. The protective group pyridyl disulfide is deprotected to create SH groups by the addition of 25 mM dithiothreitol (DTT). To remove the excess DTT, dialysis was performed in 0.1 M phosphate buffer with 0.01 M EDTA at pH 7.

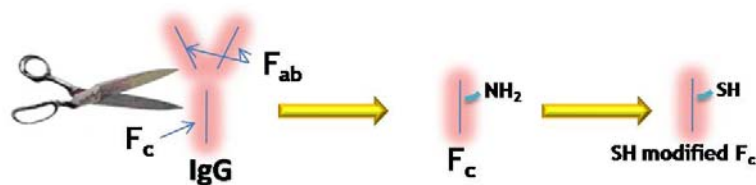


Figure 22 Schematic showing Fc fragment of IgG and modification of the fragment to create SH on it

In order to determine the amount of SH created on the Fc fragment, we used Ellman's reagent (also referred to as Dithionitrobenzoic acid, 5,5'-Dithiobis(2-nitrobenzoic acid) or DTNB). DTNB is a chemical used for measuring the amount of free thiol groups. SH reacts with DTNB cleaving the disulfide bond to give 2-nitro-5-thiobenzoate (NTB⁻), which ionizes to the NTB²⁻ dianion in water at neutral and alkaline pH. Ellman's reagent produces NTB²⁻ ions, a measurable yellow colored product when it reacts with free sulfhydryls²⁴²⁻²⁴³. This reaction is rapid and stoichiometric with every SH corresponding to one mole of NTB²⁻²⁴⁴. The NTB²⁻ is quantified using a UV/VIS spectrophotometer by measuring the absorbance of visible light at 412 nm, using an extinction coefficient of 13,700 M⁻¹ cm⁻¹.

The amount of thiol (SH) groups present on the SH modified Fc fragment was 3.0576 X 10⁻⁴ M (moles/liter). This is approximately 1:1 in ratio to the amount of protein, showing that there is approximately 1 SH group per Fc fragment. The Ellman's test performed here showed that we have successfully modified the Fc fragment to create SH groups.

III. Cell Culture

i. Cell Culture

The murine macrophage cell line, J774A.1, Mouse BALB/c (TIB-67, American Type Culture Collection, Rockville, MD) was routinely maintained in Dulbeccos Modified Eagles Medium (DMEM, Mediatech Inc, USA) supplemented with 10 vol % fetal bovine serum (Mediatech Inc, USA) and a 2 mM L-glutamine. The cells were always maintained at 37°C in a humidified atmosphere of 5% CO₂ in air. Cells were passaged by scrapping, centrifuging and resuspending in fresh medium. All experiments were performed with cells between passage numbers 1-10.

To determine the cell number and the number of vital cells used in the experiments, a cell suspension in DMEM was diluted 1:10 in a 0.05% trypan blue (VWR) solution in deionized water. This colored substance enters and stains only dead cells. The cell suspension in trypan blue was transferred into two hemocytometer chambers (Neubauer counting chamber). Using a 10x objective and light microscopy, the cells were counted in 8 fields (each field having an area of 1mm²) and the average number of cells per volume (ml) was calculated (excluding cells stained in blue which are dead).

ii. Fixing Cells

Slides containing cells were washed with cell culture media and then filled with 3% glutaraldehyde (Electron Microscopy Science Inc, Catalogue #16310) solution in distilled water. Treating cells with glutaraldehyde leads to the establishment of chemical cross-links between free amino groups²⁴⁵. When the cross-links join different molecules, a latticework of

interactions occurs that holds the overall architecture of the cell together. After extensive washing with PBS, the coverslips were mounted in Elvanol to inhibit oxidation and photobleaching.

iii. Cell Membrane Labeling and Quantification

Cell membrane was visualized using wheat germ agglutinin (WGA) attached to a fluorescent dye. Wheat-germ agglutinin is a lectin with specificity for N-acetylglucosamines present on the cell surfaces²⁴⁶. Lectins like WGA are versatile probes for detecting glycoconjugates present on the cell membrane²⁴⁷. The WGA that was used was conjugated fluorescently with Alexa Fluor 594 and was purchased from Invitrogen Inc. In order to label the cell membrane of the fixed J774a.1 cells, 5 $\mu\text{g}/\text{ml}$ of WGA concentrate (5 mg/ml) solution was diluted in PBS and the slides were incubated in this solution for 15 minutes. Once the cells were labeled, the excess WGA was removed by extensive rinsing with PBS. Figure 23 is an epi-fluorescence image of a J774a.1 cell labeled with WGA. In order to quantify the area of the cell, a threshold was manually applied to the fluorescent cell. This allowed us to outline the cell area from the background. Once the cell area was outlined, a home built MATLAB algorithm quantified the number of pixels in the outlined area of the cell.

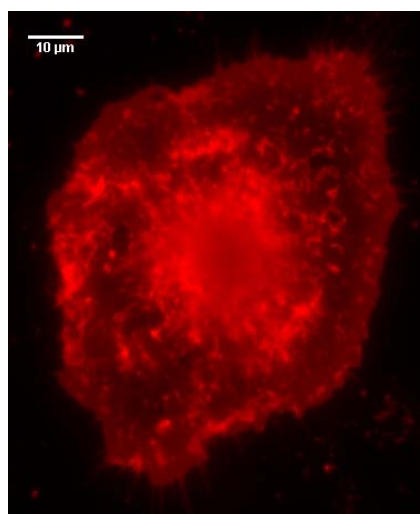


Figure 23 Epi-fluorescence image of J774a.1 cell labeled with WGA.

IV. Enzyme-linked Immunosorbent Assay (ELISA)

ELISA is a sensitive immunoassay that uses an enzyme linked to an antibody or antigen as a marker for the detection of a specific protein, especially an antigen or antibody. This technique can be used as a diagnostic tool, a qualitative and quantitative tool in determining unknown antigens in solutions. All ELISA kits were purchased from eBioscience, Inc. As shown in the schematic Figure 24, in order to determine the cytokine concentration in harvested cell culture media, the microtiter plates were coated with the appropriate antigen and the unbound sites and free sites on the microtiter plates were blocked with BSA to prevent false positive results. The cell culture media was then added to the wells and after a thorough wash, the antibody conjugated with biotin was added. This was then followed by avidin horseradish peroxidase (HRP). 3, 3', 5, 5'- tetramethylbenzidine (TMB) is a soluble

colorimetric substrate solution for HRP. When TMB is added in the presence of HRP it reacts to produce a blue by-product. The color intensity is proportional to the amount of HRP activity which in turn is proportional to the concentration of the protein in the solution. Finally, two Normal (2N) sulfuric acid (H_2SO_4) was added to stop the reaction. Sulfuric acid changes the blue colored solution to yellow, enabling accurate measurement of the intensity at 450 nm using a plate reader.

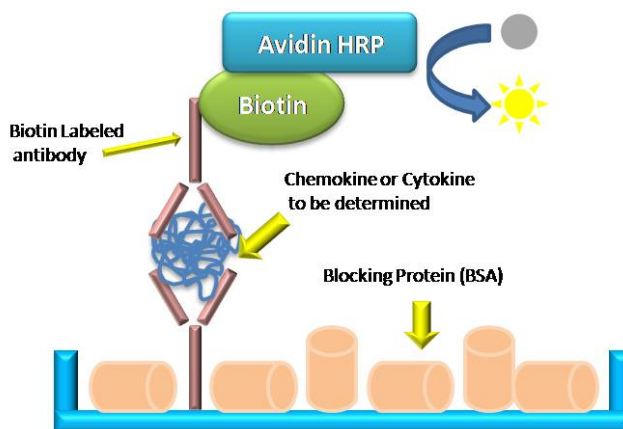


Figure 24 Schematic of the ELISA procedure

V. Optical and Atomic Force Microscopy

Epi-fluorescence microscopy was performed on an inverted Nikon TE2000 microscope equipped with a Nikon intensilight (C-HGFIE) for illumination and a Nikon EMCCD camera (DQC-FS). Images were obtained using a Plan Apo 60x water immersion objective (Nikon, NA 1.2) or a Plan Apo 100x oil immersion objective (Nikon, NA 1.4). Nikon filter cube sets were used to image fluorescent dyes in the region of UV (#96310, UV-2EC DAPI filter set, excitation 340-380 nm, dichroic mirror DM400, emission 435-485 nm), in the green (#96320, FITC/GFP HyQ filter set, excitation 460-500 nm, dichroic mirror DM505, emission (510-560 nm), and in the red (#96324, Cy5 HQ filter set, excitation 620-660 nm, dichroic mirror (DM Q660LP, emission 700-775 nm).

Imaging, friction and phase measurement of the nanostructures was performed on a Nanoscope Multimode IV, atomic force microscope (AFM) from Veeco. The AFM topography and phase images were recorded in ambient conditions using an ultra sharp AFM tip (Nanosensor, SSS-NCHR, resonant frequency 312 kHz, spring constant 37 N/m) at a drive frequency close to its resonance frequency.

VI. Quartz Crystal Microbalance (QCM)

The Quartz Crystal Microbalance (QCM) is very sensitive to changes in weight and thus is a helpful method for detecting adsorption processes at solid/gas or solid/liquid interfaces. The basis of the QCM is a thin quartz crystal exhibiting the inverse piezoelectric effect. Applying an alternating current to the crystal excites a mechanical oscillation of plate. Changes in the specific resonance frequency of the quartz are directly proportional to its mass load. The quartz crystal microbalance is an extremely sensitive sensor capable of

measuring mass changes down to 18 nanogram/cm² with a wide dynamic range extending into the 100 g/cm² range. This effect was first discovered by G. Sauerbrey in 1959. The results of his work are embodied in the Sauerbrey equation, which relates the mass change per unit area at the QCM electrode surface to the observed change in oscillation frequency of the crystal

$$\Delta_F = -C_F X \Delta_M \quad \text{Equation 4}$$

Where

- Δ_F = Observed frequency change in Hz,
 Δ_M = Change in mass per unit area, in ng/cm²,
 C_F = Sensitivity factor for the crystal (56.6 Hz g⁻¹ cm² for a 5 MHz crystal at room temperature).

All measurements were performed using the QCM 200 sensor system from Stanford Research Systems (SRS). The crystals were then mounted onto a flow chamber system. A flow rate of 50µl/min was maintained throughout the experiment. The experiments were performed at room temperature. To maintain a steady flow, an injection flow system was used. The Sauerbrey equation was used to measure the adsorbed mass. The QCM is capable of monitoring frequency changes Δ_F in a time resolved manner. Δ_M is associated with the adsorbed mass Δ_M . According to the Sauerbrey equation a Δ_F of 1Hz for the sensor chip we used with the QCM 200 correlates with a Δ_M of 18ng/cm². The 5 MHz, 1" diameter, AT-cut quartz crystal had gold coating on them. In order to interface the QCM with a flow injection system we used an axial flow cell adapter attached to a standard crystal holder. To achieve a flow we used a syringe pump connected with 1/8" tygon tubing and maintained a constant flow rate of 50µl/min.

VII. Ellipsometry

Ellipsometry is a useful instrument to determine the thickness of thin films. Ellipsometry measures a change in polarization as light reflects or transmits from a material structure. The film thickness is determined by interference between light reflecting from the surface and light traveling through the film. A VASE ellipsometer from J.A. Woollam Co, Inc. was used for the measurements. The data acquired was modeled and analyzed using WVASE32 from J.A. Woollam Co, Inc.

Since Fc bound on the gold surface can be considered as an absorbing material on a highly reflective surface. We modeled the surface using Cauchy's relationship. It was assumed that there was no anomalous dispersion and the data was taken from visible wavelength region. The equation below shows Cauchy's relationship. The three terms A, B, C are coefficients that can be determined for a material by fitting the equation to measured refractive indices at known wavelengths. n is the refractive index, λ is the wavelength.

$$n(\lambda) = A + \frac{B}{\lambda^2} + \frac{C}{\lambda^4} \quad \text{Equation 5}$$

VIII. Block Copolymer Lithography

In the present work we nanopatterned the Fc fragments by using nanostructured substrates obtained by block copolymer micellar nanolithography. Block copolymer micellar nanolithography is an excellent tool for the fabrication of nanostructured surfaces²⁴⁸⁻²⁴⁹. The accessible length scale is below 100 nm²⁵⁰.

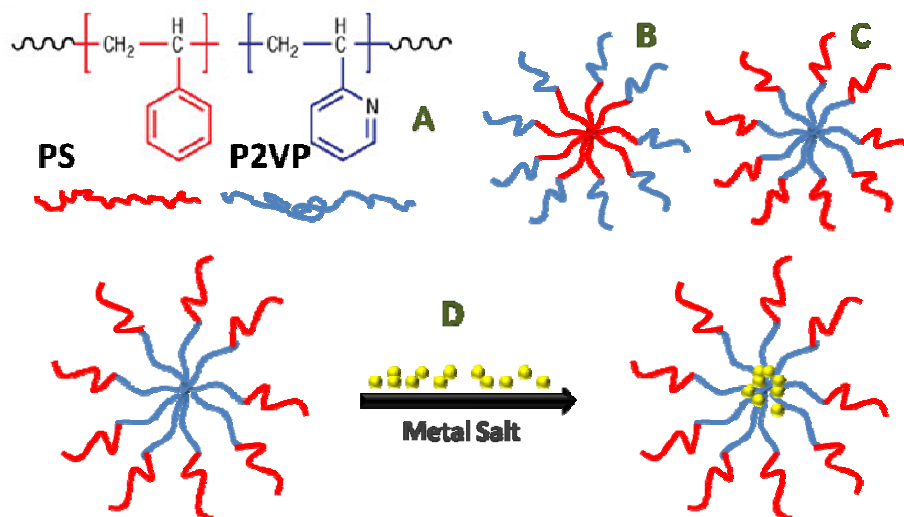


Figure 25 (A) Schematic illustration of a diblock copolymer with distinct hydrophobic (PS, red portion) and hydrophilic part (P2VP, blue portion). (B) and (C) Schematic representations of a micelle and a reverse micelle with the polar components on the outside and inside respectively. (D) Schematic illustration of a reverse micelle loading mechanism. The metal salt selectively enters into the polar micelle core.

A diblock copolymer consists of two chemically different chains²⁵¹. A micelle is a structural unit composed of a group of molecules. Micelle formation occurs when the diblock copolymer is dissolved in a solvent, which is selective for one of the blocks. In the present work we used a micelle structure comprising of hydrophobic polystyrene and hydrophilic poly-2-vinylpyridine unit. As shown in the Figure 25, a typical micelle in aqueous solution forms an aggregate with the hydrophilic "head" regions in contact with surrounding solvent, sequestering the hydrophobic tail regions in the micelle center²⁵²⁻²⁵⁵. The process of forming micelles is known as micellization. Figure 25 B is a schematic illustration of a micelle with its hydrophilic head (poly-2-vinyl pyridine, P2VP) on the outside and a reverse micelle with its hydrophilic head on the inside (C). The diameter of the micelles is controlled by the molecular weight of the block copolymers, the interactions between the polymer blocks and the interaction between the blocks with the solvent. If the blocks that form the core of the micelle or the dispersed domains are polar and able to interact with a transition metal compound, the latter can be selectively incorporated within the micelles or the domains²⁵⁶. Tetrachloroauric acid (HAuCl_4) a gold salt was used as a metal precursor that diffuses inside the core of the micelles²⁵⁷. To achieve a homogeneous distribution of the gold ions inside the micelles, constant stirring is required. The gold ions present in the micelles create nanoparticles when plasma treated. The size of the gold nanoparticles is controlled by the amount of metal precursor added to the micellar solution²⁵⁶.

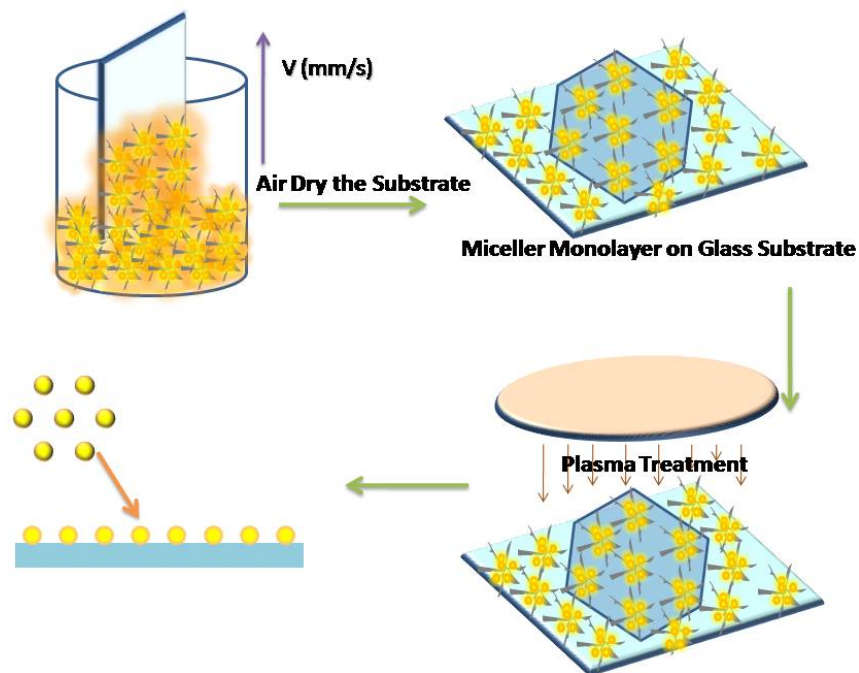


Figure 26 Schematic of the micellar nanopatterning approach. Glass substrates are dipped in the micellar solution at a constant speed. A monolayer of micelles is coated on the surface by dipping and removing the surface in a solution of micelles at a specific speed. The Surface is then air dried and plasma etched to remove the organic components present on the surface of the substrate, resulting in Au nanoparticles being organized in hexagonal order.

As shown in the Figure 26, In order to achieve a micellar monolayer we perform dip coating. In dip coating, the substrate is dipped into a micellar solution leading to the formation of a uniform micellar coating with a polymer brushlike structure^{251,258} on the surface of the substrate. During the retraction of the substrate out of the micellar solution, the micelles form a monolayer on the substrate and self assemble into a quasi-hexagonal order. This quasi-hexagonal pattern of the micelles is reflected in the pattern of the nanoparticle arrays. The driving force is the evaporation of the toluene at the immersion edge. Capillary forces, steric interactions, and electrostatic repulsion influence the final formation of the micelles on the surface²⁵⁹. During the dipping process the substrate is moved with a constant velocity. It is then treated by hydrogen or oxygen plasma, which leads to a reduction of the metal precursor to the elementary metal or metal oxide followed by the complete removal of the polymer matrix²⁶⁰⁻²⁶¹. The size of the resultant nanoparticles is controlled by the amount of salt introduced into the unloaded micelle solution, while the length of the polymer chain controls the distance between the nanoparticles²⁶⁰⁻²⁶¹. The distances between gold nanodots are varied by using diblock copolymers of different molecular weight. The average size of the gold nanodots is 8 nm.

Block copolymer micellar nanolithography has been successfully applied on many different substrates, such as glass and mica²⁶²⁻²⁶³. The only requirement for the substrate is that the material is stable in the solvent, which is in this case toluene and that it resists the plasma conditions.

IX. PEG Passivation

To ensure that cell-surface interactions on the nanopatterned surface are confined to bio-functionalized sites (i.e. the gold nanoparticles) the area in between the particles needs to be made inaccessible to cells. A substance which has proven to be useful to inhibit cell-surface interactions is poly(ethyleneglycol) (PEG)^{93,235,264-274}. PEG-derived materials are generally considered to be extremely effective in preventing non specific adsorption^{93,265}. Its capabilities in protein repellency, inhibition of unspecific interactions and bio-compatibility are widely used. In order to prevent protein adsorption in the area between the gold particles, PEG passivation using mPEG 2000-urea (methoxy polyethylene glycol triethoxysilane, Figure 27) was performed. The PEG molecule had a chain length of $n = 43$ and a molecular weight of 2000 Dalton. This molecule was designed to react with the OH (hydroxyl) groups of the glass substrate. Using x-ray photoelectron spectroscopy (XPS), Blummel *et. al*²⁷⁵ found that the PEG layer formed when this molecule was bound to glass is ~2nm in its dry state and when hydrated it was ~5nm. The block copolymer patterned glass slides were briefly plasma treated to remove any organic matter that could have bound during the storing process. The slides were then transferred to a flask that was pre heated to remove any moisture and filled with 25 mM PEG in dry toluene. The flask was filled with nitrogen and heated to 60°C while constantly stirring for 24 hours. The slides were finally rinsed with toluene, ethyl alcohol, ethanol and water respectively.

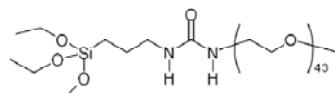


Figure 27 Chemical structure of mPEG 2000-urea

X. Fc Fragment Nanopatterning Strategy

In order to nanopattern Fc fragments, we used block copolymer nanopatterned gold particles on glass substrate as a template. The substrate obtained from this procedure allowed us to have gold particles in regular hexagonal order whose lattice could be precisely controlled. The gold particle substrates we used for the experiments had 30 nm, 60 nm, 80 nm and 125 nm of lattice spacing. The space between the gold particles can be a hindrance to the usage of these substrates for cell experiments. It is particularly troublesome for the immune cell experiments as proteins from the serum can non-specifically bind to the glass substrate between the dots and provide additional unwanted stimuli. In order to prevent this we passivated the space between the gold particles with PEG. mPEG 2000-urea was used to passivate. As shown in the schematic in Figure 28, finally to obtain the Fc fragment patterned substrates, SH modified Fc fragments (400 µg/ml in PBS) were incubated with the PEG passivated block copolymer patterns for 12 hours at 4°C.



Figure 28 Schematic of Fc protein patterning strategy.

4. Results and Discussion

I. Characterization of the Nanopatterned Bio-Interfaces for Macrophage Studies

The goal of the present work is to elicit macrophages to generate anti-inflammation cytokines by activating the cells with Fc fragments bound on the surface. We also investigate if changing Fc fragment concentration can differentially modulate the anti-inflammation cytokine production. Since quantifying the amount of Fc fragment present on glass slides is critical, we have determined how the amount of Fc concentration incubated in the solution relates to the amount of protein that is chemically bound to the surface.

In order to elicit a defined response from the macrophages, we present Fc fragments in a well defined and highly ordered nanopattern with PEG passivation in between the Fc fragments using block copolymer micellar nanolithography. A SH group was added to the Fc fragment to allow binding of the Fc fragment to gold nanoparticles in the nanopatterns. The binding of the SH modified Fc fragment to gold and its bioactivity was confirmed with QCM and Ellipsometry. The PEG passivation between the Fc fragments will prevent any non specific adsorption. To verify PEG passivation, we performed Fourier transform spectroscopy (FTIR) and Contact Angle Goniometry.

i. QCM Study of SH Modified Fc Binding to Gold and Its Bioactivity

Extensive chemical modifications of proteins can severely affect the protein function and bioactivity²⁷⁶⁻²⁷⁸. In order to verify that the SH modified Fc fragment binds to gold and further test its bioactivity, we employed the quartz crystal microbalance (QCM)²⁷⁹⁻²⁸¹ technique.

The resonance frequency of quartz decreases when material attaches to the electrode's surface as described by Sauerbrey's equation. The crystals used had gold coating on the surface. Phosphate buffer saline (PBS) was flown over the crystal chip followed by SH modified Fc fragment in PBS. As shown in the yellow region of Figure 29, the signal stabilizes after 40 minutes of flow of the SH modified Fc fragment. There was a change of approximately 26 Hz. The binding confirms that the modified Fc fragment binds to gold, which is an important criterion for patterning Fc fragments using gold nanoparticle templates. In the pink region in Figure 29, anti-Fc antibody was flown. If the modified and now bound Fc fragment is functionally bioactive, it should recognize and bind to the antibody. The anti-Fc stable signal in pink region shows antibody binding to the Fc fragment. There was approximately a change of 71 Hz in the pink region showing that anti Fc binds to the modified Fc fragment. This shows that the modified Fc fragment is bioactive. The mass of the Fc fragment is slightly more than 1/3rd the mass of IgG. $\Delta f \sim \text{mass}$ and the ratio of $\Delta f_{\text{Fc fragment}} : \Delta f_{\text{anti-Fc}}$ is 26 : 71 which is approximately 1:3. This ratio of 1:3 is consistent with the binding of one anti-Fc to each modified Fc fragment bound to the surface.

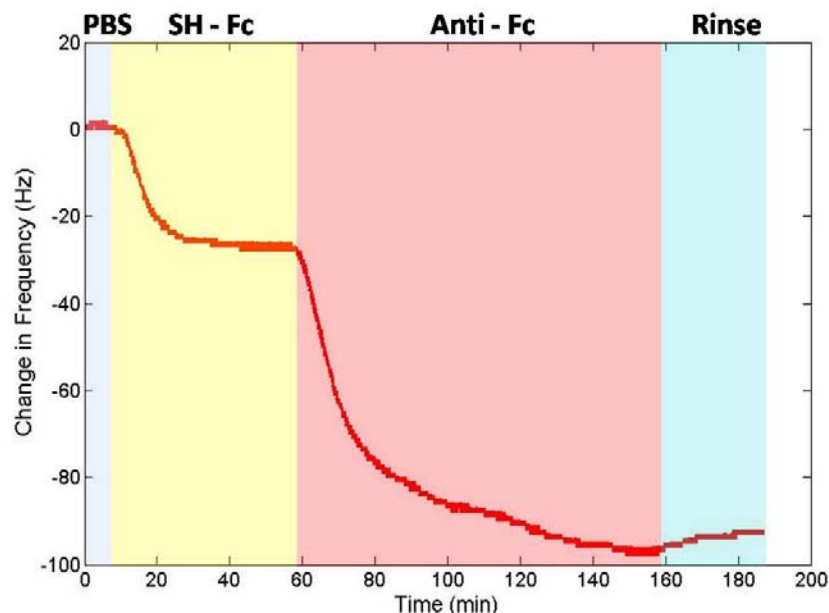


Figure 29 QCM graph displaying SH modified Fc binding to a gold film, followed by a bioactivity test. Initially PBS was flown (grey region) followed by thiolated Fc fragment. The equilibrium in yellow region shows the thiolated Fc binding to gold surface of the QCM crystal. Anti-Fc binding in the pink region shows that the thiolated Fc fragment is bioactive. The blue region shows the rinse cycle.

ii. Ellipsometry Confirmation of the Fc Bound to Gold

Ellipsometry is a powerful tool for studying protein adsorption on surfaces²⁸²⁻²⁸⁶. Ellipsometry measures the change of polarization upon reflection. The exact nature of the polarization change is determined by the sample's properties i.e. refractive index and thickness. While most of the optical techniques have a problem with the diffraction limit of light, ellipsometry exploits phase information and the polarization state of light which allows it to achieve angstrom resolution. The ellipsometric measurements were performed on a rotating analyzer ellipsometer (J A Woollam Co.) operating in the 400–1000 nm wavelength region with an angle of incidence of 65°, 70° and 75° (for further information regarding the ellipsometer refer to materials and methods).

In the present work, ellipsometry was used to confirm the modified Fc binding to gold by measuring the height change or thickness of Fc bound to gold. The gold QCM crystal from which data in Figure 29 was obtained was dried using a nitrogen blow gun. For modeling the data we considered a non-transmitting thin film of gold on which we considered the formation of Fc – anti-Fc complex film. To model the Fc - anti-Fc complex, we used Cauchy's dispersion model^{282,287-288}. Cauchy's equation is an empirical relationship between the refractive index and wavelength of light for a particular transparent material like protein and polymer films²⁸⁴⁻²⁸⁵. Since the surface roughness of the substrate affects the measured ellipsometric angle (Δ , Ψ), the optical model was established as a two phase layer model composed of gold, Fc - anti-Fc complex. The model fit showed that there was approximately 5.4 nm in thick film which corresponds to a layer of Fc and anti Fc on it within the error due to denaturation. The thickness we measured is in good agreement with values previously shown by Bae *et. al*²⁸⁹ who worked on thiolated IgG - anti-IgG complex bound to gold.

iii. Fourier Transform Infrared Spectroscopy (FTIR) to Verify PEG Passivation

Attenuated Total Reflection Infrared (ATR-FTIR) spectroscopy is used for analysis and identifying chemicals that are either organic or inorganic on the surface of materials. In attenuated total reflection infrared (ATR-FTIR) spectroscopy, infrared radiation is passed through an infrared transmitting crystal with a high refractive index, allowing the radiation to reflect within the ATR element several times. The spectra of mPEG 2000-urea bound on glass substrate was obtained by Fourier Transform Infrared Spectroscopy (FTIR) on a Perkin Elmer Spectrum 1000 FT-IR spectrometer equipped with the Perkin Elmer Fixed Angle Specular Reflectance accessory in a N₂ atmosphere in Attenuated Total Reflectance (ATR) mode. A diamond crystal was used as an ATR crystal material.

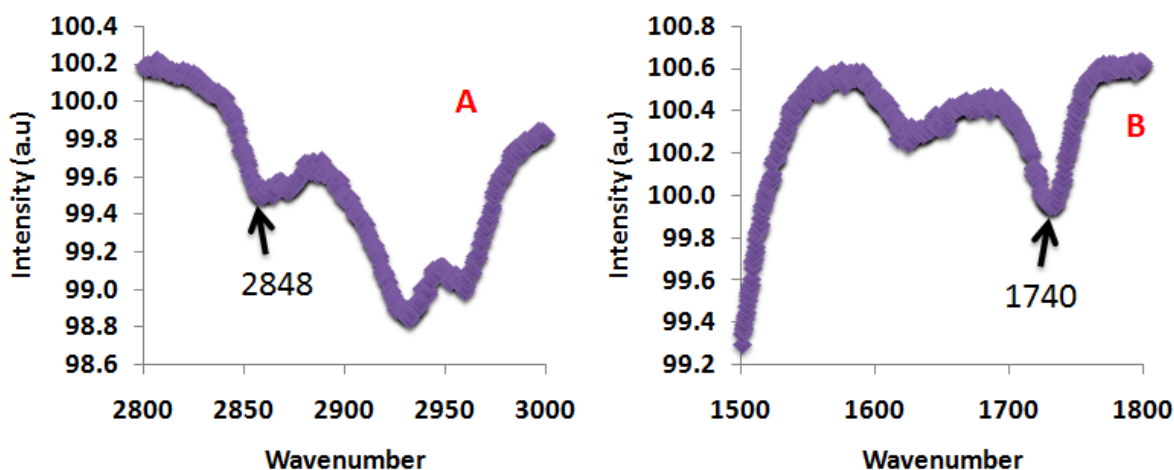


Figure 30 FTIR graph on PEG silane bound glass substrate. (A) Spectral range of carbonyl groups (C=O) and (B) Spectral range for C-H groups present on mPEG 2000-urea.

From Blümmel *et. al.*²⁹⁰ we know carbonyl (C=O) and CH₂ (C-H) groups are abundant in mPEG 2000-urea. It is known from Colthup *et. al.*²⁹¹ that CH₂ has a peak at 2870–2860 cm⁻¹. It can be seen from Figure 30A that in the FTIR spectra of PEG silane bound on glass there are C-H bond peak at 2848. As seen in Figure 30B the C=O peak²⁹¹ corresponding to carbonyl groups was also present at 1740 cm⁻¹. Since the mPEG 2000-urea present on the surfaces is around 2 nm in dry state²⁷⁵, a strong influence of the underlying silicon substrate was recorded in the spectra which was evident from the spectra recorded below 1500 cm⁻¹.

iv. Contact Angle Goniometry to Verify PEG Passivation on Nanopatterns

In order to check that we passivate the nanostructures with PEG, we performed contact angle measurements on the nanostructured surface before and after PEG passivation.

The contact angle is a quantitative measure of the wetting of a solid by a liquid. The contact angle is specific for any given system and is determined by the interaction across the solid–water interface. The shape of the droplet is determined by the Young Relation²⁹². The contact angle plays the role of a boundary condition. The wettability of a surface is determined by the outermost chemical groups present on the surface of the solid. It is known that PEG decreases the contact angle since it increases the hydrophilicity of surfaces²⁷⁴.

Static water contact angle measurements were determined at ambient laboratory temperatures with a Phoenix 150 from Surface Electro Optics Inc. To measure the contact angle, ultra pure deionized water from Fischer Scientific was used. The reported contact angle values, for all the tested polymer surfaces including the PEG functionalized substrates, are the average of 6 different measurements taken from different points on the same substrate. Further, the value of the angle was the average of advancing (θ_a) and receding (θ_r) contact angles of the water drop, which on a homogenous surface should be identical within error.

It was previously shown by Papra *et. al.*²⁶⁸ that ultrathin Poly(ethylene glycol) monolayers bound using PEG silane on pure silicon substrates have a contact angle between 36° - 39° . Figure 31 shows the contact angle measured on our 125 nm spaced nanopatterns before and after PEG passivation using mPEG 2000-urea (for PEG passivation procedure refer to materials and methods). The average contact angle before passivation was $73^\circ \pm 3^\circ$. After PEG passivation the contact angle decreased to $46^\circ \pm 1^\circ$. It is known from previous observations from Huang *et. al.*²⁹³ that block copolymer nano pattern substrates are hydrophobic and they increase the contact angle. The increase in observed angle from 39° by Papra *et. al.*²⁶⁸ to 46° observed by us may be due to the interference of gold nanopatterns on the substrates. The decrease in contact angle shows that we have successfully passivated the nanostructured surfaces.

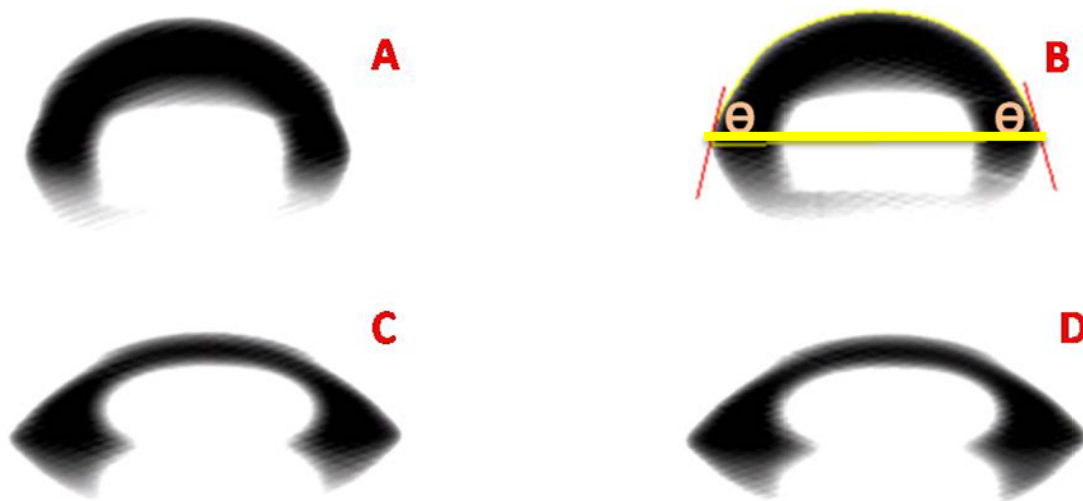


Figure 31 Contact angle on a 125 nm spaced nanopattern before (A, B) and after (C, D) PEG passivation. The hydrophilic nature of PEG can be seen in the PEG passivated nanostructures in Figure C and D. The red and yellow line shown in Figure B displays the contact angle measuring procedure.

v. AFM Conformation of Fc Fragment Binding to the Patterned Gold Dots

Although we have shown modified Fc binding to gold with QCM, ellipsometry and have shown that we can effectively passivate the nanostructured surfaces with PEG, It would be reassuring to directly visualize that there is no non specific adsorption between the dots and the modified Fc binds to the gold dots. In order to directly visualize we used AFM imaging in tapping mode. This would help us visualize if there are any Fc fragments non-

specifically bound between the gold particles. Further we performed topography or surface roughness analysis to determine if the Fc portion was bound to the gold particles. If Fc is bound on the gold, we should be able to see a change in height due the Fc portion binding.

The gold particles in block copolymer patterns were 8nm in height. On the right side of Figure 32, we can see Fc coated block copolymer nanostructures that were previously PEG passivated. Once coated with the Fc fragment there was a change of approximately 1 nm which is the size of dry Fc considering it 1/3rd the size of an ordinary IgG²⁹⁴⁻²⁹⁵. It has to be noted that in this particular sample, as seen from the images, there were a lot of defects in the hexagonal order. These defects may be due to extended storage of the sample.

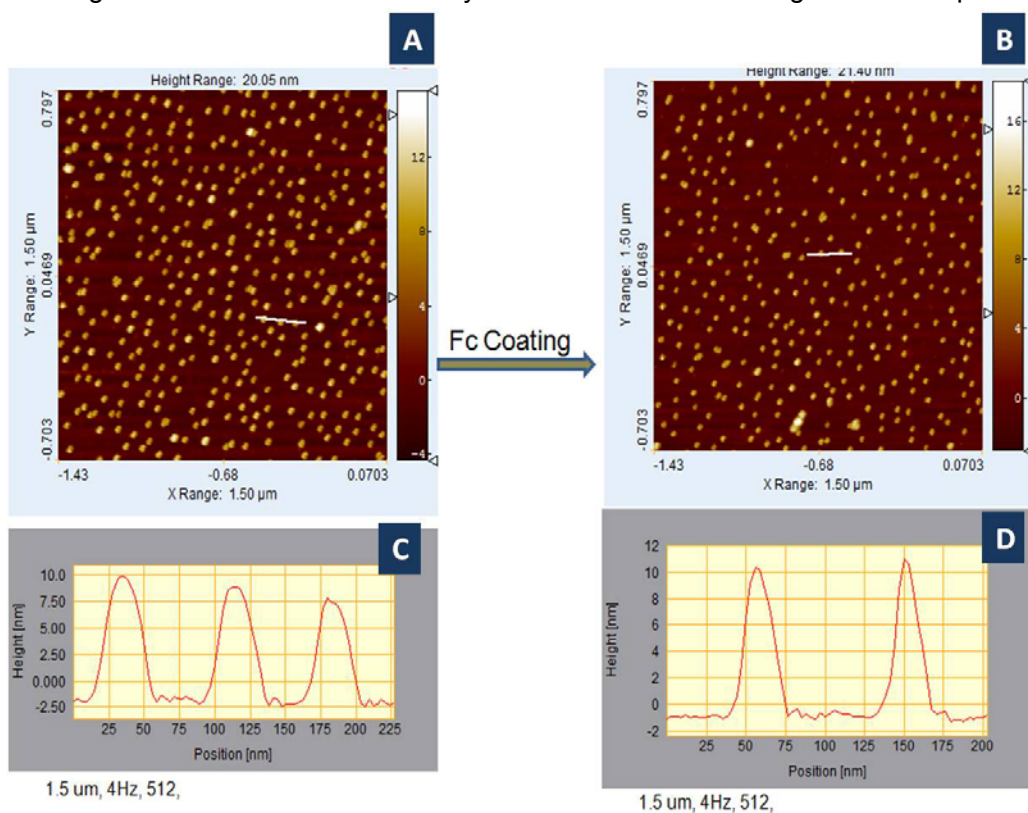


Figure 32 (A, B) AFM topography images of nanostructured surfaces with PEG coating without and with Fc respectively. (C, D) are the sample height profiles of (A, B).

vi. Fc Concentration of the Incubated Liquid versus Amount Bound On Glass Substrate

Nanopatterned substrates although are an excellent technique for presenting Fc fragments in organized and regular patterns, there is a concomitant effect of changing concentration of Fc bound with changing nanopattern spacing. This change in Fc concentration occurs as there are more gold particles with decreasing nanopattern spacing, leading to higher amount of protein bound per every cm². It has to be noted that the amount of Fc fragment bound on the nanopatterns is really low. In order to see if higher concentrations of Fc fragments have an enhanced effect on macrophages we coated glass slides with high density of Fc fragments.

Since we would like to determine the amount of Fc fragment bound on the glass. In the present experiment we have determined how the amount of Fc concentration incubated

in the solution relates to the amount of protein that is chemically bound to the surface. In order to determine the protein concentration bound on the glass slide, we used the technique from Reinhart *et. al.*²⁹⁶. The surfaces to be coated with Fc were initially treated with APTES (refer to section I of materials and methods for APTES treatment) to create amine groups. The slides were then treated with glutaraldehyde for 45 minutes. The Fc fragment was diluted in PBS to create solutions of 500 mg/ml, 250 mg/ml, 125 mg/ml, 62.5 mg/ml, 31.25 mg/ml and 15.6 mg/ml. These diluted protein solutions were incubated overnight with the glutaraldehyde treated glass slides at 4°C. The glass slides were then rinsed to remove any non-specifically bound protein, leaving a slide with Fc chemically bound to the surface.

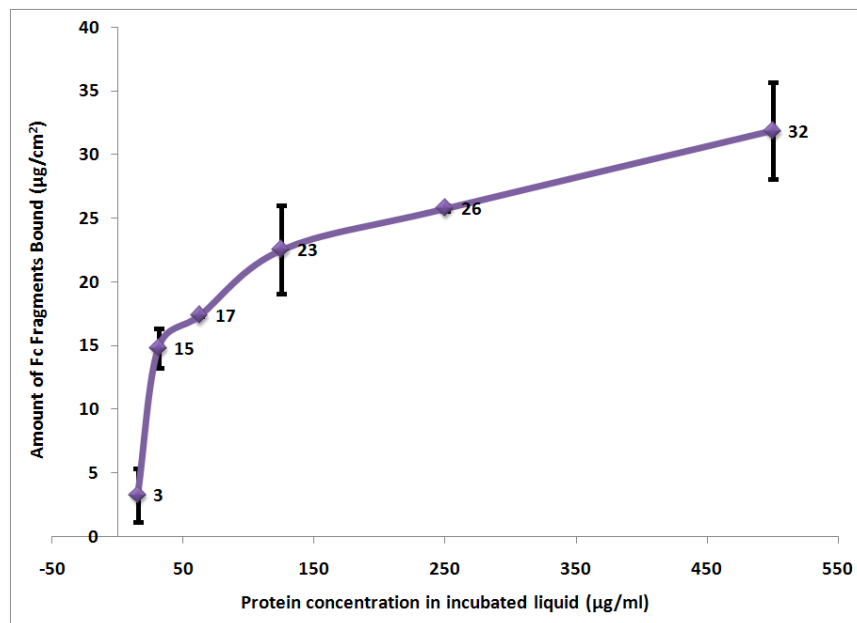


Figure 33 Graph showing protein concentration incubated versus amount of protein bound to surface.

The Fc concentration is measured by hydrolyzing the amide linkage between the Fc and the APTES treated glass slides using a solution of 5N NaOH. 140 µl of 5N NaOH was added to each Fc coated glass slide for 3 hours. The NaOH solution containing Fc was carefully collected and the Fc concentration was determined by comparing its absorbance at 280 and 260 nm to that of pure Fc fragment at different pre-determined concentrations. The plot in Figure 33 shows protein concentration incubated versus the amount of protein bound to glass surface.

II. Quantifying Cell Spreading of M2 Activated Macrophages

Phagocytosis of foreign bodies, dead cells and old tissue structures is an important macrophage function. A variant form of phagocytosis occurs when a macrophage is activated to engorge an object that is much bigger than itself. In cases where the total amount of membrane needed to phagocytose an object is larger than that in a macrophage's reserves, the macrophage instead attaches to the object's surface and spreads over a large area as it attempts to phagocytose the substrate⁷¹. This process is called frustrated phagocytosis. During frustrated phagocytosis macrophages secrete cytokines, degradative agents such as superoxides and free radicals causing damage to the foreign object²⁹⁷.

In general, activated macrophages spread over larger areas than non-activated macrophages^{200,236,298}. Although not much work was done to clearly distinguish if M1 or M2 phenotype of macrophages undergo cell spreading during activation, we hypothesize and want to confirm that in activated state, M2 phenotype spread more than normal macrophages. In order to achieve this, we monitor the change in adhesion area using optical microscopy. Further this change in adhesion area was used as a measure for cell activation. In this section, we report on how the adhesion area of macrophages varies with Fc fragment concentration on engineered surfaces. Later, in section III, this trend will be compared with biochemical data reporting the cytokine production of macrophages on the same surfaces.

In both the cell spreading study and the cytokine assay, we investigate the ability of Fc fragments bound to a surface to modulate macrophage behavior and activation. In designing the substrates, we consider the two main factors that could strongly influence the frustrated phagocytotic response of the macrophages. The first is the average concentration of Fc fragments on the surface with respect to the total cell area. The second is the local organization of the Fc fragments, in particular, their local concentration and geometry. In one scenario, the total number of Fc receptors stimulated on a macrophage cell may be the predominant influence on the macrophage response. In another possible scenario, the total number of activated Fc receptors may be irrelevant unless clusters of Fc receptors are allowed to physically form, so that a signaling cascade initiating phagocytosis is allowed to start. There is evidence that Fc receptor clustering is necessary for phagocytic signaling to initiate.

In order to distinguish between these two scenarios, our experiments will consist of two classes of surfaces and several controls. Nanopatterns of Fc fragments with varying ligand spacing will be the first surface type. The second surface type will be high concentration of covalently bound Fc fragments to glass. The concentrations of Fc on glass are much higher than what is achievable by the nanopatterns. In the nanopatterning experiments, the hypothesis that some critical geometry/ligand spacing is necessary to initiate a phagocytic signaling cascade will be tested. With the standard surfaces, we will explore how increasing the concentration dramatically impacts the cell response. Controls will include the typical response of macrophages to the endotoxin lipopolysaccharide (LPS), which is well known to elicit a strong immune response that promotes cell spreading and secretion of pro-inflammatory cytokines by macrophages²⁹⁹⁻³⁰⁰. Negative controls on glass and PEG are also included. Comparison with the positive LPS control will facilitate interpretation of the modulation of the macrophage behavior on the nanopatterned / concentration varying substrates.

i. Change in Cell Area on Glass Slides with High Fc fragment Concentration

Macrophages when ligated with Fc fragments in solution are known to secrete IL-10 and anti-inflammatory cytokines²⁰³. The primary aim of this experiment is to see if macrophages get activated and produce anti-inflammation with Fc fragments immobilized on surface. In order to analyze the activation, we compared the cell area of macrophages on high density Fc coated slides with LPS stimulated cells and macrophages on plain glass. To check the anti-inflammation activity, we performed ELISA to compare the cytokine production (section III). Since we are using really high amount of Fc fragments (more than a monolayer), the area and cytokine experiments on glass slides will help us check the effectiveness of nanopattern substrates which have about 1000 times lesser Fc fragments. If

concentration is the key player in modulating the macrophages behavior on surfaces, these high concentration Fc coated slides should outperform the nanopatterned substrates.

To chemically bind the Fc fragment to the glass slide, the glass slide was treated with APTES which created amine groups on the surface of the glass substrate. The glass slides were then cleaned and treated with glutaraldehyde for 45 minutes. The Fc fragment was diluted in phosphate buffer (pH 8) to the required concentration i.e 500 $\mu\text{g}/\text{ml}$. From Figure 33 we know that when incubated with the above concentrations we achieve 32 $\mu\text{g}/\text{cm}^2$ of Fc bound to the surface of the glass slide. After covalently binding the Fc receptors to the glass substrates, the slides were rinsed and placed in a 6 well plates. Two ml of media and 50,000 J774a.1 cells were plated onto each well. After 48 hours of incubation, the cell culture media was removed and the cells on the slides were fixed. In order to visualize the cell area, the cell membrane was labeled with wheat germ agglutinin (WGA). The cell area was quantified from the epi-fluorescence images using a home built algorithm. The experiments were performed on two separate slides and approximately 100-140 cells were measured to quantify the cell area.

It was observed that the cell area on these substrates was 1570 μm^2 , on the other hand macrophages stimulated with LPS had an average area of 1957 μm^2 . The indiscrepancy in area between Fc activated macrophages and LPS activated macrophages may be related to different activation pathways. LPS stimulation leads to M1 macrophages and Fc activation causes M2 macrophages. Although they are no well studied control stimuli for M2 macrophages, a better control could help us analyze the effectiveness of the Fc coated surfaces.

Since the area measurements themselves couldn't be used to confirm the functionality of Fc coated surfaces, we performed cytokine assays to analyze the anti-inflammatory cytokine production.

ii. Modulation of Cell Spreading On Nanopatterned Substrates

Four different nanopatterns were used to assay the influence of Fc-fragment spacing on macrophage activation. As described in the Materials and Methods section, micellar nanolithography was used to produce gold nanoparticle arrays with hexagonal ordering and an average lattice spacing of 36, 63, 80 and 125 nanometers between the gold particles. These lattice spacing correspond to interfaces with surface concentrations of 11 - 33 ng/cm^2 , 3 - 8 ng/cm^2 , 2 - 5 ng/cm^2 and 1 - 2 ng/cm^2 . Fc fragments from IgG were covalently bound to the gold and the regions in between the nanoparticles were covalently passivated with PEG. The resultant nanostructured surfaces have the advantage that they control the surface concentration and spatial arrangement of the Fc fragments on a very local scale. A less controlled non-nanopatterned surface, such as those used in the section before, is expected to have significant degree of heterogeneity in the distribution of Fc fragments on the surface. Here, the patterns are expected to be relatively homogenous, although the nanopatterns have been reported and observed by us to have some variability and defects in the hexagonal structure³⁰¹.

The biofunctionalized and passivated nanopatterns were rinsed and placed in 6 well plates with 2 ml of media in each well. 50,000 J774a.1 macrophage cells were seeded into each well and the 6 well plate was placed in cell culture incubator. After 48 hours of incubation, the cell culture media was removed for cytokine analysis and the cells on the slides were fixed. In order to visualize the cell area, the cell's plasma membrane was labeled

with a fluorescently-labelled wheat germ agglutinin (WGA). Fluorescent images of more than hundred cells on each of the four different nanopattern types were measured. The cell area was measured as described in the materials and methods. Two typical cell phenotypes appeared during the measurements. One class was elongated, while the other class was typically circular. It was observed that most cells were tightly bound to Fc coated surfaces with numerous pseudopodia like structures around them.

The results are summarized in Figure 35 for the cell spreading area (μm^2) versus the substrate concentration / lattice spacing, where 36 nm is the highest concentration (11 - 33 ng/cm^2) and 125nm is the lowest concentration (1 - 2 ng/cm^2). The LPS control shows an activated cell standard to which we compare the cell areas of the nanopatterned substrates. In this extremely activated scenario, the typical area of cell was approximately 2000 μm^2 .

Figure 34 is a bar graph with cell area on nanopatterned substrates and with LPS as a control. The control LPS, which is known to activate the macrophages leading to enhanced spreading³⁰² indeed caused the cells to spread more, compared to cells on the nanopatterned substrates. The average cell area on the nanostructured surfaces was found to decrease with increasing nano-particle spacing. It has to be noted that in any population of cells in general and in macrophages as well, unless cell cycle synchronized, there should be heterogeneity in cell area. The error bars in Figure 34 are from the deviation in cell area of some cells from the average cell area of the population. Although there is a clear modulation of the cell area in terms of the average cell area on the nanopatterned substrates, the change in cell area on 63 nm and 80 nm patterns is masked by the deviating cells in the population. There was a clear change in cell area between 125 and 36 nm patterns.

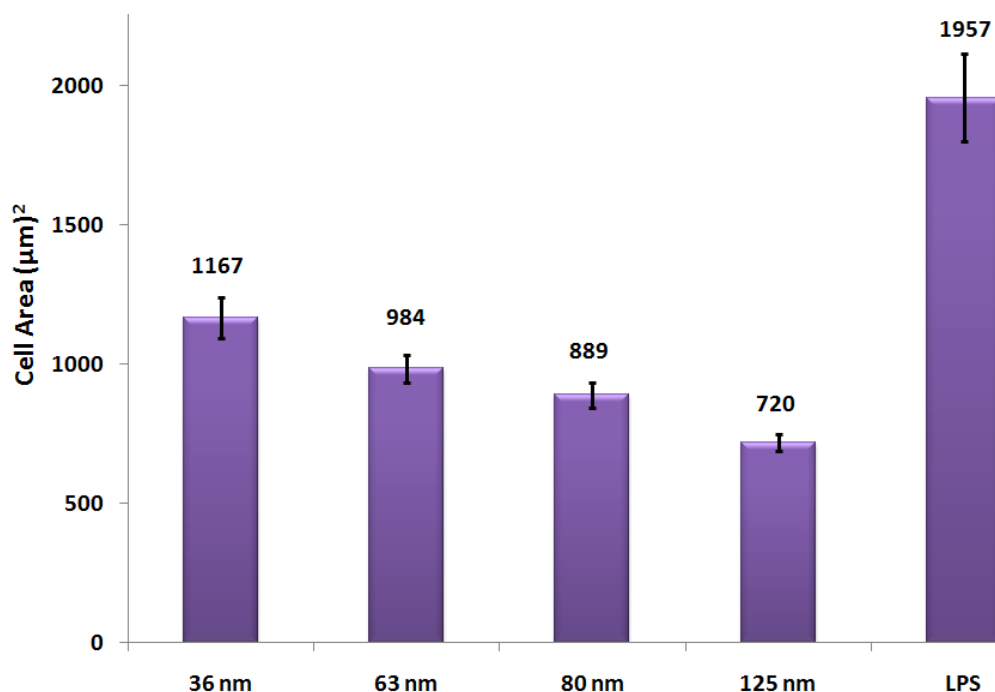


Figure 34 Cell area on nanopatterned substrates after 48 hours. There was a decrease in cell area with increasing spacing. LPS which is a positive macrophage activation signaling chemical caused the cell to spread the maximum.

The modulation in cell area observed on the nanopattern substrates may be due to organized presence of Fc fragments bound to nanodots placed at different distances (36, 63, 80 and 125 nm) on the surfaces. We know that receptor signaling can trigger an entire phagocytic response²⁰. The organized presence of Fc may lead to better and continuous coordination of FcR signaling. Swanson *et. al.*²⁰ explained the coordination in FcR as important signaling event that regulates phagocytosis. Individual FcR do not function strictly autonomously, as each receptors progression to later stages of signaling. As seen from Figure 35, the coordination could be explained as a progression of FcR signals through a series of stages, which are integrated by lipids or lipid-bound proteins that diffuse laterally in the plane of the membrane. Feedback mechanisms that define checkpoints, such as termination of signaling by phagosome closure or thresholds that reflect the overall level of FcR signaling may regulate progression from one stage to the next. So in essence if there is a larger rate of phagocytosis due to right Fc spacing it could have led to modulation of the cell behavior on the material after 48 hours.

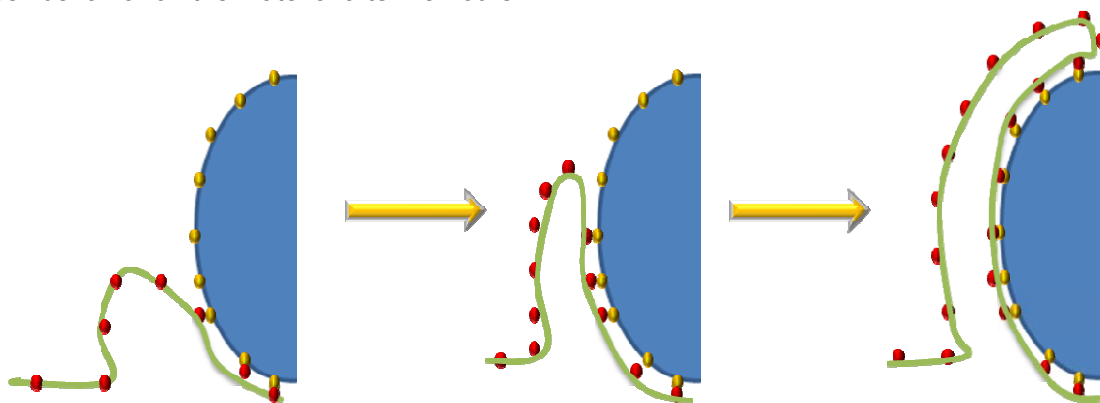


Figure 35 Coordination occurring during Fc mediated phagocytosis occurring due to signals generated near FcR passing through distinct stages. IgG molecules (gold dots) on the surface of a particle (blue) are engaged by FcR (Red) in the macrophage plasma membrane (light green). The three images indicate a sequence of movements and receptor signaling during a coordinated phagocytotic process. New interactions between IgG and FcR occur as the membrane advances over the particle. The junction between FcR recruit proteins and IgG form FcR signaling complexes.

The other plausible reason for change in cell area on the nanopatterned substrates may be concentration dependency. Although nanopatterned substrates are an excellent technique for presenting proteins in organized and regular patterns, there is a change in concentration of Fc bound with changing nanopattern spacing. This change in Fc concentration occurs as there are more gold particles with decreasing nanopattern spacing, leading to higher amount of protein bound per every cm^2 . Considering one to three Fc fragments bound to each gold particle theoretically, there should be about 11 - 33 ng/cm^2 , 3 - 8 ng/cm^2 , 2 - 5 ng/cm^2 and 1 - 2 ng/cm^2 for 36 nm, 63 nm, 80 nm and 125 nm spaced patterns. Alternative to the effect of organized presence of Fc on the substrate, just increasing the Fc concentration may have increased the surface area of the macrophages. Optimal concentration of Fc fragments and the optimal clustering activity are finely intertwined. Clustering of Fc receptors needed for activation of macrophages has not been experimentally investigated before. The clustering events occur at time scales much lower (≥ 120 minutes) than what we investigate for inflammation activity. In the present work we are interested in the inflammation activity which is aftermath of the initial frustrated phagocytosis

activity and clustering, further investigation of these initial events can help us understand the aftermath effects much more clearly.

iii. Time Dependent Modulation in Cell Area on Fc Coated Glass Slides and Control Glass Slides with No Fc

Much work has been done in understanding the effect of surface bound ligand on macrophages spreading behaviour³⁰³⁻³⁰⁵ at initial spreading phase (≥ 120 minutes). Since we are interested in the behaviour of cells at inflammation stage and the inflammation stage occurs at time scales much later than initial spreading phase, it is critical for us to see if the cell spreading is still relevant at time scales 24 and 48 hours. In order to determine this, we performed a time dependent measurement of change in cell area on Fc coated slides and compared it with cell area of macrophages on glass slides without Fc coating on them.

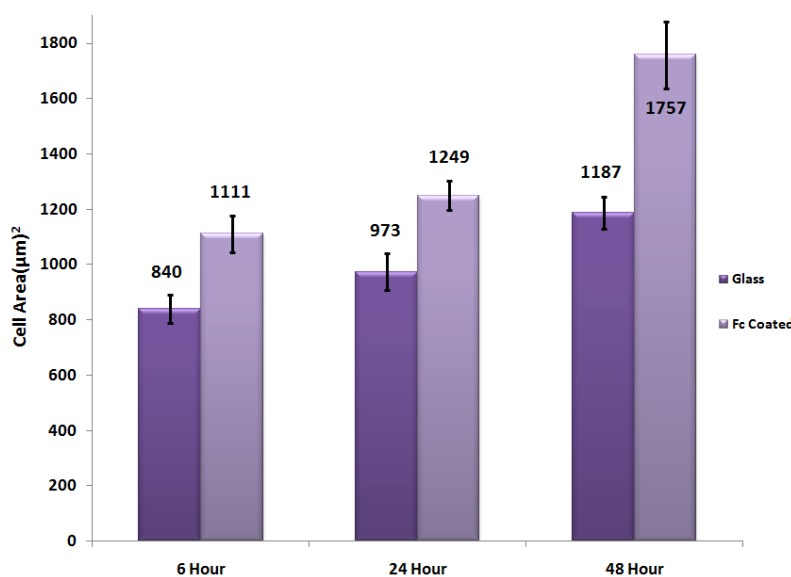


Figure 36 Change in cell area on plain glass and Fc coated slides (1 mg/ml). The cell area was determined at different time points. There was an increase in cell area with time.

From Figure 34 and 36 we know that there is change in cell area with changing Fc concentration. Figure 36 shows that there is an increase in area on both Fc coated slides and on glass slides but, the amount of change that occurs on Fc coated slides is higher than that on the glass slides. A comparison of the ratio of the area on Fc coated slides and those seeded on normal glass slides showed that there is an average difference about 1.3 times. The cells do not adhere to surfaces coated with PEG. The data clearly shows that until 48 hours, the cell area change is time dependent process and it is valid to measure change in area as a measurement criteria to validate the activation.

III. Cytokine Modulation

Macrophages play a pivotal role in both wound healing and cellular response to implants. Macrophages are potent secretory cells that release an array of cellular mediators like pro-inflammatory cytokines, growth factors, hydrolytic enzymes and reactive oxygen intermediates. Cytokines are proteins secreted by immune cells that can modulate and

orchestrate the interactions between cells. They can change the behavior of cells in the local environment. Macrophages secrete cytokines like interleukins, lymphokines and cell signaling molecules such as tumor necrosis factor. As shown in Figure 37, cytokines can orchestrate in favor or work against inflammation and wound healing.

Macrophage behavior on the nanopatterns was assessed by analyzing the production of both anti and pro inflammation cytokines. To understand the pro-inflammation effect of the nanopatterns, we checked TNF- α production by J774a.1 macrophages. To investigate the anti-inflammation behavior, TGF- β and IL-10 production were assessed.

TNF- α is a cytokine that is produced by several types of cells, but mostly by macrophages. M1 macrophages produce high amount of TNF- α . This cytokine is involved in systemic inflammation and is a member of a group of cytokines that stimulate pro-inflammation. TNF- α is responsible for apoptosis, tissue destruction and growth inhibitory processes³⁰⁶⁻³⁰⁸. Prolonged overproduction of TNF- α can have a disastrous effect including chronic inflammation, anemia³⁰⁹ and cancer³¹⁰.

Interleukin-10 (IL-10) also known as human cytokine synthesis inhibitory factor (CSIF) is an anti-inflammatory cytokine. IL-10 modulates expression of cytokines, soluble mediators and cell surface molecules which have important consequences including sustained immune and inflammatory response³¹¹. IL-10 potently inhibits production of IL-1 α , IL-1 β , IL-6, IL-12, IL-18, GM-CSF, G-CSF, M-CSF, TNF, LIF and PAF by activated macrophages³¹²⁻³¹⁷.

Transforming growth factor beta (TGF- β) is a regulatory molecule that controls cell proliferation, differentiation and migration. It plays an important role in carcinogenesis, fibrosis, wound healing, and immune response³¹⁸⁻³¹⁹. TGF- β exists in three isoforms TGF- β 1, TGF- β 2 and TGF- β 3³²⁰. TGF- β controls proliferation by stopping the cell cycle at G1 phase³²¹. TGF- β acts as chemotactic signal and attracts neutrophils and monocytes to the wound site³²². TGF- β has also been found to stimulate the production of extracellular matrix proteins like collagen³²³⁻³²⁴ and fibronectin³²⁵.

The cytokine production was accessed at 24 and 48 hours. Cells were plated on the substrates and incubated in a 5% CO₂ incubator. In order to compare the level of cytokine secretion from Fc activated substrates, cells were also activated with LPS as a control and their cytokine production was measured. LPS is a well studied endotoxin that elicits a strong immune response. LPS is known to promote the secretion of pro-inflammatory cytokines (TNF- α and IL-1 β) in macrophages²⁹⁹⁻³⁰⁰. To measure the cytokine secretion, we used ELISA, an ultrasensitive immunoassay.

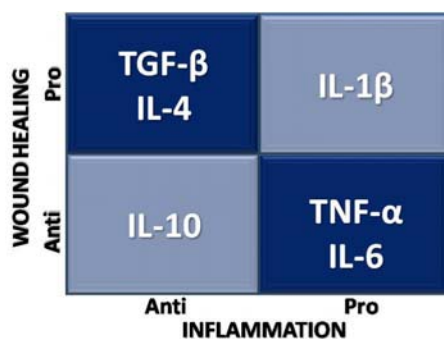


Figure 37 Cytokine classification according to their pro and anti roles in wound healing and inflammation.

i. TNF- α Production on PEG Passivated Nanopatterned Substrates without Fc

It is known that topography³²⁶⁻³²⁸ and surface chemistry³²⁹⁻³³¹ can modulate cytokine expression in macrophages. It has been shown previously that microscopic roughness on titanium surfaces induces secretion of pro-inflammation cytokines (TNF- α , IL-1 β)³²⁶. In the present work we use block copolymer derived nanopatterns as templates for Fc fragments. These surfaces create a unique topology comprising a hexagonal array of 8-10 nm gold particles with variable particle spacing. In order to inspect if the topography of the nanopattern substrate can elicit a pro-inflammation response, we investigated the production of TNF- α by macrophages that had been cultured on these substrates for 36 hours. TNF- α apart from inducing inflammation is also responsible for apoptotic cell death³³²⁻³³⁴. In Figure 38, we observed that there was less than 9% variation in TNF- α production for surfaces with gold particle spacing between 36 to 80 nm. For surfaces with 125 nm particle spacing there was a huge jump in TNF- α production. We infer from this data that there is not much change in TNF- α production for different nanopatterns except for those at 125 nm spacing.

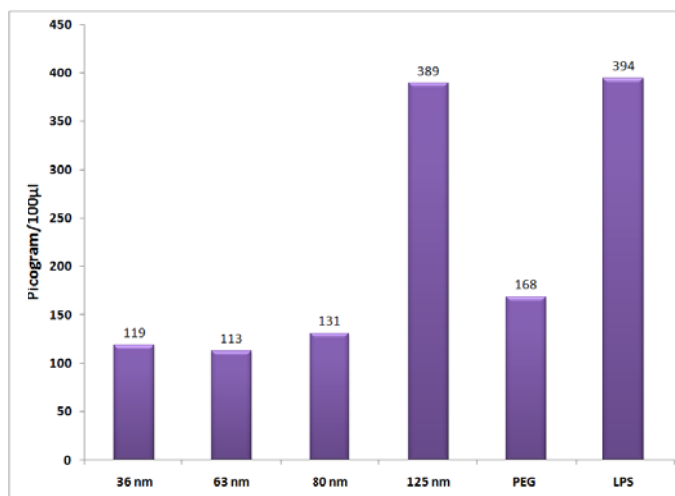


Figure 38 TNF- α production on PEG passivated nano substrates. Except for 125 nm spaced substrates, most of the substrates produced similar amount of TNF- α .

The TNF- α production on pure PEG surface, which was less than half the amount produced on 125 nm pattern substrate, negates the idea of low area for the cells to bind to the surface on 125 nm pattern as a contributing factor for the huge TNF- α production. In this case where there are no Fc fragments present the cells are likely to use an integrin based adhesion mechanism. It is previously known from Arnold *et. al*³³⁵ that integrins get differentially activated on nanopatterned substrates and a critical separation length of ≥ 73 nm between the nanopatterns dramatically reduces the cell function due to restricted integrin clustering. It was shown that at spacing's more than ≥ 73 nm the cells tend to undergo programmed death or apoptosis. The initiation of apoptosis on the 125 nm substrates could be the reason for enhanced TNF- α production.

Unlike Refai *et. al*³²⁶ who found increasing TNF- α secretion with increasing roughness, we did not have a large surface roughness dependent change in TNF- α

secretion. A reason for this discrepancy could be the scale of roughness, which is limited to nanometer range in the current work compared to micrometer range in Refai *et. al*³²⁶.

It can be concluded that for the Fc nanopatterning work, the best nanopatterned substrates would be below 80 nm in spacing between them.

ii. Anti-Inflammation Cytokine Production at 24 and 48 Hours

a. IL-10 and TGF- β Production with Changing Fc Concentration on Glass Substrate

The primary aim of the present study is to see if macrophages when stimulated with Fc receptors on surface can generate anti-inflammation. In order to verify the anti-inflammation effect we measured the cytokines TGF- β and IL-10 at 24 and 48 hrs. Since it is known that macrophages secrete IL-10 when activated with Fc fragments²⁰³, it would be interesting to see if macrophages secrete IL-10 when they are activated by Fc fragments on substrate. It has to be noted that these slides have a higher amount of Fc fragments (more than a monolayer) when compared to nanopatterned substrates.

To determine the cytokine concentration on the Fc coated slides, 50,000 cells were plated on slides with varying concentration. To confirm the expression of IL-10 and TGF- β , out of the initial 2 ml of medium that was incubated with the cells, 0.8 ml was extracted at 24 hrs and the remaining at 48 hrs. The medium was stored at -80°C until ELISA was performed. The cytokine was assessed from two slides and the measurement from each slide was duplicated. The error bars on Figure 40 and 42 are the standard deviation of the different points. All cytokines measured were measured in picograms per each well (each well had 100 μ l) i.e picograms/100 μ l.

Interleukin 10 (IL-10), initially designated cytokine synthesis inhibitory factor (CSIF), inhibits the synthesis of a number of pro-inflammatory cytokines. Figure 39 A and B show IL-10 production by macrophages at 24 and 48 hrs respectively. At both 24 and 48 hrs, from 32 μ g/cm² to 23 μ g/cm², there was a linear decrease in IL-10 with decreasing Fc concentration. From 23 μ g/cm² to 15 μ g/cm², the IL-10 produced is slightly upregulated but the trend is much weaker and is shadowed within the error. The error or deviation in sample populations IL-10 production is lesser at 48 hours than that observed at 24 hours. This uniformity in IL-10 production between the different substrates at 48 hrs leads us to the conclusion that at 48 hrs, IL-10 production on Fc coated surfaces has reached or was reaching the threshold.

A close observation at IL-10 production at 24 and 48 hours reveals that for lower concentrations i.e 15 μ g/cm² and 17 μ g/cm², there is no substantial change in the amount of IL-10 produced between 24 and 48 hrs. On the other hand, at higher concentrations i.e from 32 μ g/cm² to 23 μ g/cm², the amount of IL-10 produced doubled from 24 to 48 hours.

From Torre *et. al*³³⁶, we know that in a healthy human subject, the amount of IL-10 produced is 1.1 ± 2.3 pg/ml. At 24 and 48 hours the lowest amount of IL-10 produced (at 23 μ g/cm²) was 7.8 ng/ml and 12.62 ng/ml respectively. Since there is more than a 1000 fold increase in production, we hypothesize that the amount of IL-10 produced in our samples is relatively high and will induce the required anti-inflammation.

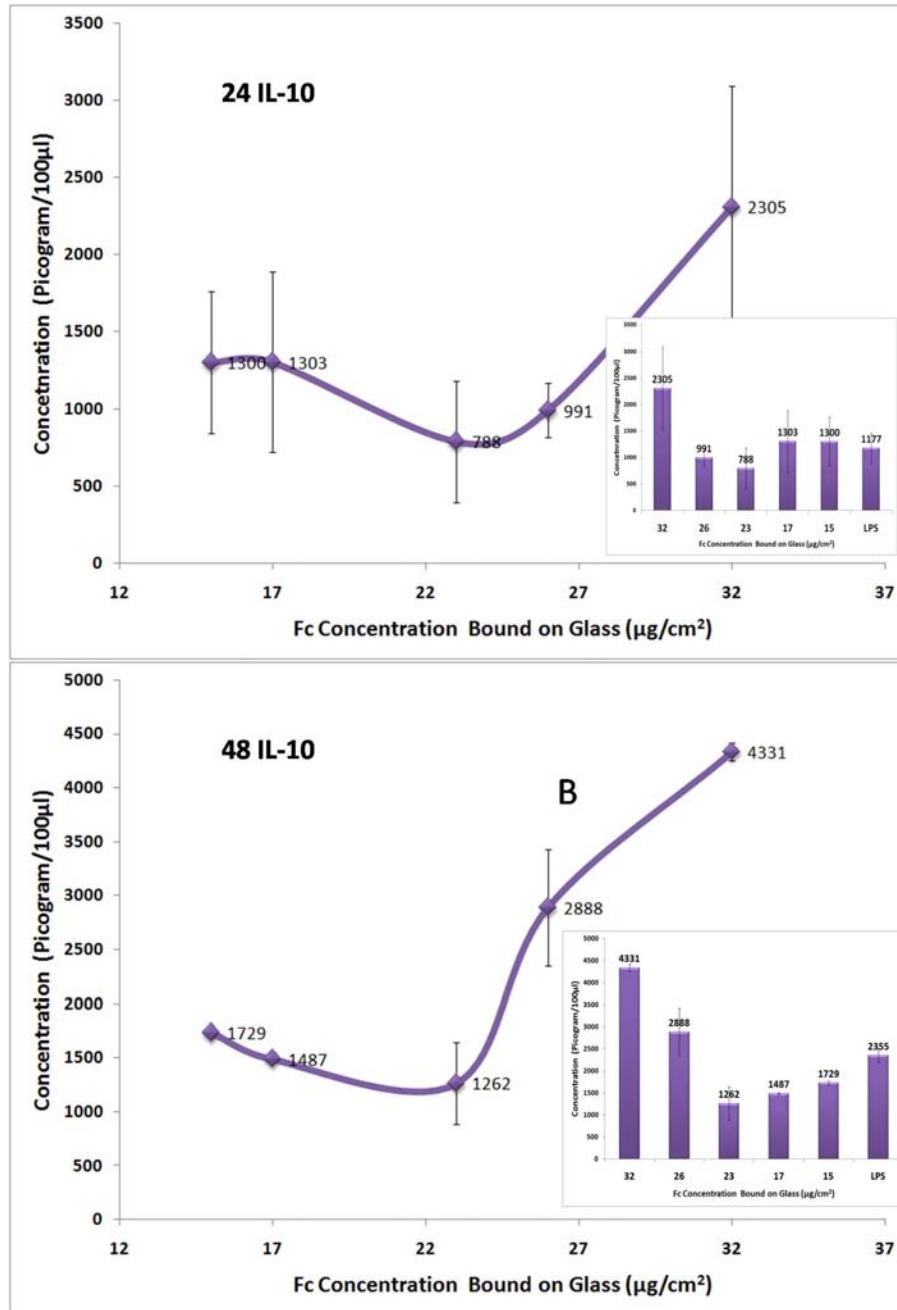


Figure 39 Anti-Inflammation cytokine IL-10 secreted by macrophages at 24 and at 48 hours on slides with changing Fc concentration on the substrate. The insert is a bar graph with control LPS included.

Transforming growth factor beta (TGF- β) is a regulatory protein that controls proliferation, cellular differentiation and plays an important part in the immune response. TGF- β is also involved in down regulating an M1 activated macrophage. Cells secrete TGF- β in an inactivated state. Only when exposed to a certain specific conditions is TGF- β activated. Heat, acidic condition, protease are some of the known physicochemical conditions that can activate TGF- β . Since we need to activate latent TGF- β to its immunoreactive form for quantification, as per manufacturer's recommendation, we initially

acidified the sample with 1N HCL and after 10 minutes of treatment, the sample was neutralized with 1N NaoH.

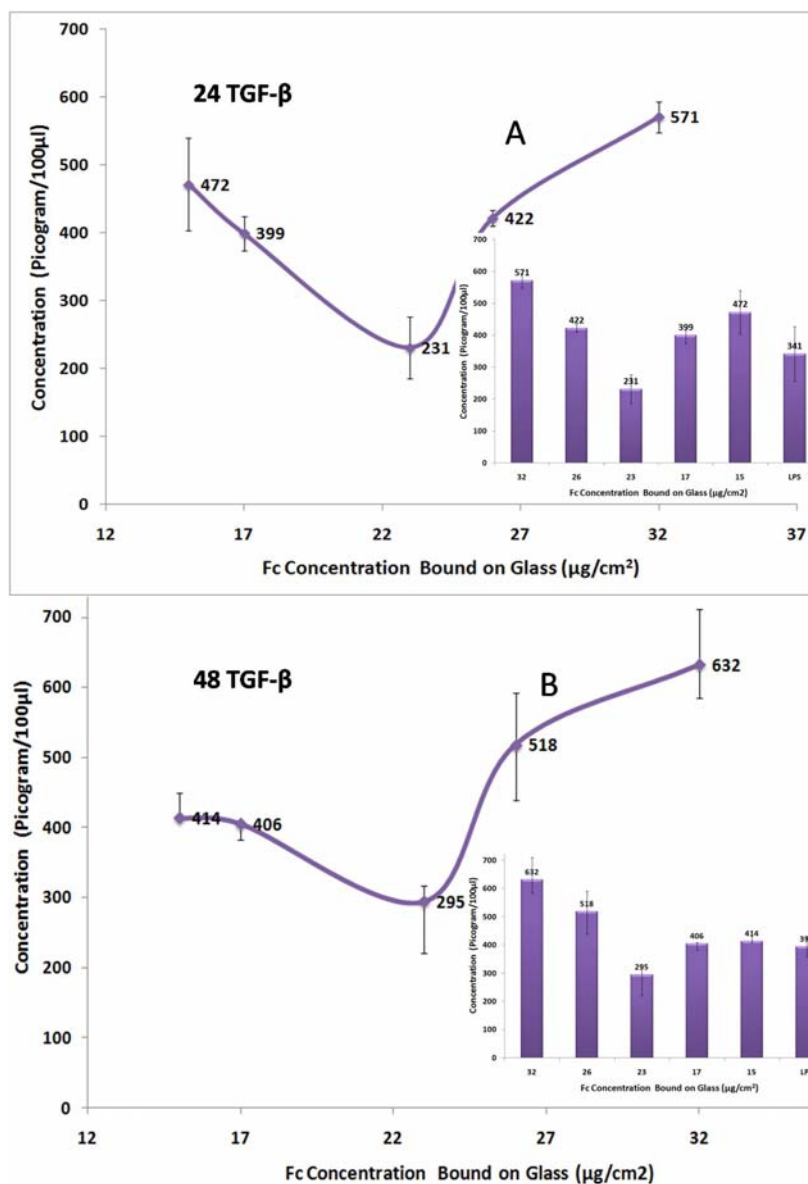


Figure 40 Anti-inflammation cytokine TGF- β secreted by macrophages at 24 and at 48 hours (A, B) on slides with changing Fc fragment concentration. The insert is a bar graph with control LPS included.

As in the IL-10, there was a concentration dependent decrease in TGF- β production from 32 $\mu\text{g}/\text{cm}^2$ to 23 $\mu\text{g}/\text{cm}^2$, at both 24 and 48 hrs. For concentrations below 23 $\mu\text{g}/\text{cm}^2$, at 24 hrs there was an increase in TGF- β production with decreasing concentration. For concentrations 32 $\mu\text{g}/\text{cm}^2$ and 32 $\mu\text{g}/\text{cm}^2$ the difference in concentration was shadowed by the error bar. The amount of TGF- β secreted by LPS stimulated cells was in the range of the amount of TGF- β secreted by Fc coated glass slides at 26-17 $\mu\text{g}/\text{cm}^2$.

From Torre et. al³³⁶ we know that a healthy subject produces 4.1 ± 1.9 pg/mL of TGF- β . The Fc fragment coated slides produced 2.3 - 4.8 ng/ml and 3 - 6.4 ng/ml of TGF- β at 24

and 48 hours respectively. The amount of TGF- β produced is 1000 times more than that reported by Torre et. al³³⁶. Although the amount of TGF- β produced at 48 hours is more than that produced at 24 hours it was not as dramatic as IL-10 where the production doubled after 48 hours.

From the data in Figure 39 and Figure 40, it can be concluded that for higher concentration i.e. between 32 $\mu\text{g}/\text{cm}^2$ to 23 $\mu\text{g}/\text{cm}^2$ of Fc bound on glass, there is a concentration dependent change in anti inflammation cytokine production and there is a decrease in both IL-10 and TGF- β production with decreasing Fc concentration. While the trend with higher concentrations is quite clear with lower concentrations i.e when the concentration reached 17 $\mu\text{g}/\text{cm}^2$ and below, there is no change or the change is within the error bar. It has to be noted that there is relatively high amount of IL-10 produced compared to TGF- β .

b. IL-10 and TGF- β Production on Fc Coated, PEG Passivated Nanopatterned Substrates

We already know from the previous experiments that we can elicit an anti-inflammation response by stimulating macrophages with Fc fragments immobilized on surface. Since immobilization of Fc fragments on nanopatterns is an effective way to present cells with defined stimuli. In the present experiment, we want to check if immobilization of Fc fragments on nanopatterns enhances the anti-inflammatory cytokine production. It would also be interesting to compare the amount of anti-inflammatory cytokines produced by macrophages stimulated on nanopatterns versus those on glass slides as theoretically, the amount of Fc fragments presented through the nanopatterns would be thousand times lower than those presented on glass slides.

In order to achieve Fc coated nanopatterns, block copolymer nanopatterns were coated with Fc and the area between the patterns was passivated with PEG to prevent non specific adsorption of other proteins from serum. The nanopattern slides were incubated with 2 ml of cell culture medium and 50,000 cells were plated on each slide. The data presented in Figure 41 and 43 are anti-inflammation cytokines (IL-10 and TGF- β) produced by macrophages at 24 and 48 hrs.

Figure 41 A and B are bar graphs of IL-10 produced at 24 and 48 hrs. It was observed that the amount of IL-10 produced at 48 hours was more than twice the amount produced at 24 hours. In terms of the absolute amount of IL-10 produced, it is incredible that 36 nm pattern which had about 1000 times lower amount of Fc fragments (11 - 33 $\times 10^{10}$ Fc fragments per cm^2) than those on 26 $\mu\text{g}/\text{cm}^2$ (26 $\times 10^{13}$ Fc fragments per cm^2) produced at 48 hrs the same amount of IL-10.

Although the trend in IL-10 production at 24 and 48 hrs was similar on Fc coated glass slides (Figure 39), the trend was predominantly different on Fc nanopattern surfaces. Also it was observed that at 24 hours the amount of IL-10 produced by macrophages stimulated by Fc nanopatterns was lesser than that secreted by macrophages stimulated with LPS. This suggests that the maximum IL-10 release starts after 24 hours on Fc nanopattern substrates.

Figure 41B shows that at 48 hours, there is a clear modulation of IL-10 by Fc nanopattern substrates. The amount of IL-10 produced by the macrophages kept increasing with decreasing spacing. The amount of IL-10 produced on 36 nm pattern was double that produced when stimulated with LPS. The macrophages on 125 nm patterns produced

slightly higher IL-10 than those stimulated with LPS and were similar to the amount produced by macrophages on PEG surface.

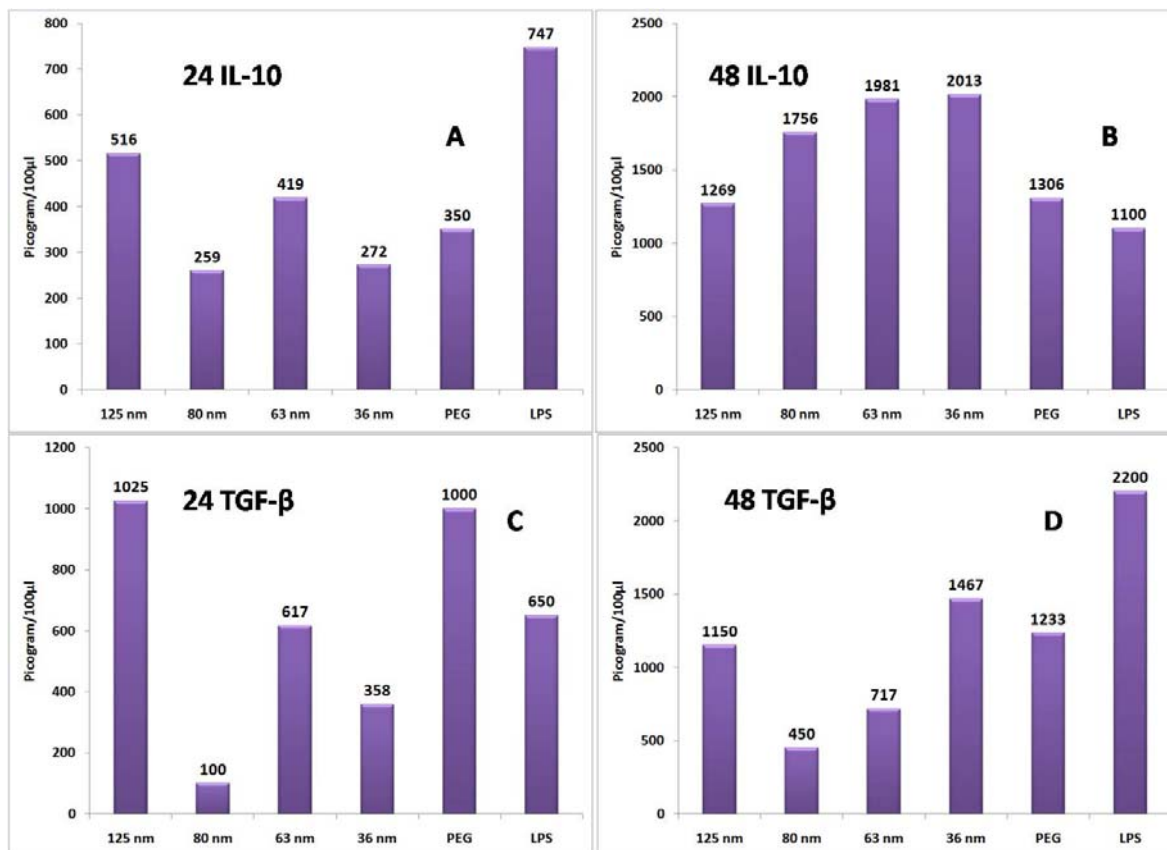


Figure 41 Anti-inflammation cytokines (IL-10, TGF-β) secreted by macrophages at 24 and 48 hours (C, D) on nanosubstrates coated with Fc.

Figure 41C and D are bar graphs with TGF-β production at 24 and 48 hours. The amount of TGF-β produced on 36 nm pattern at 48 hours was twice the amount produced by macrophages plated on glass slides at the highest concentration of Fc (32 µg/cm²). The fact that the amount of TGF-β produced by macrophages on nanopattern substrates is higher than that on Fc coated glass slides, which had about 1000 times more Fc fragments shows that Fc fragment nanopatterning strategy is much more effective in producing the anti-inflammation stimuli than simply coating Fc fragments on glass slides. Moreover the trend observed in IL-10 and TGF-β secretion at 24 hours was similar showing that the activation pathway until 24 hrs is similar. The results from the TGF-β production clearly negates our assumption that modulation occurring is a concentration dependant change. Further experiments at lower time scales which can elucidate the clustering activity and the pathway that leads to anti-inflammation activity can shed light into why the nanopatterns are more effective than presenting Fc fragments at varying concentrations.

Since the trend in the cell area observed is similar to the trends in IL-10 production, it can be concluded that there is a correlation between cell spreading area of M2 macrophages with the degree of macrophage activation.

Since TGF-β recruits other cells and stimulates the production of extracellular matrix proteins like collagen³²³⁻³²⁴ and fibronectin³²⁵, our Fc nanopattern coatings can ideally help

integrate foreign objects into the tissue more competently than just coating surfaces with Fc fragments.

iii. Pro-Inflammation Cytokine Production at 24 and 48 Hours

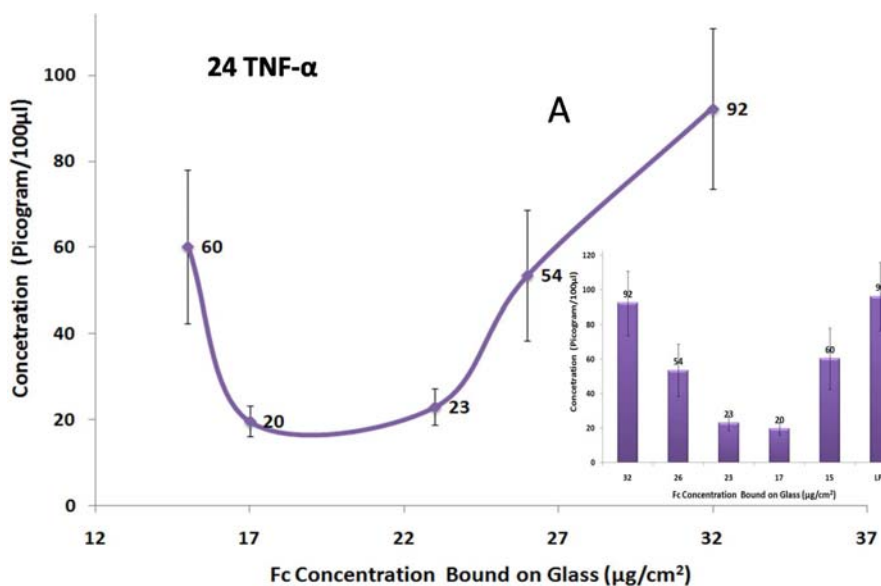
a. Pro-Inflammation Cytokine Production with Changing Fc Concentration on Glass Substrate

An ideal anti-inflammatory surface would produce anti-inflammation cytokines and reduce the amount of pro-inflammation cytokines. We know from Figure 39 and 41 that macrophages activated with Fc fragments on surface can induce anti-inflammation cytokines. In the present work we assessed pro-inflammation cytokine (TNF- α) production at 24 and 48 hours on glass substrates coated with Fc fragments.

TNF- α is produced mainly by macrophages. Its primary role is the regulation of immune cells and is involved in systemic and chronic inflammation. TNF- α promotes pro-inflammatory response that causes many of the clinical problems associated with autoimmune disorders. There are opposing influences on TNF- α production. While IL-10 suppress TNF- α production, TGF- β promotes as well as works against TNF- α production³³⁷⁻³³⁸. The measurements were performed on two slides and the measurement from each slide was duplicated.

Figure 42A and B show TNF- α production at 24 and 48 hrs. The amount of TNF- α produced at 48 hrs is more than twice the amount produced at 24 hrs. The error or standard deviation observed at 24 hrs was much higher than those observed at 48 hrs.

The TNF- α production at 24 hrs although is lower than the amount produced at 48 hrs, a closer inspection reveals that at 24 hrs, the slides at 32 $\mu\text{g}/\text{cm}^2$ had similar amount of TNF- α produced as macrophages stimulated with LPS. Since we already know that LPS is a known stimulator of TNF- α production in macrophages, comparing this with the amount of TNF- α produced on Fc fragment slides leads us to the conclusion that at 24 hours the higher concentration slides are pro-inflammatory.



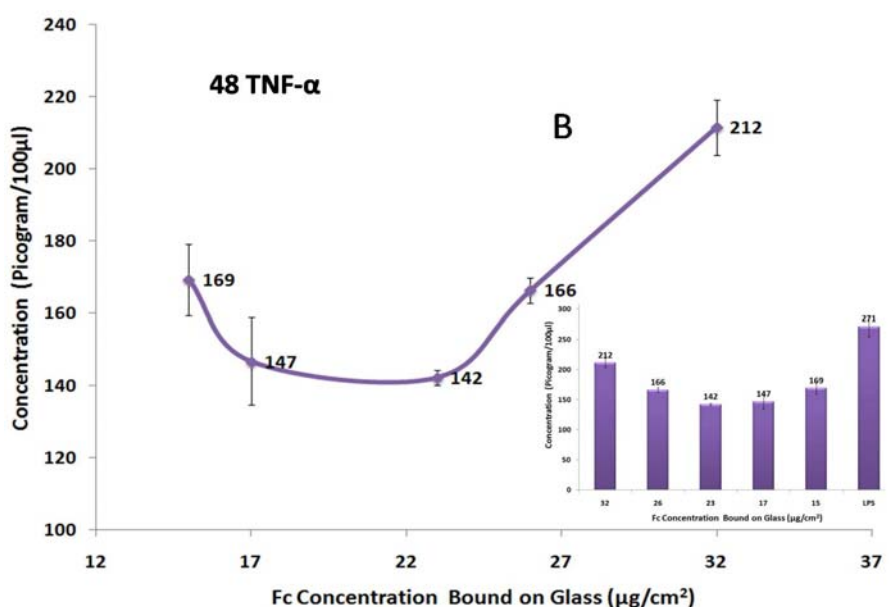


Figure 42 Pro-inflammation cytokine TNF- α secreted by macrophages at 24 and 48 hours (A, B) on slides at different concentrations. The average error or standard deviation observed was much higher in 24 hrs than those observed at 48 hours. The insert is a bar graph which includes TNF- α production by LPS stimulated macrophages.

b. Pro-Inflammation Cytokine Production on Fc Coated, PEG Passivated Nanopatterned Substrates

As discussed earlier, an ideal anti-inflammation eliciting implant coating should have low amount of pro-inflammation cytokine production and high amount of anti-inflammation cytokine production. It was observed earlier that at high concentration of Fc fragments on glass slides, the macrophages instead of being purely anti-inflammatory also produced high amount of pro-inflammatory cytokine TNF- α . Since the Fc nanopatterns have lower amount of Fc fragments than what we present on glass slides, it would be interesting to see if the nanopatterns have a lower amount of TNF- α production. Also we know from the anti-inflammation activity of TGF- β and IL-10 that nanopattern substrates are much more effective in eliciting the inflammation signal than simply presenting Fc fragments randomly on glass. Understanding the pro-inflammation cytokine production will finally help us determine the best spacing required for ideal implant coating.

In order to understand the pro-inflammatory modulation occurring on Fc nanopattern substrates, we measured macrophage's pro-inflammatory cytokines TNF- α and IL-1 β . Figure 43 shows a bar graph of these secretions at 24 and 48 hours. At 24 hours, except for 125 nm patterns, the amount of TNF- α and IL-1 β secretion was nanopattern dependent and increased with decreasing spacing. Unlike the similar trends in TNF- α production at 24 and 48 hrs observed on glass slides (Figure 42), the trend observed on the nanopattern substrates was different at 24 and 48 hours.

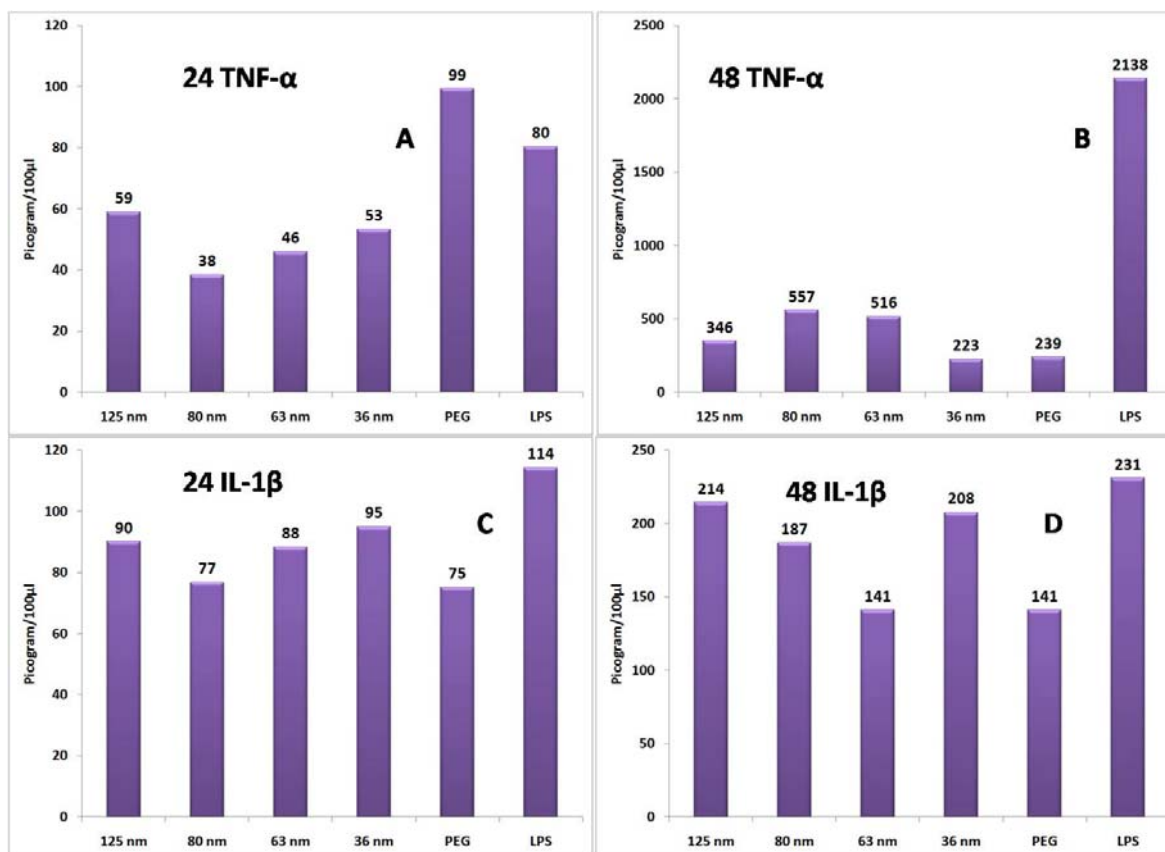


Figure 43 Pro-inflammation cytokines, TNF- α (A, B) and IL-1 β (C, D) secreted by macrophages at 24 and 48 hours on nanopatterned substrates.

LPS is an outer membrane component of Gram-negative bacteria and a potent activator of monocytes and macrophages. LPS binds to surface toll like receptor 4 (TLR4), triggering the secretion of a variety of inflammatory products, such as tumor necrosis factor- α (TNF- α) and interleukin-1 β (IL-1 β).

On nanopattern substrates, macrophages produced IL-1 β similar to what they produced when activated with LPS. This inconsistency could be due to usage of J774A.1 cell line (ATCC #TIB-67) as a model macrophage. It is known that this immortalized cell line continuously produces interleukin-1 β making it incompetent to effectively assess the IL-1 β production.

At 48 hours, as seen in Figure 43B, the amount of TNF- α produced by LPS stimulated cells was four times the highest amount of TNF- α produced by macrophages stimulated with Fc fragments on nanopatterns. Also, at 24 hrs, LPS stimulated and Fc fragment stimulated macrophages had similar TNF- α production. This behavior points us to the conclusion that the anti-inflammation effect of Fc nanopatterns which reduces the pro-inflammatory action, starts working at 48 hrs rather than at 24 hrs. This conclusion is substantiated by our previous observation with IL-10 production (Figure 41B) at 48 hrs. There was approximately 10 fold increase in IL-10 production at 48 hrs when compared to 24 hrs. Since IL-10 is a known down regulator of TNF- α , the decrease in TNF- α we see may be due to IL-10 down regulation.

Since macrophages at 48 hours on 36 nm spaced patterns produced the lowest amount of TNF- α (pro-inflammatory cytokine) and highest amount of IL-10 and TGF- β (anti-inflammatory cytokines), It is safe to conclude that out of the different nanopattern spacing's experimented in the present work, 36 nm spaced patterns are ideal for eliciting cytokine mediated anti-inflammation signaling.

5. Conclusions and Outlook

The aim of the present study is to engineer an anti-inflammatory macrophage response using bioactive nanopatterned substrates. There are several immune conditions where people have a propensity for chronic inflammation. Prolonged pro-inflammation cytokine secretion during chronic inflammation has multiple effects including a tendency toward greater matrix degradation, destruction of the tissue around implants and delayed wound healing²¹⁷⁻²¹⁸, these factors ultimately lead to the rejection of the implant. In order to suppress the prolonged pro-inflammation phase, immunosuppressive agents²³⁷, steroids²³⁸⁻²³⁹ and anti-inflammation agents³³⁹⁻³⁴¹ are generally administered. The engineered bioactive surfaces in our work can stimulate the macrophages to secrete anti-inflammatory cytokines at the implant site, easing implant integration.

We have set out to see if we can induce an anti-inflammatory response in macrophages by stimulating them with Fc-fragments immobilized on substrates. The cytokine and area measurements together showed that we can achieve this. Further correlation between cell spreading area of M2 macrophages with the degree of cytokine secretion revealed that M2 macrophages spread on the surface relative to their activation.

In order to decrease the degree of heterogeneity in the distribution of Fc fragments on the surface, block-copolymer nanopatterns were used as templates to pattern Fc fragments. These templates allowed us to pattern the Fc fragments in a well defined periodic hexagonal array with a spacing of 36, 63, 80 and 125 nm between them. We have successfully characterized and shown that we can nanopattern Fc fragments on these templates. In order to achieve this we modified the Fc fragments to include a thiol group. The binding and bioactivity of this modified Fc fragment was tested using QCM.

To stimulate the cells only with the Fc fragments presented and prevent any non-specific stimulation occurring from plasma proteins binding to the area between the proteins, the space between the proteins was passivated with PEG. Contact angle goniometry and FTIR confirmed the presence of PEG between the binding sites.

On the control PEG passivated patterns without Fc fragments, Except for 125 nm patterns, PEG passivated nanopatterns had no modulation on pro-inflammation cytokine secretion. We saw modulation of cytokine and cell morphology on these nanopatterned substrates when coated with Fc fragments. When macrophages were plated on these nanopatterned substrates the cell area decreased with increasing spacing. There was a two fold increase in IL-10 production from control on 36 nm patterns.

The effectiveness of the nanopattern substrates in generating the anti-inflammation stimuli rather than simply coating Fc fragments on glass slides was reinforced by the fact that the amount of TGF- β produced by macrophages on nanopattern substrates is higher than that on Fc fragment coated glass slides, which had about 1000 times more Fc fragments. This result also negates the assumption that only concentration of Fc fragments is important for modulation of macrophage's anti-inflammatory behavior.

Since TGF- β recruits other cells and stimulates the production of extracellular matrix proteins like collagen³²³⁻³²⁴ and fibronectin³²⁵, our Fc nanopattern coatings can ideally help integrate foreign objects into the tissue more competently than just coating surfaces with Fc fragments.

At 48 hours, the amount of TNF- α produced by LPS stimulated cells was four times the highest amount of TNF- α produced by macrophages stimulated with Fc fragments on nanopatterns. This behavior points us to the conclusion that the anti-inflammation effect of

Fc nanopatterns which reduces the pro-inflammatory effect starts working at 48 hrs rather than at 24 hrs. This conclusion is substantiated by our previous observation with IL-10 production at 48 hrs. There was approximately 10 fold increase in IL-10 production at 48 hrs when compared to 24 hrs. Since IL-10 is a known down regulator of TNF- α , the decrease in TNF- α we see may be due to IL-10 up regulation.

The ideal anti-inflammation eliciting implant coating should have low amount of pro-inflammation cytokine production and high amount of anti-inflammation cytokine production. Since macrophages at 48 hours on 36 nm spaced patterns produced the lowest amount of TNF- α (pro-inflammatory cytokine) and highest amount of IL-10 and TGF- β (anti-inflammatory cytokines), It can be concluded that out of the different nanopattern spacing's experimented in the present work, 36 nm spaced patterns are ideal for eliciting cytokine mediated anti-inflammation signaling.

This effectiveness of the nanopattern strategy may be due to presence of only Fc fragments on the surface eliciting a strong response to the stimuli with PEG preventing any other response from the plasma proteins binding to the glass. The other plausible reason could be that the organized presence of Fc fragments which is leading to a better clustering of Fc receptors.

Optimal concentration of Fc fragments and the optimal clustering activity are finely intertwined. Clustering of Fc receptors needed for activation of macrophages has not been experimentally investigated before. The clustering events occur at time scales much lower (≥ 120 minutes) than what we investigate for inflammation activity. In the present work we are interested in the inflammation activity which is aftermath of the initial frustrated phagocytosis activity and clustering, further investigation of these initial events can help us understand the aftermath effects much more clearly. These studies will also shed light as to why the nanopatterns are more effective in eliciting anti-inflammation behavior than just presenting Fc fragments on glass slides.

In conclusion, macrophages comprise a heterogeneous population of cells that undergo environmentally induced differentiation into functionally distinct populations when properly stimulated. The present work shows that when macrophages stimulated with Fc receptors on surface can alter their morphology and secretory profile of the inflammatory cytokines. Presenting Fc receptors on PEG passivated nanopatterns is an excellent way of presenting Fc at defined spacing and concentrations. A better understanding of the effect of Fc patterning approach in modulating macrophages behavior may enable us to improved surface design to specifically direct anti-inflammation response and improve implant performance.

Thermochemical Nanolithography

1. Introduction

At the forefront of nano-biotechnology and nano-science^{16,233,342-347} is the challenge to manipulate and control the position of individual proteins, nanoparticles, and other complex nanostructures. Bio-nanopatterning of surfaces is a very active interdisciplinary field of research at the interface between biotechnology and nanotechnology. The ability to spatially anchor and orient proteins at the nanoscale affords useful materials for biosensors³⁴⁸, biomaterials, and tissue engineering applications³⁴⁹.

One of the major challenges in the development of a new biomaterial for implants is the interface. The interface ideally should effectively control the interactions occurring between the material and cells in the body^{329,350-355}. Polymer based materials have found wide applications as interface materials in biomedicine³⁵⁶⁻³⁶³. It is known that cells recognize and adhere to stimulatory cues like cell adhesion molecules that are spatially organized on the nanoscale²³⁴⁻²³⁵. From chapter 2 we know that Fc protein patterns can regulate macrophages ability to produce anti-inflammation cytokines. If we could pattern these Fc fragments on a polymer surface we could combine the beneficial properties of polymer surfaces with the advantages of nanopatterning. Here, we develop a new approach to pattern multiple proteins with high resolution on a polymer film. This new patterning approach, Thermochemical nanolithography (TCNL), exploits a custom synthesized polymer that has a backbone polymethylmethacrylate (PMMA). PMMA is an FDA approved³⁶⁴ biomaterial, hence the TCNL patterning approach designed here can easily be translated to coatings on implant or bio-applications. As a polymer based approach this technique is substrate independent. The technique was designed so that we could pattern these proteins in arbitrary shapes.

A new flexible orthogonal patterning approach would not only help us design new implant interfaces but will have applications in different fields. Since disease progression is often correlated with protein levels, protein nanoarrays offer the prospect of greater sensitivity in diagnostic tests³⁶⁵. In addition, further miniaturization from protein microarrays to nanoarrays may allow for the discovery of currently undetectable disease markers. Moreover, the detection of thousands of biomarkers could be performed on one chip, resulting in a more comprehensive biosignature for a patient or disease³⁶⁶.

Several approaches have been proposed to assemble molecules on surfaces with nanometer scale resolution, including electron beam lithography³⁶⁷, micro-contact printing³⁶⁸ self-assembly²⁵⁵⁻²⁵⁶, and several scanning probe microscopy (SPM) based lithography methods, such as dip-pen nanolithography³⁶⁹, nanografting³⁷⁰, nanoshaving³⁷¹, nanopipetting³⁷², and scanning near-field optical microscopy (SNOM) lithography³⁷³. For a comprehensive list of different patterning approaches and the resolution achieved, refer to table 3.

While significant advances have been made in the nanopatterning of some inorganic nano-objects like carbon nanotubes³⁷⁴ and gold³⁷⁵, challenges still exist in particular for protein nanolithography³⁷⁶. The main challenges in protein patterning are: obtaining a resolution below fifty nanometers³⁷⁶, achieving high writing speeds³⁴³, reducing costs, producing multiple functionalities coexisting on a single surface^{372,377}, preserving biological functionality³⁷⁷, and finding a robust and accessible technique that is compatible with a variety of substrates. Bioactivity is a particularly delicate problem, because denaturation, oxidation, and dehydration in air are common drawbacks that complicate many potential

protein nanopatterning techniques³⁷⁷. This also limits the choice of surfaces. For example, proteins directly chemisorbed onto gold tend to denature.

Most protein nanopatterning techniques are incapable of making features below 100 nm³⁷⁸ and only a few have been established for independently patterning multiple protein species on the same surface^{372,377}. Self-assembly techniques have achieved nanometer patterning of proteins²³⁴ but with the disadvantage that the proteins are arranged in regular arrays rather than in tailor-made patterns. Imprint lithography³⁷⁹ although is cost effective, every time a new pattern design is needed we need to remake the imprint stamp.

In summary we would like to have a robust protein patterning approach on polymers which has high resolution, has orthogonal functionality, maintains bioactivity, is substrate independent, has arbitrary geometry and the technique should have a possibility for massive parallelization. This work will introduce a new technique that achieves all the above requirements and demonstrates its viability.

| <u>Technique</u> | <u>Resolution (nm)</u> | <u>Reference</u> |
|---|------------------------|--|
| Self Assembly Approach | | |
| Particle Lithography | 60 | Y.Cai <i>et. al</i> ³⁸⁰ |
| Miceller Nano Lithography | 8 | M.Arnold <i>et. al</i> ²³⁴ |
| DNA Templating | ~ 5 | H.Yan <i>et. al</i> ³⁸¹ , S. H.Parket. <i>al</i> ³⁸² |
| Stamping Approach | | |
| Micro/Nanocontact Printing | ~ 70 | H. W.Li <i>et. al</i> ³⁸³ |
| Nanoimprint Lithography | 75 | J. D.Hoff <i>et. al</i> ³⁷⁹ |
| Scanning Probe Microscopy Approach | | |
| Nanografting Indirect | 10 | K.Wadu-Mesthrige <i>et. al</i> ³⁷⁰ |
| Indirect Dip-Pen Nanolithography | ~80 | K. B.Lee <i>et. al</i> ³⁶⁹ |
| Direct Dip-Pen Nanolithography | ~30 | D. L.Wilson <i>et. al</i> ³⁸⁴ |
| Nanopen | 250 | H.Taha <i>et. al</i> ³⁸⁵ |
| Conductive Atomic Force Microscopy | 20 | G.Agarwal <i>et. al</i> ³⁸⁶ |
| TCNL (Thermochemical Nano Lithography) | 15 | R.Szoszkiewicz <i>et. al</i> ³⁸⁷ |
| Other Techniques | | |
| Photolithography | ~500 | K. L. Christman <i>et. al</i> ³⁸⁸ |
| Electrospray Ionization And Coulomb Force Directed Assembly | 200 | A. M. Welle <i>et. al</i> ³⁸⁹ |
| Mechanical Mismatch—Cracks | 120 | X. Y. Zhu <i>et. al</i> ³⁹⁰ |

| | | |
|---|------|--|
| Chemical Vapor Deposition— Nanowires | ~20 | F. Patolsky <i>et. al</i> ³⁹¹ |
| Electron Beam Lithography | 50 | S.Kumagai <i>et. al</i> ³⁹² |
| Focused Ion Beam Lithography | 60 | A. A.Bergman <i>et. al</i> ³⁹³ |
| Scanning Ion-Conductance Microscopy | ~300 | A. Bruckbauer <i>et. al</i> ³⁷² |

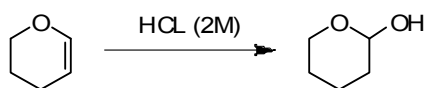
Table 3 Summary and classification of available nanopatterning techniques.

2. Materials and Methods

I. Materials, Synthesis and Characterization

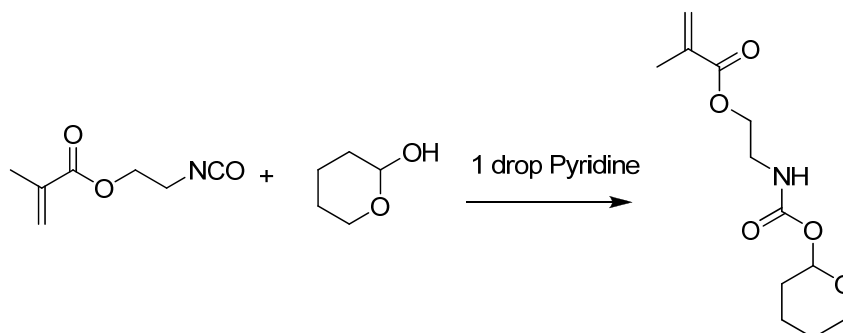
Chemicals used for synthesis were Dihydropyran (Aldrich), 2-isocyanatoethyl methacrylate (Aldrich), azobisisobutyronitrile (Aldrich), allyl bromide (Aldrich), potassium carbonate (VWR), platinum on activated carbon (10 % wt, Strem Chemicals), 4-hydroxybenzophenone (Alfa Aesar), and 3-chlorodimethyl silane (Alfa Aesar), and all solvents were reagent grade. All chemicals were used as received with the exception of chlorodimethylsilane, which was distilled under nitrogen immediately before use.

i. Synthesis of tetrahydropyran-2-ol



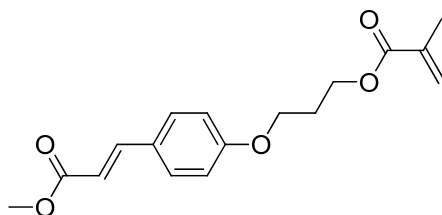
The synthesis of tetrahydropyran-2-ol was carried out according to a literature procedure³⁹⁴. The ¹H NMR spectrum was consistent with values reported in the literature³⁹⁴.

ii. Synthesis of tetrahydropyran-2-yl N-(2-methacryloxyethyl)carbamate



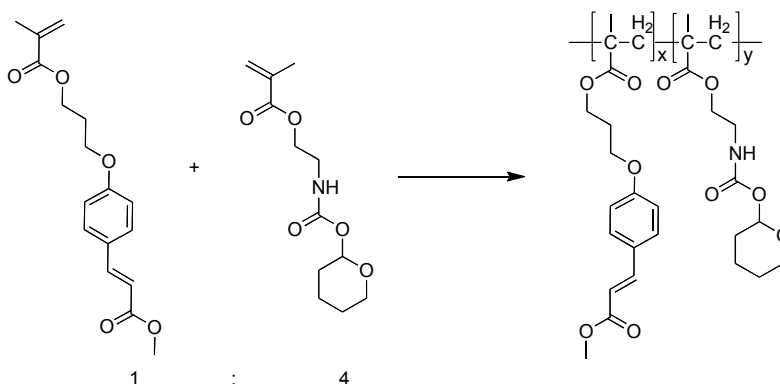
Tetrahydropyran-2-yl (2.80 mL, 28 mmol) was mixed with 2-isocyanatoethyl methacrylate (3.1 g, 20 mmol) and 1 drop of pyridine and stirred until the reaction was complete by ¹H NMR. The resulting viscous mixture was purified by column chromatography on silica to yield a white powder (2.93 g, 57 %). ¹H-NMR (300 MHz, CDCl₃): δ (ppm) 6.09 (m, 1H), 5.9 (broad, 0.2 H, minor conformer), 5.82 (broad, 0.8 H, major conformer), 5.57 (apparent quint, *J* = 1.5 Hz, 1H), 5.05 (broad, 0.8 H, major conformer *N-H*), 4.83 (broad, 0.2 H, minor conformer *N-H*), 4.21 (t, *J* = 6 Hz, 2H), 3.86 (ABXY m, *J*_{AB} = 11.5 Hz, *J*_{AX} = 4.8 Hz, *J*_{AY} = 5.1 Hz, 1H), 3.63 (ABXY m, *J*_{AB} = 11.5 Hz, *J*_{AX} = 8.6 Hz, *J*_{AY} = 3.0 Hz, 1H), 3.49 (q, *J* = 6 Hz, 2H), 1.91 (dd, *J* = 1.5, 0.9 Hz, 3H), 1.77 (apparent dd, *J* = 9.7, 2.7 Hz, 2H), 1.48-1.68 (m, 4H); ¹³C-NMR (75 MHz, CDCl₃): δ (ppm) 167.2, 155.0, 135.9, 126.0, 93.3, 63.5, 63.3, 40.0, 29.3, 24.8, 19.0, 18.2; Analysis (calc d, found for C₁₂H₁₉NO₅): C (56.02, 56.22), H (7.44, 7.36) N (5.44, 5.48).

iii. Synthesis of methyl 4-(3-methacryloyloxypropoxy)cinnamate

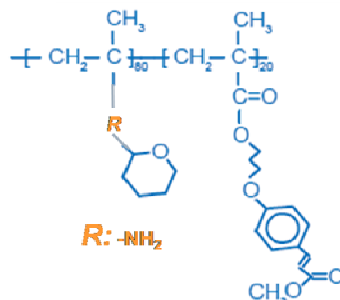


The synthesis of methyl 4-(3-methacryloyloxypropoxy)cinnamate was carried out according to a literature procedure³⁹⁵. ¹H NMR spectral features were consistent with reported values.

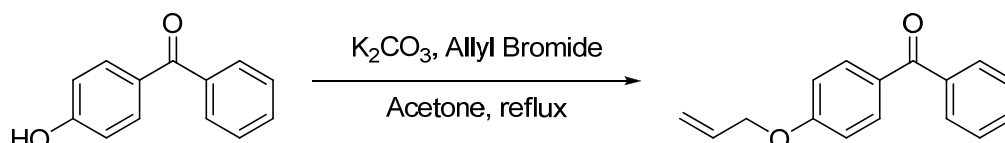
iv. Synthesis of poly((tetrahydropyran-2-yl N-(2-methacryloxyethyl)carbamate)-co-(methyl 4-(3-methacryloyloxypropoxy)cinnamate))



A mixture of tetrahydropyran-2-yl N-(2-methacryloxyethyl)carbamate (0.50 g, 1.9 mmol), methyl 4-(3-methacryloyloxypropoxy)cinnamate (0.15 g, 0.48 mmol), and azobisisobutyronitrile (AIBN) (2.0 mg, 0.012 mmol) in THF (6 mL) were added to a Schlenk ampoule using a Pasteur pipette. The flask was then freeze-pump-thawed a minimum of four times and the reaction mixture was heated at 60 °C for 20 h. Once the reaction mixture had returned to room temperature it was diluted with dichloromethane (30 mL) and added drop wise to hexanes (300 mL). The resulting precipitate was removed by vacuum filtration and dried under vacuum to yield a white powder (360 mg, 55 %). ¹H-NMR (300 MHz, CDCl₃): δ (ppm) 7.6 (d broad, $J = 16.1$ Hz, 1H), 7.5 (s broad, 2H), 6.9 (s broad, 2H), 6.3 (d broad, $J = 16.1$ Hz, 1H), 5.7-6.0 (m broad, 5.2 H), 3.3-4.2 (four apparent singlets broad, 27.2 H), 0.7-2.1 (several m broad, 50.6 H); ¹³C-NMR (75 MHz, CDCl₃): δ (ppm) 177.1, 167.8, 160.4, 155.3, 144.5, 129.8, 128.1, 127.8, 127.4, 127.2, 115.3, 114.8, 93.3, 63.6, 53.9, 51.6, 45.0, 44.7, 39.6, 39.5, 28.0, 25.0, 19.1, 17.4. Note: The ¹H-NMR spectrum is reported as observed, with integration relative to the peak at 7.5 ppm (2H, due to aromatic protons in the cinnamate group). The N-H protons were not observed in the spectrum of the polymer. Analysis (calc d, found for C₆₅H₉₆N₄O₂₅ (1: 4 cinnamate: carbamate monomer ratio)): C (58.55, 57.83), H (7.26, 7.20), N (4.20, 4.12). The results of the ¹H-NMR spectrum would suggest carbamate content slightly lower than the one expected for a cinnamate: carbamate feed ratio of 1: 4, whereas the elemental analysis (based on carbon) would suggest a higher content of the carbamate component. Below is the final structure of the polymer.

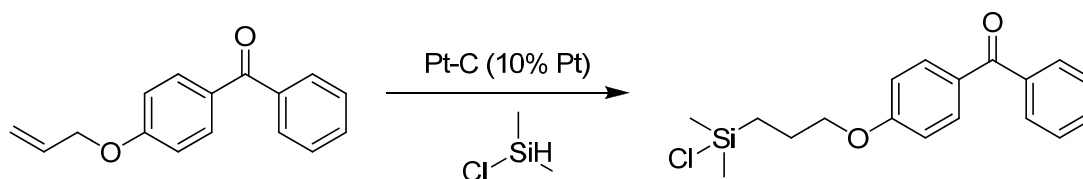


v. Synthesis of 4-allyloxybenzophenone



The synthesis of 4-allyloxybenzophenone was carried out according to a literature procedure³⁹⁶. ¹H and ¹³C NMR spectra were consistent with values reported in the literature³⁹⁶.

vi. Synthesis of 4-(3-(chlorodimethylsilyl)propoxy)benzophenone



Synthesis of 4-(3-(chlorodimethylsilyl)propoxy)benzophenone was carried out according to a literature procedure³⁹⁶. ¹H and ¹³C NMR spectra were consistent with values reported in the literature³⁹⁶.

vii. Binding of 4-(3-(chlorodimethylsilyl)propoxy)benzophenone to glass substrates

A procedure similar to the one reported in the literature was employed³⁹⁶. Specifically, several 75 × 25 mm² glass slides were cut into 25 × 25 mm² squares then cleaned with either piranha (75 % concentrated H₂SO₄ and 25 % of 30 % H₂O₂ in water) or oxygen plasma. The slide was placed in anhydrous toluene (~50 mL) under argon and a solution of 4-(3-(chlorodimethylsilyl)propoxy)benzophenone in toluene (3 mL, ca. 0.28 M) was added along with five drops of anhydrous triethylamine. The slides were left in the solution overnight. The slides were then washed with chloroform then dried with N₂. The presence of the benzophenone was confirmed by measuring the water contact angle of the treated glass slides, which was found to be around 70°, consistent with literature values³⁹⁷.

II. Transmittance Fourier Transformed Infrared Spectroscopy (FTIR) Spectra of the Polymer upon Bulk Heating

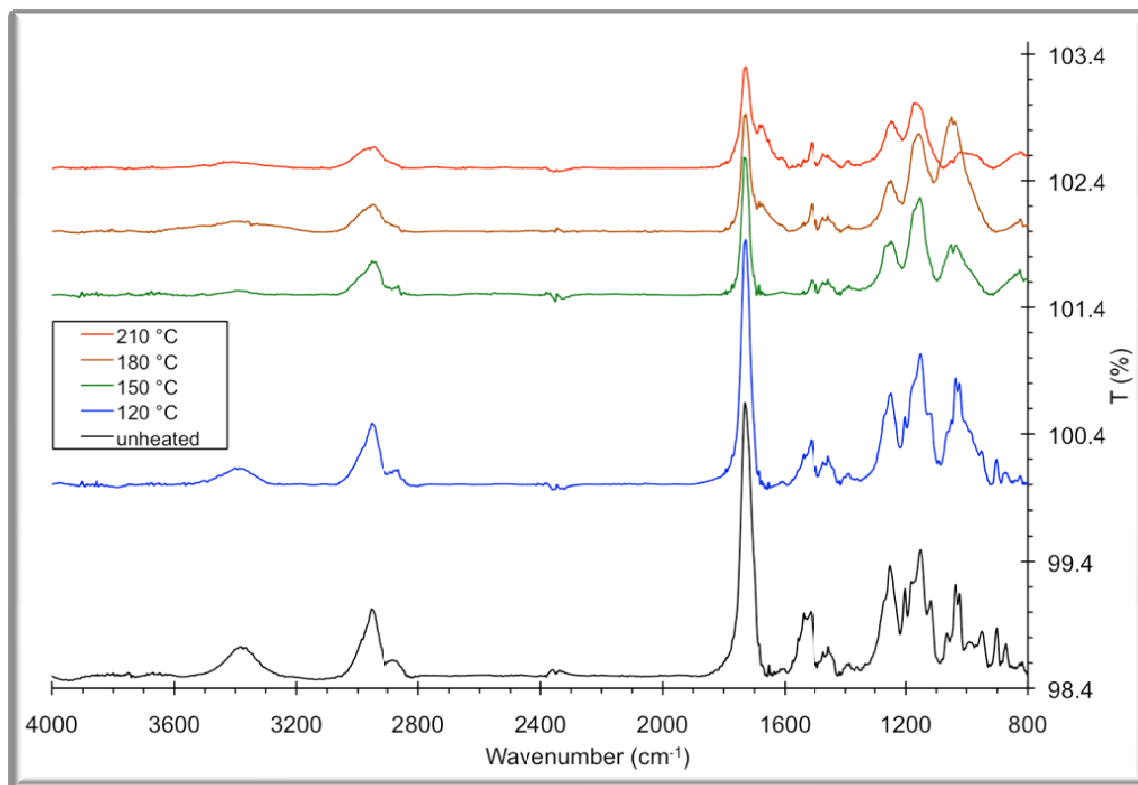


Figure 44 Transmittance FTIR spectra of the polymer upon bulk heating. The decrease in the peak at 1725 cm^{-1} starting at $150\text{ }^{\circ}\text{C}$ is consistent with the loss of the protecting group (carbamate carbonyl group).

The spectra were obtained by external reflection FTIR (Perkin Elmer Spectrum 1000 FT-IR spectrometer equipped with the Perkin Elmer Fixed Angle Specular Reflectance accessory, angle of incidence = 16°) in a N_2 atmosphere. The spectra have been rigidly shifted on the vertical axis for clarity. Several samples of polymer film were prepared as described under “Polymer film preparation”, except silicon wafers (cleaned in O_2 plasma) were used as substrates and the benzophenone treatment step was not performed. Each sample was treated on a preheated hot plate (VWR Signature 815-HPS digital hot plate stirrer) at the desired temperature for 30 minutes (automated shut-off timer) and left on the plate as it cooled to room temperature. The decrease in the peak at 1725 cm^{-1} starting at $150\text{ }^{\circ}\text{C}$ is consistent with the loss of the carbamate carbonyl group. The peak in this spectral region is not expected to disappear entirely, as other carbonyl containing functionalities are present in the polymer (Figure 44) and should not be affected by the thermal treatment. The reduction in intensity for the bands in the region from $2800 - 3000\text{ cm}^{-1}$, due to C-H stretching modes, when the temperature increases is also consistent with the loss of the tetrahydropyranyl (THP) group. The weakening of the broad band around 3400 cm^{-1} , due to N-H stretching modes, would not be expected for a transformation that creates a primary amine. However, this change could be explained by a further broadening of the peak because of hydrogen bonding. Additional experiments would be needed to confirm the

assignment of this band. More direct evidence for the formation of a primary amine is the appearance of a new band at 1670 cm^{-1} , which is likely due to N-H bending, in the spectra of samples treated at $180\text{ }^{\circ}\text{C}$ and above.

III. Atomic Force Microscopy with Thermal Cantilevers

Local heating, imaging, friction and phase measurements were all carried out with the same atomic force microscope (AFM, by Nanoscope Multimode IV, Veeco) using resistively heated cantilevers³⁹⁸ and commercial cantilevers (Nanosensor, SSS-NCHR) in air. Local chemical modifications were performed by scanning the sample with an AFM tip heated at temperatures in the range $160\text{-}240\text{ }^{\circ}\text{C}$, in contact mode with normal loads in the range $20\text{-}500\text{ nN}$, at a speed varying between $0.01\text{-}2\text{ mm/s}$ (Figure 45). The temperature calibration of the thermal cantilevers was performed following the procedure established by our collaborator W. King³⁹⁹. All the TCNL amine patterns shown in this study were made using thermal AFM tips heated at selected temperatures in ambient condition (room temperature $24\text{ }^{\circ}\text{C}$, relative humidity $20\%\text{-}50\%$). The nominal spring constant of the thermal AFM cantilevers is about 0.5 N/m . All the AFM topography and phase images were recorded in ambient conditions using an ultra sharp AFM tip (Nanosensor, SSS-NCHR, resonant frequency: 312 kHz , spring constant: 37 N/m) at a drive frequency close to its resonance frequency.

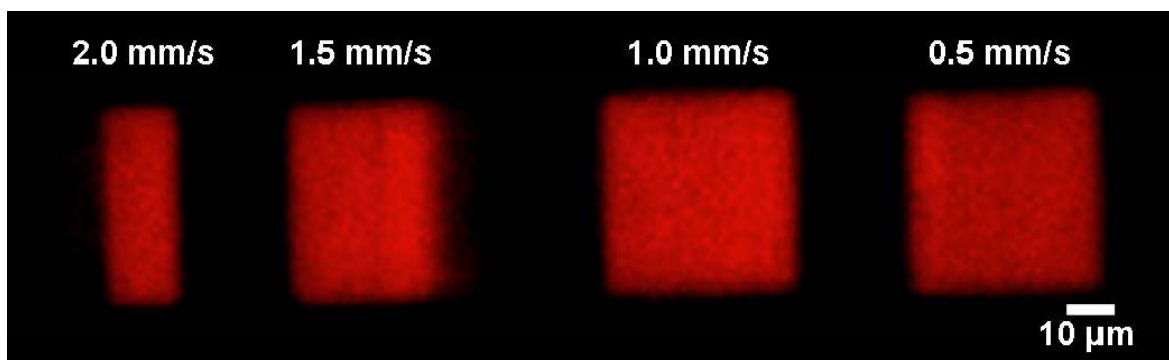


Figure 45 Fluorescence micrograph of a surface with four rectangular TCNL micropatterns written at linear speeds of $0.5, 1, 1.5, 2\text{ mm/s}$ respectively, with a normal load of 100 nN and with a tip temperature of $T = 220\text{ }^{\circ}\text{C} \pm 20\text{ }^{\circ}\text{C}$. The patterning was performed in ambient conditions (air). For visualization, the patterns were functionalized with the protocol of NHS/Bn+Cy5/SAv (For protocols refer to results section on protein patterning)

IV. Fluorescence Microscopy

Epi-fluorescence microscopy was performed on an inverted Nikon TE2000 microscope equipped with a Nikon Intensilight (C-HGFIE) for illumination and a Nikon EMCCD camera (DQC-FS). Images were obtained using a Plan Apo 60x water immersion objective (Nikon, NA 1.2) or a Plan Apo 100x oil immersion objective (Nikon, NA 1.4). Nikon filter cube sets were used to image fluorescent dyes in the region of UV (#96310, UV-2EC DAPI filter set, excitation $340\text{-}380\text{ nm}$, dichroic mirror DM400, emission $435\text{-}485\text{ nm}$), in the green (#96320, FITC/GFP HyQ filter set, excitation $460\text{-}500\text{ nm}$, dichroic mirror DM505,

emission (510-560 nm), and in the red (#96324, Cy5 HQ filter set, excitation 620-660 nm, dichroic mirror (DM Q660LP, emission 700-775 nm).

V. Thermogravimetric Analysis

Thermogravimetric Analysis or TGA is a type of testing that is performed on samples to determine changes in mass in relation to change in temperature⁴⁰⁰. Such analysis relies on a high degree of precision in three measurements: weight, temperature, and temperature change. TGA is commonly employed in research and testing to determine characteristics of materials such as polymers, to determine degradation temperatures, absorbed moisture content of materials, the level of inorganic and organic components in materials, decomposition points of explosives, and solvent residues. It is also often used to estimate the corrosion kinetics in high temperature oxidation.

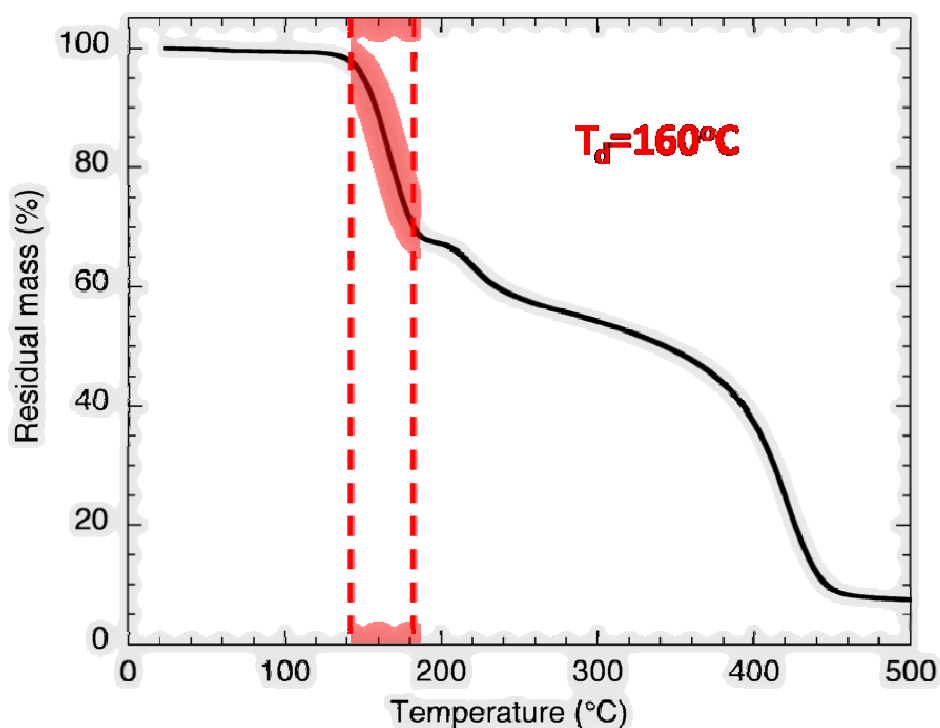


Figure 46 Thermogravimetric analysis of TCNL polymer. The transition temperature T_d at 160°C is highlighted in the graph.

Upon heating (rate: 5 °C/min), the polymer sample (poly((tetrahydropyran-2-yl N-(2-methacryloxyethyl)carbamate)-co-(methyl 4-(3-methacryloyloxypropoxy)cinnamate))) exhibits an initial weight loss around 150 °C and a subsequent one starting at about 200 °C. The T_d continuum may be due to different conformations of the polymer or the result of the carbamic acid intermediate formed due to pyrolysis stabilization. The carbamic acid would most likely be less stable than the original carbamate precluding it from requiring a higher temperature of decomposition. As shown in the schematic in Figure 47, the overall mass loss is consistent with the unmasking of the amine groups in the carbamate side chains.

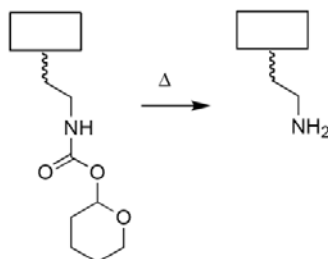


Figure 47 Schematic of the expected chemical change in the TCNL polymer at transition temperature T_d .

VI. Cell Culture and Immunostaining

Jurkat cells (clone E6-1, ATCC TIB-152) of passage 9 were maintained in RPMI-1640 media with 10% FBS, 1% L-glutamine, 1% non-essential amino acid solution, 1% sodium pyruvate, 10 mM HEPES. The cell culture media and its components were obtained from Mediatech, Inc. The cells were maintained at 37°C in a 5% CO₂ atmosphere.

Jurkat cells were seeded on anti-CD3 patterned surfaces and incubated at 37°C and 5% CO₂ for 40 min in the media containing 10 μg/ml ICAM-1. To prepare the cells for staining, they were permeabilized in 0.1% Triton X-100 (EMD Chemicals) in 3% paraformaldehyde for 5 minutes, followed by washing with PBS and incubation for 30 minutes in 3% paraformaldehyde. Non-specific binding was blocked by incubation with 1% BSA (Calbiochem) in PBS for 30 minutes. To label the PKC- θ in the cells, polyclonal anti-PKC- θ (BD Biosciences) was used as primary antibody, and Goat anti-Mouse IgG, FITC conjugate (Millipore) was used as secondary antibody. The cells were mounted in elvanol before imaging.

VII. Proteins and Reagents

Proteins and chemicals used for patterning and visualization were as follows: Recombinant Human ICAM-1/CD54/Fc Chimera (R&D Systems, 720-IC); Cy5 (PE-Cy5) anti-human CD3 and Affinity Purified anti-human CD3 (eBioscience Inc, 15-0038 and 14-0038); Bovine plasma fibronectin (EMD Biosciences Inc, 341631); Streptavidin-Cy5 (Invitrogen Corporation, 43-4316); purified anti-Human PKC- θ (BD Biosciences, 610089); Goat anti-Mouse IgG, Cy5 conjugate (Millipore, AP124S); Goat anti-Mouse IgG, FITC conjugate (Millipore, 12-506); anti-ICAM-1, FITC conjugated, clone 15.2 (Millipore, CBL450F); Alexa Fluor 350 carboxylic acid, succinimidyl ester (Invitrogen Corporation, A-10168); Atto488-NHS ester (Sigma-Aldrich, 41698); N-(7-dimethylamino-4-methylcoumarin-3-yl)maleimide (DACM) (AnaSpec Inc, 81403); N-succinimidyl 3-(2-pyridyldithio) propionate (SPDP) (Pierce Biotechnology, 21857); Dithiothreitol (DTT) (Pierce Biotechnology, 20290); D-biotin, succinimidyl ester (Invitrogen Corporation, B-1513); bovine serum albumin (BSA) (EMD Biosciences Inc, 12659); Streptavidin–Maleimide from *Streptomyces avidinii* (Sigma-Aldrich, S9415); Biotin Conjugated F(ab')₂ Fragment (Rockland Immunochemicals Inc, 709-1617); Streptavidin (Rockland Immunochemicals Inc, S000-01); Glutaraldehyde (50%, Electron Microscopy Sciences, 16316). Fluorescent labeling of the proteins was performed as per the manufactures' recommended procedures.

VIII. Polymer Film Preparation

Slides treated with 4-(3-(chlorodimethylsilyl)propoxy)benzophenone (25 × 25 mm²) as described above were then covered with a 20mg/ml solution of poly((tetrahydropyran-2-yl N-(2-methacryloxyethyl)carbamate)-co-(methyl 4-(3-methacryloyloxypropoxy)cinnamate)) in cyclohexanone. The slides were spun at 1000 RPM for 2 minutes. The slides were exposed to 352 nm radiation for one hour to activate the benzophenone moiety and attach the polymer to the surface, then to 300 nm radiation for approximately 45 minutes to crosslink the polymer via dimerization of the cinnamate moieties. Films were prepared with thicknesses ranging from 30 – 150 nm, though most experiments were performed on films with a thickness of 75 ± 5 nm, as measured by a stylus profilometer.

IX. Polymer Film Deposition on the QCM Crystal and Glass Slides

The methylacrylate copolymer (poly((tetrahydropyran-2-yl N-(2-methacryloxyethyl)carbamate)-co-(methyl 4-(3-methacryloyloxypropoxy) cinnamate))) containing tetrahydropyran (THP) was spin coated on the QCM crystal for 120 seconds at 3000 RPM. The concentration of the polymer solution used for spinning was 20mg/ml. The crystals were then treated with 4-(3'-chlorodimethylsilyl) propoxy benzophenone and exposed to ultraviolet radiation to both covalently bind the film to the substrate through the benzophenone linker (350 nm irradiation) and to crosslink the polymer at the cinnamate moieties (300 nm irradiation). Stylus profilometry performed after drying the polymer coated surfaces showed that the average thickness of polymer film on the crystals was 38 ± 6 nm. For most of the experiments performed on the glass slides the average thickness of the polymer that was coated was 75 nm.

3. Results and Discussion

I. Protein Patterning with Thermochemical Nanolithography (TCNL)

TCNL employs a resistively heated AFM tip^{387,398} to thermally activate a chemical reaction at the nanometer scale on the surface of a material, for example by local thermal de-protection of a chemical moiety in the film of a specifically-designed polymer. In our work we use a heated AFM tip^{387,398} that can be used to thermally activate the de-protection of amine groups on a polymer surface in arbitrary nano- and micro-patterns at speeds of up to 2 mm/s. This speed is faster than the speed of other AFM-based patterning approaches. For example TCNL is over 10^6 times faster than dip-pen nanolithography (performed with a single tip) and 10^3 times faster than thermal dip-pen nanolithography⁴⁰¹⁻⁴⁰². The unmasked amine nanotemplates are then selectively and covalently functionalized to create chemical patterns of thiols, maleimides, aldehydes or biotins in distinct areas of the polymer surface (Figure 48).

Previously, our co-workers demonstrated that TCNL is able to pattern 12 nm features of carboxyl groups on a copolymer surface³⁸⁷. In the present work, we extend the capabilities of TCNL by introduction of a new polymer to enable the selective patterning of amine groups. Our collaborators synthesized a methacrylate copolymer containing tetrahydropyran (THP) carbamate groups that can be thermally deprotected to unmask a primary amine. The mass loss after bulk heating of the polymer above the deprotection temperature, T_d , is consistent with this mechanism (Refer to TGA analysis, Figure 46 in Materials and Methods). Deprotection can be performed with a hot AFM tip maintained above T_d (between 150°C and 220°C), thus exposing amine groups.

This approach can be used, when combined with post-TCNL functionalization steps, to create multi-functional chemical nanopatterns coexisting on the same surface, which later can be selectively functionalized with the desired species of nano-objects. The approach is conceptually simple, as outlined in Figure 48 and Figure 49, after using TCNL to write the first of the desired amine patterns, the deprotected amines can be thiolated via a reaction with N-succinimidyl 3-(2-pyridyldithio) propionate (SPDP) (Figure 48). A second TCNL pattern can then be created on a different area of the same polymer surface (diamonds in Figure 48), exposing additional amines in a new region. The di-thiols obtained after the first patterning step are then reduced to thiols using dithiothreitol (DTT)⁴⁰³, thereby producing a surface with tailored patterns of amine and thiol groups.

Alternately, we can transform the amine pattern from the second application of TCNL, using N-hydroxysuccinimide (NHS)-biotin, thus modifying the amine functionality to biotin. At this stage, reduction with DTT can create a co-patterned surface of thiols and biotins. In order to nanopattern surfaces with three different functionalities (Figure 48c), a third application of TCNL produces a triple-patterned surface consisting of thiols, biotins, and amines.

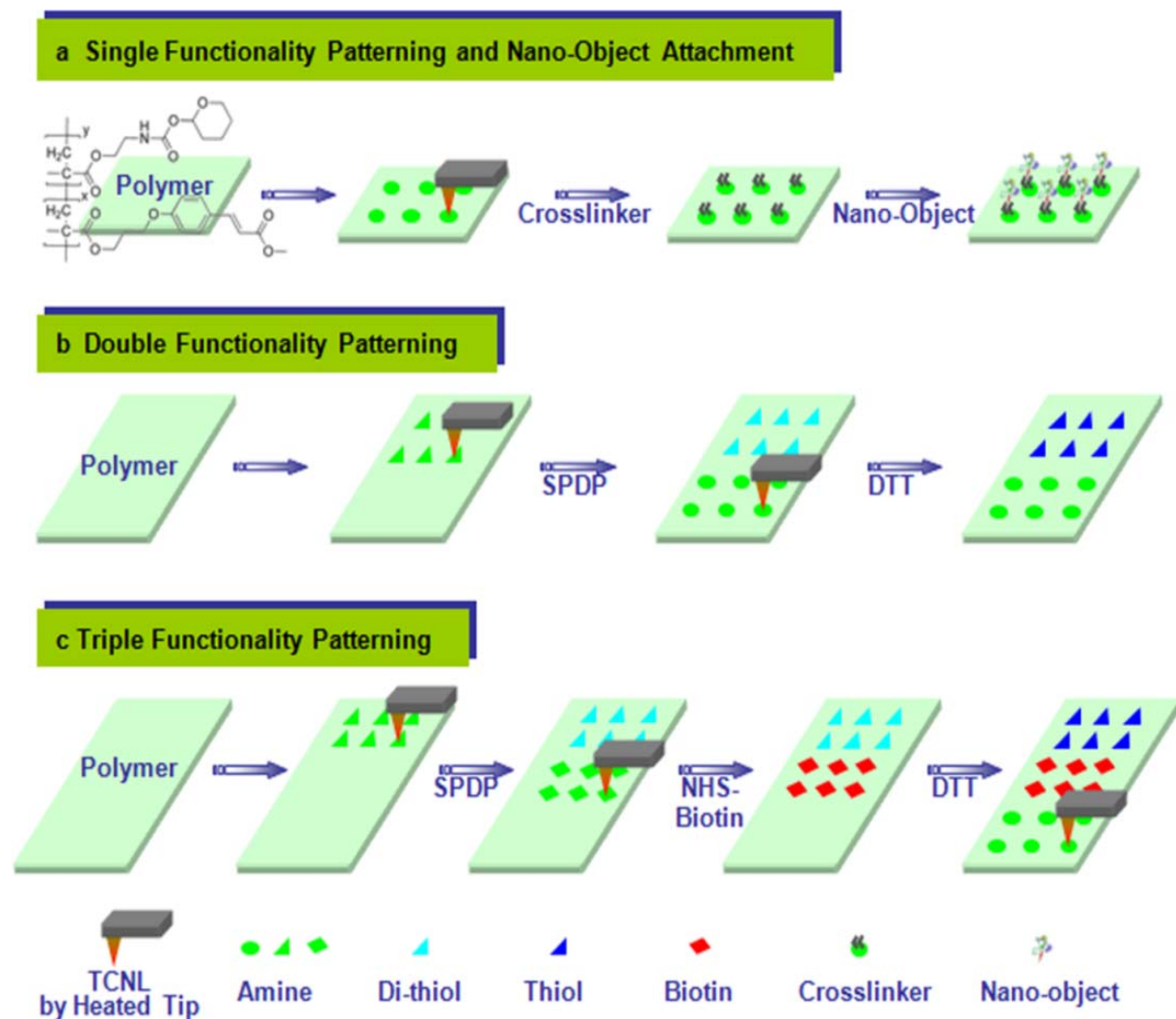


Figure 48 Schematic of TCNL patterning procedure. (a) A nanoarray of one type of nano-object is created in three steps: TCNL, crosslinker incubation and nano-object immobilization. (b) A double functionality pattern of thiols (blue triangles) and amines (green disks) is created through two rounds of TCNL and one or two rounds of incubation (post-TCNL functionalization). (c) A triple functionality pattern of thiols (blue triangles), biotins (red diamonds), and amines (green disks) is created through three rounds of TCNL and two rounds of incubation.

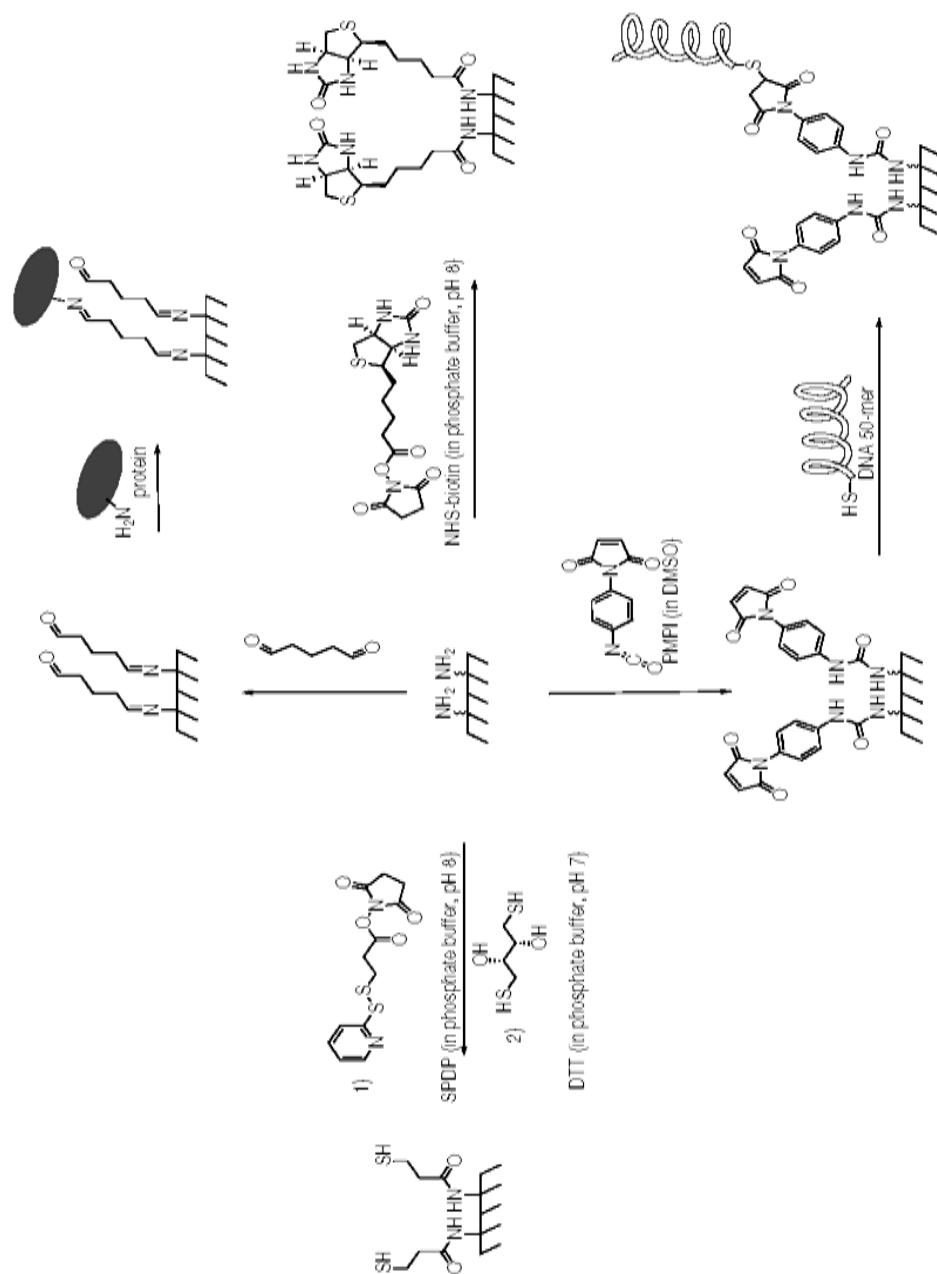


Figure 49 Flowchart illustrating how the unmasked amine nanotemplates are selectively and covalently functionalized to create patterns of thiols, maleimides, aldehydes or biotins in distinct areas of the polymer surface.

II. TCNL Micropatterns of One Protein Species

Several different approaches have been developed to immobilize proteins or other nano-objects to the nanotemplates produced by TCNL. Working demonstrations of these strategies are described in this section.

i. Protein Micropatterning with Glutaraldehyde Crosslinking

The homobifunctional crosslinking reagent glutaraldehyde was used to covalently bind proteins to TCNL patterns. As shown in the schematic in Figure 50 below, glutaraldehyde can react with primary amine groups to create Schiff bases. The Schiff base intermediate may form resonance stabilized products with α , β -unsaturated aldehydes of the glutaraldehyde (GA), predominantly at basic pH values. At alkaline pH values, the aldehyde groups form intermediate Schiff bases with available amine groups on the TCNL patterns. These aldehydes then react to bind with the lysine amino acids within the protein of interest. This is a workable strategy since in most proteins, lysines are present on the outer portion of the protein, and it has been observed that binding using the lysine portion of the protein will not in general affect the protein function. The main disadvantage of this procedure is that such binding procedure is not site specific and we cannot achieve uniform or ideal orientation of the protein on the surface.

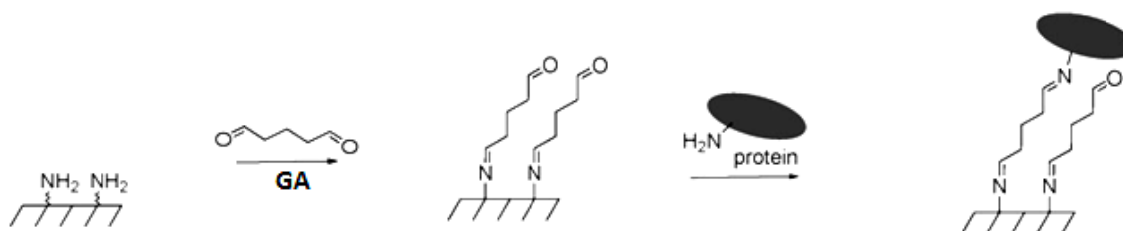


Figure 50 Mechanism of Schiff base formation on the deprotected substrate and subsequent protein binding using glutaraldehyde as a crosslinker.

As shown in Figure 51, to demonstrate the attachment of proteins to TCNL patterns using glutaraldehyde as a crosslinker, we bound fibronectin (Fn) and streptavidin (SAv) to the TCNL patterns in two different experiments. Patterns of unmasked amines were established via TCNL. They were then treated with 50% GA (Electron Microscopy Science Inc) for 60 minutes, washed with deionized water and then incubated with Atto488-labeled fibronectin (400 μ g/ml). In the streptavidin binding process, the last step was changed to incubating with Cy5 labeled streptavidin (1 mM). After incubation with the protein for 90 minutes, the surfaces were washed with deionized water to remove any non-specifically bound protein.

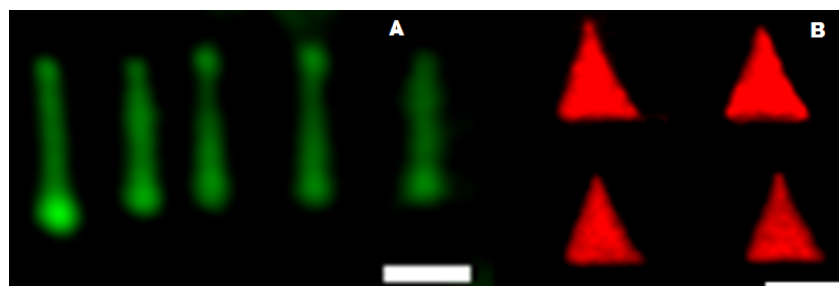


Figure 51 (A) Fibronectin patterns patterned in the form of lines labeled with Atto488. The triangles in part (B) of the image are labeled with Cy5 Streptavidin. The scale bar is 500 nm and 5 μ m for (A) and (B) respectively.

ii. Biotin-Streptavidin Based Protein Labeling

The high affinity of avidin for biotin was first exploited in histochemical applications in the mid-1970's⁴⁰⁴. This egg-white protein and its bacterial counterpart, streptavidin, have since become standard reagents for diverse detection schemes⁴⁰⁵. Streptavidin is ~53 Kda tetrameric proteins purified from the bacterium *Streptomyces avidinii*. It finds wide use in molecular biology through its extraordinarily strong affinity for biotin (also known as vitamin H); the dissociation constant (K_d) of the biotin-streptavidin complex is on the order of $\sim 10^{-14}$ mol/L, ranking among one of the strongest non-covalent interactions known in nature. The strong streptavidin-biotin bond can be used to attach various biomolecules to one another or onto a solid support.

Here we create TCNL micro patterns exploiting biotin-streptavidin binding. We also show that we can use TCNL surfaces for hierarchal architectures. Functionalization of the deprotected amines is achieved by treating the sample with 1 mM NHS-biotin for 30 minutes. The sample was then washed with deionized water and incubated with 1mM Cy5-streptavidin for 60 minutes. To further attach proteins, biotinylated proteins such as biotin-antiCD3 (labeled with alexa350) were attached to the streptavidin bound on the pattern. Figure 52 below shows a fluorescence image of a surface at the end of the post-functionalization showing fluorescence both from the Cy5-streptavidin (red triangles) and the alexa350-antiCD3 (blue triangles), bound on the streptavidin patterns.

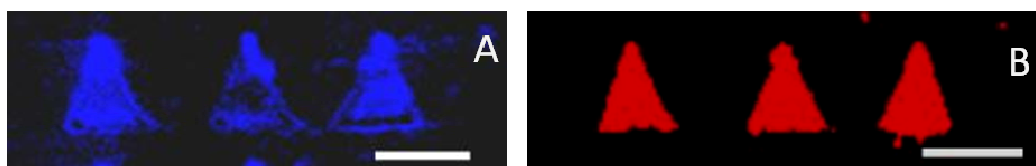


Figure 52 (A) alexa350 labeled biotin-antiCD3 patterns. The same triangles were labeled with Cy5 streptavidin before binding with biotin-antiCD3. The Cy5 fluorescence can be observed in image (B).

iii. Protein Labeling and SH Creation

Sulfhydryl (SH) groups are useful for variety of applications including protein binding and nano-bio-electronic studies because of the simplicity to bind them with gold. In order to create SH groups on TCNL deprotected amine patterns, we employed SPDP (*N*-Succinimidyl 3-(2-pyridyldithio)-propionate, Figure 53A), a heterobifunctional, thiol-cleavable crosslinker⁴⁰⁶. It contains an amine-reactive *N*-hydroxysuccinimide (NHS) ester that will react with amine patterns to form a stable amide bond. The other end of the spacer arm is terminated in the pyridyl disulfide group that will react with sulfhydryls to form a reversible disulfide bond. This disulfide bond can be converted to SH by reduction using DTT (dithiothreitol, Figure 53B).

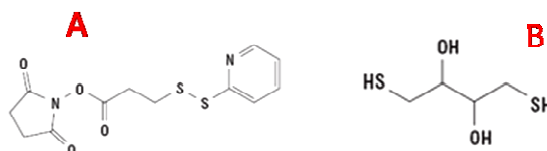


Figure 53 Chemical structure of (A) SPDP (*N*-Succinimidyl 3-(2-pyridyldithio)-propionate) and (B) DTT (dithiothreitol).

In order to covalently couple the thiol groups to the amines, the TCNL sample was treated with SPDP (1 mM, phosphate buffer, pH 8) for 60 minutes followed by a washing step and subsequent incubation with DTT (1 mM, phosphate buffer saline, pH 7) for 30 minutes. The presence of the thiol groups is then verified by a thiol-specific reaction with maleimide-streptavidin (1 mg/ml), which is incubated with the washed surface for 30 minutes. We then follow steps described in section (II-ii) above and label the streptavidin with biotinylated-anti-CD3 which is also labeled with alexa350. Figure 54 shows the final fluorescent blue pattern shows the bound anti-CD3 to the thiolated surface.

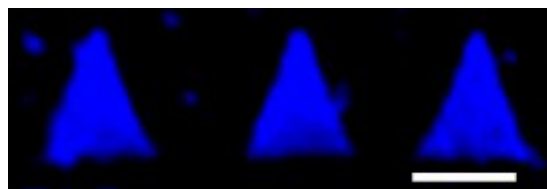


Figure 54 Alexa350 labeled anti-CD3 bound to SH groups created on TCNL patterns. The scale bar is 5 μ m.

III. Multi-Protein Micro Patterns (Orthogonal Functionality)

Creating multiple functionalities and thereby patterning multiple proteins is important for multiple applications including immunological and cell biology studies. Especially of our interest is patterning IgG and Complementary proteins at high resolution to understand how the synergetic effect helps to increase the efficacy of phagocytosis. Moreover surfaces comprising multiple signaling proteins patterned into distinct regions on cellular and sub-cellular length scales would be useful for the study of the complex, spatially organized receptor–ligand interactions that occur in many cell–cell and cell–extracellular matrix contacts. Here we show that we can create multi-functionalities or orthogonal chemical functionalities with arbitrary shapes at high resolution and then use them to pattern multiple proteins.

i. Chemical Dual Functionality

One of the key advantages of TCNL is the ability to perform serial patterning. Since we have a bottom up approach in TCNL patterning, we can perform patterning multiple types on the same substrate. Here we exploit this to create multiple chemical functionalities with arbitrary designs. In order to demonstrate this capability a co-pattern of biotin-functionalized diamonds and thiol-functionalized triangles were created as shown in the figure below. This dual functionality can be used to pattern multiple proteins or in principle, other advanced materials. The biotin/thiol co-patterns in Figure 55 are created with the following protocol: the substrate is initially patterned via TCNL, forming deprotected amines in the triangular array. The substrate is then incubated with SPDP (1 mM, phosphate buffer, pH 8) for 60 minutes. The substrate is then washed and dried. This is followed by a second round of TCNL patterning, to create the diamond array of amine groups. At this intermediate stage, the surface consists of a co-pattern of di-thiol groups (triangles) and amines (diamonds). The amines are then functionalized with biotin by reaction with NHS-biotin (1 mM, phosphate buffer, pH 8) for 30 minutes. Lastly, following a washing step, the di-thiols are reduced to

thiols using DTT (10 mM, phosphate buffer saline, pH 7, 30 min incubation). To label the thiol and biotin co-pattern, the surface was incubated with maleimide containing dye DACM (1 mM, phosphate buffer, pH 7) and then Cy5-streptavidin (1mM).

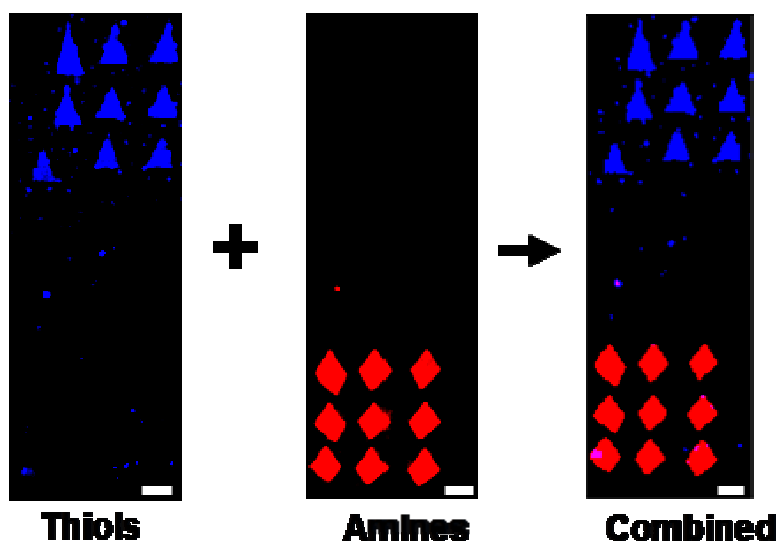


Figure 55 Epi-fluorescence image of DACM and Cy5-streptavidin orthogonal functionality patterns on the same surface. Blue DACM was crosslinked to amine-terminated triangles by means of SPDP-DTT thiolation, while red Cy5-streptavidin was crosslinked to amine-terminated diamonds by means of NHS-biotin. The scale bar is 5 μm .

ii. Two Protein Patterning

In order to demonstrate that we can use the chemically orthogonal patterns to pattern multiple proteins, we patterned an adhesion protein and an antibody. Figure 56 shows an adhesion protein (ICAM-1) and an antibody (anti-CD3) bound to the surface. The substrate is initially patterned via TCNL, forming deprotected amines in the triangular array or creating the inner square in the concentric square pattern. The substrate is then incubated with 1 mM NHS-biotin for 45 minutes, followed by a wash and drying step. This is followed by a second round of TCNL patterning, to create the diamond array or outer square (for the concentric pattern) of patterned amine groups. At this stage we have two functional groups on the surface (biotins and amines). This substrate was then incubated in GA followed by incubation with ICAM-1 (100 $\mu\text{g/ml}$) for 60 minutes. The substrate is then incubated with bovine serum albumin BSA (1 mg/ml) to prevent non-specific interactions and block any free aldehyde functionalities on the surface. The surface was then incubated in streptavidin (1 mg/ml) for 60 minutes followed by an incubation with biotin anti-CD3 labeled with Cy5 (200 $\mu\text{g/ml}$) for 120 minutes. Finally the ICAM-1 was fluorescently labeled by incubating the sample with Anti-ICAM-1 (FITC). Note this is also a positive result for the bioactivity of GA-bound ICAM-1. Optimization of the protein concentrations and incubation times is still work in process.

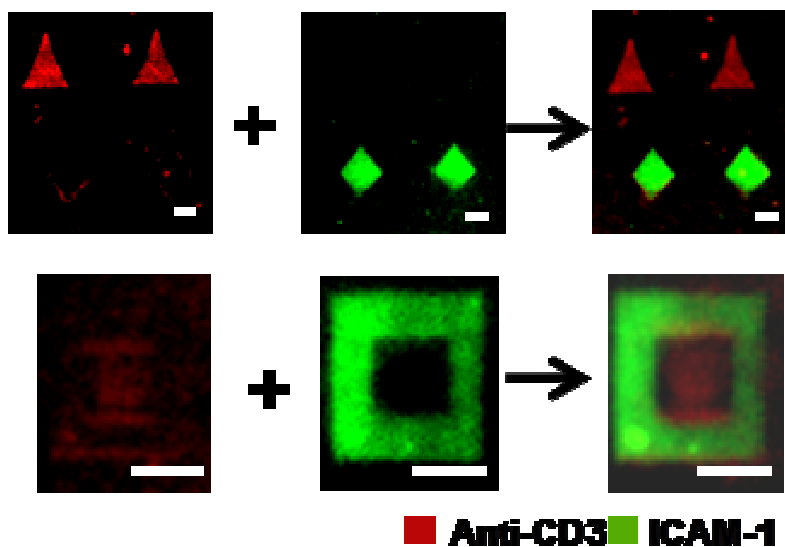


Figure 56 Anti-CD3 and ICAM-1 closely co-patterned on a single surface. These images show how we can pattern the proteins in arbitrary designs. Scale bars: 5 μm .

IV. Protein Nano Arrays

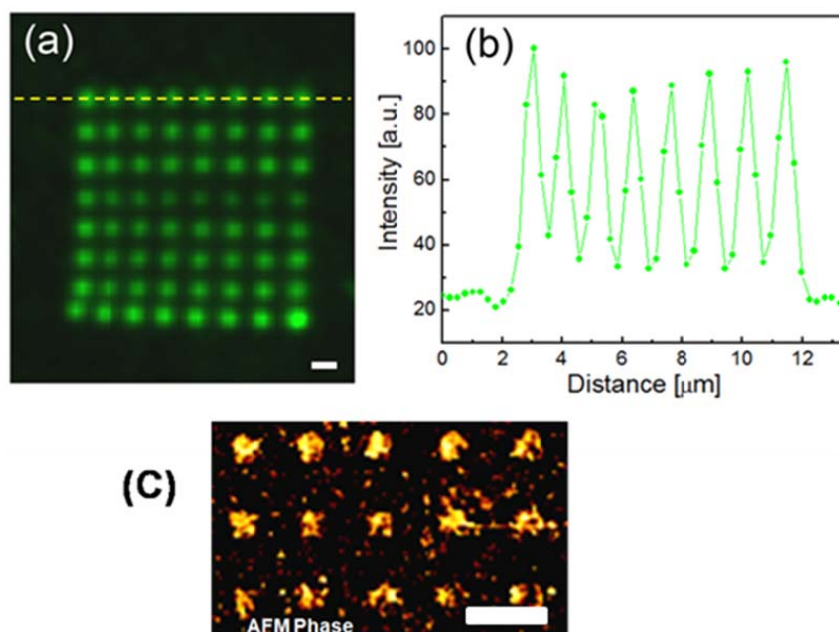


Figure 57 500 nm fibronectin nanoarray. Epi-fluorescence image of a regular array of Atto488 fibronectin patches (a) and cross section profile (b). A linear interpolation (solid line) has been used to interpolate the fluorescence data points (dots) obtained by optical microscopy. Fibronectin was crosslinked to amine groups by means of GA. (c) is the AFM phase image of the fibronectin array. Scale bar: 1 μm . It should be mentioned that the radius of the features is comparable in size with the resolution of the optical image ($\sim 0.61 \lambda/\text{NA}$, where λ is the wavelength used and NA is the numerical aperture of the objective), so other techniques should be used to determine the distribution of proteins within each feature.

TCNL is capable of extremely high resolution chemical patterning of surfaces due to the high temperature gradients in the vicinity of the heated tip³⁸⁷. Therefore, we investigated our ability to organize small amounts of proteins with high definition. Using a single touchdown approach at each feature, we produced an array of 500 nm features decorated with fluorescently-labeled fibronectin, as shown in Figure 57 above. The size of a single feature is inferred from AFM imaging of the protein pattern. To investigate length scales below the resolution limit of optical microscopy, we thus employed topographical and phase AFM imaging in ambient conditions. Using again a single touchdown approach at each feature but with a shorter dwell time, TCNL was used to de-protect amines in extremely small areas. Three such features are shown in figure below as topographical and phase images. The AFM phase image provides information on the local viscoelasticity of the sample. A larger phase change is indicative of a “softer” surface, which is what we expect in the patterns decorated with proteins. The topography indicates a shallow indentation of approximately 10 nm. This depth can be varied by changing the temperature of the tip, higher temperatures producing deeper indentations³⁸⁷. The surface was then functionalized with fibronectin see figure below or with streptavidin see figure below. The topographical data revealed that the TCNL ‘holes’ were filled with proteins. The phase images are also consistent with the deposition of proteins in the holes. Figure 58 shows fibronectin phase features as small as 40 nm and streptavidin as small as 60 nm. These values compares well with previous measurements of single dry fibronectin molecules⁴⁰⁷. Considering the AFM tip convolution during imaging, and a tip radius of about 15 nm, it is reasonable to suggest that there are as few as 1 or 2 fibronectin molecules covalently attached to each location.

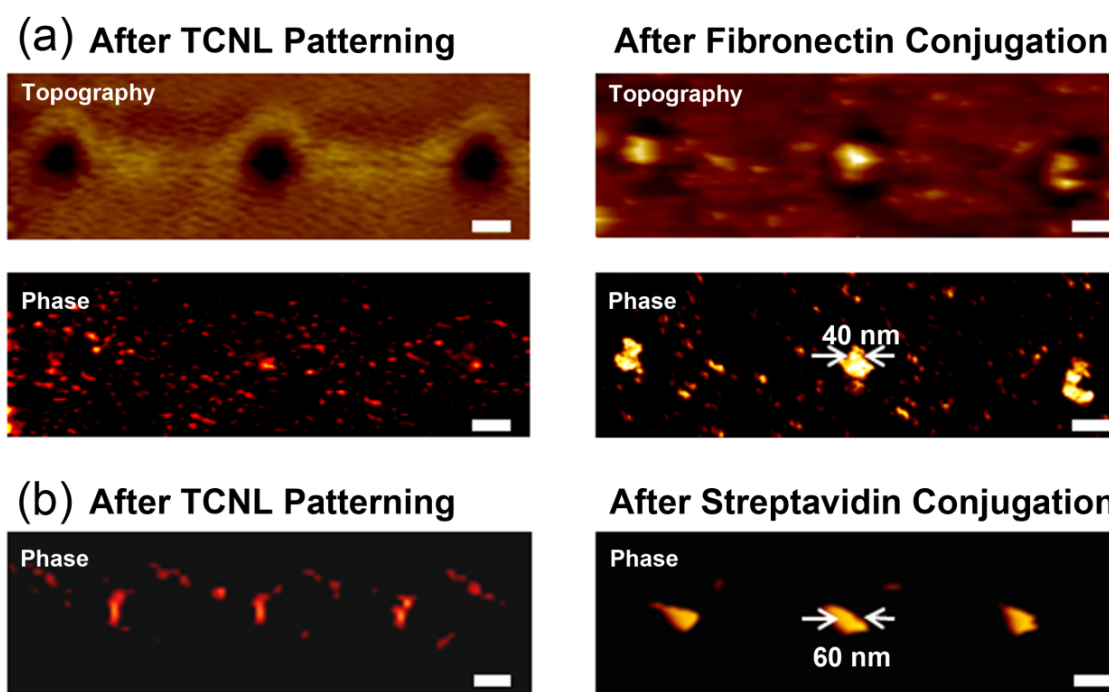


Figure 58 Fibronectin and streptavidin nanoarray down to 40 nm. AFM topography and phase images of a TCNL nanoarray before and after fibronectin (a) and streptavidin (b) attachment. The topography z-range in (a) is 20 nm. Scale bars: 100 nm.

V. Oriented Immobilization

Problems associated with the loss of biological activity of the antibodies upon immobilization have been noticed in many cases²⁷⁶. One of the main reasons for such loss is attributed to the random orientation of the asymmetric macromolecules on support surfaces. The orientation of the immobilized protein can play a vital role in the quality of the bioactivity of the immobilized protein. To demonstrate that we can achieve this on TCNL patterned surfaces, as shown in Figure 59, we immobilized ICAM-1 in an oriented fashion using the antibody binding of the Fc portion on the ICAM-1 with the F(ab')₂ portion of the biotin F(ab')₂. To achieve this, TCNL patterned surface was post-treated with GA for 60 minutes. After washing, the surface was then incubated with 1mg/ml streptavidin for 30 minutes followed by exposure to biotin F(ab')₂ fragment (2 mg/ml) for 30 minutes. Finally, ICAM-1/Fc (100 µg/ml) was immobilized on the pattern by means of non-covalent antibody binding of the Fc to the F(ab')₂. To demonstrate the biological functionality of the ICAM-1, anti-ICAM-1 conjugated with FITC was incubated with the surface for 120 min. The ridges seen in the figure may be due to the topography change occurring during TCNL. Topography changes occur when the deprotected polymer is pushed during the writing leading to a higher amount of deprotected amines on the edges.

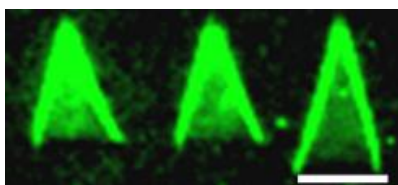


Figure 59 Oriented patterning of ICAM-1 labeled with anti-ICAM (FITC)

VI. DNA Arrays

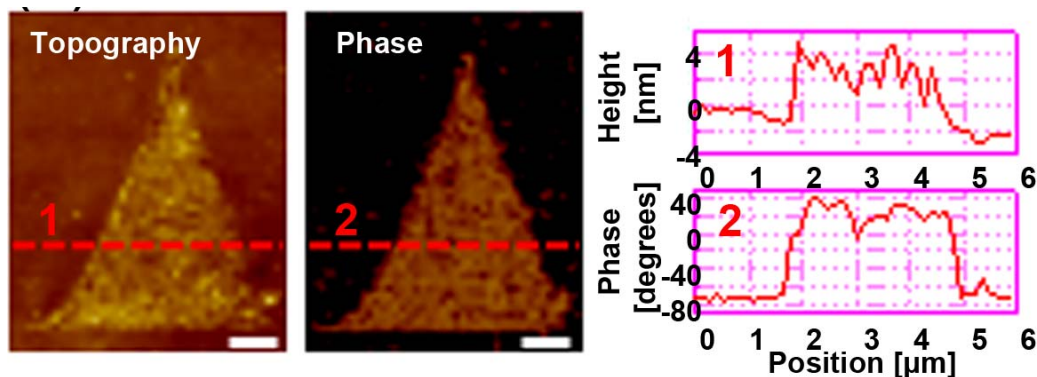


Figure 60 AFM topography and phase images of a triangular pattern of thiol-terminated DNA single strands crosslinked to amines through PMPI. The height profiles for the topography and phase image can be seen in the graphs on the right side of the image.

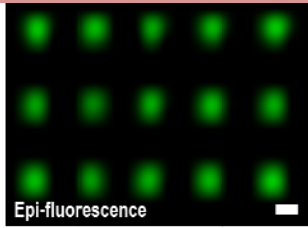
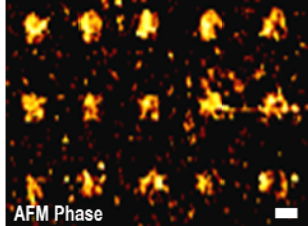

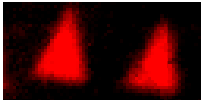
There is a growing sense in the scientific and technical community that technologies based on manipulation and assembling of DNA could lead to revolutionary industrial processes. Modern biotechnology has made it possible to modify DNA in various ways and with various functional objects⁴⁰⁸⁻⁴¹⁰. In this work we introduced a special method to form complex nanopatterns of DNA molecules on solid substrates. Possible applications for large

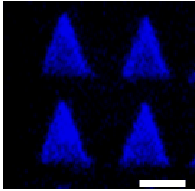
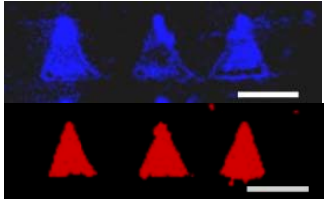
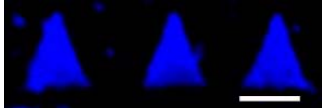
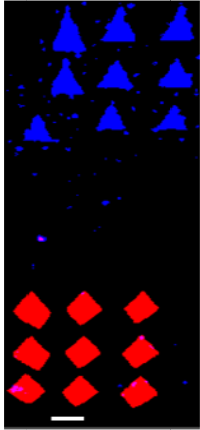
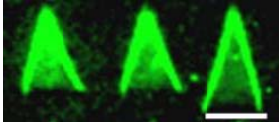
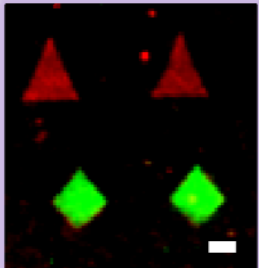
scale arrays of biomolecules include DNA sequencing-by-hybridization⁴¹¹, DNA-based sensors, enzyme or antibody-based sensors, and peptide or nucleic acid oligomer libraries for screening ligand binding⁴¹²⁻⁴¹³.

To pattern DNA on the TCNL patterned surface, the surface was treated with N-[p-maleimidophenyl]isocyanate (PMPI) in dimethylsulfoxide for 4 hours. The sample was then washed and incubated with single strand DNA (5'- /5ThioMC6-D/TCC CAA AGA ACA GTG GTG GCT CAA GCT ACG GCC CCT CAT GAA AAT CCT GC/36-FAM/ - 3') for 12 hours. Before imaging the pattern the sample were washed and briefly sonicated to remove any non-specific adsorption. As seen from the topography image in Figure 60 there was uniform coverage of DNA on the patterns.

VII. Summary of the Functionalization Strategies

TCNL is a versatile tool that can be used to generate wide range of functionalities and attach various nano objects. The table below summarizes the different functionalization strategies employed in TCNL.

| # | Type | Protocol | Result |
|----------------------------------|--|------------------|--|
| Single Protein Patterning | | | |
| 1 | Single Protein Patterning using GA | GA + Atto488/Fn |  <p>Epi-fluorescence</p>  <p>AFM Phase</p> <p>(Nano Patterns of Fibronectin)</p>  <p>Phase</p> <p>60 nm</p> <p>(Nano patterns of Streptavidin)</p> |
| 2 | Single Protein Patterning using Bn-SAv binding | NHS/Bn + Cy5/SAv |  |

| | | | |
|----------------------------------|--|--|---|
| | | NHS/Bn + SAV + Bn /anti-CD3(alexa350) |  |
| 3 | Single Protein Patterning using Bn-SAV binding | NHS/Bn + Cy5/SAV + Bn/anti-CD3(alexa350) |  |
| 4 | Single Protein Patterning using SH | SPDP + DTT +Maleimide SAV + Bn /Anti-CD3(Alexa350) |  |
| Dual Functionality | | | |
| 5 | Double Functionality Patterning of Bn and SH | SPDP + NHS/Bn + DTT + DACM + Cy5/SAV |  |
| Oriented Immobilization | | | |
| 6 | Selective binding of patterned ICAM-1 via antibody | GA + SAV + BN/Fab + Human IgG-1 Fc/ Human ICAM1+Mouse anti-Human ICAM-1/FITC |  |
| Two Protein Co-Patterning | | | |
| 9 | Two protein patterning via GA and Bn | Surface prepatterned with NH2 and biotin + GA+ ICAM-1+ BSA + SAV+Bn/Anti-CD3(Cy5) +Anti-ICAM-1(FITC) |  |

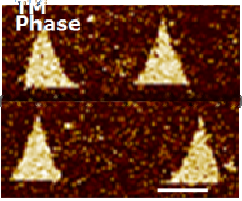
| DNA Patterning | | | |
|----------------|-------------------------|-----------------|---|
| 10 | DNA patterning via PMPI | PMPI/DMSO + DNA |  |

Table 4 Table above summarizes the wide array of functional group and protein patterning thus far demonstrated by combining TCNL with specialized conjugation strategies. **A** = Glutaraldehyde, **Fn** = Fibronectin, **SAv** = Streptavidin, **Bn** = Biotin

VIII. Viability and Bioactivity of TCNL Patterned Proteins

Maintaining the bioactivity of surface-patterned proteins is crucial for most applications²³³. However, many potential protein patterning techniques do not provide ideal conditions for preserving bioactivity²⁷². Here we show that patterned proteins remain bioactive and can initiate cell activity. In order to demonstrate this we choose to pattern anti-CD3.

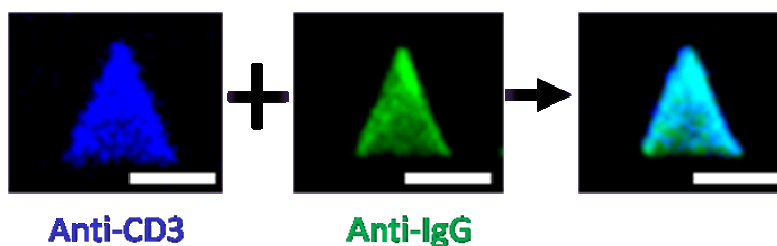


Figure 61 Epi-fluorescence image of anti-CD3 bioactivity. Alexa350 labeled biotinylated anti-human CD3 (blue) bound to the TCNL amine pattern by means of NHS-biotin and streptavidin shows bioactive molecular recognition of FITC-labeled IgG (green).

Figure 61 above demonstrates the bioactivity of an antibody bound to TCNL surfaces. We initially bound the biotin-bound anti-CD3 to the patterns and we verified the bioactivity by checking the ability of anti-CD3 (blue triangle) to bind to secondary antibody, anti-IgG (green triangle). In a separate bioactivity study, we also showed that GA-bound intracellular adhesion molecule-1 (ICAM-1) binds specifically to anti-ICAM-1. See Figure 62 below.

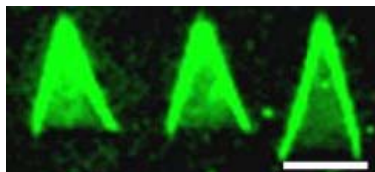


Figure 62 Patterned ICAM-1 labeled with anti-ICAM (FITC).

To further demonstrate that we could use these substrates for cell experiments we used a well established system of T-cell signaling and immune synapse formation⁴¹⁴. Anti-CD3 is known to stimulate specific cell signaling pathways when interacting with Jurkat cells, an immortalized line of T lymphocyte cells (T-cell) that are used to investigate T-cell signaling and immune synapse formation. In a cellular assay to demonstrate the bioactivity of bound anti-CD3, we looked for spatial correlation of protein kinase C- θ (PKC- θ) inside a T-cell interacting with the underlying anti-CD3 pattern⁴¹⁴. Immunofluorescence cell staining of PKC- θ in a cell interacting with a triangle shaped anti-CD3 micropattern (Figure 63) shows the halo of the PKC- θ echoing the triangular shape of the anti-CD3 micropattern. Thus, we have both molecular and cellular evidence for the preserved bioactivity of TCNL patterned proteins.

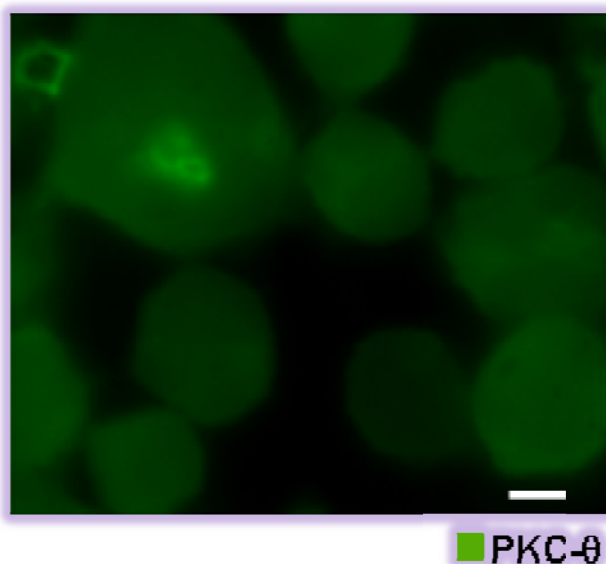


Figure 63 Jurkat cells, immunostained for PKC- θ , lying on a triangular anti-CD3 pattern. The PKC- θ accumulation above the cell–pattern contact site can be observed.

IX. Storage of TCNL Patterns and Aging

TCNL creates nano- and micro- templates that act as chemically active surfaces for covalent functionalization of proteins in well-organized and pre-determined amounts. The thermally deprotected amines are stable, as are the post-TCNL chemically modified groups. The resultant substrates can be stored for weeks and can subsequently be used for the attachment of nano-objects using standard chemical protocols. In order to test the robustness and aging of the substrates, the surfaces have been patterned with the desired chemical groups and the substrates were stored in a desiccator for later functionalization with proteins. The chemical groups tested so far were amines and biotin. The amines show that thermally deprotected amines are stable and the biotin patterns show that patterns with post TCNL groups are also stable. Thus far, we have stored the nano-patterned surfaces for a maximum duration of three weeks before successful implementation of two-protein functionalization. In future studies, we will investigate longer storage times.

X. PEG Passivation

PEG is polymerized ethylene oxide and has low toxicity⁴¹⁵. Poly(ethylene glycol) (PEG) can be used to create coatings that can resist protein adsorption⁴¹⁶. PEG is soluble both in water and alcohols like methanol. When placed in water or aqueous solutions, PEG swells undergoing extensive hydrogen bonding, this swelling creates a dense layer of PEG on the surface, creating a resisting non-specific adsorbing layer. This unique property of PEG has been used in biomedical materials, microfluidic devices, microarrays, and biosensors^{260,417-419}. So how does PEG prevent protein adsorption?, several mechanisms have been proposed to explain the passivating behavior of PEG films⁴²⁰. The possible molecular mechanisms are: (i) the entropic cost caused by the binding of a biopolymer to the flexible PEG chains⁴²¹ (ii) the electrostatic repulsion induced by the adsorption of hydroxide ions onto the polymer surface⁴²² and (iii) the presence of a localized, high-viscosity water layer at the PEG/solvent interface⁴²³. One common requirement is a dense layer of PEG film with no structural defects⁴²⁰. As the number of applications for PEG coated surfaces for basic and biomedical applications started increasing^{260,265,424} many methods have been developed to graft PEG layers onto solid substrates including silicates, silicon, gold, and metal oxides. For silicate and glass, these methods include the coupling of aldehyde²⁷¹ or epoxy-terminated PEG²⁶⁶ onto aminopropyl trialkoxysilane-derived layers, the binding of PEG-bis(amine) onto aldehyde-bearing silanized surfaces²⁷³, and the direct grafting of methoxy-PEG derivatives with terminal trialkoxysilane²⁶⁸ or methacrylate⁴²⁵. The surface modification of gold, by comparison is achieved by thiol-functionalized PEG or oligo(ethylene glycol)^{422,426-427}. For passivating anionic surfaces like oxide surfaces, copolymers such as poly(L-lysine)-g-poly(ethylene glycol) are electrostatically adsorbed onto the substrate surface^{267,269}.

i. PEG Passivation of Polymer Coated Slides and QCM Crystals

In order to passivate and create a layer of PEG on the polymer coated slides for TCNL, we initially convert the deprotected amines (from bulk heating) present on the polymer to aldehyde and then bind PEG-bis(amine) in cloud point conditions onto aldehyde-bearing slides. The cloud point of a fluid is the temperature at which dissolved solids are no longer completely soluble, precipitating as a second phase, thus giving the fluid a cloudy appearance²⁶⁴. It is known that the best surface coverage of PEG is possible at cloud point condition of PEG polymer²⁷¹. In order to achieve cloud point condition of PEG we heat PEG to 60°C in toluene solution under nitrogen environment. It is known from Norde *et. al*⁴²⁸ that the grafting density increases with reduction in solubility and interchain repulsion of PEGs with increasing temperature.

Initially the polymer that has thermally protected amine groups is spin coated on glass surfaces(glass slides or QCM crystals). To thermally activate and deprotect the amine groups on a polymer surface, as before, the polymer spin coated crystals were heated at 180° C for 3 min on a hotplate to produce amine on the surface. To convert the amines into aldehydes the surface was then incubated with 50% glutaraldehyde for 2 hours. A clean glass flask was heated to 120°C to remove moisture and then filled with dry nitrogen gas to prevent any moisture from entering when present at room temperature. To maximize the grafting density the samples were rinsed and placed in flask containing 25 mM aminopolyethylene glycol 3,000 (Fluka catalogue # 07969) in 10 ml dry toluene. The flask

was then heated to 60° C for 24 hours where the solution in the flask was constantly stirred. Under these reaction conditions, PEG undergoes a reversible phase change due to disruption of the hydration shell surrounding the PEG chains, which results in reduced interchain repulsion distances and association between PEG molecules²⁷¹. As a consequence, at the cloudpoint, the PEG chains no longer are well solvated as individual random coils. As the effective radius of gyration and the hydrodynamic volume of individual chains is much reduced, denser packing of grafted chains is possible if sufficiently dense reactive pinning sites are available on the surface. The samples were then cleaned and rinsed with ethylacetate, acetone, methanol, ethanol - in that order. The PEG used (Figure 64) has a linear formula $\text{NH}_2(\text{CH}_2\text{CH}_2\text{O})_n\text{H}$. The samples were then finally dried under a flow of dry nitrogen.

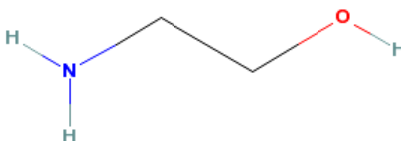


Figure 64 Chemical structure of *O*-(2-aminoethyl)polyethylene glycol, also called aminopolyethylene glycol, used for passivating the polymer surfaces.

ii. Effect of Salt

As repulsion between PEG chains is a limiting factor under well-solvated conditions, PEG chains of sufficient length adopt a highly hydrated coil configuration and will be attached to the surface in this configuration. Grafting well-hydrated PEG chains produces a coating consisting of coils or ‘mushrooms’, as opposed to the desirable ‘brush’ state, where the majority of the molecules are stretched out fully away from the surface. For well-solvated molecules in random or extended coil conformations and at low grafting densities, there is no driving force to (further) extend their length upon surface immobilization. When one attaches solvated coils to a surface, attached molecules will exclude others from their hydration volume, and this will determine the maximal possible packing density. Clearly, in this situation, increasing the density of surface pinning groups is not beneficial beyond a point, since the coating density will be determined by the diameter of the PEG coils rather than the pinning group density. When such coatings are then immersed in aqueous solutions at lower temperature, the PEG chains will try to reestablish solvation. As shown in Figure 65, If the chains adopted a configuration partway between brush and mushroom, the PEG chains maybe better able to cover transient ‘gaps’ between chains and thereby prevent protein reaching the substrate polymer.

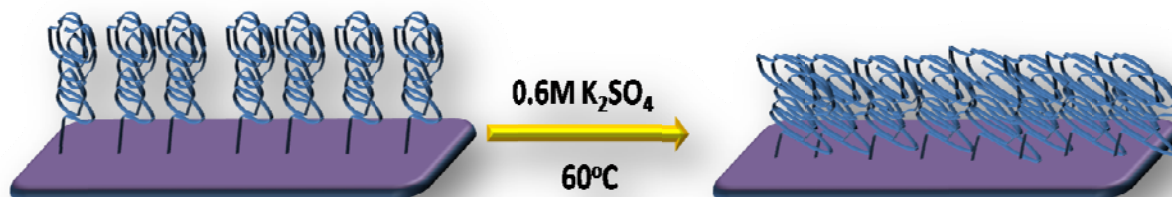


Figure 65 Schematic of the effect of salt treatment on PEG coverage. By salt treatment, the transient gaps between the chains are reduced and a much denser pattern with no gaps that covers the substrate is achieved.

In order to achieve a higher density without transient gaps, we dip the dried PEG passivated surface in a salt solution of 0.6M K_2SO_4 in a flask filled with nitrogen. The electrostatic charge between the PEG chains is masked in this way making them move away from mushroom configuration. The flask was then heated to 60°C for 6 hours after which the samples were washed and placed in distilled water to rehydrate and re-establish the PEG chains adopting a configuration partway between brush and mushroom filling the gaps between the individual chains. As shown in the contact angle measurements the contact angle substantially decreases once we salt treat the PEG samples showing that there is a lesser transient gaps in the PEG chains once we salt treat and there is a better coverage.

iii. Fluorescent PEG Passivation: Fluorescent Testing of PEG Binding on Surface

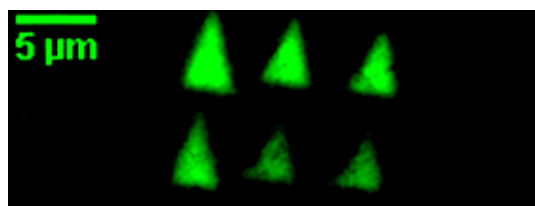


Figure 66 Fluorescent image of FITC labeled PEG on TCNL patterns

In order to investigate the PEG binding and test if it was bound to the surface, the surface was passivated using fluorescent PEG-amine, MW 3400 (Nanocs Inc., New York, USA). The chemical structure of FITC-PEG-amine can be seen in Figure 68. Using fluorescent PEG allowed us to optically verify the degree and quality of PEG binding on the polymer surface. By binding fluorescent PEG on the TCNL micro patterns or alternatively on the background areas between a TCNL micro pattern we prove that we can spatially control PEG passivation on our polymer surfaces. Initially the fluorescent PEG was bound to TCNL patterned area using the procedure described above for PEG passivating polymer coated slides. As shown in the Figure 66 above, you can see the pattern is fluorescent in the FITC channel, confirming that we can bind PEG to micro patterned areas.

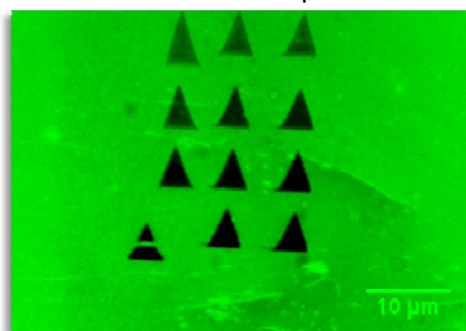


Figure 67 Fluorescent image of fluorescent FITC PEG bound everywhere except the TCNL patterned area.

To further investigate if we can bind PEG everywhere except the patterned areas (background of the patterns), we bound biotin to TCNL patterns and then heated the sample on hot plate for 180°C for 3 min and then bound FITC-PEG-NH₂ to the bulk deprotected amines. The amine portion of the PEG binds to the deprotected background of the TCNL biotin patterns leading to biotin patterns with PEG passivation in the background. The Figure

67 above shows fluorescent FITC PEG on the background of TCNL patterns which had biotin in them. The dark triangles are the biotin patterns.

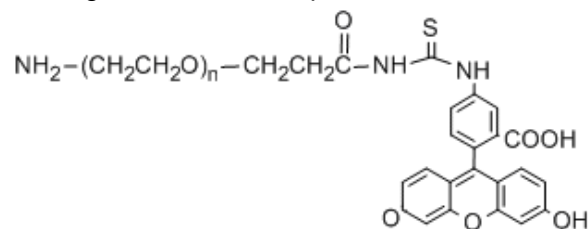


Figure 68 Chemical structure of FITC-PEG-NH₂, Fluorescein PEG amine (MW 3400).

iv. Passivating TCNL Patterned Polymer Slides

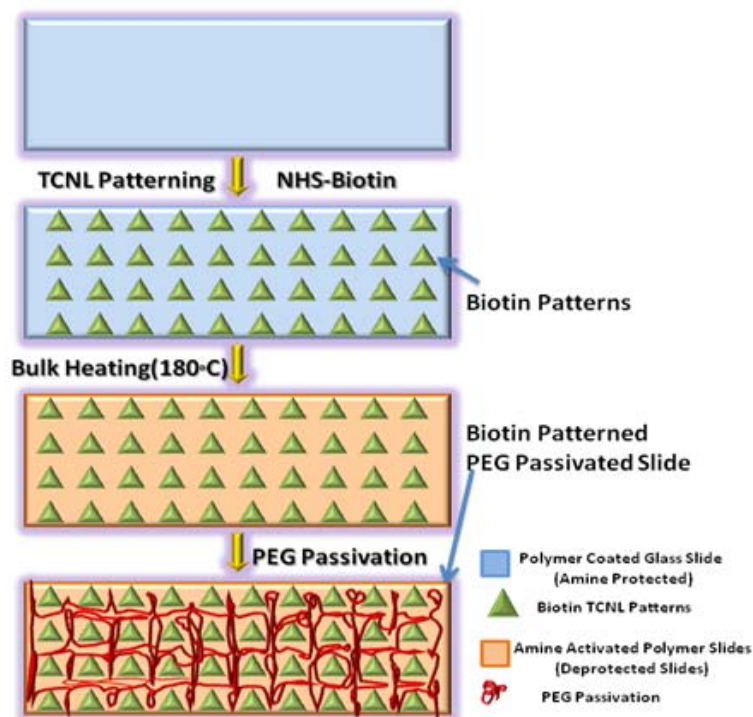


Figure 69 Schematic illustration of a PEG passivation on TCNL patterned surfaces. The polymer spin coated samples were TCNL patterned using a hot AFM tip. The samples were then incubated with NHS biotin to get biotin patterns. The sample with biotin patterns was heated on a hot plate for 3 mins at 180 °C, which created de-protected amines on the back with biotin patterns. The sample was then incubated with glutaraldehyde. The aldehyde surface was passivated using amine PEG. The final samples had biotin patterns with the area between them passivated with PEG.

In order to PEG passivate TCNL chemically-patterned slides as shown in the schematic in Figure 69, the polymer spin coated slides were patterned by using a heated AFM tip. This procedure leads to amine patterns on polymer slides. The sample was then immersed in a solution of NHS-Biotin for 45 minutes. The biotin patterned slides were then heated to 180 °C for 3 mins on a hotplate. An independent thermometer was also used to check that the temperature on the hot plate reached 180 °C. It has to be noted that the melting temperature of biotin is 232 °C. Heating the polymer slide deprotected the amines on

the background of the patterned slides leading to biotin patterns with amines filled in the background. The samples were then passivated with PEG to fill the space outside the biotin patterns. This was performed as described in the procedure above when the polymer coated slides were passivated. This led to finally biotin patterns with PEG passivated in the area between them.

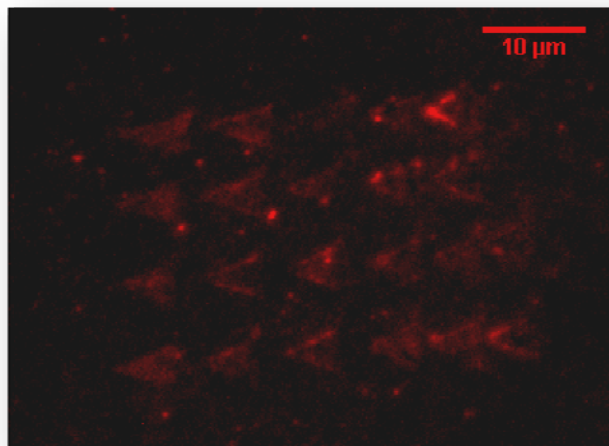


Figure 70 PEG passivated slide with biotin patterns. The biotin patterns were then bound to Cy5 streptavidin which can be seen from the fluorescence image.

The fluorescence image in Figure 70 is the proof that we can passivate TCNL patterned slides and it doesn't destroy the previous biotin patterns already present before PEG passivation. It can be seen that the biotin is still active as it is bound to fluorescent streptavidin. Figure 70 when compared to standard streptavidin patterns like Figure 52B is spotty. This spotty binding of streptavidin to these patterns may be because of the patterned biotin partially losing its function, affecting the binding of streptavidin or a result of interference from the PEG binding to free spots on biotin patterns. The polymer melting and filling the patterned spots also can't be ruled out. Further work needs to be performed to optimize this process.

v. Contact Angle Measurement

Static water contact angle measurements were determined at ambient laboratory temperatures with a Phoenix 150; Surface Electro Optics Inc. Contact angle is a quantitative measure of the wetting of a solid by a liquid. The contact angle is specific for any given system and is determined by the interaction across the solid – water interface. The shape of the droplet is determined by the Young Relation. The contact angle plays the role of a boundary condition. The wettability of a surface is determined by the outermost chemical groups present on the surface of the solid. It is known that PEG decreases the contact angle since it increases the hydrophilicity of surfaces²⁷⁴.

To measure the contact angle, ultra pure deionized water from Fischer Scientific was used. The reported contact angle values, for all the tested polymer surfaces including the PEG functionalized substrates, are the average of 12 different measurements taken on 2 individually prepared samples. Further, the value of the angle was the average of advancing (θ_a) and receding (θ_r) contact angles of the water drop, which on a homogenous surface

should be identical within error. As shown in Figure 71, It was found that for protected polymer samples, the average contact angle was 69° . For deprotected slides the average was 62° . The contact angle for the PEG passivated slides was 51° and for PEG passivated and salt treated slides it was 5° . The low contact angle of the final PEG passivated polymer surface shows that they are really hydrophilic which may be because the surface is completely covered with PEG with low or no transient gaps. For a more concrete thorough understanding and a chemical confirmation of presence of PEG on the surface, FT-IR and XPS are being performed. To characterize the non-specific adsorption of protein on the PEG passivated polymer, QCM experiments were performed.

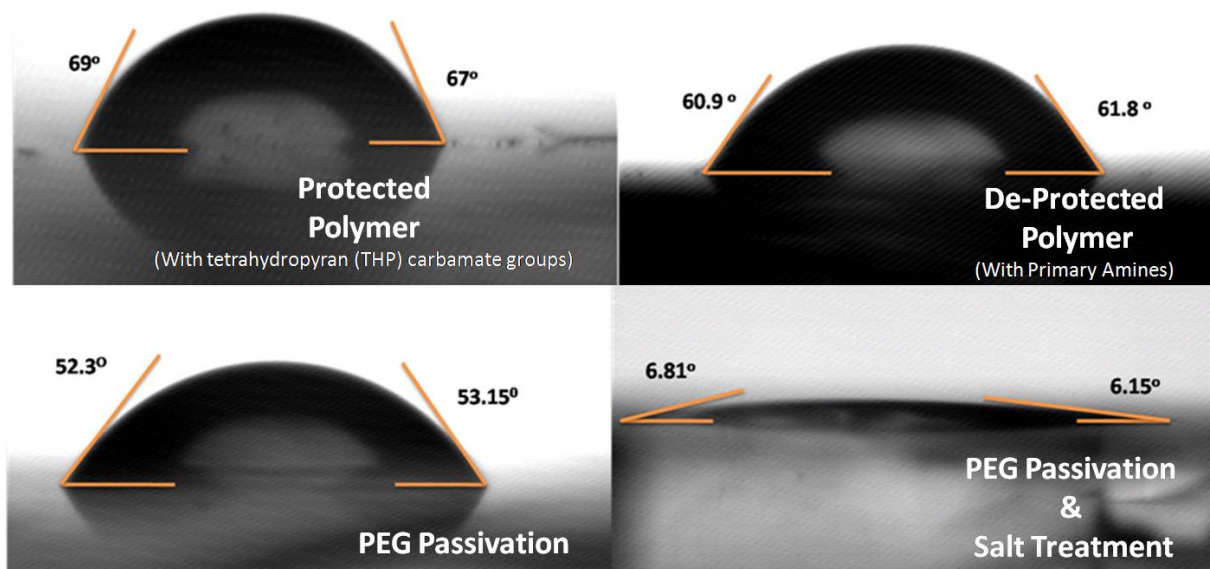


Figure 71 Contact angle on protected polymer, deprotected polymer, PEG passivated (standard) and salt-treated PEG passivated surfaces.

XI. QCM Analysis of Non-Specific Adsorption

The Quartz Crystal Microbalance (QCM) is very sensitive to changes in weight and thus a helpful method for detecting adsorption processes at solid/gas or solid/liquid interfaces. The basis of the QCM is a thin quartz crystal exhibiting the inverse piezoelectric effect. Applying an alternating current to the crystal excites a mechanical oscillation of plate. Changes in the specific resonance frequency of the quartz are directly proportional to its mass load. The quartz crystal microbalance is an extremely sensitive sensor capable of measuring mass changes upto 18 nanogram/cm^2 with a wide dynamic range extending into the 100 g/cm^2 range. This effect was first discovered by G. Sauerbrey in 1959. The results of his work are embodied in the Sauerbrey equation, which relates the mass change per unit area at the QCM electrode surface to the observed change in oscillation frequency of the crystal.

$$\Delta_F = -C_F X \Delta_M \quad \text{Equation 6}$$

Where

- Δ_F = Observed frequency change in Hz,
 Δ_M = Change in mass per unit area, in ng/cm²,
 C_F = The sensitivity factor for the crystal (56.6 Hz g⁻¹ cm² for a 5 MHz crystal at room temperature).

All measurements were performed using the QCM 200 sensor system from Stanford Research Systems (SRS). The sensor crystals were cleaned and coated as described in the Materials and Methods. The polymer coated-crystals were then pegylated by using procedure mentioned in the Materials and Methods. The crystals were then mounted onto a flow chamber system. A flow rate of 50µl/min was maintained throughout the experiment and all the experiments were performed at room temperature. To maintain a steady flow, an injection flow system was used. After the system was equilibrated with distilled water, the coated sensors were subjected to a BSA solution at a concentration of 20µg/ml in water. Once equilibrium was obtained, to remove the non-adsorbed BSA, a secondary flow of distilled water was applied to the surface for washing until the QCM signal approached equilibrium. The Sauerbrey equation was used to measure the adsorbed mass. The QCM is capable of monitoring frequency changes Δ_F in a time resolved manner. Δ_M is associated with the adsorbed mass Δ_M . According to the Sauerbrey equation a Δ_F of 1 Hz for the sensor chip we used with the QCM200 correlates with a Δ_M of 18ng/cm².

i. Comparison of Non-Specific Adsorption of BSA on Different Polymer Coated QCM Crystals

To check the non-specific adsorption of protein onto the carbamate polymer surface during TCNL, we coated the QCM sensor crystals with TCNL carbamate polymer and checked the non specific adsorption by flowing BSA onto the crystal. As the crosslinker 4-(3'-chlorodimethylsilyl) propoxy benzophenone changes the properties of the TCNL polymer, especially its stiffness and charge present on the surface; which are known to change the non-specific adsorption of proteins. To check the effect of the crosslinker we coated the crystals with TCNL polymer with and without the crosslinker and compared the non-specific adsorption. Finally we passivated the TCNL polymer surface with PEG (see material and methods for PEG passivation procedure), as expected PEG prevented the non specific adsorption of proteins on the TCNL surface.

From Figure 72, it can be concluded that the amount of non-specific adsorption depends on the surface chemistry on the sensor crystals. The non-specific adsorption was quantified assuming the polymer thin film on the crystal to be rigid film. The non-specific adsorption on the crystals was 738 ng/cm², 648 ng/cm², and 36 ng/cm² respectively for carbamate without crosslinker, carbamate with crosslinker and PEG passivated QCM sensor crystals. The data clearly indicates that the PEG passivation on polymer coated crystal works and is effective in decreasing the non-specific adsorption of protein on the polymer surface. Detailed discussion of the adsorbed values follow in the next section.

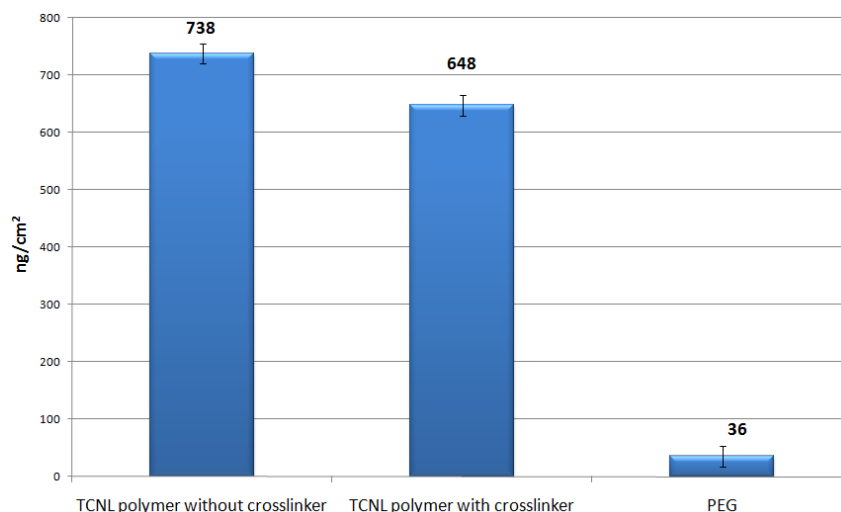


Figure 72 Bar graph of non-specific protein adsorption on QCM crystals coated with polymer films of different types and processing. The amount or mass of protein non-specifically adsorbed on the surface is also mentioned on the bar graphs.

It can be seen from figure 73-80 that there are several graphs where there is a lot of noise and the graphs are not perfectly smooth, these changes or noise may be due to the electronic noise arising from the QCM instrument used. This electronic noise may be just parasitic capacitance occurring in the circuits or between the electrodes.

ii. Non-Specific Adsorption of BSA on TCNL Polymer without Crosslinking

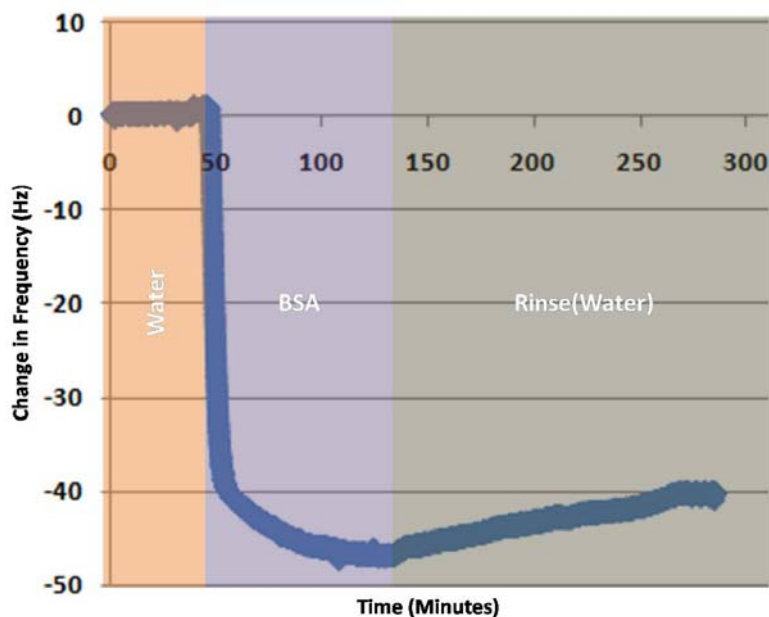


Figure 73 QCM measurement with a frequency versus time measurement on TCNL polymer without crosslinker. The graph is a dynamic measurement with a flow of water, BSA, water in a sequence. BSA was flown to check the non-specific adsorption and subsequently washed and rinsed with distilled and deionized water to remove the free standing protein.

To understand the non-specific adsorption of protein BSA on non-crosslinked TCNL polymer, BSA at a concentration of 20 $\mu\text{g/ml}$ was flown on the QCM crystals coated with this polymer. Finally a rinse cycle was performed with water to remove any freestanding protein (protein not bound to surface and lying freely) on the crystals. The polymer coated crystal was immersed in distilled water for 3 hours before the experiment was started. The samples were pre-incubated in water to prevent any noise arising due to polymer absorbing water. As shown in Figure 73, the frequency decreased substantially when BSA was exposed to the surface, indicating significant non-specific adsorption of BSA protein on the polymer-coated sensor crystal. When the rinse cycle was performed, the frequency increased due to removal of some weakly adsorbed protein on the surface. A step-by-step quantitative explanation of each stage is discussed below. The complete experiment was performed at a flow rate of 50 $\mu\text{l/min}$ at room temperature.

Figure 74 shows 20 $\mu\text{g/ml}$ of BSA in distilled water flown on the non-crosslinked polymer crystal, there was a steep decline in the frequency. When the frequency was stabilized, the difference in frequency was about ~ 47 Hz. Applying Sauerbrey equation to the difference in frequency, the amount non-specific adsorption was about 846 ng/cm^2 .

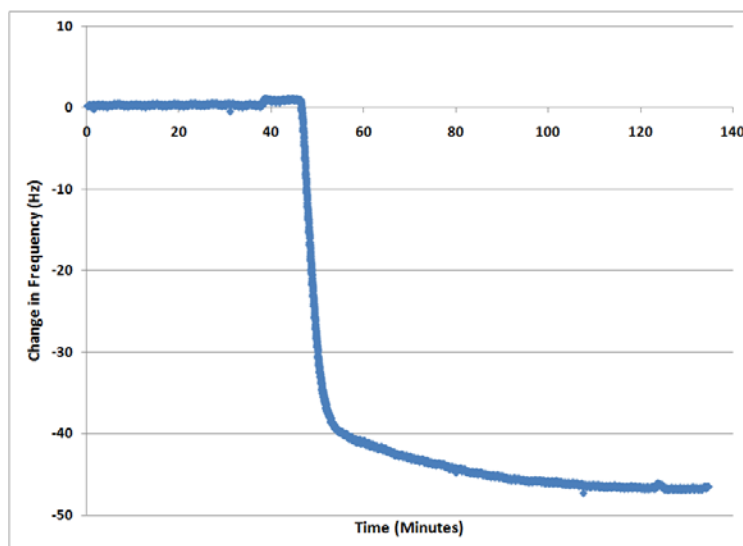


Figure 74 Quartz crystal microbalance graph of frequency change versus time on a non cross-linked polymer coated QCM crystal with a flow of water and BSA in sequence. Change in frequency over time is displayed. The change in frequency is due to non-specific adsorption of BSA onto the polymer crystal.

In order to remove any freestanding protein (non bound or lying free) on the polymer crystals, distilled water was flown over the crystal and stopped after the signal stabilized, as indicated by a plateau in the change in the frequency value (Figure 75). For the non-crosslinked carbamate polymer, there was an increase in frequency during the rinse cycle. The change or difference in frequency was about 6 Hz, corresponding to a reduction of approximately 108 ng/cm^2 , or 6.84% of the adsorbed amount. Thus, the final amount of non-specific adsorption on the non-crosslinked carbamate polymer was about 738 ng/cm^2 . This was about 41 Hz in frequency difference.

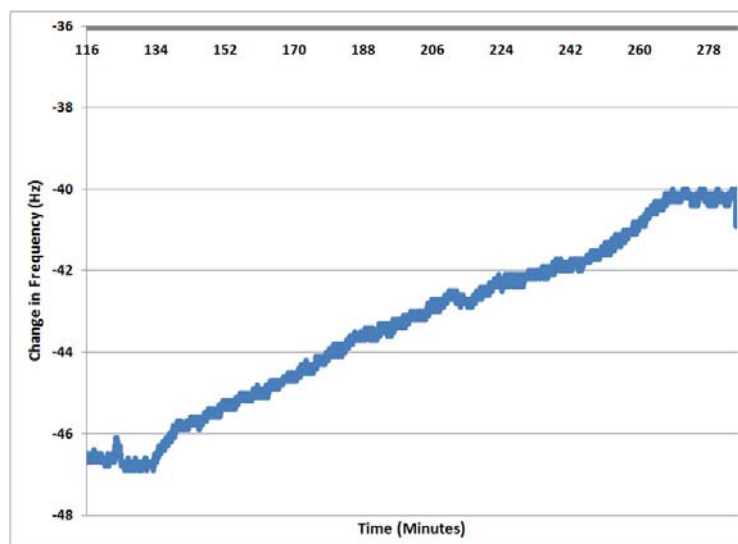


Figure 75 Quartz crystal microbalance graph with a rinse cycle on non-crosslinked polymer coated surface. The rinse was performed with a flow of distilled water. Change in frequency over time is displayed. It can be observed in the graph the signal stabilizes showing that there is no more removal of protein adsorption after some time.

iii. **Non-Specific Adsorption of BSA On 4-(3'-Chlorodimethylsilyl) Propoxy Benzophenone Crosslinked Carbamate Polymer Coated Sensors**

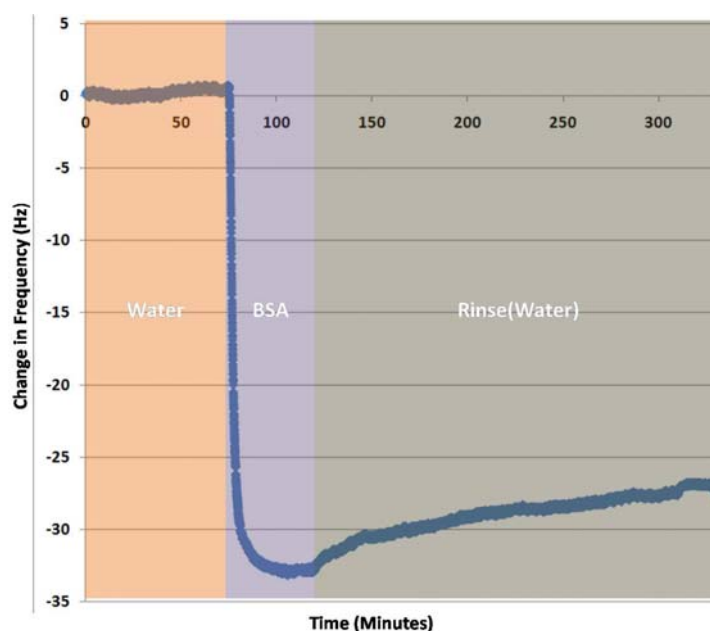


Figure 76 QCM measurement on TCNL polymer coated crystal. The graph is a dynamic measurement of change in frequency versus time, with a flow of water, BSA, water in a sequence.

To understand the non-specific adsorption of protein BSA on TCNL polymer, i.e. polymer with 4-(3'-chlorodimethylsilyl) propoxy benzophenone. BSA at 20 $\mu\text{g}/\text{ml}$ was flown after a stable signal was achieved with treatment of distilled water. After equilibrium was reached with BSA he flowing on the TCNL polymer coated crystal, a rinse cycle was

performed with distilled water to remove any freestanding protein on the crystals. As before, the polymer-coated crystal was immersed in distilled water for 3 hours before the experiment was started. A detailed quantitative explanation of each stage of Figure 76 is shown below, graphically and reviewed in the text. The complete experiment was performed at a flow rate of 50 $\mu\text{l}/\text{min}$ at room temperature.

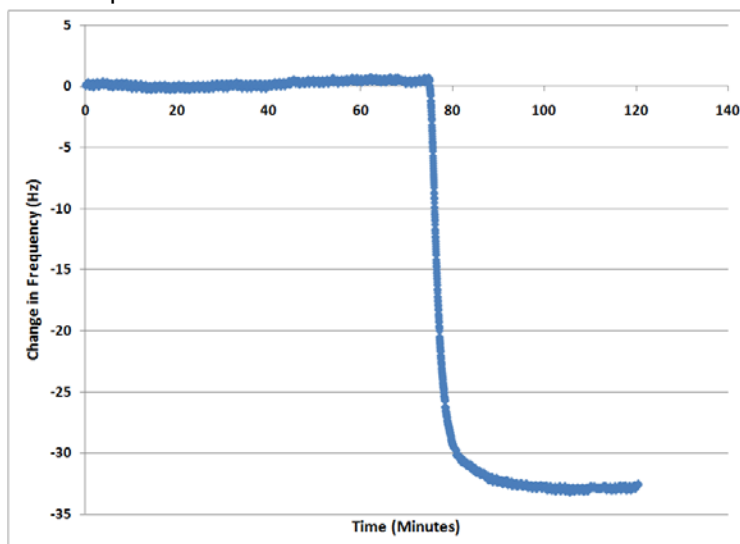


Figure 77 Quartz crystal microbalance graph on a TCNL polymer coated crystal with a flow of water and BSA in sequence. Change in frequency over time is displayed.

When 20 $\mu\text{g}/\text{ml}$ BSA in distilled water was flown on 4-(3'-chlorodimethylsilyl) propoxy benzophenone crosslinked carbamate polymer crystal there was a steep decline in the frequency (Figure 77). When the frequency was stabilized the difference in frequency was about 42 Hz. Applying Sauerbrey equation to the difference in frequency the amount non-specific adsorption was about 756 ng/cm^2 .

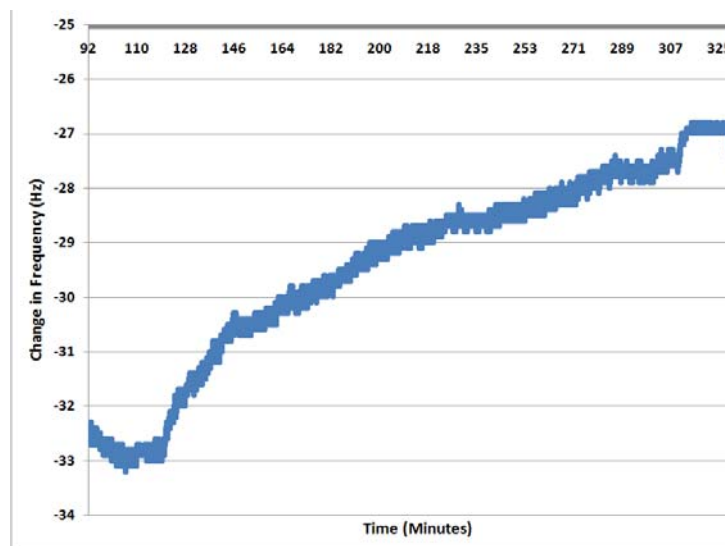


Figure 78 Quartz crystal microbalance graph with a rinse cycle on the TCNL polymer coated crystals. The rinse was performed with a flow of distilled water. Change in frequency over time is displayed. It can be observed in the graph the signal stabilizes after 3 hours.

When the rinse cycle was performed as shown in the Figure 78, the change or difference in frequency was about 6 Hz. Applying Sauerbrey's equation this change in frequency amounts to 108 ng/cm^2 . So there was about 108 ng/cm^2 of freestanding protein on the crystals. The final amount of non-specific adsorption on 4-(3'-chlorodimethylsilyl) propoxy benzophenone crosslinked carbamate polymer was about 648 ng/cm^2 . This was about 36 Hz in frequency difference.

From Figure 77, we know that when the TCNL polymer was not crosslinked with the crosslinker, there was a change of about 41 Hz which corresponds to about 738 ng/cm^2 . Comparing the absorption with and without the crosslinker, we know that crosslinker reduced the absorption by 5 Hz or around 90 ng/cm^2 . The crosslinker reduced the absorption by 12%. This change could be due to polymer surface becoming much more rigid with no transient gaps in between the polymer mesh. There may also be a change in the overall surface charge due to crosslinking.

iv. Non-Specific Adsorption of BSA on Pegylated Polymer Coated Sensors

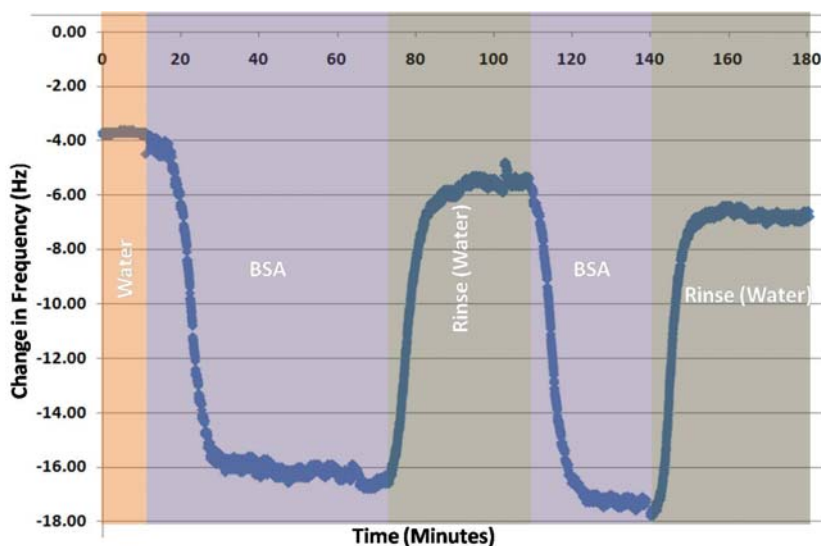


Figure 79 QCM graph with a frequency versus time measurement on a PEG coated TCNL polymer surface. The graph is a dynamic measurement with a flow of water, BSA, water in a sequence for two times. BSA was flown to check the non-specific adsorption and subsequently washed to remove the free flowing protein. This was performed two times sequentially.

To prevent non-specific adsorption, the crosslinked TCNL carbamate polymer was passivated with PEG. As shown in the Figure 79, when PEG passivation was performed there was very low amount of non specific adsorption.

When $20 \mu\text{g/ml}$ BSA in distilled water was flown on the non crosslinked polymer sensor crystal there was a steep decline in the frequency. When the frequency was stabilized the difference in frequency was about 14 Hz. Applying Sauerbrey equation to the difference in frequency the amount non-specific adsorption was about 252 ng/cm^2 .

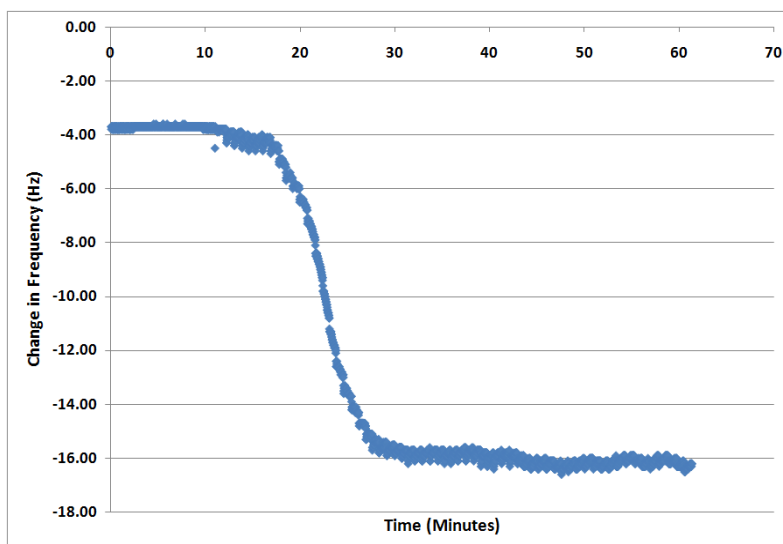


Figure 80 Quartz crystal microbalance graph on a PEG coated polymer crystal. There was a flow of water and BSA in sequence. Change in frequency over time is displayed.

In order to remove the freestanding protein on the polymer crystals, distilled water was flown on the crystals and stopped after the signal stabilized. There was an increase in frequency during the rinse cycle. The change or difference in frequency was about 12 Hz. Applying Sauerbrey's equation this change in frequency amounts to 216 ng/cm² so there was about 216 ng/cm² of freestanding protein on the crystals. There was really low amount protein removed during the rinse cycle. The final amount of non-specific adsorption on PEG passivated polymer coated crystals was about 36 ng/cm². This was about 2 Hz in frequency difference.

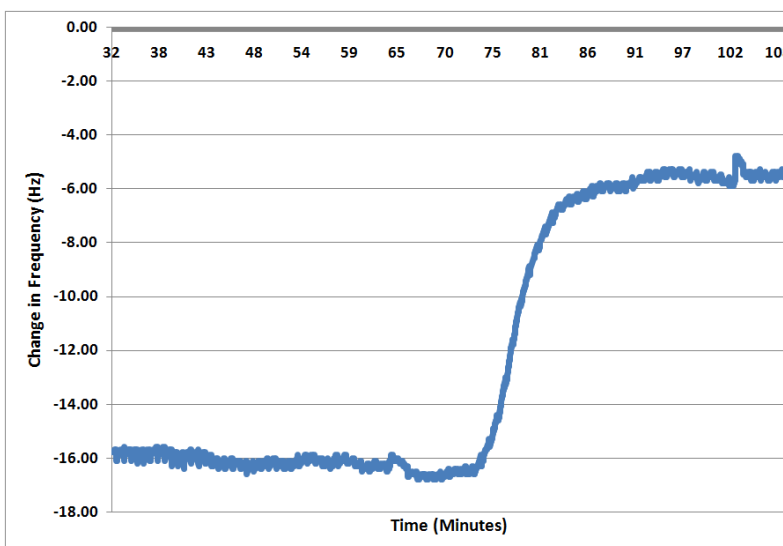


Figure 81 Quartz crystal microbalance graph with a rinse cycle on PEG coated polymer QCM crystal. The rinse was performed with a flow of distilled water. Change in frequency over time is displayed. It can be observed in the graph that the signal stabilizes in the later part of the graph showing that there is no more removal of protein adsorption after some time.

From these QCM studys we found that crosslinking the polymer decreased the non specific adsorption of proteins to the polymer coated substrates. The crosslinker reduced the absorption by 12%. This change could be due to polymer surface becoming much more rigid with no transient gaps in between the polymer mesh. There may also be a change in the overall surface charge due to crosslinking.

PEG passivation is a good way to prevent non specific adsorption of proteins on surfaces. When compared to non-crosslinked TCNL polymer, PEG passivation was 21 times better in preventing the protein adsorption. When compared to crosslinked TCNL polymer, PEG passivation was 18 times better at preventing protein adsorption.

4. Conclusions and Outlook

Polymer based material have been found to have wide biomedical applications³⁵⁶⁻³⁶³. The main goal of the present work is to generate a patterning approach that can pattern on polymers at high resolution in arbitrary shapes. Using TCNL approach, we can generate bioactive surfaces that can be used for a lot of biomedical applications. TCNL's polymers backbone is Polymethylmethacrylate (PMMA), an FDA approved³⁶⁴ biomaterial, hence the TCNL patterning approach designed here can easily be translated to coatings on implant materials.

We have shown the use of TCNL to produce on a polymer surface, at speeds of mm/s, nanopatterns of five different orthogonal chemical functionalities (amines, aldehydes, thiols, biotins, maleimides), which can be used, in a second stage, to attach with standard functionalization methods different classes of nano-objects, such as proteins, nucleic acids, and potentially many others, to the surface. This new TCNL/covalent functionalization (CF)/molecular recognition (MR) approach is conceptually straightforward and, with our current generation of materials, patterns can be written at high resolution (at least 40 nm), and can be potentially massively parallelized, which would enable patterning of large areas (> than 100 cm²) at speeds up to one meter per second. While we have demonstrated the technique on glass substrates, given the fact that the polymer can planarize any substrate, the technique is not limited to atomically smooth substrates and should be applicable to any oxide to which the polymer can be cross-linked. Furthermore, it is significant to note that the surfaces can be pre-patterned and stored for later bio/nano functionalization (at least weeks later). Thus the multi-protein/nano-object patterning can take place under native conditions in a second laboratory without the TCNL equipment or expertise in nanolithography. These features were deliberately built into our protocol to increase the accessibility of the technique to a variety of researchers not only interested in nanolithography, but basic science research in areas of biochemistry, nano-science and nano-biotechnology more broadly.

PEG passivation is important for effective protein patterning and preventing cell adhesion or other cell activity on non patterned area. To prevent the non-specific binding of proteins, an optimal PEG passivation strategy was developed. It was found that when the TCNL polymer was crosslinked, the non-specific binding was reduced by 12%. The PEG passivated surfaces on the other hand were quite effective and reduced the non-specific binding by approximately 20 times.

To test the flexibility of the patterning approach, we patterned an antibody and protein side by side (anti-CD3 and ICAM). We showed the flexibility of this approach by patterning these molecules in different shapes and in concentric patterns. Maintaining the bioactivity of surface-patterned proteins is crucial, we tested the patterned biomolecules using two different assays. We verified the bioactivity by checking the ability of anti-CD3 to bind to secondary antibody, anti-IgG and showed that the patterned antibody is bioactive. Since the ultimate goal is to use the patterned biomolecules for cell sensing, we tested the bioactivity and viability of patterned substrates with a well studied system of immune synapse and T cell activation⁴¹⁴. The spatial correlation of protein kinase C- θ (PKC- θ) inside a T-cell interacting with the underlying anti-CD3 pattern proves that the patterned biomolecules are bioactive.

We foresee that the TCNL can have a direct impact on the development of nano-devices, biosensors, and on many cell studies that require interaction with two or more proteins in tailor-made patterns. Studies to increase the reliability of the initial patterning and

of the sample preparation protocols, to improve the resolution and create concentration gradients of functional groups, and to expand the range of chemical transformation activated by the technique, are currently underway and should further expand the applicability and robustness of the technique.

Abbreviations

| | |
|--------------------------------|---|
| AFM | Atomic Force Microscope |
| APTES | 3-aminopropyltriethoxysilane (C ₉ H ₂₃ NO ₃ Si) |
| ARP2/3 | Actin Related Protein 2/3 |
| ATP | Adenosine-5'-triphosphate |
| ATR | Attenuated Total Reflectance |
| BSA | Bovine Serum Albumin |
| CD3 | Cluster of Differentiation (T-Cell Co-Receptor) |
| CDC 42 | Cell Division Control Protein 42 |
| CPD | Critical Point Dryer |
| CR | Compliment Receptors |
| CSIF | Cytokine Synthesis Inhibitory Factor |
| DACM | n-(7-dimethylamino-4-methylcoumarin-3-yl)maleimide |
| DMEM | Dulbeccos Modified Eagle Medium |
| DMSO | Dimethyl Sulfoxide |
| DNA | Deoxyribonucleic Acid |
| DTNB | Dithionitrobenzoic Acid, 5,5'-Dithiobis(2-nitrobenzoic acid) |
| DTT | Dithiothreitol |
| EDTA | Ethylenediaminetetraacetic Acid |
| ELISA | Enzyme-linked Immunosorbant Assay |
| ERK | Extracellular Signal-Regulated Protein Kinases |
| FAK | Focal Adhesion Kinase |
| FBS | Fetal Bovine Serum |
| FDA | Food and Drug Administration |
| FITC | Fluorescein Isothiocyanate |
| Fn | Fibronectin |
| FTIR | Fourier Transformed Infrared Spectroscopy |
| GA | Glutaraldehyde |
| GEF | Guanine Nucleotide Exchange Factors |
| GM-CSF | Granulocyte Macrophage Colony-Stimulating Factor |
| GTP | Guanosine-5'-triphosphate |
| H ₂ SO ₄ | Sulfuric Acid |
| H ₂ O ₂ | Hydrogen Peroxide |
| HAuCl ₄ | Tetrachloroauric Acid |
| HCL | Hydrochloric Acid |
| HRP | Horseradish Peroxidase |
| ICAM | Inter-Cellular Adhesion Molecule |
| IFN-γ | Interferon-Gamma |
| IgG | Immunoglobulin G |
| IL-1β | Interleukin 1β |
| IL-10 | Interleukin 10 |
| IL-6 | Interleukin 6 |
| ITAM | Immunoreceptor Tyrosine Based Activation Motif |
| ITIM | Immunoreceptor Tyrosine Based Inhibitory Motif |

| | |
|--------------------------------|--|
| K ₂ CO ₃ | Potassium Carbonate |
| K ₂ SO ₄ | Potassium Sulfate |
| LDL | Low Density Lipoprotein |
| LPS | Lipopolysaccharide |
| MEMS | Microelectrical Mechanical Systems |
| mPEG2000-urea | Methoxy Polyethylene Glycol Triethoxysilane |
| NaOH | Sodium Hydroxide |
| NHS | N-Hydroxysuccinimide |
| NH ₂ | Amine |
| NTB | 2-Nitro-5-Thiobenzoate |
| OH | Hydroxylate Group |
| P2VP | Poly-2-Vinyl Pyridine |
| PAH | Poly(Allylamine Hydrochloride) |
| PBS | Phosphate Buffered Saline |
| PDMS | Polydimethylsiloxane |
| PEG | Poly(Ethylene Glycol) |
| PI3-K | Phosphoinositide 3-Kinase |
| PKC-θ | Protein Kinase C-θ |
| PMPI | N-[p-Maleimidophenyl]isocyanate |
| PMMA | Poly(Methyl Methacrylate) |
| PS | Polystyrol |
| PSS | PolyStyrene Sulfonate |
| PtdIns | Phosphatidylinositol |
| QCM | Quartz Crystal Microbalance |
| Rac | Ras-Related C3 Botulinum Toxin Substrate |
| SAv | Streptavidin |
| SEM | Scanning Electron Microscope |
| SH | Thiol, Sulfur-Hydrogen Bond, Sulfhydryl Group |
| SOCS-3 | Suppressor of Cytokine Signaling 3 |
| SPDP | N -Succinimidyl 3-(2-Pyridyldithio)-Propionate |
| SPM | Scanning Probe Microscopy |
| SNOM | Scanning Near-Field Optical Microscopy |
| SYK | Spleen Tyrosine Kinase |
| TCNL | Thermo-Chemical Nanolithography |
| TEM | Transmission Electron Microscopy |
| TGA | Thermogravimetric Analysis |
| TGF-β | Transforming Growth Factor Beta |
| THF | Tetrahydrofuran |
| TLR4 | Surface Toll like Receptor 4 |
| THP | Tetrahydropyranyl |
| TMB | 3,3',5,5' – tetramethylbenzidine |
| TNF-α | Tumor Necrosis Factor-Alpha |
| WASP | Wiskott-Aldrich Syndrome Protein |
| WGA | Wheat Germ Agglutinin |
| XPS | X-Ray Photoelectron Spectroscopy |

Table of Figures

| | |
|--|----|
| Figure 1 (A) Depicts stages involved in phagocytotic uptake. The uptake process occurs in a series of stages rather than just one gulp. (B) Contractile force applied on the target during phagocytotic uptake. (C) Tensile force measured during phagocytotic uptake by most biophysical techniques. | 5 |
| Figure 2 Depiction of pathway for FcγR mediated phagocytotic uptake. | 9 |
| Figure 3 Schematic images of pillar arrays used in this study to analyze frustrated phagocytotic traction forces. (A) Top view of cell lying on a pillar substrate. Pillar bending is related to the forces a cell exerts on their environment. By measuring the displacement of the pillar heads in a top view approach, the exerted forces can be obtained. (B) Side view of a cell lying on a pillar array. | 12 |
| Figure 4 Schematic of a polyelectrolyte capsule being engulfed by a macrophage during phagocytotic uptake. | 13 |
| Figure 5 Schematic of pillar array preparation. The pillar array is prepared by spincoating a silicon or glass slide with a layer of negative photo resist. After developing the SU-8 with holes in it, PDMS is poured into this mold. Curing is performed at 65 °C and subsequently the PDMS pillar array can be peeled off. | 14 |
| Figure 6 Schematic of preparation and IgG coating of the hollow capsules. Consecutive adsorption of PAH (Red) and PSS (Blue) is performed on a core particle. After achieving the required dimensions, the core is dissolved leading to formation of hollow capsules. Finally the protein (IgG) is bound on the surface by electrostatic forces. | 16 |
| Figure 7 Schematic of capsule swelling and shrinking as a result of temperature changes. Heating causes the capsule to soften and increase in size, while cooling of the annealed capsule induces shrinking. | 18 |
| Figure 8 SEM image of PDMS arrays acting as force sensors in frustrated phagocytosis. (A) Image of a macrophage on an array taken at 45° showing that the cell deflecting a pillar by 59.7°. (B) and (C) Array images at different magnifications. (D) Schematic of an individual pillar in the pillar array. The force F exerted by the cell can be calculated by measuring the displacement $2r$ | 21 |
| Figure 9 SEM image of PDMS arrays acting as force Sensors in frustrated phagocytosis. (A) and (B) Images of a macrophage on an array taken at 45° showing cells deflecting pillars. The blue arrow shows the problem of the macrophages trying to eat the pillar instead of spreading during frustrated phagocytosis. (C) Schematic of expected frustrated phagocytosis and macrophage spreading for accurate calculation of force and a schematic showing the problem in measuring the forces as the cells start spreading on the edges. (D) Macrophage engulfing a pillar. | 22 |
| Figure 10 (A) Schematic illustration of a capsule being deformed by the AFM. By applying defined force and measuring the resulting deformation we can understand and calibrate the mechanical properties of the polyelectrolyte capsules. (B) A simple mechanical equivalent circuitry representation of the force being applied to capsules. | 23 |
| Figure 11 Graph showing force versus deformation of the 9 layers 4.5 μm diameter PSS/ PAH polyelectrolyte capsules. The red line indicates the linear regime of the capsule. In this regime the capsules are perfectly elastic and go back to their original state when the applying force is relaxed. The buckling regime or irreversible deformation of the capsule occurs around 150 nN. | 24 |
| Figure 12 (A) Histogram of capsule stiffness in the linear regime. The average stiffness of the capsules was 0.12 nN/nM. (B) Histogram of the force required to buckle or irreversibly deform the capsules. The average buckling force of the capsules was 150 nN. | 25 |
| Figure 13 (A, B, C, D, E, F, G) show macrophages J774a.1 with 4.5 μm diameter PSS/PAH capsules engulfed by cells after 90 minutes. It can be observed that most of the capsules were buckled. Round unbuckled capsules can be seen outside the cell area in the right hand corner of images (C) and (F). | 26 |
| Figure 14 Four images with capsules in pH 4 buffer after 24 hours. It can be seen that most of the capsules are perfectly spherical. | |
| Figure 15 A mechanistic model of the phagocytotic cup formation showing how the signaling events are interlinked like gears in a device. The phagocytotic signaling starts with the receptor recognition followed by different signaling events including SYK activation leads to PI3-Kinase and the signaling event continues until the phagocytotic cup closure occurs. | 28 |
| Figure 16 (A, B, C, D) Shows macrophages J774a.1 with 4.5 μm diameter PSS/PAH capsules engulfed by cells after 90 minutes. The PI3-Kinase is inhibited by adding 50 μM LY294002. It can be observed that most of the capsules were oval but not buckled after 90 minutes. Round spherical capsule can also be seen outside the cell area in the top left hand corner of image (A). | 29 |
| Figure 17 Macrophages J774a.1 with 4.5 μm diameter PSS/PAH capsules engulfed by cells after 90 minutes. The SYK kinase activity was inhibited by adding piceatannol. It can be observed that most of the capsules were slightly oval but not buckled after 90 minutes. Round spherical capsule can also be seen outside the cell area in middle portion of the image. | 30 |
| Figure 18 Eccentricity of a capsule after phagocytosis is initiated. The capsules outline for some of the data points can be seen in the inserts. | 32 |
| Figure 19 Methodology of eccentricity determination of the capsules. In order to determine the eccentricity as shown in images Figure 21 (Aa) column, we initially did a maximum intensity projection of the 4d movie. As shown in (Ab) we then found the edges of the capsules. As shown in the Figure 21 (C) we found the dimensions of maximum axis/ minimum axis of the ellipse to determine the eccentricity. The top right portion (B) of the Figure 21 shows the eccentricity changes with time during phagocytotic uptake of the capsules. | 33 |

| | |
|--|----|
| Figure 20 Schematic showing key properties and functions of the two different macrophage phenotypes M1 and M2. Macrophages acquire different functional properties in response to environment-derived stimuli and express different cytokines. | 41 |
| Figure 21 Schematic of amine derivatization on glass using APTES treatment. | 42 |
| Figure 22 Schematic showing Fc fragment of IgG and modification of the fragment to create SH on it..... | 43 |
| Figure 23 Epi-fluorescence image of J774a.1 cell labeled with WGA..... | 44 |
| Figure 24 Schematic of the ELISA procedure..... | 45 |
| Figure 25 (A) Schematic illustration of a diblock copolymer with distinct hydrophobic (PS, red portion) and hydrophilic part (P2VP, blue portion). (B) and (C) Schematic representations of a micelle and a reverse micelle with the polar components on the outside and inside respectively. (D) Schematic illustration of a reverse micelle loading mechanism. The metal salt selectively enters into the polar micelle core..... | 47 |
| Figure 26 Schematic of the micellar nanopatterning approach. Glass substrates are dipped in the micellar solution at a constant speed. A monolayer of micelles is coated on the surface by dipping and removing the surface in a solution of micelles at a specific speed. The Surface is then air dried and plasma etched to remove the organic components present on the surface of the substrate, resulting in Au nanoparticles being organized in hexagonal order..... | 48 |
| Figure 27 Chemical structure of mPEG 2000-urea..... | 49 |
| Figure 28 Schematic of Fc protein patterning strategy. | 49 |
| Figure 29 QCM graph displaying SH modified Fc binding to a gold film, followed by a bioactivity test. Initially PBS was flown(grey region) followed by thiolated Fc fragment . The equilibrium in yellow region shows the thiolated Fc binding to gold surface of the QCM crystal. Anti-Fc binding in the pink region shows that the thiolated Fc fragment is bioactive. The blue region shows the rinse cycle. | 51 |
| Figure 30 FTIR graph on PEG silane bound glass substrate. (A) Spectral range of carbonyl groups(C=O) and (B) Spectral range for C-H groups present on mPEG 2000-urea. | 52 |
| Figure 31 Contact angle on a 125 nm spaced nanopattern before (A, B) and after (C, D) PEG passivation. The hydrophilic nature of PEG can be seen in the PEG passivated nanostructures in Figure C and D. The red and yellow line shown in Figure B displays the contact angle measuring procedure. | 53 |
| Figure 32 A, B AFM topography images of nanostructured surfaces with PEG coating without and with Fc respectively. C,D are the sample height profiles of A,B. | 54 |
| Figure 33 Graph showing protein concentration incubated versus amount of protein bound to surface. | 55 |
| Figure 34 Cell area on nanopatterned substrates after 48 hours. There was a decrease in cell area with increasing spacing. LPS which is a positive macrophage activation signaling chemical caused the cell to spread the maximum..... | 58 |
| Figure 35 Coordination occurring during Fc mediated phagocytosis occurring due to signals generated near FcR passing through distinct stages. IgG molecules (gold dots) on the surface of a particle (blue) are engaged by FcR (Red) in the macrophage plasma membrane (light green). The three images indicate a sequence of movements and receptor signaling during a coordinated phagocytotic process. New interactions between IgG and FcR occur as the membrane advances over the particle. The junction between FcR recruit proteins and IgG form FcR signaling complexes. | 59 |
| Figure 36 Change in cell area on plain glass and Fc coated slides (1 mg/ml). The cell area was determined at different time points. There was an increase in cell area with time. | 60 |
| Figure 37 Cytokine classification according to their pro and anti roles in wound healing and inflammation..... | 61 |
| Figure 38 TNF- α production on PEG passivated nano substrates. Except for 125 nm spaced substrates, most of the substrates produced similar amount of TNF- α | 62 |
| Figure 39 Anti-Inflammation cytokine IL-10 secreted by macrophages at 24 and at 48 hours on slides with changing Fc concentration on the substrate. The insert is a bar graph with control LPS included. | 64 |
| Figure 40 Anti-inflammation cytokine TGF- β secreted by macrophages at 24 and at 48 hours on slides with changing Fc fragment concentration. The insert is a bar graph with control LPS included..... | 65 |
| Figure 41 Anti-inflammation cytokines (IL-10, TGF- β) secreted by macrophages at 24 and 48 hours on nano substrates coated with Fc..... | 67 |
| Figure 42 Pro-inflammation cytokine TNF- α secreted by macrophages at 24 and 48 hours on slides at different concentrations. The average error or standard deviation observed was much higher in 24 hrs than those observed at 48 hours. The insert is a bar graph which includes TNF- α production by LPS stimulated macrophages..... | 69 |
| Figure 43 Pro-inflammation cytokines, TNF- α and IL-1 β secreted by macrophages at 24 and 48 hours on nanopatterned substrates..... | 70 |
| Figure 44 Transmittance FTIR spectra of the polymer upon bulk heating. The decrease in the peak at 1725 cm ⁻¹ starting at 150 °C is consistent with the loss of the protecting group (carbamate carbonyl group). | 82 |
| Figure 45 Fluorescence micrograph of a surface with four rectangular TCNL micropatterns written at linear speeds of 0.5, 1, 1.5, 2 mm/s respectively, with a normal load of 100 nN and with a tip temperature of T = 220 °C \pm 20 °C. The patterning was performed in ambient conditions (air). For visualization, the patterns were functionalized with the protocol of NHS/Bn+Cy5/SAv (For protocols refer to results section on protein patterning)..... | 83 |

| | |
|--|-----|
| Figure 46 Thermogravimetric analysis of TCNL polymer. The transition temperature T_d at 160°C is highlighted in the graph. | 84 |
| Figure 47 Schematic of the expected chemical change in the TCNL polymer at transition temperature T_d | 85 |
| Figure 48 Schematic of TCNL patterning procedure. (a) A nanoarray of one type of nano-object is created in three steps: TCNL, crosslinker incubation and nano-object immobilization. (b) A double functionality pattern of thiols (blue triangles) and amines (green disks) is created through two rounds of TCNL and one or two rounds of incubation (post-TCNL functionalization). (c) A triple functionality pattern of thiols (blue triangles), biotins (red diamonds), and amines (green disks) is created through three rounds of TCNL and two rounds of incubation. | 88 |
| Figure 49 Flowchart illustrating how the unmasked amine nanotemplates are selectively and covalently functionalized to create patterns of thiols, maleimides, aldehydes or biotins in distinct areas of the polymer surface. | 89 |
| Figure 50 Mechanism of Schiff base formation on the deprotected substrate and subsequent protein binding using glutaraldehyde as a crosslinker. | 90 |
| Figure 51 (A) Fibronectin patterns patterned in the form of lines labeled with Atto488. The triangles in part (B) of the image are labeled with Cy5 Streptavidin. The scale bar is 500 nm and $5\mu\text{m}$ for (A) and (B) respectively. | 90 |
| Figure 52 (A) alexa350 labeled biotin-antiCD3 patterns. The same triangles were labeled with Cy5 streptavidin before binding with biotin-antiCD3. The Cy5 fluorescence can be observed in image (B). | 91 |
| Figure 53 Chemical structure of (A) SPDP (N -Succinimidyl 3-(2-pyridyldithio)-propionate) and (B) DTT (dithiothreitol). | 91 |
| Figure 54 Alexa350 labeled anti-CD3 bound to SH groups created on TCNL patterns. The scale bar is $5\mu\text{m}$ | 92 |
| Figure 55 Epi-fluorescence image of DACM and Cy5-streptavidin orthogonal functionality patterns on the same surface. Blue DACM was crosslinked to amine-terminated triangles by means of SPDP-DTT thiolation, while red Cy5-streptavidin was crosslinked to amine-terminated diamonds by means of NHS-biotin. The scale bar is $5\mu\text{m}$ | 93 |
| Figure 56 Anti-CD3 and ICAM-1 closely co-patterned on a single surface. These images show how we can pattern the proteins in arbitrary designs. Scale bars: $5\mu\text{m}$ | 94 |
| Figure 57 500 nm fibronectin nanoarray. Epi-fluorescence image of a regular array of Atto488 fibronectin patches (a) and cross section profile (b). A linear interpolation (solid line) has been used to interpolate the fluorescence data points (dots) obtained by optical microscopy. Fibronectin was crosslinked to amine groups by means of GA. (C) is the AFM phase image of the fibronectin array. Scale bar: $1\mu\text{m}$. It should be mentioned that the radius of the features is comparable in size with the resolution of the optical image ($\sim 0.61 \lambda/\text{NA}$, where λ is the wavelength used and NA is the numerical aperture of the objective), so other techniques should be used to determine the distribution of proteins within each feature. | 94 |
| Figure 58 Fibronectin and streptavidin nanoarray down to 40 nm. AFM topography and phase images of a TCNL nanoarray before and after fibronectin (a) and streptavidin (b) attachment. The topography z-range in (a) is 20 nm. Scale bars: 100 nm. | 95 |
| Figure 59 Oriented patterning of ICAM-1 labeled with anti-ICAM (FITC). | 96 |
| Figure 60 AFM topography and phase images of a triangular pattern of thiol-terminated DNA single strands crosslinked to amines through PMPI. The height profiles for the topography and phase image can be seen in the graphs on the right side of the image. | 96 |
| Figure 61 Epi-fluorescence image of anti-CD3 bioactivity. Alexa350 labeled biotinylated anti-human CD3 (blue) bound to the TCNL amine pattern by means of NHS-biotin and streptavidin shows bioactive molecular recognition of FITC-labeled IgG (green). | 99 |
| Figure 62 Patterned ICAM-1 labeled with anti-ICAM (FITC). | 99 |
| Figure 63 Jurkat cells, immunostained for PKC- θ , lying on a triangular anti-CD3 pattern. The PKC- θ accumulation above the cell-pattern contact site can be observed. | 100 |
| Figure 64 Chemical structure of O-(2-aminoethyl)polyethylene glycol, also called aminopolyethylene glycol, used for passivating the polymer surfaces. | 102 |
| Figure 65 Schematic of the effect of salt treatment on PEG coverage. By salt treatment, the transient gaps between the chains are reduced and a much denser pattern with no gaps that covers the substrate is achieved. | 102 |
| Figure 66 Fluorescent image of FITC labeled PEG on TCNL patterns. | 103 |
| Figure 67 Fluorescent image of fluorescent FITC PEG bound everywhere except the TCNL patterned area. | 103 |
| Figure 68 Chemical structure of FITC-PEG-NH ₂ , Fluorescein PEG amine (MW 3400). | 104 |
| Figure 69 Schematic illustration of a PEG passivation on TCNL patterned surfaces. The polymer spin coated samples were TCNL patterned using a hot AFM tip. The samples were then incubated with NHS biotin to get biotin patterns. The sample with biotin patterns was heated on a hot plate for 3 mins at 180°C , which created de-protected amines on the back with biotin patterns. The sample was then incubated with glutaraldehyde. The aldehyde surface was passivated using amine PEG. The final samples had biotin patterns with the area between them passivated with PEG. | 104 |
| Figure 70 PEG passivated slide with biotin patterns. The biotin patterns were then bound to Cy5 streptavidin which can be seen from the fluorescence image. | 105 |
| Figure 71 Contact angle on protected polymer, deprotected polymer, PEG passivated (standard) and salt-treated PEG passivated surfaces. | 106 |

| | |
|--|-----|
| Figure 72 Bar graph of non-specific protein adsorption on QCM crystals coated with polymer films of different types and processing. The amount or mass of protein non-specifically adsorbed on the surface is also mentioned on the bar graphs.. | 108 |
| Figure 73 QCM measurement with a frequency versus time measurement on TCNL polymer without crosslinker. The graph is a dynamic measurement with a flow of water, BSA, water in a sequence. BSA was flown to check the non-specific adsorption and subsequently washed and rinsed with distilled and deionized water to remove the free standing protein. | 108 |
| Figure 74 Quartz crystal microbalance graph of frequency change versus time on a non cross-linked polymer coated QCM crystal with a flow of water and BSA in sequence. Change in frequency over time is displayed. The change in frequency is due to non-specific adsorption of BSA onto the polymer crystal. | 109 |
| Figure 75 Quartz crystal microbalance graph with a rinse cycle on non-crosslinked polymer coated surface. The rinse was performed with a flow of distilled water. Change in frequency over time is displayed. It can be observed in the graph the signal stabilizes showing that there is no more removal of protein adsorption after some time. | 110 |
| Figure 76 QCM measurement on TCNL polymer coated crystal. The graph is a dynamic measurement of change in frequency versus time, with a flow of water, BSA, water in a sequence | 110 |
| Figure 77 Quartz crystal microbalance graph on a TCNL polymer coated crystal with a flow of water and BSA in sequence. Change in frequency over time is displayed. | 111 |
| Figure 78 Quartz crystal microbalance graph with a rinse cycle on the TCNL polymer coated crystals. The rinse was performed with a flow of distilled water. Change in frequency over time is displayed. It can be observed in the graph the signal stabilizes after 3 hours. | 111 |
| Figure 79 QCM graph with a frequency versus time measurement on a PEG coated TCNL polymer surface. The graph is a dynamic measurement with a flow of water, BSA, water in a sequence for two times. BSA was flown to check the non-specific adsorption and subsequently washed to remove the free flowing protein. This was performed two times sequentially. | 112 |
| Figure 80 Quartz crystal microbalance graph on a PEG coated polymer crystal. There was a flow of water and BSA in sequence. Change in frequency over time is displayed..... | 113 |
| Figure 81 Quartz crystal microbalance graph with a rinse cycle on PEG coated polymer QCM crystal. The rinse was performed with a flow of distilled water. Change in frequency over time is displayed. It can be observed in the graph that the signal stabilizes in the later part of the graph showing that there is no more removal of protein adsorption after some time. | 113 |

Bibliography

- 1 Jones SL, L. F., Brown EJ. in *Fundamental Immunology* (ed WE Paul) 997-1020 (Lippincott-Raven, 1999).
- 2 Aderem, A. & Underhill, D. M. Mechanisms of phagocytosis in macrophages. *Annu. Rev. Immunol.* 17, 593-623 (1999).
- 3 May, R. & Machesky, L. Phagocytosis and the actin cytoskeleton. *J Cell Sci* 114, 1061-1077 (2001).
- 4 Garcia-Garcia, E. & Rosales, C. Signal transduction during Fc receptor-mediated phagocytosis. *J Leukoc Biol* 72, 1092-1108 (2002).
- 5 Swanson, J. A. *et al.* A contractile activity that closes phagosomes in macrophages. *J Cell Sci* 112, 307-316 (1999).
- 6 Stendahl, O., Hartwig, J., Brotschi, E. & Stossel, T. Distribution of actin-binding protein and myosin in macrophages during spreading and phagocytosis. *J. Cell Biol.* 84, 215 (1980).
- 7 Yamamoto, K., Pardee, J., Reidler, J., Stryer, L. & Spudich, J. Mechanism of interaction of Dictyostelium severin with actin filaments. *J. Cell Biol.* 95, 711 (1982).
- 8 Griffin, F., Jr, Griffin, J., Leider, J. & Silverstein, S. Studies on the mechanism of phagocytosis. I. Requirements for circumferential attachment of particle-bound ligands to specific receptors on the macrophage plasma membrane. *J Exp Med* 142, 1263-1282, doi:10.1084/jem.142.5.1263 (1975).
- 9 Griffin, F. M., Jr. & Silverstein, S. C. Segmental Response of the Macrophage Plasma Membrane to a Phagocytic Stimulus. *J. Exp. Med.* 139, 323-336, doi:10.1084/jem.139.2.323 (1974).
- 10 Southwick, F. S. & Stossel, T. P. Contractile proteins in leukocyte function. *Semin Hematol.* 20, 305-321 (1983).
- 11 Choquet, D., Felsenfeld, D. P. & Sheetz, M. P. Extracellular Matrix Rigidity Causes Strengthening of Integrin-Cytoskeleton Linkages. *Cell* 88, 39-48, doi:10.1016/S0092-8674(00)81856-5 (1997).
- 12 Sheetz, M. P., Felsenfeld, D. P. & Galbraith, C. G. Cell migration: regulation of force on extracellular-matrix-integrin complexes. *Trends Cell Biol* 8, 51-54 (1998).
- 13 Wang, N., Butler, J. P. & Ingber, D. E. Mechanotransduction across the cell surface and through the cytoskeleton. *Science* 260, 1124-1127, doi:10.1126/science.7684161 (1993).
- 14 Shiratsuchi, H. & Basson, M. D. Extracellular pressure stimulates macrophage phagocytosis by inhibiting a pathway involving FAK and ERK. *Am J Physiol Cell Physiol* 286, C1358-1366, doi:10.1152/ajpcell.00553.2003 (2004).
- 15 Shiratsuchi, H. & Basson, M. D. Activation of p38 MAPK{alpha} by extracellular pressure mediates the stimulation of macrophage phagocytosis by pressure. *Am J Physiol Cell Physiol* 288, C1083-1093, doi:10.1152/ajpcell.00543.2004 (2005).
- 16 Vonna, L., Wiedemann, A., Aepfelbacher, M. & Sackmann, E. Local force induced conical protrusions of phagocytic cells. *J Cell Sci* 116, 785-790, doi:10.1242/jcs.00230 (2003).
- 17 Bausch, A. R., Moller, W. & Sackmann, E. Measurement of Local Viscoelasticity and Forces in Living Cells by Magnetic Tweezers. *Biophys. J.* 76, 573-579 (1999).
- 18 Kress, H. *et al.* Filopodia act as phagocytic tentacles and pull with discrete steps and a load-dependent velocity. *Proc Natl Acad Sci U S A* 104, 11633-11638, doi:10.1073/pnas.0702449104 (2007).
- 19 Evans, E., Leung, A. & Zhelev, D. Synchrony of cell spreading and contraction force as phagocytes engulf large pathogens. *J. Cell Biol.* 122, 1295-1300, doi:10.1083/jcb.122.6.1295 (1993).
- 20 Swanson, J. A. & Hoppe, A. D. The coordination of signaling during Fc receptor-mediated phagocytosis. *J Leukoc Biol* 76, 1093-1103, doi:10.1189/jlb.0804439 (2004).
- 21 Smith, L. A., Aranda-Espinoza, H., Haun, J. B., Dembo, M. & Hammer, D. A. Neutrophil Traction Stresses are Concentrated in the Uropod during Migration. *Biophys. J.* 92, L58-L60 (2007).
- 22 Ofek, I., Goldhar, J., Keisari, Y. & Sharon, N. Nonopsonic Phagocytosis of Microorganisms. *Annu Rev Microbiol* 49, 239-276, doi:10.1146/annurev.mi.49.100195.001323 (1995).
- 23 Ravetch, J. V. & Kinet, J. P. Fc Receptors. *Annu Rev Immunol* 9, 457-492, doi:10.1146/annurev.iy.09.040191.002325 (1991).
- 24 Carroll, M. C. The Role of Complement and Complement Receptors in Induction and Regulation of Immunity. *Annu Rev Immunol* 16, 545-568, doi:10.1146/annurev.immunol.16.1.545 (1998).
- 25 Steele, C. *et al.* Alveolar Macrophage-mediated Killing of *Pneumocystis carinii* f. sp. muris Involves Molecular Recognition by the Dectin-1 {beta}-Glucan Receptor. *J. Exp. Med.* 198, 1677-1688, doi:10.1084/jem.20030932 (2003).
- 26 Cambier, J. C. New nomenclature for the Reth motif (or ARH1/TAM/ARAM/YXXL). *Immunol. Today* 16, doi:10.1016/0167-5699(95)80105-7 (1995).
- 27 Van den Herik-Oudijk, I., Capel, P., van der Bruggen, T. & Van de Winkel, J. Identification of signaling motifs within human Fc gamma RIIa and Fc gamma RIIb isoforms. *Blood* 85, 2202-2211 (1995).
- 28 Reth, M. Antigen receptor tail clue. *Nature* 338, 383-384 (1989).
- 29 Ghazizadeh, S., Bolen, J. B. & Fleit, H. B. Tyrosine phosphorylation and association of Syk with Fc gamma RII in monocytic THP-1 cells. *Biochem. J.* 305, 669-674 (1995).
- 30 Greenberg, S., Chang, P., Wang, D. C., Xavier, R. & Seed, B. Clustered syk tyrosine kinase domains trigger phagocytosis. *Proc Natl Acad Sci U S A* 93, 1103-1107 (1996).

- 31 Latour, S., Chow, L. M. L. & Veillette, A. Differential Intrinsic Enzymatic Activity of Syk and Zap-70 Protein-tyrosine Kinases. *J. Biol. Chem.* 271, 22782-22790, doi:10.1074/jbc.271.37.22782 (1996).
- 32 Kiefer, F. *et al.* The Syk Protein Tyrosine Kinase Is Essential for Fc γ Receptor Signaling in Macrophages and Neutrophils. *Mol. Cell. Biol.* 18, 4209-4220 (1998).
- 33 Crowley, M. T. *et al.* A Critical Role for Syk in Signal Transduction and Phagocytosis Mediated by Fc γ Receptors on Macrophages. *J. Exp. Med.* 186, 1027-1039, doi:10.1084/jem.186.7.1027 (1997).
- 34 Matsuda, M. *et al.* Abrogation of the Fc γ receptor IIA-mediated phagocytic signal by stem-loop Syk antisense oligonucleotides. *Mol. Biol. Cell* 7, 1095-1106 (1996).
- 35 Cox, D., Chang, P., Kurosaki, T. & Greenberg, S. Syk Tyrosine Kinase Is Required for Immunoreceptor Tyrosine Activation Motif-dependent Actin Assembly. *J. Biol. Chem.* 271, 16597-16602, doi:10.1074/jbc.271.28.16597 (1996).
- 36 Oliver, J., Burg, D., Wilson, B., McLaughlin, J. & Geahlen, R. Inhibition of mast cell Fc ϵ R1-mediated signaling and effector function by the Syk-selective inhibitor, piceatannol. *J. Biol. Chem.* 269, 29697-29703 (1994).
- 37 Martin, T. F. J. Phosphoinositide Lipids as Signaling Molecules: Common Themes for Signal Transduction, Cytoskeletal Regulation, and Membrane Trafficking. *Annu Rev Cell Dev Biol* 14, 231-264, doi:10.1146/annurev.cellbio.14.1.231 (1998).
- 38 Strzelecka, A. *et al.* Syk kinase, tyrosine-phosphorylated proteins and actin filaments accumulate at forming phagosomes during Fc γ receptor-mediated phagocytosis. *Cell Motil Cytoskeleton* 38, 287-296 (1997).
- 39 Chacko, G. W., Brandt, J. T., Coggeshall, K. M. & Anderson, C. L. Phosphoinositide 3-Kinase and p72[IMAGE] Noncovalently Associate with the Low Affinity Fc[IMAGE] Receptor on Human Platelets through an Immunoreceptor Tyrosine-based Activation Motif. *J. Biol. Chem.* 271, 10775-10781, doi:10.1074/jbc.271.18.10775 (1996).
- 40 Sobota, A. *et al.* Binding of IgG-Opsonized Particles to Fc γ R Is an Active Stage of Phagocytosis That Involves Receptor Clustering and Phosphorylation. *J Immunol* 175, 4450-4457 (2005).
- 41 Rameh, L. E., Chen, C.-S. & Cantley, L. C. Phosphatidylinositol (3,4,5)P3 interacts with SH2 domains and modulates PI 3-kinase association with tyrosine-phosphorylated proteins. *Cell* 83, 821-830 (1995).
- 42 Ninomiya, N. *et al.* Involvement of phosphatidylinositol 3-kinase in Fc γ receptor signaling. *J. Biol. Chem.* 269, 22732 (1994).
- 43 Araki, N., Hatae, T., Furukawa, A. & Swanson, J. A. Phosphoinositide-3-kinase-independent contractile activities associated with Fc γ -receptor-mediated phagocytosis and macropinocytosis in macrophages. *J Cell Sci* 116, 247-257, doi:10.1242/jcs.00235 (2003).
- 44 Cox, D., Tseng, C.-C., Bjekic, G. & Greenberg, S. A Requirement for Phosphatidylinositol 3-Kinase in Pseudopod Extension. *J. Biol. Chem.* 274, 1240-1247, doi:10.1074/jbc.274.3.1240 (1999).
- 45 Seastone, D. J., Lee, E., Bush, J., Knecht, D. & Cardelli, J. Overexpression of a Novel Rho Family GTPase, RacC, Induces Unusual Actin-based Structures and Positively Affects Phagocytosis in Dictyostelium discoideum. *Mol. Biol. Cell* 9, 2891-2904 (1998).
- 46 Lowry, M. B., Duchemin, A.-M., Coggeshall, K. M., Robinson, J. M. & Anderson, C. L. Chimeric Receptors Composed of Phosphoinositide 3-Kinase Domains and Fc γ Receptor Ligand-binding Domains Mediate Phagocytosis in COS Fibroblasts. *J. Biol. Chem.* 273, 24513-24520, doi:10.1074/jbc.273.38.24513 (1998).
- 47 Botelho, R. J. *et al.* Localized Biphasic Changes in Phosphatidylinositol-4,5-Bisphosphate at Sites of Phagocytosis. *J. Cell Biol.* 151, 1353-1368, doi:10.1083/jcb.151.7.1353 (2000).
- 48 Anne, J. R. Rho proteins, PI 3-kinases, and monocyte/macrophage motility. *FEBS Lett.* 498, 168-171 (2001).
- 49 Giovanna Chimini, P. C. Function of Rho family proteins in actin dynamics during phagocytosis and engulfment. *Nat Cell Biol* 2, E191 - E196, doi:10.1038/35036454 (2000).
- 50 Hackam, D. J., Rotstein, O. D., Schreiber, A., Zhang, W.-j. & Grinstein, S. Rho is Required for the Initiation of Calcium Signaling and Phagocytosis by Fc γ Receptors in Macrophages. *J. Exp. Med.* 186, 955-966, doi:10.1084/jem.186.6.955 (1997).
- 51 Caron, E. & Hall, A. Identification of Two Distinct Mechanisms of Phagocytosis Controlled by Different Rho GTPases. *Science* 282, 1717-1721, doi:10.1126/science.282.5394.1717 (1998).
- 52 Cox, D. *et al.* Requirements for Both Rac1 and Cdc42 in Membrane Ruffling and Phagocytosis in Leukocytes. *J. Exp. Med.* 186, 1487-1494, doi:10.1084/jem.186.9.1487 (1997).
- 53 Castellano, F. *et al.* Inducible recruitment of Cdc42 or WASP to a cell-surface receptor triggers actin polymerization and filopodium formation. *Curr Biol* 9, 351-361 (1999).
- 54 Welch, M. D., Iwamatsu, A. & Mitchison, T. J. Actin polymerization is induced by Arp 2/3 protein complex at the surface of *Listeria monocytogenes*. *Nature* 385, 265-269 (1997).
- 55 Lorenzi, R., Brickell, P. M., Katz, D. R., Kinnon, C. & Thrasher, A. J. Wiskott-Aldrich syndrome protein is necessary for efficient IgG-mediated phagocytosis. *Blood* 95, 2943-2946 (2000).
- 56 Mammen, M. *et al.* Optically controlled collisions of biological objects to evaluate potent polyvalent inhibitors of virus-cell adhesion. *Chem. Biol.* 3, 757-763 (1996).
- 57 Svoboda, K., Schmidt, C. F., Schnapp, B. J. & Block, S. M. Direct observation of kinesin stepping by optical trapping interferometry. *Nature* 365, 721-727 (1993).

- 58 Koster, D. A., Palle, K., Bot, E. S. M., Bjornsti, M.-A. & Dekker, N. H. Antitumour drugs impede DNA uncoiling by topoisomerase I. *Nature* 448, 213-217 (2007).
- 59 Chi-Han, C., Yu-Yen, H., Meng-Han, C., Huei-Huang, L. & Gwo-Bin, L. New magnetic tweezers for investigation of the mechanical properties of single DNA molecules. *Nanotechnology*, 1217 (2006).
- 60 Hinterdorfer, P. & Dufrene, Y. F. Detection and localization of single molecular recognition events using atomic force microscopy. *Nat. Mater.* 3, 347-355 (2006).
- 61 Rief, M., Gautel, M., Oesterhelt, F., Fernandez, J. M. & Gaub, H. E. Reversible Unfolding of Individual Titin Immunoglobulin Domains by AFM. *Science* 276, 1109-1112, doi:10.1126/science.276.5315.1109 (1997).
- 62 Tan, J. L. *et al.* Cells lying on a bed of microneedles: An approach to isolate mechanical force. *Proc Natl Acad Sci U S A* 100, 1484-1489, doi:10.1073/pnas.0235407100 (2003).
- 63 Balaban, N. Q. *et al.* Force and focal adhesion assembly: a close relationship studied using elastic micropatterned substrates. *Nat Cell Biol* 3, 466-472 (2001).
- 64 Henson, P. M. Interaction of Cells with Immune Complexes: Adherence, Release of Constituents and Tissue Injury. *J. Exp. Med.* 134, 114-135 (1971).
- 65 Takemura, R., Stenberg, P., Bainton, D. & Werb, Z. Rapid redistribution of clathrin onto macrophage plasma membranes in response to Fc receptor-ligand interaction during frustrated phagocytosis. *J. Cell Biol.* 102, 55-69, doi:10.1083/jcb.102.1.55 (1986).
- 66 Rabinovitch, M. & DeStefano, M. J. Macrophage spreading in vitro. Inducers of spreading. *Exp. Cell Res.* 77, 323-334 (1973).
- 67 Anderson, J. M., Rodriguez, A. & Chang, D. T. Foreign body reaction to biomaterials. *Semin. Immunol.* 20, 86-100 (2008).
- 68 Remes, A. & Williams, D. in *The Biomaterials Silver Jubilee Compendium the Best Papers Published in Biomaterials, 1980-2004* Vol. 13 11-79 (2006).
- 69 Harris, A. K., Wild, P. & Stopak, D. Silicone rubber substrata: a new wrinkle in the study of cell locomotion. *Science* 208, 177-179, doi:10.1126/science.6987736 (1980).
- 70 Heiple, J., Wright, S., Allen, N. & Silverstein, S. Macrophages form circular zones of very close apposition to IgG-Coated surfaces. *Cell Motil Cytoskeleton* 15, 260-270 (1990).
- 71 Cannon, G. & Swanson, J. The macrophage capacity for phagocytosis. *J Cell Sci* 101, 907 (1992).
- 72 McNeil, P., Swanson, J., Wright, S., Silverstein, S. & Taylor, D. Fc-receptor-mediated phagocytosis occurs in macrophages without an increase in average $[Ca^{++}]_i$. *J. Cell Biol.* 102, 1586 (1986).
- 73 Balaban, N. *et al.* Force and focal adhesion assembly: a close relationship studied using elastic micropatterned substrates. *Nat Cell Biol* 3, 466-472 (2001).
- 74 Podgornik, R. & Lier, M. Polyelectrolyte bridging interactions between charged macromolecules. *Curr. Opin. Colloid Interface Sci.* 11, 273-279 (2006).
- 75 Sukhorukov, G. *et al.* Microencapsulation by means of step-wise adsorption of polyelectrolytes. *J. Microencapsulation* 17, 177-185 (2000).
- 76 Geest, B. G. D., Sanders, N. N., Sukhorukov, G. B., Demeester, J. & Smedt, S. C. D. Release mechanisms for polyelectrolyte capsules. *Chem. Soc. Rev* 36, 636-649, doi:10.1039/b600460c (2007).
- 77 F. Dubreuil, N. E. a. A. F. Elastic properties of polyelectrolyte capsules studied by atomic-force microscopy and RICM. *Eur. Phys. J. E* 12, 215-221, doi:10.1140/epje/i2003-10056-0 (2003).
- 78 Whitesides, G., Ostuni, E., Takayama, S., Jiang, X. & Ingber, D. Soft Lithography in Biology and Biochemistry. *Annu. Rev. Biomed. Eng.* 3, 335-373 (2001).
- 79 Chen, C., Mrksich, M., Huang, S., Whitesides, G. & Ingber, D. Geometric control of cell life and death. *Science* 276, 1425 (1997).
- 80 Ganz, A. *et al.* Traction forces exerted through N-cadherin contacts. *Biol. Cell* 98, 721-730, doi:10.1042/bc20060039 (2006).
- 81 Andersson, H. & Van Den Berg, A. *Lab-on-chips for cellomics: micro and nanotechnologies for life science.* (Springer Verlag, 2007).
- 82 Armand, M. Polymer electrolytes. *Annu. Rev. Mater. Res.* 16, 245-261 (1986).
- 83 Caruso, F., Trau, D., Mhwald, H. & Renneberg, R. Encapsulation of crystals via multilayer coatings. United States patent (2004).
- 84 Schlenoff, J., Ly, H. & Li, M. Charge and mass balance in polyelectrolyte multilayers. *J. Am. Chem. Soc* 120, 7626-7634 (1998).
- 85 Mendelsohn, J. *et al.* Fabrication of microporous thin films from polyelectrolyte multilayers. *Langmuir* 16, 5017-5023 (2000).
- 86 Decher, G. & Schlenoff, J. *Multilayer thin films: sequential assembly of nanocomposite materials.* (Vch Verlagsgesellschaft Mbh, 2003).
- 87 Chen, W. & McCarthy, T. Layer-by-layer deposition: a tool for polymer surface modification. *Macromolecules* 30, 78-86 (1997).
- 88 Lee, S.-S. *et al.* Layer-by-Layer Deposited Multilayer Assemblies of Ionene-Type Polyelectrolytes Based on the Spin-Coating Method. *Macromolecules* 34, 5358-5360, doi:10.1021/ma0022304 (2001).
- 89 Izquierdo, A., Ono, S. S., Voegel, J. C., Schaaf, P. & Decher, G. Dipping versus Spraying: Exploring the Deposition Conditions for Speeding Up Layer-by-Layer Assembly. *Langmuir* 21, 7558-7567, doi:10.1021/la047407s (2005).

- 90 Schlenoff, J. B., Dubas, S. T. & Farhat, T. Sprayed Polyelectrolyte Multilayers. *Langmuir* 16, 9968-9969, doi:10.1021/la001312i (2000).
- 91 Antipov, A. *et al.* Polyelectrolyte multilayer capsule permeability control. *Colloids Surf., A* 198, 535-541 (2002).
- 92 Sukhorukov, G., Fery, A., Brumen, M. & Möhwald, H. Physical chemistry of encapsulation and release. *Phys. Chem. Chem. Phys.* 6, 4078-4089 (2004).
- 93 Khopade, A. J. & Caruso, F. Surface-Modification of Polyelectrolyte Multilayer-Coated Particles for Biological Applications. *Langmuir* 19, 6219-6225, doi:10.1021/la030016d (2003).
- 94 Serizawa, T., Kamimura, S., Kawanishi, N. & Akashi, M. Layer-by-Layer Assembly of Poly(vinyl alcohol) and Hydrophobic Polymers Based on Their Physical Adsorption on Surfaces. *Langmuir* 18, 8381-8385, doi:10.1021/la0204491 (2002).
- 95 Wang, L. *et al.* A new approach for the fabrication of an alternating multilayer film of poly(4-vinylpyridine) and poly(acrylic acid) based on hydrogen bonding. *Macromol. Rapid Commun.* 18, 509-514 (1997).
- 96 Stockton, W. B. & Rubner, M. F. Molecular-Level Processing of Conjugated Polymers. 4. Layer-by-Layer Manipulation of Polyaniline via Hydrogen-Bonding Interactions. *Macromolecules* 30, 2717-2725, doi:10.1021/ma9700486 (1997).
- 97 Farkhad G. Aliev, M. A. C.-D., Arif Mamedov, John W. Ostrander, Michael Giersig, Lius M. Liz-Marzán, Nicholas A. Kotov. Layer-By-Layer Assembly of Core-Shell Magnetite Nanoparticles: Effect of Silica Coating on Interparticle Interactions and Magnetic Properties. *Adv. Mater.* 11, 1006-1010 (1999).
- 98 Lvov, Y., Decher, G. & Sukhorukov, G. Assembly of thin films by means of successive deposition of alternate layers of DNA and poly(allylamine). *Macromolecules* 26, 5396-5399 (1993).
- 99 Keller, S. W., Kim, H.-N. & Mallouk, T. E. Layer-by-Layer Assembly of Intercalation Compounds and Heterostructures on Surfaces: Toward Molecular "Beaker" Epitaxy. *J. Am. Chem. Soc* 116, 8817-8818 (1994).
- 100 Lvov, Y., Ariga, K., Ichinose, I. & Kunitake, T. Assembly of Multicomponent Protein Films by Means of Electrostatic Layer-by-Layer Adsorption. *J. Am. Chem. Soc* 117, 6117-6123 (1995).
- 101 Lvov, Y. *et al.* Successive Deposition of Alternate Layers of Polyelectrolytes and a Charged Virus. *Langmuir* 10, 4232-4236 (1994).
- 102 Cassiera T, S. A., Offenhäuser A and H. Möhwald. Homogeneity, electrical resistivity and lateral diffusion of lipid bilayers coupled to polyelectrolyte multilayers. *Colloids Surf., B* 15, 215-225, doi:10.1016/S0927-7765(99)00090-9 (1999).
- 103 Caruso, F. Hollow capsule processing through colloidal templating and self-assembly. *Chem Eur J* 6, 413-419 (2000).
- 104 Fernández-Suárez, M. & Ting, A. Fluorescent probes for super-resolution imaging in living cells. *Nat Rev Mol Cell Biol* 9, 929-943 (2008).
- 105 Imhof, A. *et al.* Spectroscopy of fluorescein (FITC) dyed colloidal silica spheres. *J. Phys. Chem. B* 103, 1408-1415 (1999).
- 106 Panchuk-Voloshina, N. *et al.* Alexa Dyes, a Series of New Fluorescent Dyes that Yield Exceptionally Bright, Photostable Conjugates. *J. Histochem. Cytochem.* 47, 1179-1188 (1999).
- 107 Teske, C., Schroeder, M., Simon, R. & Hubbuch, J. Protein-labeling effects in confocal laser scanning microscopy. *J. Phys. Chem. B* 109, 13811-13817 (2005).
- 108 Pawley, J. & Masters, B. *Handbook of biological confocal microscopy. Vol. 13* (2008).
- 109 Haaijman, J. & Van Dalen, J. Quantification in immunofluorescence microscopy a new standard for fluorescein and rhodamine emission measurement. *J. Immunol. Methods* 5, 359-374 (1974).
- 110 Atto-Tech. *Recommended Procedures for Labeling*, <www.atto-tec.com> (2009).
- 111 Johnstone, A. & Thorpe, R. *Immunochemistry in practice. (Blackwell Science Cambridge, 1996)*.
- 112 Köhler, K. & Sukhorukov, G. B. Heat Treatment of Polyelectrolyte Multilayer Capsules: A Versatile Method for Encapsulation. *Adv. Funct. Mater.* 17, 2053-2061 (2007).
- 113 Changyou Gao, S. L. S. M. E. D. H. M. Swelling and Shrinking of Polyelectrolyte Microcapsules in Response to Changes in Temperature and Ionic Strength. *Chem. Eur. J.* 9, 915-920 (2003).
- 114 Ibarz, G., Dahne, L., Donath, E. & Mohwald, H. Controlled Permeability of Polyelectrolyte Capsules via Defined Annealing. *Chem. Mater.* 14, 4059-4062, doi:10.1021/cm011300y (2002).
- 115 Leporatti, S., Gao, C., Voigt, A., Donath, E. & Möhwald, H. Shrinking of ultrathin polyelectrolyte multilayer capsules upon annealing: A confocal laser scanning microscopy and scanning force microscopy study. *Eur. Phys. J. E* 5, 13-20 (2001).
- 116 Goldstein, J. *et al.* *Scanning electron microscopy. Vol. 1* (1977).
- 117 Boyde, A. Pros and cons of critical point drying and freeze drying for SEM. *Scanning electron microscopy* 2, 303-314 (1978).
- 118 Cohen, A. *Critical point drying. Vol. 1* (1974).
- 119 Labow, R. S., Meek, E. & Santerre, J. P. Neutrophil-mediated biodegradation of medical implant materials. *J. Cell. Physiol.* 186, 95-103 (2001).
- 120 Rabinovitch, M. & DeStefano, M. Macrophage spreading in vitro. Inducers of spreading. *Exp. Cell Res.* 77, 323-334 (1973).
- 121 Ratner, B., Hoffman, A., Schoen, F. & Lemons, J. *Biomaterials science: an introduction to materials in medicine. (Academic press, 2004)*.

- 122 Ainslie, K. & Thakar, R. ***Inflammatory Response to Implanted Nanostructured Materials***. (Springer, 2009).
- 123 Ulmer, J. ***Quantitative Measurements of Force Distribution in Single and Multi Cellular Systems*** PhD thesis, Universität Heidelberg, (2005).
- 124 Crandall, S. ***An Introduction to the Mechanics of Solids***. (McGraw-Hill, 1978).
- 125 Stuart, J. & Hlady, V. Reflection interference contrast microscopy combined with scanning force microscopy verifies the nature of protein-ligand interaction force measurements. ***Biophys. J.*** 76, 500-508 (1999).
- 126 Ducker, W. A., Senden, T. J. & Pashley, R. M. Direct measurement of colloidal forces using an atomic force microscope. ***Nature*** 353, 239-241 (1991).
- 127 Butt, H. J. & Jaschke, M. Calculation of thermal noise in atomic force microscopy. ***Nanotechnology*** 6, 1-7 (1995).
- 128 Hutter, J. L. & Bechhoefer, J. Calibration of atomic-force microscope tips. ***Rev. Sci. Instrum.*** 64, 1868-1873 (1993).
- 129 Gleb B. Sukhorukov, A. A. A., Andreas Voigt, Edwin Donath, Helmuth Möhwald, pH-Controlled Macromolecule Encapsulation in and Release from Polyelectrolyte Multilayer Nanocapsules. ***Macromol. Rapid Commun.*** 22, 44-46 (2001).
- 130 Lowack, K. & Helm, C. A. Molecular Mechanisms Controlling the Self-Assembly Process of Polyelectrolyte Multilayers. ***Macromolecules*** 31, 823-833, doi:doi:10.1021/ma9614454 (1998).
- 131 Losche, M., Schmitt, J., Decher, G., Bouwman, W. G. & Kjaer, K. Detailed Structure of Molecularly Thin Polyelectrolyte Multilayer Films on Solid Substrates as Revealed by Neutron Reflectometry. ***Macromolecules*** 31, 8893-8906, doi:doi:10.1021/ma980910p (1998).
- 132 Lulevich, V. V. & Vinogradova, O. I. Effect of pH and Salt on the Stiffness of Polyelectrolyte Multilayer Microcapsules. ***Langmuir*** 20, 2874-2878, doi:doi:10.1021/la049934h (2004).
- 133 Cantley, L. The phosphoinositide 3-kinase pathway. ***Science*** 296, 1655 (2002).
- 134 Zheleznyak, A. & Brown, E. Immunoglobulin-mediated phagocytosis by human monocytes requires protein kinase C activation. Evidence for protein kinase C translocation to phagosomes. ***J. Biol. Chem.*** 267, 12042 (1992).
- 135 Breton, A. & Descoteaux, A. Protein kinase C- participates in Fc R-mediated phagocytosis in macrophages. ***Biochem. Biophys. Res. Commun.*** 276, 472-476 (2000).
- 136 Diakonova, M., Bokoch, G. & Swanson, J. Dynamics of cytoskeletal proteins during Fc γ receptor-mediated phagocytosis in macrophages. ***Mol. Biol. Cell*** 13, 402 (2002).
- 137 Araki, N. Role of microtubules and myosins in Fc gamma receptor-mediated phagocytosis. ***Front Biosci*** 11, 1479-1490 (2006).
- 138 Araki, N., Johnson, M. & Swanson, J. A role for phosphoinositide 3-kinase in the completion of macropinocytosis and phagocytosis by macrophages. ***J. Cell Biol.*** 135, 1249-1260, doi:10.1083/jcb.135.5.1249 (1996).
- 139 Majeed, M., Cavegion, E., Lowell, C. & Berton, G. Role of Src kinases and Syk in Fc {gamma} receptor-mediated phagocytosis and phagosome-lysosome fusion. ***J. Leukocyte Biol.*** 70, 801 (2001).
- 140 Vlahos, C., Matter, W., Hui, K. & Brown, R. A specific inhibitor of phosphatidylinositol 3-kinase, 2-(4-morpholinyl)-8-phenyl-4H-1-benzopyran-4-one (LY294002). ***J. Biol. Chem.*** 269, 5241-5248 (1994).
- 141 Greenberg, S. Modular components of phagocytosis. ***J Leukoc Biol*** 66, 712-717 (1999).
- 142 Suzuki, T. *et al.* Differential Involvement of Src Family Kinases in Fc{gamma} Receptor-Mediated Phagocytosis. ***J Immunol*** 165, 473-482 (2000).
- 143 Leverrier, Y. *et al.* Class I Phosphoinositide 3-Kinase p110{beta} Is Required for Apoptotic Cell and Fc{gamma} Receptor-mediated Phagocytosis by Macrophages. ***J. Biol. Chem.*** 278, 38437-38442, doi:10.1074/jbc.M306649200 (2003).
- 144 Mahabeleshwar, G. & Kundu, G. Syk, a protein-tyrosine kinase, suppresses the cell motility and nuclear factor kappa B-mediated secretion of urokinase type plasminogen activator by inhibiting the phosphatidylinositol 3'-kinase activity in breast cancer cells. ***J. Biol. Chem.*** 278, 6209 (2003).
- 145 Sada, K., Takano, T., Yanagi, S. & Yamamura, H. Structure and function of Syk protein-tyrosine kinase. ***J. Biol. Chem*** 130, 177 (2001).
- 146 Rodriguez-Viciana, P. *et al.* Role of phosphoinositide 3-OH kinase in cell transformation and control of the actin cytoskeleton by Ras. ***Cell*** 89, 457-468 (1997).
- 147 Indik, Z., Park, J., Hunter, S. & Schreiber, A. The molecular dissection of Fc gamma receptor mediated phagocytosis. ***Blood*** 86, 4389-4399 (1995).
- 148 Vossebeld, P. J. *et al.* Tyrosine phosphorylation-dependent activation of phosphatidylinositide 3-kinase occurs upstream of Ca²⁺-signalling induced by Fc γ receptor cross-linking in human neutrophils. ***Biochem. J.*** 323, 87-94 (1997).
- 149 Duckworth, B. C. & Cantley, L. C. Conditional Inhibition of the Mitogen-activated Protein Kinase Cascade by Wortmannin. Dependence on Signal Strength. ***J. Biol. Chem.*** 272, 27665-27670, doi:10.1074/jbc.272.44.27665 (1997).
- 150 L.R. Stephens, T. R. J., P.T. Hawkins. Agonist-stimulated synthesis of phosphatidylinositol(3,4,5)-trisphosphate: A new intracellular signalling system? ***Biochim. Biophys. Acta, Mol. Cell. Res*** 1179, 27-75, doi:10.1016/0167-4889(93)90072-W (1993).

- 151 R Dhand, K. H., I Hiles, B Bax, I Gout, G Panayotou, M J Fry, K Yonezawa, M Kasuga, and M D Waterfield. PI 3-kinase: structural and functional analysis of intersubunit interactions. *EMBO J* 13, 511-521, doi:PMCID: PMC394840 (1994).
- 152 Hu, P. & Schlessinger, J. Direct association of p110 beta phosphatidylinositol 3-kinase with p85 is mediated by an N-terminal fragment of p110 beta. *Mol. Cell. Biol.* 14, 2577-2583 (1994).
- 153 Anne J. Ridley, H. F. P., Caroline L. Johnston, Dagmar Diekmann, and Alan Hall. The Small GTP-Binding Protein rac Regulates Growth Factor-Induced Membrane Ruffling. *Cell* 70, 401-410, doi:10.1016/0092-8674(92)90164-8 (1992).
- 154 Chrzanowska-Wodnicka, M. & Burridge, K. Rho-stimulated contractility drives the formation of stress fibers and focal adhesions. *J. Cell Biol.* 133, 1403-1415, doi:10.1083/jcb.133.6.1403 (1996).
- 155 O'Malley, D. *Imaging in Depth: Controversies and Opportunities.* (Academic Press, 2008).
- 156 Jin, F., Jang, J. S. & Javidi, B. Effects of device resolution on three-dimensional integral imaging. *Opt. Lett.* 29, 1345-1347 (2004).
- 157 Wallace, W., Schaefer, L. H. & Swedlow, J. R. A workingperson's guide to deconvolution in light microscopy. *Biotechniques* 31, 1076-1097 (2001).
- 158 Swedlow, J. R. & Platani, M. Live Cell Imaging Using Wide-Field Microscopy and Deconvolution. *Cell Struct Funct* 27, 335-341 (2002).
- 159 McNally, J. G., Karpova, T., Cooper, J. & Conchello, J. A. Three-Dimensional Imaging by Deconvolution Microscopy. *Methods* 19, 373-385 (1999).
- 160 Pawley, J. B. & Masters, B. R. Handbook of Biological Confocal Microscopy, Third Edition. *J Biomed Opt* 13, 029902-029903 (2008).
- 161 Murray, J. M. *Confocal microscopy, deconvolution, and structured illumination methods.* (Cold Spring Harbor Laboratory Pr, 2006).
- 162 Sandison, D. R., Williams, R. M., Wells, K. S., Strickler, J. & Webb, W. W. Quantitative fluorescence confocal laser scanning microscopy (CLSM). *Handbook of Biological Confocal Microscopy*, 39-53 (1995).
- 163 Sibarita, J. B. Deconvolution microscopy. *Adv. Biochem. Engin./Biotechnol.* 95, 201-244 (2005).
- 164 Thomas, C., DeVries, P., Hardin, J. & White, J. Four-Dimensional Imaging: Computer Visualization of 3D Movements in Living Specimens. *Science* 273, 603-607 (1996).
- 165 Manders, E. M. M., Kimura, H. & Cook, P. R. Direct Imaging of DNA in Living Cells Reveals the Dynamics of Chromosome Formation. *J. Cell Biol.* 144, 813-822, doi:10.1083/jcb.144.5.813 (1999).
- 166 Platani, M., Goldberg, I., Lamond, A. I. & Swedlow, J. R. Cajal Body dynamics and association with chromatin are ATP-dependent. *Nat Cell Biol* 4, 502-508 (2002).
- 167 He, X., Asthana, Saurabh, Sorger, Peter K. Transient Sister Chromatid Separation and Elastic Deformation of Chromosomes during Mitosis in Budding Yeast. *Cell* 101, 763-775, doi:10.1016/S0092-8674(00)80888-0 (2000).
- 168 Hammond, A. T. & Glick, B. S. Raising the speed limits for 4D fluorescence microscopy. *Traffic* 1, 935-940 (2000).
- 169 Benson, D. M., Bryan, J., Plant, A. L., Gotto Jr, A. M. & Smith, L. C. Digital imaging fluorescence microscopy: spatial heterogeneity of photobleaching rate constants in individual cells. *J. Cell Biol.* 100, 1309 (1985).
- 170 Gerlich, D., Beaudouin, J., Gebhard, M., Ellenberg, J. & Eils, R. Four-dimensional imaging and quantitative reconstruction to analyse complex spatiotemporal processes in live cells. *Nat Cell Biol* 3, 852-855, doi:doi:10.1038/ncb0901-852 (2001).
- 171 Cox, D. *et al.* Myosin X is a downstream effector of PI(3)K during phagocytosis. *Nat Cell Biol* 4, 469-477 (2002).
- 172 Chavrier, P. May the force be with you: Myosin-X in phagocytosis. *Nat Cell Biol.* 4, E169-E171 (2002).
- 173 Hall, A. Rho GTPases and the Actin Cytoskeleton. *Science* 279, 509-514, doi:10.1126/science.279.5350.509 (1998).
- 174 Cascalho, M. & Platt, J. L. The immunological barrier to xenotransplantation. *Immunity* 14, 437-446 (2001).
- 175 Chang, D. T. *et al.* Lymphocyte/macrophage interactions: Biomaterial surface-dependent cytokine, chemokine, and matrix protein production. *System* 2008 (1927).
- 176 Thomsen, P. & Gretzer, C. Macrophage interactions with modified material surfaces. *Curr Opin Solid St M* 5, 163-176 (2001).
- 177 Wilson, C. J., Clegg, R. E., Leavesley, D. I. & Percy, M. J. Mediation of biomaterial-cell interactions by adsorbed proteins: a review. *Tissue Eng* 11, 1-18 (2005).
- 178 François, P., Vaudaux, P. & Lew, P. D. Role of Plasma and Extracellular Matrix Proteins in the Physiopathology of Foreign Body Infections. *Ann Vasc Surg* 12, 34-40 (1998).
- 179 Sawyer, A. A., Hennessy, K. M. & Bellis, S. L. The effect of adsorbed serum proteins, RGD and proteoglycan-binding peptides on the adhesion of mesenchymal stem cells to hydroxyapatite. *Biomaterials* 28, 383-392 (2007).
- 180 Anderson, J. M. Biological Responses to Materials. *Annu. Rev. Mater. Res.* 31, 81-110 (2001).
- 181 Anderson, J. M. Inflammatory response to implants. *ASAIO Journal* 34, 101 (1988).
- 182 Singer, A. J. & Clark, R. A. F. Cutaneous Wound Healing. *N Engl J Med* 341, 738-746, doi:10.1056/nejm199909023411006 (1999).

- 183 Webb, J. C. J. & Tricker, J. A review of fracture healing. *Curr Orthop* 14, 457-463 (2000).
- 184 Anderson, J. M. Mechanisms of inflammation and infection with implanted devices. *Cardiovasc. Pathol.* 2, 33-41 (1993).
- 185 Davies, J. E. *The bone-biomaterial interface.* (University of Toronto Press Toronto, 1991).
- 186 Schwartz, Z. & Boyan, B. D. Underlying mechanisms at the bone-biomaterial interface. *J. Cell. Biochem.* 56, 340-347 (1994).
- 187 DiPietro, L. A. Wound healing: the role of the macrophage and other immune cells. *Shock* 4, 233 (1995).
- 188 Murphy, W. L., Peters, M. C., Kohn, D. H. & Mooney, D. J. Sustained release of vascular endothelial growth factor from mineralized poly(lactide-co-glycolide) scaffolds for tissue engineering. *Biomaterials* 21, 2521-2527 (2000).
- 189 Laurencin, C. T. *et al.* Poly(lactide-co-glycolide)/hydroxyapatite delivery of BMP-2-producing cells: a regional gene therapy approach to bone regeneration. *Biomaterials* 22, 1271-1277 (2001).
- 190 Udipi, K. *et al.* Modification of inflammatory response to implanted biomedical materials in vivo by surface bound superoxide dismutase mimics. *J. Biomed. Mater. Res.* 51, 549-560 (2000).
- 191 Kunze, C., Freier, T., Kramer, S. & Schmitz, K. P. Anti-inflammatory prodrugs as plasticizers for biodegradable implant materials based on poly (3-hydroxybutyrate). *J Mater Sci Mater Med* 13, 1051-1055 (2002).
- 192 Ronca, F., Palmieri, L., Panicucci, P. & Ronca, G. Anti-inflammatory activity of chondroitin sulfate. *Osteoarthr. Cartil.* 6, 14-21 (1998).
- 193 Benkirane-Jessel, N. *et al.* Control of monocyte morphology on and response to model surfaces for implants equipped with anti-inflammatory agent. *Adv. Mater.* 16, 1507-1511 (2004).
- 194 DiPietro, L. A., Burdick, M., Low, Q. E., Kunkel, S. L. & Strieter, R. M. MIP-1alpha as a critical macrophage chemoattractant in murine wound repair. *J. Clin. Invest.* 101, 1693 (1998).
- 195 Kovacs, E. J. & DiPietro, L. A. Fibrogenic cytokines and connective tissue production. *FASEB J.* 8, 854 (1994).
- 196 Mantovani, A., Sica, A. & Locati, M. Macrophage polarization comes of age. *Immunity* 23, 344-346 (2005).
- 197 Mantovani, A. *et al.* The chemokine system in diverse forms of macrophage activation and polarization. *Trends Immunol.* 25, 677-686 (2004).
- 198 Mantovani, A., Sozzani, S., Locati, M., Allavena, P. & Sica, A. Macrophage polarization: tumor-associated macrophages as a paradigm for polarized M2 mononuclear phagocytes. *Trends Immunol.* 23, 549-555 (2002).
- 199 Martinez, F. O., Sica, A., Mantovani, A. & Locati, M. Macrophage activation and polarization. *Front. Biosci.* 13, 453 (2008).
- 200 Mosser, D. M. The many faces of macrophage activation. *J Leukoc Biol* 73, 209-212, doi:10.1189/jlb.0602325 (2003).
- 201 Ho, V. W. H. & Sly, L. M. Vol. 531 173-185 (2008).
- 202 Gordon, S. Alternative activation of macrophages. *Nat. Rev. Immunol.* 3, 23-35 (2003).
- 203 Sutterwala, F. S., Noel, G. J., Salgame, P. & Mosser, D. M. Reversal of Proinflammatory Responses by Ligating the Macrophage Fc{gamma} Receptor Type I. *J. Exp. Med.* 188, 217-222, doi:10.1084/jem.188.1.217 (1998).
- 204 Damien, C. J. & Parsons, J. R. Bone graft and bone graft substitutes: A review of current technology and applications. *J Appl Biomater* 2, 187-208 (1991).
- 205 Woods, T. C. & Marks, A. R. Drug-eluting stents. *Annu. Rev. Med.* (2004).
- 206 DiFrancesco, D. Pacemaker mechanisms in cardiac tissue. *Annu. Rev. Physiol.* 55, 455-472 (1993).
- 207 Loeb, G. E. Cochlear prosthetics. *Annu. Rev. Neurosci.* 13, 357-371 (1990).
- 208 Wilson, B. S., Lawson, D. T., Müller, J. M., Tyler, R. S. & Kiefer, J. Cochlear Implants: Some Likely Next Steps. *Annu. Rev. Biomed. Eng.* 5, 207-249 (2003).
- 209 Albrektsson, T., Zarb, G., Worthington, P. & Eriksson, A. R. The long-term efficacy of currently used dental implants: a review and proposed criteria of success. *Int J Oral Maxillofac Implants* 1, 11 (1986).
- 210 Meffert, R. M., Langer, B. & Fritz, M. E. Dental implants: a review. *J. Periodontol.* 63, 859 (1992).
- 211 Ong, J. L. & Chan, D. C. N. Hydroxyapatite and their use as coatings in dental implants: a review. *Crit Rev Biomed Eng* 28, 667-707 (2000).
- 212 I.W.Fong. in *Emerging Infectious Diseases of the 21st Century* 299-326 (2009).
- 213 Boyan, B. D., Hummert, T. W., Dean, D. D. & Schwartz, Z. Role of material surfaces in regulating bone and cartilage cell response. *Biomaterials* 17, 137-146 (1996).
- 214 Gilroy, D. W., Lawrence, T., Perretti, M. & Rossi, A. G. Inflammatory resolution: new opportunities for drug discovery. *Nat Rev Drug Discov* 3, 401 (2004).
- 215 Wetzler, C., Kämpfer, H., Stallmeyer, B., Pfeilschifter, J. & Frank, S. Large and sustained induction of chemokines during impaired wound healing in the genetically diabetic mouse: prolonged persistence of neutrophils and macrophages during the late phase of repair. *J. Invest. Dermatol.* 115, 245-253 (2000).
- 216 Goova, M. T. *et al.* Blockade of receptor for advanced glycation end-products restores effective wound healing in diabetic mice. *Am. J. Pathol.* 159, 513 (2001).

- 217 Brown, D. L., Kao, W. W. Y. & Greenhalgh, D. G. Apoptosis down-regulates inflammation under the advancing epithelial wound edge: Delayed patterns in diabetes and improvement with topical growth factors. *Surgery* 121, 372-380 (1997).
- 218 Singleton, J. R., Smith, A. G., Russell, J. W. & Feldman, E. L. Microvascular complications of impaired glucose tolerance. *Diabetes* 52, 2867 (2003).
- 219 Aronson, D., Bloomgarden, Z. & Rayfield, E. J. Potential mechanisms promoting restenosis in diabetic patients. *J. Am. Coll. Cardiol.* 27, 528-535 (1996).
- 220 Eltchaninoff, H., Koning, R., Tron, C., Gupta, V. & Cribier, A. Balloon angioplasty for the treatment of coronary in-stent restenosis: immediate results and 6-month angiographic recurrent restenosis rate. *J. Am. Coll. Cardiol.* 32, 980-984 (1998).
- 221 Feldman, L. J. *et al.* Interleukin-10 Inhibits Intimal Hyperplasia After Angioplasty or Stent Implantation in Hypercholesterolemic Rabbits. *Circulation* 101, 908-916 (2000).
- 222 Rogers, C., Welt, F. G. P., Karnovsky, M. J. & Edelman, E. R. Monocyte recruitment and neointimal hyperplasia in rabbits: coupled inhibitory effects of heparin. *Arterioscler. Thromb. Vasc. Biol.* 16, 1312 (1996).
- 223 Luttkhuizen, D. T., Harmsen, M. C. & Luyn, M. Cellular and molecular dynamics in the foreign body reaction. *Tissue. Eng.* 12, 1955-1970 (2006).
- 224 Boyle, J. J. Macrophage activation in atherosclerosis: pathogenesis and pharmacology of plaque rupture. *Current Vascular Pharmacology* 3, 63-68 (2005).
- 225 Morra, M. Biomolecular modification of implant surfaces. *Expert Rev Med Devices* 4, 361-372 (2007).
- 226 de Waal Malefyt, R., Abrams, J., Bennett, B., Figdor, C. & de Vries, J. Interleukin 10(IL-10) inhibits cytokine synthesis by human monocytes: an autoregulatory role of IL-10 produced by monocytes. *J. Exp. Med.* 174, 1209-1220, doi:10.1084/jem.174.5.1209 (1991).
- 227 Opal, S. M. & DePalo, V. A. Anti-Inflammatory Cytokines. *Chest* 117, 1162-1172, doi:10.1378/chest.117.4.1162 (2000).
- 228 Ma, J. *et al.* Regulation of macrophage activation. *Cell. Mol. Life Sci.* 60, 2334-2346 (2003).
- 229 Katakura, T., Miyazaki, M., Kobayashi, M., Herndon, D. N. & Suzuki, F. CCL17 and IL-10 as Effectors That Enable Alternatively Activated Macrophages to Inhibit the Generation of Classically Activated Macrophages. *J Immunol* 172, 1407-1413 (2004).
- 230 Bogdan, C., Vodovotz, Y. & Nathan, C. Macrophage deactivation by interleukin 10. *J. Exp. Med.* 174, 1549-1555, doi:10.1084/jem.174.6.1549 (1991).
- 231 Fiorentino, D., Zlotnik, A., Mosmann, T., Howard, M. & O'Garra, A. IL-10 inhibits cytokine production by activated macrophages. *J Immunol* 147, 3815-3822 (1991).
- 232 O'Farrell, A. M., Liu, Y., Moore, K. W. & Mui, A. L. IL-10 inhibits macrophage activation and proliferation by distinct signaling mechanisms: evidence for Stat3-dependent and-independent pathways. *The EMBO Journal* 17, 1006 (1998).
- 233 Christman, K. L., Enriquez-Rios, V. D. & Maynard, H. D. Nanopatterning proteins and peptides. *Soft Matter* 2, 928-939 (2006).
- 234 Marco Arnold, E. A. C.-A., Roman Glass, Jacques Blümmel, Wolfgang Eck, Martin Kantlehner, Horst Kessler, Joachim P. Spatz., Activation of Integrin Function by Nanopatterned Adhesive Interfaces. *ChemPhysChem* 5, 383-388 (2004).
- 235 Cavalcanti-Adam, E. A. *et al.* Cell Spreading and Focal Adhesion Dynamics Are Regulated by Spacing of Integrin Ligands. *Biophys. J.* 92, 2964-2974 (2007).
- 236 Ezekowitz, R. A. & Gordon, S. Alterations of surface properties by macrophage activation: expression of receptors for Fc and mannose-terminal glycoproteins and differentiation antigens. *Contemp Top Immunobiol* 13, 33 (1984).
- 237 Schmidmaier, G. *et al.* Local application of growth factors (insulin-like growth factor-1 and transforming growth factor- 1) from a biodegradable poly (D, L-lactide) coating of osteosynthetic implants accelerates fracture healing in rats. *Bone* 28, 341-350 (2001).
- 238 Shaw, L. M., Kaplan, B. & Kaufman, D. Toxic effects of immunosuppressive drugs: mechanisms and strategies for controlling them. *Clin. Chem.* 42, 1316 (1996).
- 239 Mihatsch, M. J. *et al.* The side-effects of ciclosporine-A and tacrolimus. *Clin. Nephrol.* 49, 356 (1998).
- 240 Cassatella, M. A. *et al.* Interleukin-10 (IL-10) Selectively Enhances CIS3/SOCS3 mRNA Expression in Human Neutrophils: Evidence for an IL-10-Induced Pathway That Is Independent of STAT Protein Activation. *Blood* 94, 2880-2889 (1999).
- 241 Berlato, C. *et al.* Involvement of Suppressor of Cytokine Signaling-3 as a Mediator of the Inhibitory Effects of IL-10 on Lipopolysaccharide-Induced Macrophage Activation. *J Immunol* 168, 6404-6411 (2002).
- 242 Ellman, G. L. Tissue sulfhydryl groups. *Arch. Biochem. Biophys.* 82, 70 (1959).
- 243 Riddles, P. W., Blakeley, R. L. & Zerner, B. Reassessment of Ellman's reagent. *Methods Enzymol.* 91, 49 (1983).
- 244 Riener, C. K., Kada, G. & Gruber, H. J. Quick measurement of protein sulfhydryls with Ellman's reagent and with 4, 4'-dithiodipyridine. *Anal. Bioanal. Chem.* 373, 266-276 (2002).
- 245 Peters, K. & Richards, F. M. Chemical cross-linking: reagents and problems in studies of membrane structure. *Annu. Rev. Biochem.* 46, 523-551 (1977).

- 246 Nagata, Y. & Burger, M. M. Wheat germ agglutinin. Molecular characteristics and specificity for sugar binding. *J. Biol. Chem.* 249, 3116 (1974).
- 247 Lis, H. & Sharon, N. Lectins as molecules and as tools. *Annu. Rev. Biochem.* 55, 35-67 (1986).
- 248 Potemkin, I. I. *et al.* Nanopattern of Diblock Copolymers Selectively Adsorbed on a Plane Surface. *Langmuir* 15, 7290-7298, doi:doi:10.1021/la9900730 (1999).
- 249 Thomas, C. P. a. J. Y. a. E. L. Enabling nanotechnology with self assembled block copolymer patterns. *Polymer* 44, 7779 - 7779, doi:10.1016/j.polymer.2003.09.052 (2003).
- 250 Bhushan, B. *Springer Handbook of Nanotechnology.* (Springer, 2004).
- 251 Li, Z. *et al.* Self-Ordering of Diblock Copolymers from Solution. *J. Am. Chem. Soc* 118, 10892-10893, doi:doi:10.1021/ja961713d (1996).
- 252 L. Isaacs, D. N. C., N. Bowden, Y. Xia, and G. M. Whitesides. *Supermolecular Materials and Technologies, chapter Supermolecular Materials and Technologies.*, (JohnWiley & Sons, 1999).
- 253 Stephan Förster, T. P. Von selbstorganisierenden Polymeren zu Nanohybrid- und Biomaterialien. *Angew Chem* 114, 712-739 (2002).
- 254 M. Geissler, Y. X. Patterning: Principles and Some New Developments. *Adv. Mater.* 16, 1249-1269 (2004).
- 255 Spatz, J. P., Sheiko, S. & Moller, M. Ion-Stabilized Block Copolymer Micelles: Film Formation and Intermicellar Interaction. *Macromolecules* 29, 3220-3226, doi:doi:10.1021/ma951712q (1996).
- 256 Joachim P. Spatz, T. H., Stefan Mößmer, Paul Ziemann, Martin Möller. Micellar Inorganic-Polymer Hybrid Systems - A Tool for Nanolithography. *Adv. Mater.* 11, 149-153 (1999).
- 257 G. Kästle, H. G. B., F. Weigl, G. Lengl, T. Herzog, P. Ziemann, S. Riethmüller, O. Mayer, C. Hartmann, J. P. Spatz, M. Möller, M. Ozawa, F. Banhart, M. G. Garnier, P. Oelhafen. Micellar Nanoreactors - Preparation and Characterization of Hexagonally Ordered Arrays of Metallic Nanodots. *Adv. Funct. Mater.* 13, 853-861 (2003).
- 258 Johner, A. & Joanny, J. F. Block copolymer adsorption in a selective solvent: a kinetic study. *Macromolecules* 23, 5299-5311, doi:doi:10.1021/ma00228a001 (1990).
- 259 Liu, Y. *et al.* Surface-Induced Ordering in Asymmetric Block Copolymers. *Macromolecules* 27, 4000-4010, doi:doi:10.1021/ma00092a047 (1994).
- 260 R. Glass, M. A. J. B. A. K. M. M. J. P. S. Micro-Nanostructured Interfaces Fabricated by the Use of Inorganic Block Copolymer Micellar Monolayers as Negative Resist for Electron-Beam Lithography. *Adv. Funct. Mater.* 13, 569-575 (2003).
- 261 Roman, G., Martin, M. & Joachim, P. S. Block copolymer micelle nanolithography. *Nanotechnology*, 1153 (2003).
- 262 Bansmann, J. *et al.* Controlling the Interparticle Spacing of Au-Salt Loaded Micelles and Au Nanoparticles on Flat Surfaces. *Langmuir* 23, 10150-10155, doi:doi:10.1021/la7012304 (2007).
- 263 Aizawa, M. & Buriak, J. M. Block Copolymer-Templated Chemistry on Si, Ge, InP, and GaAs Surfaces. *J. Am. Chem. Soc* 127, 8932-8933, doi:doi:10.1021/ja052281m (2005).
- 264 Holmberg, K. *et al.* Effects on protein adsorption, bacterial adhesion and contact angle of grafting PEG chains to polystyrene. *J. Adhes. Sci. Technol.* 7, 503-517 (1993).
- 265 Inada, Y. *et al.* Biomedical and biotechnological applications of PEG-and PM-modified proteins. *Trends Biotechnol.* 13, 86-91 (1995).
- 266 Malmsten, M., Emoto, K. & Van Alstine, J. M. Effect of Chain Density on Inhibition of Protein Adsorption by Poly(ethylene glycol) Based Coatings. *J. Colloid Interface Sci.* 202, 507-517 (1998).
- 267 Huang, N.-P. *et al.* Poly(L-lysine)-g-poly(ethylene glycol) Layers on Metal Oxide Surfaces: Surface-Analytical Characterization and Resistance to Serum and Fibrinogen Adsorption. *Langmuir* 17, 489-498 (2001).
- 268 Papra, A., Gadegaard, N. & Larsen, N. B. Characterization of Ultrathin Poly(ethylene glycol) Monolayers on Silicon Substrates. *Langmuir* 17, 1457-1460 (2001).
- 269 Ruiz-Taylor, L. A. *et al.* Monolayers of derivatized poly(L-lysine)-grafted poly(ethylene glycol) on metal oxides as a class of biomolecular interfaces. *Proc Natl Acad Sci U S A* 98, 852-857 (2001).
- 270 Zhu, X. Y. *et al.* Grafting of High-Density Poly(Ethylene Glycol) Monolayers on Si(111). *Langmuir* 17, 7798-7803 (2001).
- 271 Kingshott, P., Thissen, H. & Griesser, H. J. Effects of cloud-point grafting, chain length, and density of PEG layers on competitive adsorption of ocular proteins. *Biomaterials* 23, 2043-2056 (2002).
- 272 Veisoh, M., Zareie, M. H. & Zhang, M. Highly Selective Protein Patterning on Gold-Silicon Substrates for Biosensor Applications. *Langmuir* 18, 6671-6678, doi:10.1021/la025529j (2002).
- 273 Schlapak, R. *et al.* Glass Surfaces Grafted with High-Density Poly(ethylene glycol) as Substrates for DNA Oligonucleotide Microarrays. *Langmuir* 22, 277-285 (2006).
- 274 Schlapak, R., Armitage, D., Saucedo-Zeni, N., Hohage, M. & Howorka, S. Dense Passivating Poly(ethylene glycol) Films on Indium Tin Oxide Substrates. *Langmuir* 23, 10244-10253, doi:10.1021/la7011414 (2007).
- 275 Blümmel, J. *Entwicklung biofunktionalisierter Nanostrukturen an Grenzflächen zur Untersuchung der Kinetik des molekularen Motorproteins Eg5* PhD thesis, University of Heidelberg, (2005).
- 276 Rusmini, F., Zhong, Z. & Feijen, J. Protein Immobilization Strategies for Protein Biochips. *Biomacromolecules* 8, 1775-1789, doi:10.1021/bm061197b (2007).

- 277 Shacter, E. Quantification and significance of protein oxidation in biological samples. *Drug Metab Rev* 32, 307-326, doi:doi:10.1081/DMR-100102336 (2000).
- 278 Hubbell, J. A. Bioactive biomaterials. *Curr. Opin. Biotechnol.* 10, 123-129 (1999).
- 279 Sauerbrey, G. Verwendung von Schwingquarzen zur Wägung dünner Schichten und zur Mikrowägung. *Zeitschrift für Physik A Hadrons and Nuclei* 155, 206-222 (1959).
- 280 Johannsmann, D., Mathauer, K., Wegner, G. & Knoll, W. Viscoelastic properties of thin films probed with a quartz-crystal resonator. *Phys. Rev. B* 46, 7808 (1992).
- 281 Schumacher, R. The Quartz Microbalance: A Novel Approach to the In-Situ Investigation of Interfacial Phenomena at the Solid/Liquid Junction [New Analytical Methods (40)]. *Angew. Chem. Int. Ed.* 29, 329-343 (1990).
- 282 Elwing, H. Protein absorption and ellipsometry in biomaterial research. *Biomaterials* 19, 397-406 (1998).
- 283 Hook, F. *et al.* Variations in coupled water, viscoelastic properties, and film thickness of a Mefp-1 protein film during adsorption and cross-linking: a quartz crystal microbalance with dissipation monitoring, ellipsometry, and surface plasmon resonance study. *Anal. Chem* 73, 5796-5804 (2001).
- 284 Höök, F. *et al.* A comparative study of protein adsorption on titanium oxide surfaces using in situ ellipsometry, optical waveguide lightmode spectroscopy, and quartz crystal microbalance/dissipation. *Colloids Surf., B* 24, 155-170 (2002).
- 285 Tengvall, P., Lundström, I. & Liedberg, B. Protein adsorption studies on model organic surfaces: an ellipsometric and infrared spectroscopic approach. *Biomaterials* 19, 407-422 (1998).
- 286 Malmsten, M. Ellipsometry studies of the effects of surface hydrophobicity on protein adsorption. *Colloids Surf., B* 3, 297-308 (1995).
- 287 Poksinski, M. & Arwin, H. Protein monolayers monitored by internal reflection ellipsometry. *Thin Solid Films* 455, 716-721 (2004).
- 288 Spaeth, K., Brecht, A. & Gauglitz, G. Studies on the Biotin-Avidin Multilayer Adsorption by Spectroscopic Ellipsometry. *J Colloid Interface Sci* 196, 128-135 (1997).
- 289 Bae, Y. M., Oh, B. K., Lee, W., Lee, W. H. & Choi, J. W. Study on orientation of immunoglobulin G on protein G layer. *Biosensors and Bioelectronics* 21, 103-110 (2005).
- 290 Blümmel, J. *et al.* Protein repellent properties of covalently attached PEG coatings on nanostructured SiO₂-based interfaces. *Biomaterials* 28, 4739-4747 (2007).
- 291 Colthup, N. B., Daly, L. H. & Wiberley, S. E. *Introduction to infrared and Raman spectroscopy.* (Academic Press New York, 1964).
- 292 de Coninck, J. & Dunlop, F. Partial to complete wetting: A microscopic derivation of the Young relation. *J. Stat. Phys.* 47, 827-849 (1987).
- 293 Huang, J. *et al.* Impact of Order and Disorder in RGD Nanopatterns on Cell Adhesion. *Nano Letters* 9, 1111-1116, doi:10.1021/nl803548b (2009).
- 294 Zhang, Y., Sheng, S. & Shao, Z. Imaging biological structures with the cryo atomic force microscope. *Biophys. J.* 71, 2168-2176 (1996).
- 295 Coen, M. C. *et al.* Adsorption and bioactivity of protein A on silicon surfaces studied by AFM and XPS. *J. Colloid Interface Sci.* 233, 180-189 (2001).
- 296 Reinhart-King, C. A., Dembo, M. & Hammer, D. A. The dynamics and mechanics of endothelial cell spreading. *Biophys. J.* 89, 676-689 (2005).
- 297 Remes, A. & Williams, D. Immune response in biocompatibility. *The Biomaterials Silver Jubilee Compendium the Best Papers Published in Biomaterials, 1980-2004* 13, 11-79 (2006).
- 298 Edelson, P., Zwiebel, R. & Cohn, Z. The pinocytotic rate of activated macrophages. *J. Exp. Med.* 142, 1150 (1975).
- 299 Bradley, S. G. Cellular and Molecular Mechanisms of Action of Bacterial Endotoxins. *Annu. Rev. Microbiol.* 33, 67-94, doi:10.1146/annurev.mi.33.100179.000435 (2003).
- 300 Elin, R. J. & Wolff, S. M. Biology of Endotoxin. *Annu. Rev. Med.* 27, 127-141, doi:10.1146/annurev.me.27.020176.001015 (2003).
- 301 Glass, R. *et al.* Block copolymer micelle nanolithography on non-conductive substrates. *New J. Phys.* 6, 101 (2004).
- 302 Amano, F. & Akamatsu, Y. A lipopolysaccharide (LPS)-resistant mutant isolated from a macrophagelike cell line, J774.1, exhibits an altered activated-macrophage phenotype in response to LPS. *Infect. Immun.* 59, 2166-2174 (1991).
- 303 Eccles, M. H. & Glauert, A. M. The response of human monocytes to interaction with immobilized immune complexes. *J. Cell Sci.* 71, 141 (1984).
- 304 Oliver, R. C., Glauert, A. M. & Thorne, K. J. Mechanism of Fc-mediated interaction of eosinophils with immobilized immune complexes: I. Effects of inhibitors and activators of eosinophil function. *J. Cell Sci.* 56, 337 (1982).
- 305 Cannon, G. J. & Swanson, J. A. The macrophage capacity for phagocytosis. *J. Cell Sci.* 101, 907 (1992).
- 306 Tracey, M. D. K. J. & Cerami, P. D. A. Tumor Necrosis Factor: A Pleiotropic Cytokine and Therapeutic Target. *Annu. Rev. Med.* 45, 491-503, doi:10.1146/annurev.med.45.1.491 (2003).
- 307 Nathan, C. F. Secretory products of macrophages. *The Journal of Clinical Investigation* 79, 319-326 (1987).

- 308 Beutler, B. & Cerami, A. Cachectin and tumour necrosis factor as two sides of the same biological coin. **Nature** 320, 584-588 (1986).
- 309 Moldawer, L. *et al.* Cachectin/tumor necrosis factor- α alters red blood cell kinetics and induces anemia in vivo. **FASEB J.** 3, 1637-1643 (1989).
- 310 Karin, M. & Greten, F. R. NF- κ B: linking inflammation and immunity to cancer development and progression. **Nature Reviews Immunology** 5, 749 (2005).
- 311 Moore, K. W., O'Garra, A., Malefyt, R. W., Vieira, P. & Mosmann, T. R. Interleukin-10. **Annu. Rev. Immunol.** 11, 165-190 (1993).
- 312 de Waal Malefyt, R., Abrams, J., Bennett, B., Figdor, C. G. & De Vries, J. E. Interleukin 10 (IL-10) inhibits cytokine synthesis by human monocytes: an autoregulatory role of IL-10 produced by monocytes. **J. Exp. Med.** 174, 1209 (1991).
- 313 Fiorentino, D. F., Zlotnik, A., Mosmann, T. R., Howard, M. & O'Garra, A. IL-10 inhibits cytokine production by activated macrophages. **J. Immunol.** 147, 3815 (1991).
- 314 de Waal Malefyt, R. *et al.* Effects of IL-13 on phenotype, cytokine production, and cytotoxic function of human monocytes. Comparison with IL-4 and modulation by IFN- γ or IL-10. **J. Immunol.** 151, 6370 (1993).
- 315 D'Andrea, A. *et al.* Interleukin 10 (IL-10) inhibits human lymphocyte interferon gamma-production by suppressing natural killer cell stimulatory factor/IL-12 synthesis in accessory cells. **J. Exp. Med.** 178, 1041 (1993).
- 316 Gruber, M. F., Williams, C. C. & Gerrard, T. L. Macrophage-colony-stimulating factor expression by anti-CD45 stimulated human monocytes is transcriptionally up-regulated by IL-1 β and inhibited by IL-4 and IL-10. **J. Immunol.** 152, 1354 (1994).
- 317 Moore, K. W., de Waal Malefyt, R., Coffman, R. L. & O'Garra, A. Interleukin-10 and the Interleukin-10 Receptor. **Annu. Rev. Immunol.** 19, 683-765, doi:10.1146/annurev.immunol.19.1.683 (2003).
- 318 Blobel, G. C., Schiemann, W. P. & Lodish, H. F. Role of transforming growth factor in human disease. **N Engl J Med** 342, 1350-1358 (2000).
- 319 Li, M. O., Wan, Y. Y., Sanjabi, S., Robertson, A. K. L. & Flavell, R. A. Transforming growth factor-regulation of immune responses. (2006).
- 320 Cupp, A. S., Kim, G. & Skinner, M. K. Expression and Action of Transforming Growth Factor Beta (TGF β 1, TGF β 2, and TGF β 3) during Embryonic Rat Testis Development. **Biology of Reproduction** 60, 1304-1313 (1999).
- 321 Massagué, J., Blain, S. W. & Lo, R. S. TGF signaling in growth control, cancer, and heritable disorders. **Cell** 103, 295-309 (2000).
- 322 Wahl, S. M. *et al.* Transforming growth factor type beta induces monocyte chemotaxis and growth factor production. **Proc Natl Acad Sci U S A** 84, 5788 (1987).
- 323 Throckmorton, D. C., Brogden, A. P., Min, B., Rasmussen, H. & Kashgarian, M. PDGF and TGF- β mediate collagen production by mesangial cells exposed to advanced glycosylation end products. **Kidney Int** 48, 111-117 (1995).
- 324 Varga, J., Rosenbloom, J. & Jimenez, S. A. Transforming growth factor beta (TGF β) causes a persistent increase in steady-state amounts of type I and type III collagen and fibronectin mRNAs in normal human dermal fibroblasts. **Biochemical Journal** 247, 597 (1987).
- 325 Wikner, N. E., Persichitte, K. A., Baskin, J. B., Nielsen, L. D. & Clark, R. A. F. Transforming Growth Factor- β Stimulates the Expression of Fibronectin by Human Keratinocytes. **J Investig Dermatol** 91, 207-212 (1988).
- 326 Refai, A. K., Textor, M., Brunette, D. M. & Waterfield, J. D. Effect of titanium surface topography on macrophage activation and secretion of proinflammatory cytokines and chemokines. **J. Biomed. Mater. Res. Part A.** 70, 194-205 (2004).
- 327 Chou, L., Firth, J. D., Uitto, V. J. & Brunette, D. M. Effects of titanium substratum and grooved surface topography on metalloproteinase-2 expression in human fibroblasts. **J. Biomed. Mater. Res.** 39, 437-445 (1998).
- 328 Martin, J. Y. *et al.* Effect of titanium surface roughness on proliferation, differentiation, and protein synthesis of human osteoblast-like cells (MG63). **J. Biomed. Mater. Res.** 29, 389-402 (1995).
- 329 Brodbeck, W. G. *et al.* Biomaterial surface chemistry dictates adherent monocyte/macrophage cytokine expression in vitro. **Cytokine** 18, 311-319 (2002).
- 330 Brodbeck, W. G. *et al.* Biomaterial adherent macrophage apoptosis is increased by hydrophilic and anionic substrates in vivo. **Proc Natl Acad Sci U S A** 99, 10287 (2002).
- 331 Brodbeck, W. G. *et al.* In vivo leukocyte cytokine mRNA responses to biomaterials are dependent on surface chemistry. **J. Biomed. Mater. Res.** 64, 320-329 (2003).
- 332 Ashkenazi, A. & Dixit, V. M. Death receptors: signaling and modulation. **Science** 281, 1305 (1998).
- 333 Nagata, S. Apoptosis by death factor. **Cell** 88, 355-366 (1997).
- 334 Thompson, E. B. Apoptosis. **Annu Rev Physiol** 60, 525-532, doi:10.1146/annurev.physiol.60.1.525 (2003).
- 335 Arnold, M. *et al.* Activation of Integrin Function by Nanopatterned Adhesive Interfaces. **ChemPhysChem** 5, 383-388 (2004).
- 336 Torre, D. *et al.* Anti-inflammatory response of IL-4, IL-10 and TGF- β in patients with systemic inflammatory response syndrome. **Mediators of Inflammation** 9, 193 (2000).

- 337 Bogdan, C. & Nathan, C. Modulation of macrophage function by transforming growth factor beta, interleukin-4, and interleukin-10. *Annals of the New York Academy of Sciences* 685, 713 (1993).
- 338 Ulich, T. R. *et al.* Intratracheal injection of endotoxin and cytokines. II. Interleukin-6 and transforming growth factor beta inhibit acute inflammation. *The American Journal of Pathology* 138, 1097 (1991).
- 339 Lind, M. Growth factor stimulation of bone healing. Effects on osteoblasts, osteomies, and implants fixation. *Acta orthopaedica Scandinavica. Supplementum* 283, 2 (1998).
- 340 Balooch, G. *et al.* TGF- β regulates the mechanical properties and composition of bone matrix. *Proc Natl Acad Sci U S A* 102, 18813-18818, doi:10.1073/pnas.0507417102 (2005).
- 341 Mistry, A. S. & Mikos, A. G. Tissue engineering strategies for bone regeneration. *Adv. Biochem. Eng. Biotechnol.* 94, 1-22 (2005).
- 342 Chiu, D. T. *et al.* Patterned deposition of cells and proteins onto surfaces by using three-dimensional microfluidic systems. *Proc Natl Acad Sci U S A* 97, 2408-2413 (2000).
- 343 Mendes, P., Yeung, C. & Preece, J. Bio-nanopatterning of Surfaces. *Nano. Res. Lett.* 2, 373-384 (2007).
- 344 Salaita, K., Wang, Y. & Mirkin, C. A. Applications of dip-pen nanolithography. *Nature Nanotech.* 2, 145-155 (2007).
- 345 Nie, Z. & Kumacheva, E. Patterning surfaces with functional polymers. *Nat. Mater.* 7, 277-290 (2008).
- 346 Huo, F. *et al.* Polymer Pen Lithography. *Science* 321, 1658-1660, doi:10.1126/science.1162193 (2008).
- 347 Bita, I. *et al.* Graphoepitaxy of Self-Assembled Block Copolymers on Two-Dimensional Periodic Patterned Templates. *Science* 321, 939-943, doi:10.1126/science.1159352 (2008).
- 348 Lin, C., Liu, Y. & Yan, H. Self-Assembled Combinatorial Encoding Nanoarrays for Multiplexed Biosensing. *Nano Letters* 7, 507-512, doi:10.1021/nl062998n (2007).
- 349 Gadegaard, N., Martines, E., Riehle, M. O., Seunarine, K. & Wilkinson, C. D. W. Applications of nanopatterning to tissue engineering. *Microelectron. Eng.* 83, 1577-1581.
- 350 Brodbeck, W. G. *et al.* Influence of biomaterial surface chemistry on the apoptosis of adherent cells. *J. Biomed. Mater. Res.* 55, 661-668 (2001).
- 351 Hunt, J. A., Flanagan, B. F., McLaughlin, P. J., Strickland, I. & Williams, D. F. Effect of biomaterial surface charge on the inflammatory response: evaluation of cellular infiltration and TNF α production. *J. Biomed. Mater. Res.* 31, 139-144 (1996).
- 352 Hench, L. L. & Ethridge, E. C. Biomaterials-the interfacial problem. *Adv Biomed Eng* 5, 35-150 (1975).
- 353 Jones, J. A. *et al.* Proteomic analysis and quantification of cytokines and chemokines from biomaterial surface-adherent macrophages and foreign body giant cells. *J. Biomed. Mater. Res. Part A* 83, 585 (2007).
- 354 Shen, M. & Horbett, T. A. The effects of surface chemistry and adsorbed proteins on monocyte/macrophage adhesion to chemically modified polystyrene surfaces. *J. Biomed. Mater. Res.* 57, 336-345 (2001).
- 355 MacKintosh, E. E., Patel, J. D., Marchant, R. E. & Anderson, J. M. Effects of biomaterial surface chemistry on the adhesion and biofilm formation of *Staphylococcus epidermidis* in vitro. *J. Biomed. Mater. Res. Part A* 78, 836 (2006).
- 356 Suchanek, W. & Yoshimura, M. Processing and properties of hydroxyapatite-based biomaterials for use as hard tissue replacement implants. *J. Mater. Res.* 13, 94-117 (1998).
- 357 Lewis, A., Tolhurst, L. & Stratford, P. Analysis of a phosphorylcholine-based polymer coating on a coronary stent pre-and post-implantation. *Biomaterials* 23, 1697-1706 (2002).
- 358 Abraham, S., Brahim, S., Ishihara, K. & Guiseppi-Elie, A. Molecularly engineered p (HEMA)-based hydrogels for implant biochip biocompatibility. *Biomaterials* 26, 4767-4778 (2005).
- 359 Price, J., Tencer, A., Arm, D. & Bohach, G. Controlled release of antibiotics from coated orthopedic implants. *J. Biomed. Mater. Res.* 30, 281-286 (1996).
- 360 Schmidmaier, G., Wildemann, B., Stemberger, A., Haas, N. & Raschke, M. Biodegradable poly (D, L-lactide) coating of implants for continuous release of growth factors. *J. Biomed. Mater. Res.* 58, 449-455 (2001).
- 361 Schmidmaier, G., Lucke, M., Wildemann, B., Haas, N. & Raschke, M. Prophylaxis and treatment of implant-related infections by antibiotic-coated implants: a review. *Injury* 37, 105-112 (2006).
- 362 Liu, Y., De Groot, K. & Hunziker, E. BMP-2 liberated from biomimetic implant coatings induces and sustains direct ossification in an ectopic rat model. *Bone* 36, 745-757 (2005).
- 363 Hetrick, E. & Schoenfisch, M. Reducing implant-related infections: active release strategies. *Chem. Soc. Rev* 35, 780-789 (2006).
- 364 CDRH. (ed Division of General Orthopedic Devices Branch, Restorative, and Neurological Devices, Office of Device Evaluation, FDA) (2002).
- 365 Ling, M. M., Ricks, C. & Lea, P. Multiplexing molecular diagnostics and immunoassays using emerging microarray technologies. *Expert Rev Mol Diagn* 7, 87-98, doi:10.1586/14737159.7.1.87 (2007).
- 366 Malinowski, D. P. Multiple biomarkers in molecular oncology. I. Molecular diagnostics applications in cervical cancer detection. *Expert Rev Mol Diagn* 7, 117-131, doi:doi:10.1586/14737159.7.2.117 (2007).
- 367 Frédéric A. Denis, A. P., Bernard Nysten, Alain M. Jonas, Christine C. Dupont-Gillain,. Alignment and Assembly of Adsorbed Collagen Molecules Induced by Anisotropic Chemical Nanopatterns. *Small* 1, 984-991 (2005).

- 368 Huang, H., Kamm, R. D. & Lee, R. T. Cell mechanics and mechanotransduction: pathways, probes, and physiology. *Am J Physiol Cell Physiol* 287, C1-11, doi:10.1152/ajpcell.00559.2003 (2004).
- 369 Lee, K.-B., Park, S.-J., Mirkin, C. A., Smith, J. C. & Mrksich, M. Protein Nanoarrays Generated By Dip-Pen Nanolithography. *Science* 295, 1702-1705, doi:10.1126/science.1067172 (2002).
- 370 Wadu-Mesthrige, K., Xu, S., Amro, N. A. & Liu, G.-y. Fabrication and Imaging of Nanometer-Sized Protein Patterns. *Langmuir* 15, 8580-8583, doi:10.1021/la991196n (1999).
- 371 Zhao, Z., Banerjee, I. A. & Matsui, H. Simultaneous Targeted Immobilization of Anti-Human IgG-Coated Nanotubes and Anti-Mouse IgG-Coated Nanotubes on the Complementary Antigen-Patterned Surfaces via Biological Molecular Recognition. *J. Am. Chem. Soc* 127, 8930-8931, doi:10.1021/ja051053p (2005).
- 372 Bruckbauer, A. *et al.* An Addressable Antibody Nanoarray Produced on a Nanostructured Surface. *J. Am. Chem. Soc* 126, 6508-6509, doi:10.1021/ja0317426 (2004).
- 373 Kobayashi, Y. *et al.* Writing and Reading Methodology for Biochips with Sub-100-nm Chemical Patterns Based on Near-Field Scanning Optical Microscopy. *Anal. Sci.* 24, 571-576 (2008).
- 374 Wei, B. Q. *et al.* Microfabrication technology: Organized assembly of carbon nanotubes. *Nature* 416, 495-496 (2002).
- 375 Lazzari, M. & López-Quintela, M. A. Block Copolymers as a Tool for Nanomaterial Fabrication. *Adv. Mater.* 15, 1583-1594 (2003).
- 376 S. W. Lee, B.-K. O., R. G. Sanedrin, K. Salaita, T. Fujigaya, C. A. Mirkin,. Biologically Active Protein Nanoarrays Generated Using Parallel Dip-Pen Nanolithography. *Adv. Mater.* 18, 1133-1136 (2006).
- 377 Tinazli, A., Piehler, J., Beuttler, M., Guckenberger, R. & Tampe, R. Native protein nanolithography that can write, read and erase. *Nature Nanotech.* 2, 220-225 (2007).
- 378 David S. Ginger, H. Z., Chad A. Mirkin,. The Evolution of Dip-Pen Nanolithography. *Angew. Chem. Int. Ed.* 43, 30-45 (2004).
- 379 Hoff, J. D., Cheng, L.-J., Meyhofer, E., Guo, L. J. & Hunt, A. J. Nanoscale Protein Patterning by Imprint Lithography. *Nano Letters* 4, 853-857, doi:10.1021/nl049758x (2004).
- 380 Cai, Y. & Ocko, B. M. Large-Scale Fabrication of Protein Nanoarrays Based on Nanosphere Lithography. *Langmuir* 21, 9274-9279, doi:10.1021/la051656e (2005).
- 381 Yan, H., Park, S. H., Finkelstein, G., Reif, J. H. & LaBean, T. H. DNA-Templated Self-Assembly of Protein Arrays and Highly Conductive Nanowires. *Science* 301, 1882-1884, doi:10.1126/science.1089389 (2003).
- 382 Park, S. H. *et al.* Programmable DNA Self-Assemblies for Nanoscale Organization of Ligands and Proteins. *Nano Letters* 5, 729-733, doi:10.1021/nl050175c (2005).
- 383 Li, H.-W., Muir, B. V. O., Fichet, G. & Huck, W. T. S. Nanocontact Printing: A Route to Sub-50-nm-Scale Chemical and Biological Patterning. *Langmuir* 19, 1963-1965, doi:10.1021/la0269098 (2003).
- 384 Wilson, D. L. *et al.* Surface organization and nanopatterning of collagen by dip-pen nanolithography. *Proc Natl Acad Sci U S A* 98, 13660-13664 (2001).
- 385 Taha, H. *et al.* Protein printing with an atomic force sensing nanofountainpen. *Appl. Phys. Lett.* 83, 1041-1043 (2003).
- 386 Agarwal, G., Naik, R. R. & Stone, M. O. Immobilization of Histidine-Tagged Proteins on Nickel by Electrochemical Dip Pen Nanolithography. *J. Am. Chem. Soc* 125, 7408-7412, doi:10.1021/ja029856p (2003).
- 387 Szoszkiwicz, R. *et al.* High-Speed, Sub-15 nm Feature Size Thermochemical Nanolithography. *Nano Letters* 7, 1064-1069, doi:10.1021/nl070300f (2007).
- 388 Christman, K. L. *et al.* Submicron Streptavidin Patterns for Protein Assembly. *Langmuir* 22, 7444-7450, doi:10.1021/la0608213 (2006).
- 389 Welle, A. M. & Jacobs, H. O. Printing of organic and inorganic nanomaterials using electrospray ionization and Coulomb-force-directed assembly. *Appl. Phys. Lett.* 87, 263119 (2005).
- 390 Zhu, X. *et al.* Fabrication of reconfigurable protein matrices by cracking. *Nat. Mater.* 4, 403-406 (2005).
- 391 Patolsky, F. *et al.* Electrical detection of single viruses. *Proc Natl Acad Sci U S A* 101, 14017-14022, doi:10.1073/pnas.0406159101 (2004).
- 392 Kumagai, S. *et al.* Electrostatic placement of single ferritin molecules. *Appl. Phys. Lett.* 88, 153103-153103 (2006).
- 393 Bergman, A. A. *et al.* Nanometer-Scale Arrangement of Human Serum Albumin by Adsorption on Defect Arrays Created with a Finely Focused Ion Beam. *Langmuir* 14, 6785-6788, doi:10.1021/la980642o (1998).
- 394 Kimura, M., Shimizu, M., Tanaka, S. & Tamaru, Y. Pd-catalyzed nucleophilic allylic alkylation of aliphatic aldehydes by the use of allyl alcohols. *Tetrahedron* 61, 3709-3718 (2005).
- 395 Zhang, Y.-D. *et al.* Photo-crosslinkable polymers as hole-transport materials for organic light-emitting diodes. *J. Mater. Chem* 12, 1703-1708 (2002).
- 396 Prucker, O., Naumann, C. A., Ruhe, J., Knoll, W. & Frank, C. W. Photochemical Attachment of Polymer Films to Solid Surfaces via Monolayers of Benzophenone Derivatives. *J. Am. Chem. Soc* 121, 8766-8770, doi:10.1021/ja990962+ (1999).
- 397 Griep-Raming, N., Karger, M. & Menzel, H. Using Benzophenone-Functionalized Phosphonic Acid To Attach Thin Polymer Films to Titanium Surfaces. *Langmuir* 20, 11811-11814, doi:10.1021/la0485327 (2004).

- 398 Jungchul, L. *et al.* Electrical, Thermal, and Mechanical Characterization of Silicon Microcantilever Heaters. *J Microelectromech S* 15, 1644-1655 (2006).
- 399 Wang, D. B. *et al.* Local wettability modification by thermochemical nanolithography with write-read-overwrite capability. *Appl. Phys. Lett.* 91, 243104-243103 (2007).
- 400 A. W. Coats, J. P. R. Thermogravimetric analysis. A review. *Analyst* 88, 906 - 924, doi:10.1039/AN9638800906 (1963).
- 401 Piner, R. D., Zhu, J., Xu, F., Hong, S. & Mirkin, C. A. "Dip-Pen" Nanolithography. *Science* 283, 661-663, doi:10.1126/science.283.5402.661 (1999).
- 402 Sheehan, P. E., Whitman, L. J., King, W. P. & Nelson, B. A. Nanoscale deposition of solid inks via thermal dip pen nanolithography. *Appl. Phys. Lett.* 85, 1589-1591 (2004).
- 403 Hermanson, G. T. *Bioconjugate Techniques*. 2 - 2008 edn, (Academic Press).
- 404 Heitzmann, H. & Richards, F. M. Use of the Avidin-Biotin Complex for Specific Staining of Biological Membranes in Electron Microscopy. *Proc Natl Acad Sci U S A* 71, 3537-3541 (1974).
- 405 Meir Wilchek, E. A. B. The avidin-biotin complex in bioanalytical applications. *Anal Biochem* 171, 1-32, doi:10.1016/0003-2697(88)90120-0 (1988).
- 406 Cumber AJ, F. J., Foxwell BM, Ross WC, Thorpe PE. in *Methods Enzymol* Vol. 112 207-225 (1985).
- 407 Hu, Y., Das, A., Hecht, M. H. & Scoles, G. Nanografting De Novo Proteins onto Gold Surfaces. *Langmuir* 21, 9103-9109, doi:doi:10.1021/la046857h (2005).
- 408 Braun, E., Eichen, Y., Sivan, U. & Ben-Yoseph, G. DNA-templated assembly and electrode attachment of a conducting silver wire. *Nature* 391, 775-778 (1998).
- 409 Porath, D., Bezryadin, A., de Vries, S. & Dekker, C. Direct measurement of electrical transport through DNA molecules. *Nature* 403, 635-638 (2000).
- 410 Fink, H.-W. & Schonenberger, C. Electrical conduction through DNA molecules. *Nature* 398, 407-410 (1999).
- 411 Khrapko, K. R. *et al.* An oligonucleotide hybridization approach to DNA sequencing. *FEBS Lett.* 256, 118-122 (1989).
- 412 Alper, J. Drug Discovery on the Assembly Line. *Science* 264, 1399-1401 (1994).
- 413 Ramsay, G. DNA chips: State-of-the art. *Nat Biotech* 16, 40-44 (1998).
- 414 Doh, J. & Irvine, D. J. Immunological synapse arrays: Patterned protein surfaces that modulate immunological synapse structure formation in T cells. *Proc Natl Acad Sci U S A* 103, 5700-5705, doi:10.1073/pnas.0509404103 (2006).
- 415 Duncan, R. & Izzo, L. Dendrimer biocompatibility and toxicity. *Adv. Drug Delivery Rev.* 57, 2215-2237 (2005).
- 416 Harris, Z. *Poly(ethylene glycol) chemistry and biological applications*. Vol. 680 (ACS Symp. Ser. 680, 1997).
- 417 McPherson, T., Kidane, A., Szleifer, I. & Park, K. Prevention of Protein Adsorption by Tethered Poly(ethylene oxide) Layers: Experiments and Single-Chain Mean-Field Analysis. *Langmuir* 14, 176-186, doi:doi:10.1021/la9706781 (1998).
- 418 Delamarche, E. *et al.* Microcontact Printing Using Poly(dimethylsiloxane) Stamps Hydrophilized by Poly(ethylene oxide) Silanes. *Langmuir* 19, 8749-8758, doi:doi:10.1021/la034370n (2003).
- 419 Papra, A. *et al.* Microfluidic Networks Made of Poly(dimethylsiloxane), Si, and Au Coated with Polyethylene Glycol for Patterning Proteins onto Surfaces. *Langmuir* 17, 4090-4095, doi:doi:10.1021/la0016930 (2001).
- 420 Herrwerth, S., Eck, W., Reinhardt, S. & Grunze, M. Factors that Determine the Protein Resistance of Oligoether Self-Assembled Monolayers - Internal Hydrophilicity, Terminal Hydrophilicity, and Lateral Packing Density. *J. Am. Chem. Soc* 125, 9359-9366, doi:doi:10.1021/ja034820y (2003).
- 421 Jeon, S. I., Lee, J. H., Andrade, J. D. & De Gennes, P. G. Protein-surface interactions in the presence of polyethylene oxide: I. Simplified theory. *J. Colloid Interface Sci.* 142, 149-158 (1991).
- 422 Feldman, K., Hahner, G., Spencer, N. D., Harder, P. & Grunze, M. Probing Resistance to Protein Adsorption of Oligo(ethylene glycol)-Terminated Self-Assembled Monolayers by Scanning Force Microscopy. *J. Am. Chem. Soc* 121, 10134-10141, doi:doi:10.1021/ja991049b (1999).
- 423 Vogler, E. A. Structure and reactivity of water at biomaterial surfaces. *Adv. Colloid Interface Sci.* 74, 69-117 (1998).
- 424 Harris, J. M. *Poly(ethylene glycol) chemistry: biotechnical and biomedical applications*. (Plenum Press New York, 1992).
- 425 Inoue, S., Kakikawa, H., Nakadan, N., Imabayashi, S.-i. & Watanabe, M. Thermal Response of Poly(ethoxyethyl glycidyl ether) Grafted on Gold Surfaces Probed on the Basis of Temperature-Dependent Water Wettability. *Langmuir* 25, 2837-2841 (2009).
- 426 Chan, Y.-H. M., Schweiss, R., Werner, C. & Grunze, M. Electrokinetic Characterization of Oligo- and Poly(ethylene glycol)-Terminated Self-Assembled Monolayers on Gold and Glass Surfaces. *Langmuir* 19, 7380-7385, doi:doi:10.1021/la0343977 (2003).
- 427 Pale-Grosdemange, C., Simon, E. S., Prime, K. L. & Whitesides, G. M. Formation of self-assembled monolayers by chemisorption of derivatives of oligo(ethylene glycol) of structure HS(CH₂)₁₁(OCH₂CH₂)_mOH on gold. *J. Am. Chem. Soc* 113, 12-20 (1991).

- 428 Norde, W. & Gage, D. Interaction of Bovine Serum Albumin and Human Blood Plasma with PEO-Tethered Surfaces: Influence of PEO Chain Length, Grafting Density, and Temperature. *Langmuir* 20, 4162-4167, doi:10.1021/la030417t (2004).

